FINAL REPORT

Demonstration of a Fractured Rock Geophysical Toolbox (FRGT) for Characterization and Monitoring of DNAPL Biodegradation in Fractured Rock Aquifers

ESTCP Project ER-201118

SEPTEMBER 2015

Lee Slater
Rutgers University – Newark

Fred Day-Lewis
U.S. Geological Survey

Judy Robinson
Rutgers University – Newark

Tim Johnson
Pacific Northwest National Laboratory

ESTCP

REPORT DOCUMENTATION PAGE

Form Approved
OMB No. 0704-0188

1. REPORT DATE *(DD-MM-YYYY)*
29-09-2015

2. REPORT TYPE
Final Report

3. DATES COVERED *(From - To)*

4. TITLE AND SUBTITLE

Demonstration of a Fractured Rock Geophysical Toolbox (FRGT) for Characterization and Monitoring of DNAPL Biodegradation in Fractured Rock Aquifers

5a. CONTRACT NUMBER
W912HQ-11-C-0027

5b. GRANT NUMBER

5c. PROGRAM ELEMENT NUMBER

6. AUTHOR(S)
Slater, Lee; Day-Lewis, Fred; Robinson, Judy; Johnson, Tim.

5d. PROJECT NUMBER
ER-201118

5e. TASK NUMBER

5f. WORK UNIT NUMBER

7. PERFORMING ORGANIZATION NAME(S) AND ADDRESS(ES)

Department of
Earth/Environmental Science
101 Warren Street
Newark, NJ 07102

8. PERFORMING ORGANIZATION REPORT NUMBER

9. SPONSORING / MONITORING AGENCY NAME(S) AND ADDRESS(ES)
SERDP/ESTCP
4800 Mark Center Drive
Suite 17D08
Alexandria, VA 22350-6386

10. SPONSOR/MONITOR'S ACRONYM(S)
ESTCP

11. SPONSOR/MONITOR'S REPORT NUMBER(S)
ER-201118

12. DISTRIBUTION / AVAILABILITY STATEMENT

Approved for public release; distribution is unlimited

13. SUPPLEMENTARY NOTES

14. ABSTRACT
The overall objective of this project is to demonstrate a method for characterization and monitoring of dense non-aqueous phase liquid (DNAPL) biodegradation (including free and dissolved phase) in fractured rock aquifers based on a fractured rock geophysical toolbox (FRGT). Specific technical objectives include demonstrations of (1) fracture network characterization using geophysical methods sensitive to fracture strike and dip patterns and spanning a wide range of measurement scales; (2) long-term, minimally invasive autonomous monitoring of proxies of the timing and extent of amendment delivery and/or DNAPL degradation in fractured rock using combined geophysical and geochemical measurements sensitive to biodegradation; (3) the application of "informed" inversion to produce estimates of fracture location, distribution, and orientation with better resolution than is currently possible with commercially available tools; and (4) identification and monitoring of geophysical attributes that are soft measures of progress of DNAPL biodegradation in fractured rock. The project team aims to demonstrate how such geophysically imaged "soft" hydrological information can be used to guide decisions regarding sampling frequency and duration. This effort will include comparison of dense 4D geophysical monitoring results with sparser (in time and space) point chemistry data in order to fully understand geophysical signatures of DNAPL amendment treatments and remediation processes.

15. SUBJECT TERMS

16. SECURITY CLASSIFICATION OF:

a. REPORT	b. ABSTRACT	c. THIS PAGE

17. LIMITATION OF ABSTRACT

18. NUMBER OF PAGES

19a. NAME OF RESPONSIBLE PERSON
Lee Slater

19b. TELEPHONE NUMBER *(include area code)*
973-353-5109

Standard Form 298 (Rev. 8-98)
Prescribed by ANSI Std. Z39.18

TABLE OF CONTENTS

LIST OF FIGURES

viii

LIST OF TABLES

ACRONYM LIST

ATV	Acoustical televiewer
BOC	Bottom of casing
COTS	Commercial off-the-shelf
cDCE	cis-dichloroethylene
CVOC	Chlorinated volatile organic compound
DNAPL	Dense non-aqueous phase liquid
E4D	4D electrical resistivity tomography forward and inverse modeling code
ERT	Electrical resistivity tomography
FEM	Finite element mesh
FRGT	Fractured Rock Geophysical Toolbox
GPR	Ground penetrating radar
HPFM	Heat pulse flow meter
NAWC	Naval Air Warfare Center
OTV	Optical televiewer
SC	Fluid specific conductance
SP	Self potential
TOC	Top of casing
TCE	Trichloroethylene
VOC	Volatile organic compound
VC	Vinyl chloride
$\mathbf{W_m}$	Model regularization matrix
σ	Conductivity
ρ	Resistivity

ACKNOWLEDGEMENTS

EXECUTIVE SUMMARY

OBJECTIVES OF THE DEMONSTRATION

Contaminated sites in fractured rock are particularly difficult and expensive to remediate, because characterization and monitoring is problematic in the presence of extreme heterogeneity. The performance objectives of this demonstration focused on evaluating: [1] fracture network characterization using a fractured rock geophysics toolbox (FRGT); [2] autonomous monitoring of amendment delivery and subsequent contaminant biodegradation using geophysical technologies that sense beyond the borehole; [3] application of an 'informed inversion strategy' to improve the geophysical imaging of fractured rock settings relative to what can currently be achieved with off-the-shelf functionality. Specific performance objectives were largely met, although the physical characteristics of the primary demonstration site, being the Naval Air Warfare Center (NAWC) in W. Trenton (NJ), limited the performance of some methods in the FRGT. The primary benefit of the FRGT is the ability to provide information on variations in physical properties and the fate of amendment injections into fractured rock beyond the vicinity of local borehole observations. The potential impact on DOD operations relates to improved management decisions that can result from an improved understanding of flow and transport processes at fractured rock site, particularly the effectiveness of amendment treatments in targeting contaminants of concern.

TECHNOLOGY DESCRIPTION

In the FRGT, geophysical characterization data are fed into the processing of geophysical monitoring datasets in order to provide appropriate constraints on the inversion and regularization of the data/images resulting in predictions of the transport of amendments and/or progress of biodegradation beyond the vicinity of boreholes. The characterization data include information from established borehole logging instruments that provide high resolution information on physical properties close to the borehole and less established between borehole imaging methods that capture the continuity of structures beyond individual boreholes. The FRGT incorporates multiple geophysical techniques as it is based on the fundamental premise that there is no silver bullet with respect to geophysical technologies and that multiple methods must be tested at a particular site to determine the ones that will provide the most information beyond the boreholes. At the NAWC demonstration site, the most effective technology for characterization and monitoring beyond the borehole was cross-borehole electrical resistivity tomography (ERT). The performance objectives associated with informed inversion therefore focused on advancing the utility of ERT for characterization and monitoring in fractured rock subject to constraints provided by other technology components of the FRGT.

DEMONSTRATION RESULTS

The demonstration focused on characterization and monitoring using a dense array of seven boreholes each drilled through ~70 ft of unweathered rock. A critical part of the demonstration was the design, development and testing of a first-of-its-kind integrated array containing electrodes, packers and injection/sampling ports. This array was constructed to demonstrate *in situ* ERT monitoring of amendment injections/longer term biodegradation occurring in fractured rock whilst maintaining hydraulically and electrically isolated intervals in all seven boreholes.

The demonstration also advanced the functionality of E4D a high-performance computing code for the inversion of large ERT datasets. Advancements focused on implementation of new regularization constraints that favor site conditions in fractured rock and provide flexibility for incorporating information on the boreholes. Limited laboratory studies were performed to determine the most favorable (from an ERT imaging perspective) amendment substrate from the candidates highlighted as effective at the site. The field demonstration primarily focused on an intensive multi-method downhole and crosshole geophysical characterization campaign followed by a suite of tracer tests and a longer term amendment injection that were imaged with ERT.

The FRGT produced an unprecedented image revealing the continuity of relatively permeable zones within approximately 600 m^3 of rock. The images resolve the alternating sequence of laminated and massive mudstones at the site and the results are validated by borehole logging and crosshole hydraulic testing datasets. Time lapse ERT monitoring was able to monitor the evolution of injected tracers and amendments within targeted fracture zones that control the flow and transport characteristics of this site. The time-lapse ERT images capture strong evidence for channelized flow occurring within the fracture zone and provide unique information on the efficacy of targeted amendment emplacement. The images also offer the possibility of estimating fracture surface area impacted by an amendment treatment, with direct implications for the performance of such remediation treatments with respect to remediation goals. Limited testing of the FRGT at a second site, the Eastland Woolen Mill, Corinna, ME, highlighted the potential benefits of directional cross borehole ground penetrating radar (DBHGPR) for imaging the continuity of major fracture zones beyond borehole walls.

IMPLEMENTATION ISSUES

Most of the technologies explored in the FRGT are not subject to any specific regulations beyond what is typical for working in boreholes at contaminated sites and acquiring samples. However, continuous open holes are needed for ERT to be effective in fractured rock. Some states regulate the length of open holes to prevent cross contamination between multiple fractures or aquifers connected to the borehole. In this study, a deviation was readily obtained from the state. The specific borehole technology developed in the course of this research—centered on integrated electrode/sampling/packer arrays—helped to address the open-hole regulatory implementation issue, as fractures were hydraulically isolated during tracer experiments and electrical monitoring. Metal borehole casings would prevent the effective use of most geophysical techniques included in the FRGT, although some of the tools in the FRGT can operate effectively though PVC casing.

This demonstration involved an extensive technology transfer effort where end-user concerns were specifically addressed through lectures, field demonstrations and hands-on Q&A sessions with individuals. In total, our tech-transfer courses directly engaged 230 remediation professionals and regulators via short courses approved for continuing ed credits. These efforts revealed that end users were typically poorly equipped to make informed decisions about the likely appropriateness of specific components of the FRGT based on the conditions of a particular site. In order to address this implementation issue, an Excel-based decision support tool was developed to provide recommendations for the selection of specific geophysical techniques for a given project objective and subject to the constraints imposed by the site conditions.

1.0 INTRODUCTION

1.1 BACKGROUND

According to the National Research Council there are an estimated 300,000-400,000 groundwater contaminated sites in the U.S.A. (NRC, 1994), with an estimated cleanup cost as high as $1 trillion. Contaminated sites in fractured rock are particularly difficult and expensive to remediate, because characterization and monitoring is problematic in the presence of extreme heterogeneity. Fractured rock aquifers are typically dual porosity and dual permeability systems, with flow and transport constrained to discrete fractures that provide the effective porosity of the aquifer and channelize transport. Typically, flow and transport is highly anisotropic, with directions that can depend more on interconnectivity and fracture strike than the direction of hydraulic gradients. Consequently, the characterization and monitoring of amendment-stimulated biodegradation of dense non-aqueous phase liquid (DNAPL) in fractured rock aquifers is a daunting technological problem.

Boreholes are almost always required to acquire information on contaminant fate in fractured rock, particularly when the contaminant is located at depths beyond the range of surface excavations or the range that meaningful information can be acquired using surface geophysical surveys. Existing technologies typically require involve a local measurement from a borehole. Drilling boreholes in fractured rock is expensive and potentially problematic, as boreholes can connect permeable zones that would otherwise be isolated by low permeability units. Such concerns provide a strong incentive to develop technologies that can reduce the number of boreholes that must be drilled in order to obtain a working understanding of the flow and transport characteristics of a fractured rock site.

Existing borehole-based measurements based on sampling and analysis typically provide information that represents the physical or chemical conditions local to the borehole environment, raising questions about the relevance of the observations across larger scales beyond the borehole wall. Conventional geophysical logging technologies have the potential to provide information on the physical and chemical characteristics of the formation local to the borehole, but the support volume of these measurements is typically small relative to the scale of the heterogeneity controlling flow and transport at a site. Furthermore, spatial interpolation of small-scale measurements made using a sparse array of boreholes is notoriously poor at accurately representing upscaled variations in physical and chemical properties.

Geophysical imaging technologies have the potential to provide cost effective, non-invasive techniques for imaging physical properties and transport processes beyond the borehole. Specifically, these technologies may (1) characterize structures controlling flow and transport beyond the borehole and, (2) diagnose likely changes in pore fluid chemistry within fractured rock associated with amendment delivery and resulting biodegradation that can be verified using a limited (in scope and expense) direct measurement method. Technologies are required to provide site managers with the information necessary to better determine fracture geometries away from wells, fracture connectivity, and the progress of amendment treatments targeting dense non-aqueous phase liquids (DNAPLs) within fractured rock. Such information will ultimately assist decision making regarding, (1) the viability of amendment treatment as a remediation option in fractured rock, (2) identification of critical target zones for delivery of

4

amendment treatments, and (3) variations in amendment frequency needed to optimize remediation.

The motivation of this project is that the proposed technology would result in far fewer wells being required to understand the major connected fracture networks dictating flow and transport of an amendment (and subsequent biodegradation induced) in a fractured rock environment. The drilling of fewer wells will reduce direct contact with contaminants, and minimize the problem whereby boreholes act as preferential pathways for contaminant transport between vertically separated fractures thereby facilitating greater transport of contaminants away from the source zone. Furthermore, our geophysical technologies could lead to significant cost savings not only as a result of the need for fewer wells, but also as a result of reduced monitoring requirements (e.g. wells, samples, analyses) required to determine the progress of amendment treatments.

1.2 OBJECTIVE OF THE DEMONSTRATION

The overall objective of this project was to demonstrate a method for characterization and monitoring of amendment delivery and subsequent biodegradation of dense non-aqueous phase liquid (DNAPL) (including free and dissolved phase) in fractured rock aquifers based on a Fractured Rock Geophysical Toolbox (FRGT). Specific technical objectives of the project included demonstrations of (1) fracture network characterization using geophysical methods sensitive to fracture strike and dip patterns and spanning a wide range of measurement scales; (2) minimally invasive autonomous monitoring of proxies of the timing and extent of amendment delivery and/or DNAPL degradation in fractured rock using combined geophysical and geochemical measurements sensitive to amendment concentration and biodegradation; and (3) the application of "informed" inversion to produce estimates of fracture location, distribution, and orientation with better resolution than is currently possible with commercially available tools; The project also focused on demonstrating how geophysically imaged "soft" hydrological information could be used to guide decisions regarding frequency and duration of sampling events needed to verify amendment delivery and biodegradation of contaminants. The work included efforts to compare dense 4D geophysical monitoring results with sparse (in time and space) point chemistry data in order to verify the significance of geophysical signatures of DNAPL amendment and remediation processes.

For the characterization component of the FRGT, this project explored the performance of three under-exploited technologies: (1) directional borehole ground penetrating radar (DBHGPR) for providing unique high-resolution data on fracture orientation (strike and dip); (2) resistivity and induced polarization (IP) imaging for visualizing the spatial distribution of fracture density and fracture surface area; and (3) new borehole IP and nuclear magnetic resonance (NMR) tools to improve assessment of the vertical distribution of physical parameters controlling mass transfer. For the amendment injection and DNAPL monitoring component of the toolkit, this project set out to investigate the performance of (1) electrical resistivity imaging for tracking variations in bulk conductivity associated with changes in groundwater chemistry during amendment injection and subsequent DNAPL degradation, (2) self potential (SP) imaging of the changes in the distribution of natural current sources resulting from redox zonation produced by DNAPL degradation, and (3) electrodic potential (EP) monitoring of changes in redox chemistry local to electrodes. The data analysis component focused on demonstrating how new inversion technologies could (1) better characterize fracture networks respecting specialized model

constraints derived from borehole logging data and (2) reconstruct the changes in geophysical attributes that are related to amendment delivery and subsequent DNAPL biodegradation using model constraints that are encouraged to limit changes within the images to discrete fractures or fracture zones identified during the characterization phase.

1.3 REGULATORY DRIVERS

Our demonstration project set out to promote wider acceptance of innovative geophysical monitoring technologies for characterization and monitoring of fractured rock aquifers. Although recent research in the peer-review literature has firmly established the potential benefits of specific geophysical technologies for characterization and monitoring in fractured rock aquifers, a full field-scale demonstration applying multiple methods was necessary to rigorously address operational aspects and costs savings over conventional methods of monitoring. This project committed to the publication of protocol documents, serving as a how-to manual for the FRGT and facilitating future applications within the remediation and environmental industries. The USGS team led the development of training workshops, online training materials and webinars to optimize the transfer of these technologies to industry.

The demonstration (including both the application of the FRGT and verification) was designed to provide end users with the information needed on both the performance of the method (and specific FRGT components) in fractured rock, as well the associated issues regarding spatial and temporal resolution and costs. Tech transfer efforts were integral to the project and designed to give end users the information needed to make informed decisions on future applications of this technology. In order to receive guidance with such efforts, we consulted with Kathy Davies, US EPA, Region 3, early in the project to promote introduction of the information generated under this demonstration to groundwater science personnel in regulatory agencies. We recognize that acceptance by regulatory agencies of methods of monitoring are a key factor in activities that are ultimately undertaken at sites of groundwater contamination.

2.0 TECHNOLOGY

2.1 TECHNOLOGY DESCRIPTION

Our project set out to demonstrate the performance of a 'fractured rock geophysical toolbox' (FRGT) that is summarized in the overall schematic of the technology shown in Figure 2.1. In the FRGT, geophysical characterization data are fed into the processing of geophysical monitoring datasets in order to provide appropriate constraints on the inversion and regularization of the data/images resulting in predictions of the transport of amendments and/or progress of biodegradation beyond the vicinity of boreholes. The technology is directed towards acquiring reliable information on structures, amendment delivery and longer term geochemical transformations beyond boreholes and thus beyond the range of conventional sampling methods. The technology offers the potential to provide spatially continuous information that reduces the challenges of uncertain interpolation based on sparse datapoints in boreholes. It also presents an opportunity to acquire data at a scale more typical of the heterogeneity controlling flow and transport in the subsurface, in contrast to small scale point measurements made in boreholes.

The FRGT incorporates multiple geophysical techniques as it is based on the fundamental premise that there is no silver bullet with respect to geophysical technologies and that multiple methods must be tested at a particular site to determine the ones that will provide the most information beyond the boreholes. Significant redundancy is integrated into the FRGT in that not all the methods will be utilized in full development of a site characterization and monitoring strategy as described here.

Fractured Rock Characterization and Monitoring Methods

Our FRGT characterization toolbox incorporates multiple methods that provide information at multiple scales. Central to this toolbox are two under-exploited technologies: (1) directional borehole ground penetrating radar (DBHGPR), which can provide unique data on fracture strike and dip (Lane et al., 1998a; Lane et al., 1998b; Olsson et al., 1992; Wright and Jr., 1998); and (2) resistivity/induced polarization (IP) imaging, repeatedly shown to be sensitive to fracture densities, connectivity and surface area (e.g. Slater et al., 1997). These are complemented with borehole geophysical logging and other data acquired at boreholes.
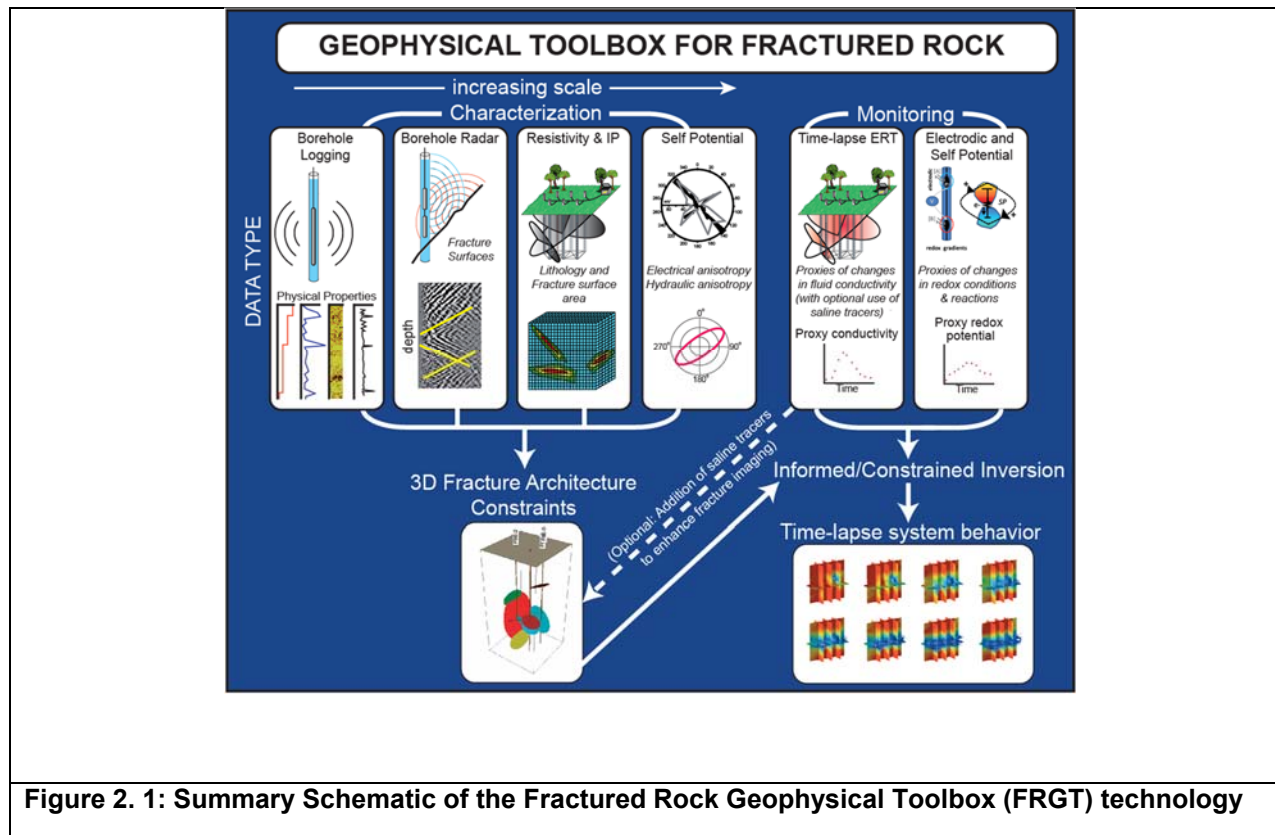
Figure 2. 1: Summary Schematic of the Fractured Rock Geophysical Toolbox (FRGT) technology

Our monitoring toolkit of the FRGT exploits geophysical measurements with recognized sensitivity to pore fluid conductivity and redox chemistry at contaminated sites. The established resistivity imaging (ERI) method is well suited for tracking changes in bulk conductivity resulting from changes in groundwater chemistry associated with amendment deliver and/or accompanying DNAPL degradation (Johnson et al., 2010). Self potential (SP) is an evolving technology that has might ultimately be capable of imaging the distribution of natural current sources describing the redox zonation associated with microbial degradation of DNAPL (Naudet et al., 2004). With appropriate sensor design, electrodic potentials (EP) can be simultaneously measured in order to infer changes in redox chemistry local to electrodes (Slater et al., 2008).

Borehole Electrical Instrumentation (Resistivity, Induced Polarization, Self Potential and Electrodic Potential)

Hardware and data analysis for electrical imaging are well established (Binley and Kemna, 2005). For this project, we collected electrical data using a Rutgers-owned Syscal Pro constructed by Iris Instruments (France). The system is configured for the acquisition of resistivity, IP, and SP measurements, and can also be used for electrodic potential (EP) measurements (Figure 2.2).
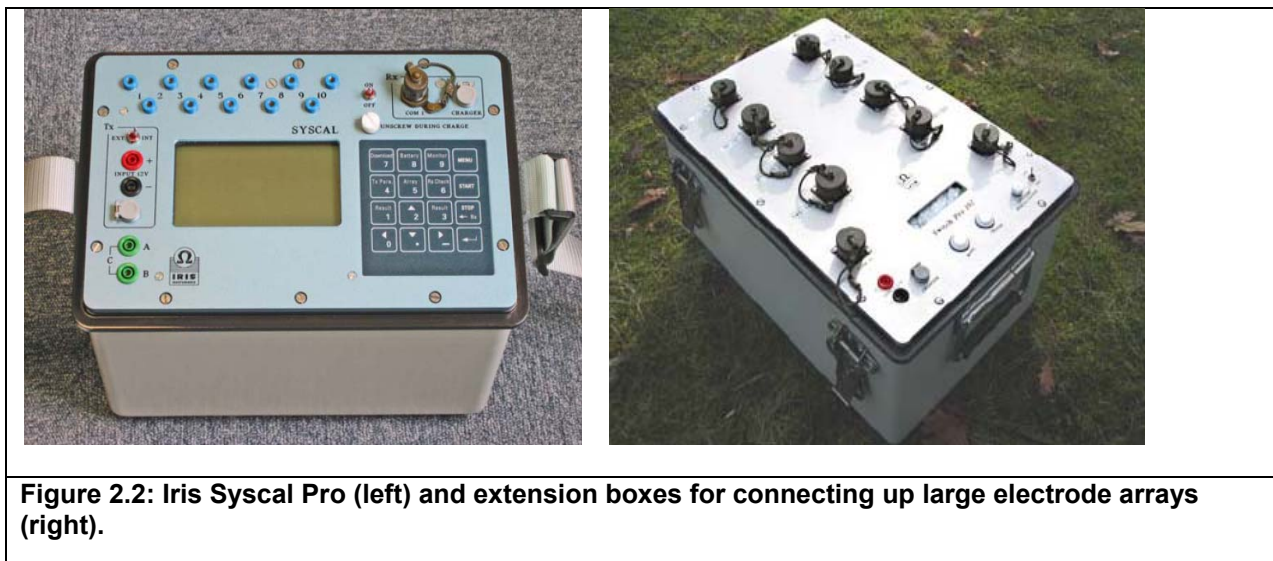
Figure 2.2: Iris Syscal Pro (left) and extension boxes for connecting up large electrode arrays (right).

Three additional Rutgers-owned multiplexers allowed for the use of up to 144 electrodes (Figure 2.2). This system is configured with an internal 250W DC power supply, allowing for injection of up to 2.5 A. Measurement precision of 0.2% is typical (http://www.iris-instruments.com/Pdf%20file/SyscalPro_Gb.pdf). Rutgers University and the USGS have used this system for diverse applications ranging from monitoring permeable reactive barriers to investigation groundwater-surface water interaction. The Rutgers University system is adapted for autonomous monitoring both on and off the grid (Figure 2.3).

Electrical methods involve measurement of potential differences between pairs of electrodes, where the potentials either (1) result from an applied current (i.e., the basis of the ER method), or (2) are associated with naturally occurring current sources in the earth, for instance those resulting from redox conditions (i.e., the basis of the SP method). A third measurement involves the recording of the decay of potential with time after shutoff of an applied current (the basis of the IP method) and is a function of capacitance, and thus the properties of fluid-grain boundaries in porous media. Finally, it is possible to simply measure an open circuit potential of an electrode relative to a reference, which will depend on the redox gradient between electrode locations. This measurement is defined as an electrodic potential.

Fractures in saturated rock result in very strong resistivity contrasts relative to competent rock. Common amendments have significant resistivity contrasts with natural ground groundwater and these contrasts can readily be enhanced by spiking the amendment with an appropriate ion, Furthermore, biodegradation of DNAPL following amendment delivery might further result in a diagnostic electrical signature in monitoring datasets. Fractures surfaces will contribute the primary capacitance in fractured rocks. Redox gradients associated with DNAPL attenuation have the potential to drive SP signatures due to current sources in the rock, as well as EP signals proximal to electrodes.
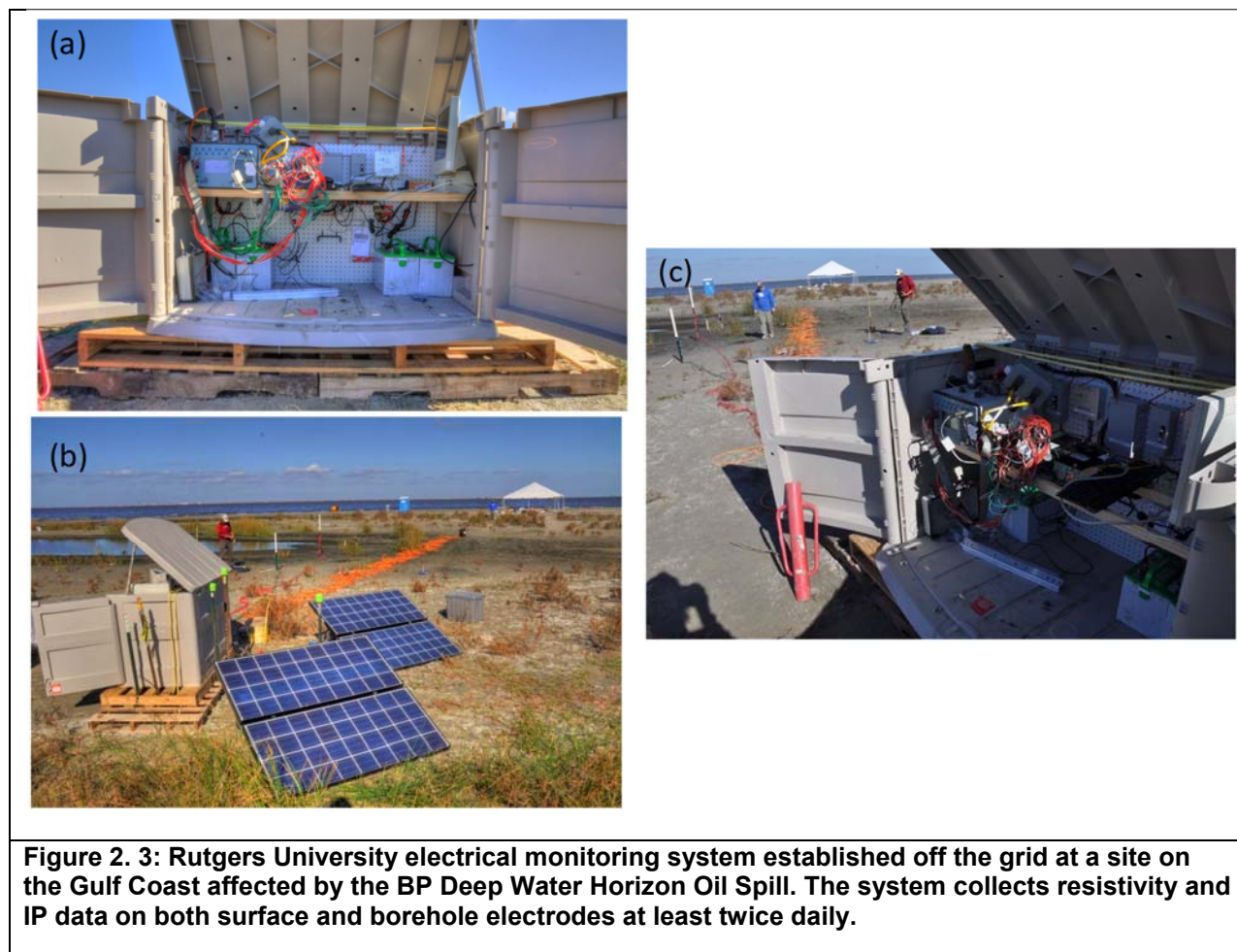
Figure 2. 3: Rutgers University electrical monitoring system established off the grid at a site on the Gulf Coast affected by the BP Deep Water Horizon Oil Spill. The system collects resistivity and IP data on both surface and borehole electrodes at least twice daily.

Electrical Resistivity: Resistivity methods have been extensively exploited for obtaining information on discrete fractures and/or fracture density as electrolytic conduction in fractured rock is largely through the fractures (Slater et al., 1997). Electrical resistivity imaging (ERI) has also been used to monitor amendment treatments (Johnson et al., 2010; Johnson et al., 2014) and capture indirect evidence of biodegradation (Slater et al., 2009). ERI has also been used to verify the installation of permeable reactive barriers Slater (Slater and Binley, 2003).

Induced Polarization (IP): Whereas electrical resistivity is sensitive to pore fluid conductivity (and thus total dissolved solids or ionic strength), the IP method measures the capacitive properties of the subsurface, which depend strongly on the properties of the mineral surface. Recent empirical relations show a strong power law dependence of IP on surface area to pore volume (S_{por}) (Slater, 2007; Weller et al. 2010) that can be exploited for characterizing fracture-surface density. IP is also potentially sensitive to biogeochemical changes occurring at pore-grain interfaces, due to biological activity associated with biodegradation (Abdel Aal et al., 2006).

10

Self-Potential: The SP method has long been used in mineral resources exploration for ore bodies, which represent electrically conductive bodies between oxidizing and reducing areas. In environmental geophysics, the SP method is increasingly used to study redox conditions (Naudet et al., 2004). Given the importance of redox conditions to understanding the efficiency of amendment treatments, SP is a promising approach for performance monitoring. Borehole SP measurements require careful electrode construction to prevent contamination. Borehole Ag-AgCl porous pot SP electrodes have been successfully used at the DOE Savannah River site (Minsley et al., 2007). These borehole SP electrodes utilize AgCl saturated agar gel in place of the solution used in conventional surface SP electrodes.

Electrodic Potential (EP): The EP method measures a proxy of redox activity local to the electrode and is based on concepts that have been pioneered for the exploration of redox chemistry in the deep oceans (Berner, 1963). Despite the distinctly different signals recorded, both SP and EP measurements can be acquired using the same recording instrumentation but using different electrodes. EP measurements can be performed using borehole Ag electrodes placed in direct contact with the formation fluid.

Directional Borehole Ground Penetrating Radar instrumentation

Radar methods use radio-frequency electromagnetic (EM) waves to measure spatial or temporal variations in EM-wave velocity, being a function of bulk dielectric permittivity, and EM-wave attenuation, which are both a function of electrical conductivity. During the late 1990's there was significant interest in, and development of, directional borehole ground penetrating radar (DBHGPR) for characterizing fracture distributions within bedrock. The basic concepts of the method are summarized in Figure 2.4.

Figure 2. 4: Borehole radar antenna (left) and schematic showing operation of reflection-mode data acquisition and interpretation.
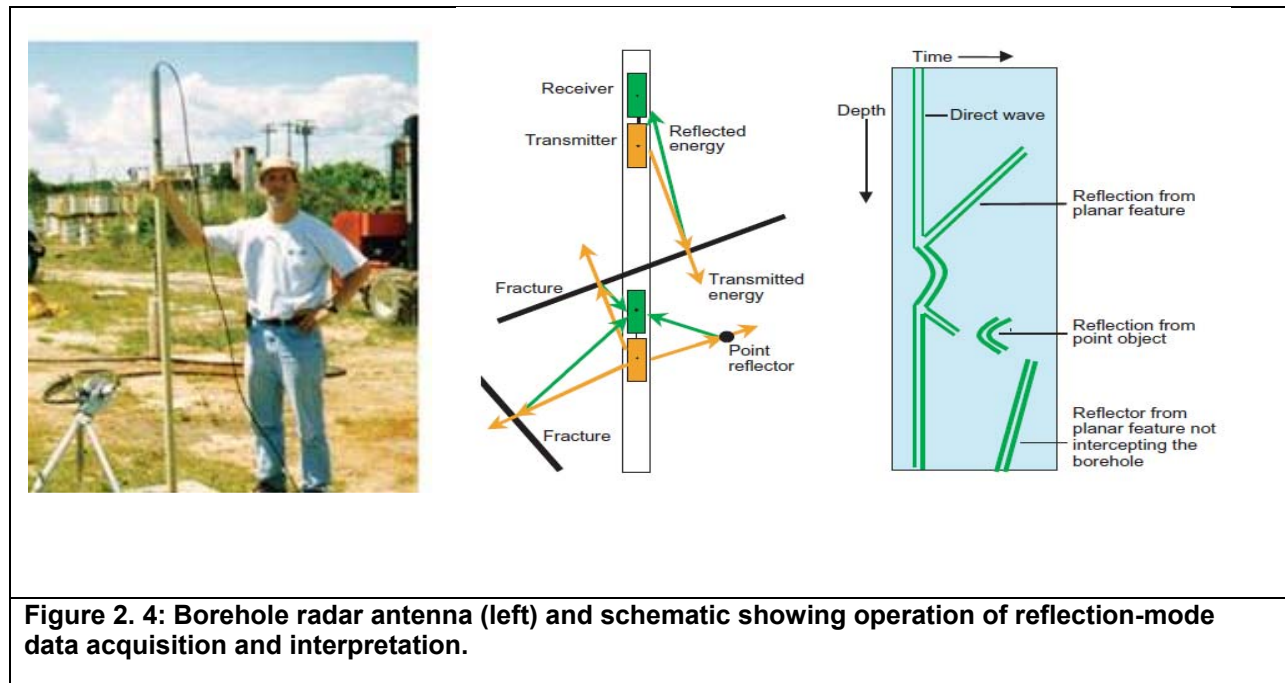
Early successes include research in Sweden for the characterization of deep fractured rock aquifers for the disposal of nuclear waste (Niva et al., 1988; Olsson et al., 1992). Directional antennas permitted estimation of fracture strike, in addition to dip. In the US, the United States Geological Survey (USGS) Branch of Geophysics has used DBHGPR at fractured-rock sites for both geotechnical and environmental investigations including research at the landmark USGS Mirror Lake Site, in New Hampshire (Day-Lewis et al., 2003; Lane et al., 1998a), Superfund sites including Parson's Casket Hardware Site in Belvidere, Illinois (Lane et al., 1998b), the former Loring AFB in Maine (Gregoire et al., 2006), and in geotechnical projects including water tunnel facilities around New York City (Stumm et al., 2001). Surprisingly, the technique has seen little other use in the US. This method is important for the characterization phase of the project but not in the monitoring phase of the FRGT as collection of radar data is more labor-intensive and autonomous, automated data acquisition is not practical with current technology. The USGS borehole radar system (Mala Geosciences) include directional 60 MHz borehole antennas.

Borehole Logging Methods

<u>Conventional logging methods</u>

Conventional borehole logging methods (e.g., caliper, electromagnetic conductivity, gamma, neutron porosity) and advanced methods (e.g., acoustic and optical televiewer, borehole flowmeter) alike are used increasingly for environmental and geotechnical applications. Such logs are readily interpretable by using commercially available software (Wellcad) to identify rock type, geologic structures (bedding, faults), fracture locations, and fracture orientations at the well. USGS codes now exist to analyze steady-state single-hole flowmeter logs (Paillet, 1998) in terms of fracture transmissivity and ambient far-field head controlling flow between connected fractures (Day-Lewis et al., 2011), and also transient crosshole flowmeter logs (Roubinet et al., 2015). Although used throughout the nation by USGS, relatively few environmental and geophysical contractors are using borehole flowmeter logging (Figure 2.5) to its full potential, i.e., modeling data to estimate fracture properties.

Figure 2. 5: USGS cross-borehole flowmeter logging at the NAWC site. Vertical flow in one borehole is measured during pumping from another borehole.

Emerging logging methods

Two novel and emerging borehole geophysical technologies that represent very new additions to the FRGT are induced polarization (IP) logging and nuclear magnetic resonance (NMR) logging. The IP logging tool measures the same properties pertaining to the capacitive characteristics of the rock as described earlier under borehole electrical instrumentation. The NMR method is unique in geophysics in that it is directly sensitive to the presence of hydrogen associated with water or hydrocarbons. Borehole tools were developed for use in the petroleum industry to determine water and hydrocarbon content and estimate permeability and pore-size distributions in petroleum reservoirs (e.g. Kleinberg et al., 1992). Recent technological developments have led to a new NMR borehole tool (Figure 2.6) that is used to collect measurements in near-surface boreholes (Walsh et al., 2010). An NMR measurement involves determining the rate at which the bulk nuclear magnetization of the hydrogen nuclei returns to equilibrium after being perturbed by a radio- frequency EM pulse; these nuclei are found in the water or hydrocarbons located within pores of rocks and sediments. The initial signal amplitude is proportional to the total water and hydrocarbon content located in the pore space. The distribution of relaxation times typically corresponds to the distribution of pore radii within the measured volume; short times correspond to small pores and large times correspond to large pores (e.g. Arns, 2004). This relaxation time distribution has been used in the petroleum industry to distinguish regions of

13

immobile fluids (associated with small pores) from mobile fluids (associated with large or well connected pores) by assigning a time that represents the cutoff between immobile and mobile porosity (Coates et al., 1997).

Figure 2. 6: USGS nuclear magnetic resonance logging system.

2.2 TECHNOLOGY DEVELOPMENT

The FRGT contains a number of individual technologies that were at different stages of development before the start of this ESTCP project. As described later, some elements of the FRGT technologies were ineffective at the primary study site due to the site conditions, or proved too impractical for implementation with the FRGT elements that were identified as likely to be most effective. Therefore, we focus here on a summary of the technology development of the most valuable components of the FRGT at the selected demonstration site as these were significantly advanced with respect to implementation to fractured rock aquifers under this demonstration.

3D Cross Borehole Electrical Resistivity Imaging

Under a previous ESTCP project (ER-0717), several of our team members (F.D Day-Lewis, T.C. Johnson, and J.W. Lane, Jr.) demonstrated 3D cross-borehole electrical resistivity imaging of amendment delivery and subsequent effects. A field demonstration was performed to monitor amendment emplacement and behavior during a biostimulation remediation effort conducted at the Department of Defense Reutilization and Marketing Office (DRMO) Yard, in Brandywine, MD, USA. For over two years, data were autonomously collected, uploaded to a server, inverted, and results were made available to project participants in near real-time. For

calibration/validation, geochemical fluid sampling was used to develop a petrophysical relation in order to predict groundwater indicators of amendment distribution. The petrophysical relations were field validated by comparing predictions to sequestered fluid sample results, thus demonstrating the potential of electrical geophysics for quantitative assessment of amendment-related geochemical properties. Crosshole radar zero-offset profile and borehole geophysical logging were also performed to augment the data set and validate interpretation. In addition to delineating amendment transport in the first 10 months after emplacement, the time-lapse ERT results show later changes in bulk electrical properties interpreted as mineral precipitation (Figure 2.7). Results support the use of more cost-effective surface-based ERT in conjunction with limited field sampling to improve spatial and temporal monitoring of amendment emplacement and remediation performance. Compared to the current project, ER-0717 focused on (1) application of ERT in shallow, sedimentary environments, (2) ERT imaging, with little consideration of IP or SP, and (3) initial amendment emplacement rather than longterm monitoring of bioremediation.

A number of specific developments of cross-borehole ERT imaging were realized in this project in order to improve the performance of the method in fractured rock settings. First of a kind instrumentation for performing cross-borehole ERT simultaneous with pumped injections and/or sampling from packed off intervals was designed, developed, tested and implemented. Developments in ERT data modeling an inversion were made to

Figure 2. 7. Example 3D time-lapse ERT images from the ESTCP ER-0717 project showing bioamendment (ABC) emplacement and movement, seen as increased bulk electrical conductivity (first column), followed by later increase in bulk conductivity arising from FeS precipitation resulting from microbial activity (second column). The Brandywine time-lapse ERT work demonstrated the capabilities of electrical imaging to provide near real-time, actionable information to remediation operators in the field. (from Johnson et al., 2014).

specifically incorporate the 3D electrically conductive boreholes in the problem. Image regularization constraints were implemented to more accurately represent the electrical conductivity structure at the borehole wall. These same constraints were extensively explored for application to fracture zones identified in borehole geophysical logs and other available characterization data. This resulted in the development of the informed inversion concept (Figure 2.8) in fractured rock where the geophysical monitoring of tracers and amendments is constrained by available characterization data. These developments are described in greater detail later in the report.

15
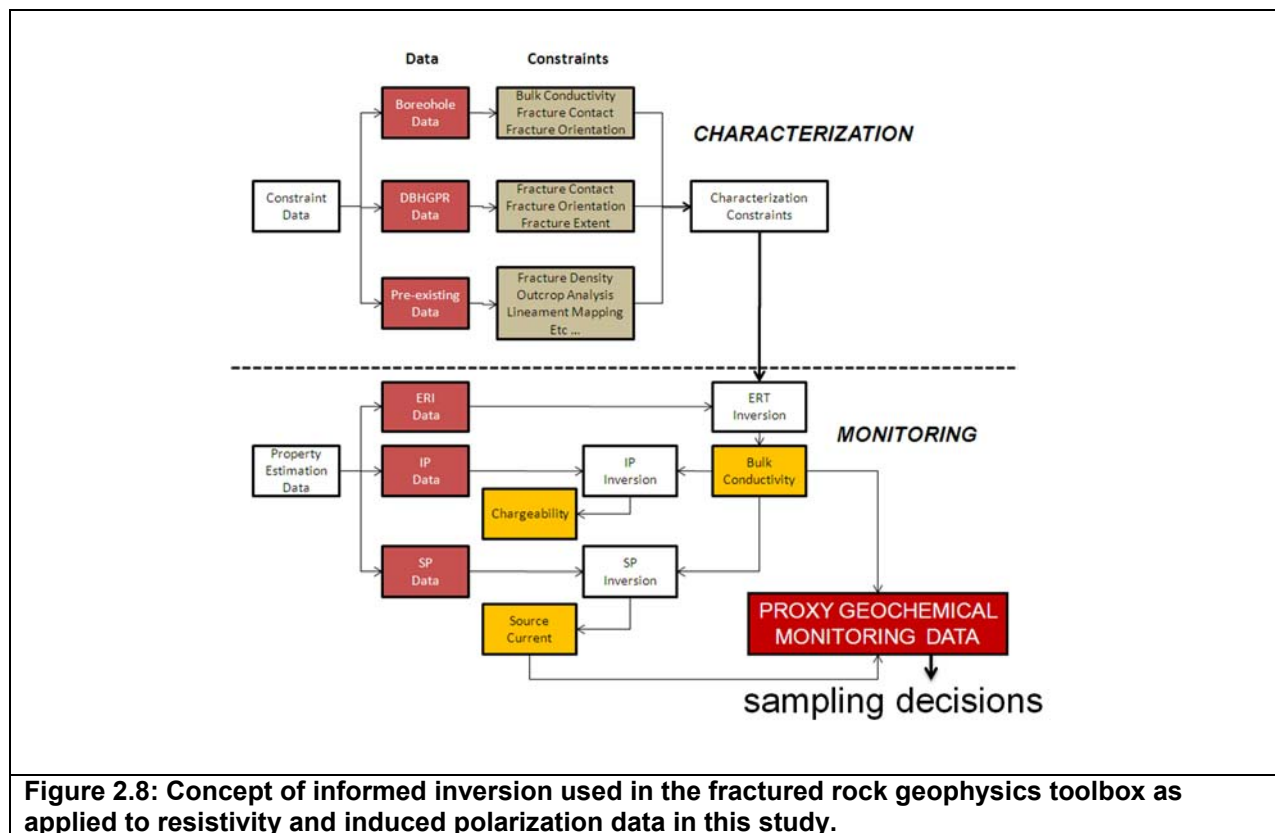
Figure 2.8: Concept of informed inversion used in the fractured rock geophysics toolbox as applied to resistivity and induced polarization data in this study.

2.3 ADVANTAGES AND LIMITATIONS OF THE TECHNOLOGY

The major advantage of the FRGT is the ability to see beyond the boreholes and into the volume of the subsurface between boreholes. Conventional methods for characterization of fractured rock aquifers and monitoring of amendment delivery and subsequent attenuation most often rely on measurements made in boreholes. Such measurements only provide information local to the borehole. The interpolation of observations recorded on a sparse array of boreholes to obtain more continuous distributions of physical and chemical properties is highly uncertain, and likely to result in misinterpretation of the subsurface. Furthermore, measurements made at a limited number of boreholes may fail to sample the distribution of amendments injected into a contaminated aquifer if the boreholes do not intercept the primary flow paths. This problem is accentuated in fractured rock aquifers, which are highly heterogeneous systems and display strong anisotropy in hydraulic properties governing flow and transport. For example, at the primary demonstration site (Naval Air Warfare Center, NAWC), previous experiments with amendment delivery have been confounded by the inability to fully capture the spatiotemporal evolution of amendments into the fractured rock system from a limited number of borehole observations. Another major advantage of the technology is that measurements are made at spatial scales that better capture the heterogeneity dictating flow and transport.

The greatest benefits of the FRGT stand to be reaped when it is deployed as a low cost temporal monitoring system, whereby successive geophysical surveys will be conducted autonomously over time to track amendment delivery and possibly subsequent biogeochemical alterations associated with attenuation. By examining changes relative to background conditions, changes over time will be attributable to changes in the fluid conductivity, as the differencing between successive surveys subtracts out the effect of the underlying geologic variability on the geophysical measurements. Such changes can then be correlated to amendment concentrations and possibly specific biogeochemical conditions, although care must be taken in defining these correlations (as discussed later). Coupled with an understanding of the underlying geologic structures then, the FRGT has the potential to provide critically needed information on fracture geometries, the spatial distribution of the amendment delivery and resulting attenuation within the usually inaccessible fractures and rock mass beyond the zone of the borehole. Such information could significantly improve understanding of the success of amendment delivery to the contaminated zones within fractures and the rock mass, and the effectiveness of these amendments in promoting attenuation of contaminants.

The major limitation of the FRGT is that the geophysical techniques do not provide direct estimates of hydraulic properties and/or changes in aqueous geochemical parameters associated with amendment treatment and subsequent contaminant attenuation. In fact, we stress that the direct estimation of geochemical properties solely from geophysical measurements at complex field sites (e.g. NAWC) is unlikely to succeed and this cannot be our validation goal. However, when used in conjunction with a limited set of direct measurements in boreholes, the geophysical proxy measurements of fluid and rock properties beyond the boreholes have the potential to improve understanding of the spatial distribution of fracture and rock properties and the spatial and temporal changes in fluid properties. For example it is reasonable to expect that salient features of related geophysical and geochemical time series (e.g. timings of peaks in electrical conductivity and solute concentration) can be interpreted in a straightforward manner. The success of the FRGT lies in respecting the limitations of geophysical datasets whilst taking advantage of the unique ability of the FRGT to provide information on the system state beyond the boreholes. This mandates a "soft" approach to the interpretation of the FRGT monitoring datasets, whereby any reliance on highly uncertain predictive relationships (attempting to link geophysical measurements directly to geochemical properties) is dropped in favor of examining specific attributes of the datasets that are more likely to be robust indicators of the progress of amendment delivery and subsequent attenuation.

3.0 PERFORMANCE OBJECTIVES

Specific <u>performance objectives</u> related to each tool within the FRGT including (1) data to be used and evaluated with respect to meeting the objectives, and (2) definition of what constitutes success, are described below and summarized in Table 1.

Evaluation of our performance objectives is largely based on comparison of metrics of our soft geophysical datasets with hard data available from established methods that provide high-resolution hard data local to the borehole. We performed validation tests to evaluate the success of components of the FRGT. These tests built on a concept introduced under ER-0717 (Day-Lewis and Lane, co-PIs), whereby geophysical predictions were compared to borehole logs and groundwater samples. In contrast to ER-0717, predictions here were not of contaminant presence/absence or concentration levels per se, but rather qualitative parameters such as: (1) transmissive vs. non-transmissive intervals or presence/absence of fracturing; and (2) changes to the system accompanying biostimulation (Table 1). Predictions were made independently of geochemical sampling (i.e., blindly) but these predictions were only informally sequestered from the team performing geochemical sampling, in contrast to our original plan which included a fully blind prediction/validation exercise as performed in ER-0717. Under ER-0717, (1) our project team had complete control over the timelines for geophysical data collection and sampling, facilitating the prediction/validation exercise, and (2) our team members were responsible for both geophysical prediction and sampling, which might appear to generate a conflict of interest. Under this grant, at NAWC we capitalized on ongoing USGS research and sampling efforts, and aligned our work with other ongoing projects. Thus, we made predictions independently of the sampling performed by others and could not submit both geophysical and USGS sampling data separately to a third party. We stress, however, the integrity of our prediction/validation exercise, with sampling following USGS protocols and performed by USGS staff not included as PI's or co-PI's.

The hard data on fracture densities and distributions required to conduct validation tests on the characterization component of our FRGT came from the borehole logging datasets collected as part of this demonstration project, supplemented with preexisting site data made available to us. The borehole geophysical logs acquired represent a gold standard for performance evaluation of the characterization components of the toolbox. The data required to perform blind validation tests on the monitoring component of our FRGT were primarily groundwater samples acquired during and after tracer or amendment injection. Established biogeochemical and hydrogeologic measurements were used to ground truth the initial state of the groundwater environment prior to any manipulations, as well as changes to that state resulting from manipulations. Direct estimation of geochemical properties from geophysical measurements at complex field sites (e.g. NAWC) is unlikely to succeed and this therefore was not our validation goal. <u>However, it is reasonable to expect that salient features of related geophysical and geochemical time series (e.g. timings of peaks in electrical conductivity and solute concentration) can be interpreted in a straightforward manner. We therefore adopted a "soft" approach to the interpretation of the FRGT monitoring datasets, whereby any reliance on highly uncertain relationships linking geophysical attributes to geochemical parameters was dropped in favor of examining specific attributes of the datasets that are more likely to be robust indicators of the delivery of amendments and any subsequent progress of accelerated and/or natural biodegradation.</u>

Not all performance objectives defined in the demonstration plan were met, partly because some components of the FRGT did not perform well given the particular geological conditions of the performance site. This was expected and underscores the importance of adopting a toolbox approach to fractured-rock characterization and monitoring. It was necessary to focus on the components of the FRGT evaluated to have the highest chances of success at NAWC, recognizing that it would be impractical and cost-prohibitive to simultaneously measure all cross-borehole datasets in the FRGT (resistivity, IP, SP and BHGPR) including ones determined not to work at NAWC (BHGPR). This issue was raised at the first IPR meeting for the project, along with a request for supplemental funding to perform FRGT measurements at a second fractured rock site with distinctly different geology to NAWC. Approval by the IPR panel permitted us to perform limited testing of the FRGT, primarily focusing on DHGPR and ERT, at the Eastland Woolen Mill (EWM) site in Corinna, Maine. Whereas NAWC is characterized by an interlayered sequence of laminated and massive mudstones, the EWM site is characterized by dark gray slate or phyllite, alternating with thin layers of light gray siltstone or sandstone. Table 1 summarizes the primary performance objectives defined in the Demonstration Plan for the project, associated data requirements and defined success criteria used to confirm successful performance of individual toolbox components. Performance objectives highlighted in red in Table 1 were not met at the demonstration site(s) and those highlighted in blue were only partially met.

Table 3.1: Summary of Primary Performance Objectives, Associated Data Requirements and Defined Success Criteria as Defined in the Demonstration Plan

Performance Objective	Data Requirements	Success Criteria	Degree Met
[1] FRACTURE NETWORK CHARACTERIZATION			
Quantitative performance objective			
[1.1] Identify strikes, dips and connectivity of fractures away from boreholes	Borehole Ground Penetrating Radar (BHGPR) combined with borehole logging data	**Fracture dip identified by GPR within 5% of actual dip observed with borehole logging in boreholes** **Fracture strike identified by GPR within 5% of actual dip observed with borehole logging in boreholes**	**PARTLY**
Qualitative Performance Objective			

[1.2] Determine distribution of transmissive and connected fractures (away from boreholes) above a threshold	Resistivity imaging and DBHGPR during tracer injection combined with flow meter logging	**Accurate grouping of fractures into transmissive or non transmissive based on threshold consistent with flow meter logs** **Statistics:** *non-linear analysis e.g. Markov-Bayes hardness*	**FULLY**
[2] AUTONOMOUS MONITORING OF AMENDMENT DELIVERY AND/OR BIODEGRADATION			
Quantitative Performance Objective			
[2.1] Measure distribution of injected amendments away from boreholes	Electrical resistivity imaging combined with ground water sampling (specific conductance) from boreholes	**Electrical conductivity changes predicted in the images at boreholes consistent with specific conductance changes recorded in boreholes** *Statistics: correlation analysis*	**FULLY**
[2.2] Measure redox gradient changes away from boreholes	Self potential and electrodic potential measurements combined with oxidation reduction potential (ORP) measurements in boreholes	**Direction and magnitude of redox changes correct as compared to borehole analyses**	**PROCUREMENT ISSUES PREVENTED IMPLEMENTATION**
Qualitative Performance Objective			
[2.3] Infer distribution of primary geochemical parameters of interest (e.g. chloride, TCE)	Resistivity and induced polarization measurements combined with geochemical analysis of groundwater samples	• **Demonstrate correlation of geochemistry with resistivity and induced polarization** • *Statistics: ANOVA and multiple regression*	**PARTLY**
[2.4] Determine timing of changes in redox potential distribution driven by biodegradation away from boreholes	Self potential combined with redox chemistry from groundwater sampling and ORP measurements	Demonstrated correlation of geochemistry with resistivity and self potentials *Statistics: ANOVA and multiple regression*	**PROCUREMENT ISSUES PREVENTED IMPLEMENTATION**

[3] APPLICATION OF "INFORMED" INVERSION TO IMPROVE IMAGING OF FRACTURED ROCK			
Qualitative Performance Objective			
[3.1] Optimized high-resolution imaging of fractured networks	Resistivity and induced polarization inversion combined with DBHGPR and borehole logs to define appropriate regularization constraints for fractured rock systems Model predictions from Inverse codes developed under this project and those predictions obtained from commercially available existing software (e.g. Res2DInv)	Improved resolution of fracture networks when using inverse codes developed under this project relative to existing commercial codes. Validation of improvement using synthetic model scenarios based on NAWC (where true model is known) as well as field data acquired at NAWC	**FULLY**
[3.2] Optimized high-resolution imaging of spatial extent and timing of amendment delivery and subsequent attenuation	Resistivity and self potential inversion combined with DBHGPR and borehole logs to define regularization constraints Model predictions from Inverse codes developed under this project and those predictions obtained from commercially available existing software (e.g. Res2DInv)	Improved resolution of amendment distribution and attenuation using inverse codes developed under this project relative to existing commercial codes. Validation of improvement using synthetic model scenarios based on NAWC (where true model is known) as well as field data acquired at NAWC	**PARTLY**

SPECIFIC OBJECTIVES OF INDIVIDUAL FRGT COMPONENTS

This section gives further details of the specific objectives for the three major elements of the FRGT demonstration as originally defined in the Demonstration Plan and to what extent each objective was met. As emphasized in Section 2, geophysics offers no silver bullet and the success of individual methods depends partly on the site conditions. Indeed, the limitations of individual geophysical methods motivated the premise underlying the FRGT, i.e., no single method works everywhere, and multiple methods (a toolbox approach), is necessary. The FRGT contains multiple technologies to account for the fact that some methods will be ineffective at specific sites. Consequently, failure to meet some performance objectives based on specific elements of the FRGT was expected given that the demonstration was by necessity largely

focused on a single site and distinct geological conditions that were not conducive to all methods in the FRGT. A detailed discussion of the performance objectives and the degree to which they were met in the project follows below, with each section numbered consistent with the numbering shown in Table 1.

[1] Fracture network characterization

[1.1] In our original project plan, this performance objective primarily focused on demonstrating the use of DBHGPR to identify the locations, extents, and orientations of major fractures away from boreholes, for use as constraints on ERT inversion; however, a pilot-scale DHGPR field experiment at the NAWC site indicated that the site-specific utility of the method was severely limited by the electrically conductive bedrock. Approval by the IPR panel permitted us to perform limited testing of the FRGT, focusing on DHGPR (and also ERT) at the EWM site described above, Maine. DHGPR at the EWM site produced detailed 3D descriptions of fracture architecture, including strike, dip, and extent. Although not all fractures seen by DHGPR or televiewer can be cross referenced, DHGPR results compare favorably. The primary assessment was based on comparison against fracture densities and orientations available from borehole logging datasets and cross-hole hydraulic testing, representing our gold standard for information on fracture properties in a well.

The results of the DBHGPR were originally intended for use in construction of the finite-element meshes required in the inversion of electrical data, allowing major fractures to be "hardwired" into models (described below). However, based on extensive modeling of ERT data and inversion of field data from a fractured rock site in the UK (Robinson et al., 2015), we determined that application of such constraints in ERT inversion is problematic. Constraining the inversion to 'hardwired' fractures can introduce major errors and confound interpretation of results if the fracture locations and orientations are not known with very high accuracy. We concluded that use of quantitative information from DHGPR for ERT constraints is problematic, and we therefore revised our goal for this method to focus on qualitative information measures related to interwell connectivity.

[1.2] A qualitative objective of the fracture network characterization phase was to use geophysical imaging to characterize fracture transmissivity relative to some appropriate threshold discriminating transmissive from non-transmissive fractures. This was defined as a qualitative objective as it is currently impossible to quantitatively estimate fracture transmissivity from geophysical imaging techniques. However, the techniques do have the potential to discriminate connected, transmissive fractures from fractures exhibiting poor connectivity. Both resistivity imaging and DBHGPR data acquisition were planned in conjunction with injection of electrical tracers. However, it proved impractical to have instrumentation installed in boreholes to permit simultaneous acquisition of both datasets during injection of tracers. Consequently, only resistivity imaging was performed as the conditions at the NAWC demonstration site were not conducive to effective use of DBHGPR. The primary assessment measure included fracture transmissivity estimates local to boreholes provided from flow meter logging conducted as part of the borehole logging campaign and cross-hole hydraulic testing. Success was evaluated based on the ability to accurately group fractures into transmissive or non transmissive based on a

transmissivity threshold defined from flow meter logging and cross-hole hydraulic testing data. Although DHGPR was used at the EWM site, we could not instrument the EWM site with the packers required to perform tracer injections; thus, the goal of that work was to characterize fracture architecture and not discriminate transmissive from non-transmissive fractures.

The resistivity imaging at the NAWC site was partly successful in determining the large scale transmissivity structure. The largest interconnected, high electrical conductivity zone in the ERT characterization image coincided with the major hydraulically connected interval identified from crosshole hydraulic testing. However, discrete bedding plane fracture zones occurring at the interface between alternating massive and laminated mudstone units were not directly observed in the ERT images due to resolution limitations.

[2] Autonomous monitoring of amendment delivery and/or biodegradation

[2.1] One critical quantitative objective of the autonomous geophysical monitoring was to determine the distribution of injected amendments away from boreholes. The performance site has been studied in previous SERDP projects involving amendment injections where the fate of amendments injected into boreholes was poorly constrained by groundwater samples extracted from a sparse array of boreholes. Given that this was considered a major challenge for understanding remediation effectiveness at the demonstration site, this became one of our most critical performance objectives during the demonstration. This objective was achieved by deploying an autonomous electrical monitoring system to acquire resistivity datasets at high temporal resolution during amendment delivery. Performance was assessed based on the predictive capabilities of the resistivity monitoring to determine timing of changes in major ion chemistry associated with the amendment composition. The primary assessment measure was in situ TDS measurements in boreholes along with analytes recorded for samples obtained before, during and after amendment injections. Success was evaluated by comparison of electrical conductivity changes predicted in the images with specific conductance changes recorded local to boreholes.

[2.2] A second quantitative objective defined in the Demonstration Plan was to measure relative redox gradient changes away from boreholes resulting from amendment delivery and resulting attenuation. This objective was to be achieved via an inversion of self potential (SP) datasets for distributions of current sources related to major redox gradients in the system. Performance was to be assessed by comparison of electrodic potential and oxidation reduction potential (ORP) measurements in boreholes. Success was to be evaluated based on whether the directions of redox changes inferred from SP inversion were correct when compared to borehole datasets. Statistical analysis of the field SP and EP data was to be performed assess the significance of identified correlations. This performance objective was not met for two reasons: [1] procurement issues (as described in Section 8) associated with the electrodes that would have been required to implement this part of the FRGT; [2] it proved impractical to engineer borehole infrastructure to facilitate time-lapse SP and EP measurements without jeopardizing the borehole infrastructure needed to acquire other data considered to be more effective at the demonstration site based on preliminary characterization data acquired early in the project. The use of cross-borehole SP and EP data was ultimately considered premature with respect to the level of maturity of these

technologies and the uncertainly regarding the return (in terms of information content) with respect to the cost and effort burden. Consequently cross-borehole SP was omitted from the FRGT spreadsheet decision tool (described below) that was developed to help end users assess the likely success of different components of the FRGT at a specific site and for a particular objective.

[2.3] A qualitative objective of the monitoring was to infer changes in the distribution of primary geochemical parameters of interest (e.g. chloride, TCE) resulting from amendment delivery and subsequent attenuation away from boreholes. This was defined as a qualitative objective as we considered it impossible to directly quantify changes in specific geochemical parameters from geophysical datasets. However, it was considered reasonable to expect that salient features of related geophysical and geochemical time series (e.g. timings of peaks in electrical conductivity and chloride concentration) could be interpreted in a relatively straightforward manner. Resistivity and induced polarization monitoring were used to achieve this objective and performance was evaluated by comparison against geochemical analysis of groundwater samples from boreholes. Success was measured based on demonstrated correlation of resistivity and induced polarization with major geochemical parameters. With respect to amendment delivery, this objective met with great success and is a highlight of the FRGT demonstration as applied to the NAWC site. The demonstration provided a striking example of the ability of ERT to monitor amendment delivery into a fractured bedding plane feature at unprecedented spatiotemporal resolution. Multiple injections of tracers and amendments illustrated how ERT can identify the fractional surface area of a bedding plane fracture impacted by an injection and differences that can result from varying the geometry and timing of injection/amendment delivery. This objective is listed as 'partly met' only because the timeframe of the project was insufficient to continue long-term monitoring of the amendment delivery needed to determine whether ERT can also track the progress of biodegradation initiated by the amendment injection.

[2.4] A second closely related qualitative objective was to infer timing in changes of redox potential distribution driven by amendment delivery and subsequent attenuation away from boreholes. This was again defined as a qualitative objective as it was not considered possible to directly quantify changes in redox chemistry from the geophysical datasets. However, it is reasonable to expect that salient features of related geophysical and geochemical time series (e.g. timings of peaks in SP and redox potential) might be interpreted in a straightforward manner. Self potential monitoring was proposed to achieve this objective with performance evaluated by comparison against geochemical analysis of ORP and electrodic potentials in boreholes. Success was to be measured based on a demonstrated correlation of self potential with ORP and electrodic potentials. This performance objective was not met for the same two reasons as mentioned in Section 2.3 above: [1] procurement issues (as described in Section 8) associated with the electrodes that would have been required to implement this part of the FRGT; [2] it proved impractical to engineer borehole infrastructure to facilitate time-lapse SP and EP measurements without jeopardizing the borehole infrastructure needed to acquire other data considered to be more effective at the demonstration site based on preliminary characterization data acquired early in the project. The use of cross-borehole SP and EP data was ultimately considered premature with respect to the level of maturity of these technologies and uncertainly regarding the return (in terms of information content) with respect to the cost and effort burden. Consequently cross-borehole SP was omitted from the FRGT spreadsheet decision tool

(described below) that was developed to help end users assess the likely success of different components of the FRGT at a specific site and for a particular objective

[3] Data Analyses

Our objective of the data analysis was to predict the best estimates of the subsurface distribution of geophysical attributes (characterization) or changes in those attributes (monitoring) that satisfy the geophysical measurements required and simultaneously respect available model constraints appropriate for the fractured rock system under investigation based on information available at boreholes. This performance objective was achieved through advancing available inversion routines for reconstructing estimates of the distribution of electrical properties from resistivity and induced polarization datasets.

[3.1] Two primary qualitative performance objectives are listed in Table 1. The first objective was optimized high-resolution imaging of fractured networks. The critical aspect of the approach was to use available information on fracture geometry (borehole logging, DBHGPR, core data from drilling) to incorporate appropriate model constraints in the inversion of resistivity and induced polarization data for estimates of fracture geometries and connectivity away from boreholes. Performance was assessed by comparing model predictions from new regularization approaches developed under this project with those predictions using the standard regularization constraints found in commercially available existing software (e.g. Res2DInv) and less suited to fractured rock settings. These predictions were performed for both synthetic models that simulate the NAWC geology and the field datasets obtained during this work. Success was evaluated based on improved resolution of fracture networks when using inverse codes with appropriate regularization constraints developed under this project. Quantification of this improvement was assessed using synthetic model scenarios where the true model structure (simulating the NAWC site) was known.

[3.2] The second qualitative objective was high-resolution imaging of the spatial extent and timing of amendment delivery and subsequent attenuation. This objective was again achieved by adopting novel regularization constraints in the geophysical inversion. Specifically, routines were modified to constrain the inversion of time-lapse monitoring data such that changes in geophysical properties were encouraged to occur within and proximal to discrete fractures or fracture zones identified during the characterization phase. Performance was again assessed by comparing model predictions from new regularization approaches developed under this project with those predictions obtained when using standard regularization constraints found in commercially available existing software (e.g. Res2DInv) and less suited to fractured rock settings. These predictions were again examined for both synthetic models that simulate the NAWC geology and the field datasets obtained during this work. Success was again evaluated by improvements in the resolution of amendment distribution and attenuation using inverse codes developed under this project relative to existing commercial codes. Quantification of this improvement was confirmed using the synthetic model scenarios where the true model structure (simulating the NAWC demonstration site) was known.

RECOMMENDATIONS AND PRODUCTS RESULTING FROM THE ASSESSMENT OF THE PERFORMANCE OBJECTIVES

This demonstration highlighted the important fact that we have repeatedly emphasized earlier: i.e. that not all geophysical methods will perform well at all fractured rock sites. During this project, we recognized a clear need to develop technology transfer tools that can assist site managers in assessing what components of the FRGT will work at what fractured sites. In response to this need, we developed an interactive spreadsheet (Figure 3.1) that can be used to guide decision making regarding what FRGT components are most likely to be worth investing in at a specific site. The spreadsheet considers both the objectives of the site characterization/monitoring effort and the most important parameters relating to the conditions/characteristic of the site under investigation. The spreadsheet also considers the anticipated budget of the study.

The USGS-OGW Branch of Geophysics team led this effort, building on previous similar decision support tools that they have developed to facilitate tech transfer. The spreadsheet was programmed in an Excel spreadsheet with Visual Basic controls. The spreadsheet is intended to discourage the user from investing in component tools of the FRGT at sites where these tools are likely to produce minimal useful information. As an example, Figure 3.2 shows the output of the FRGT spreadsheet for the NAWC site. The information input on the site geology at NAWC results in DHGPR being flagged as a technique that is unlikely to provide useful information at this site. Indeed, the electrically conductive mudstones at the site resulted in DHGPR being ineffective at NAWC. The spreadsheet correctly identifies those technologies that were most effective at NAWC.
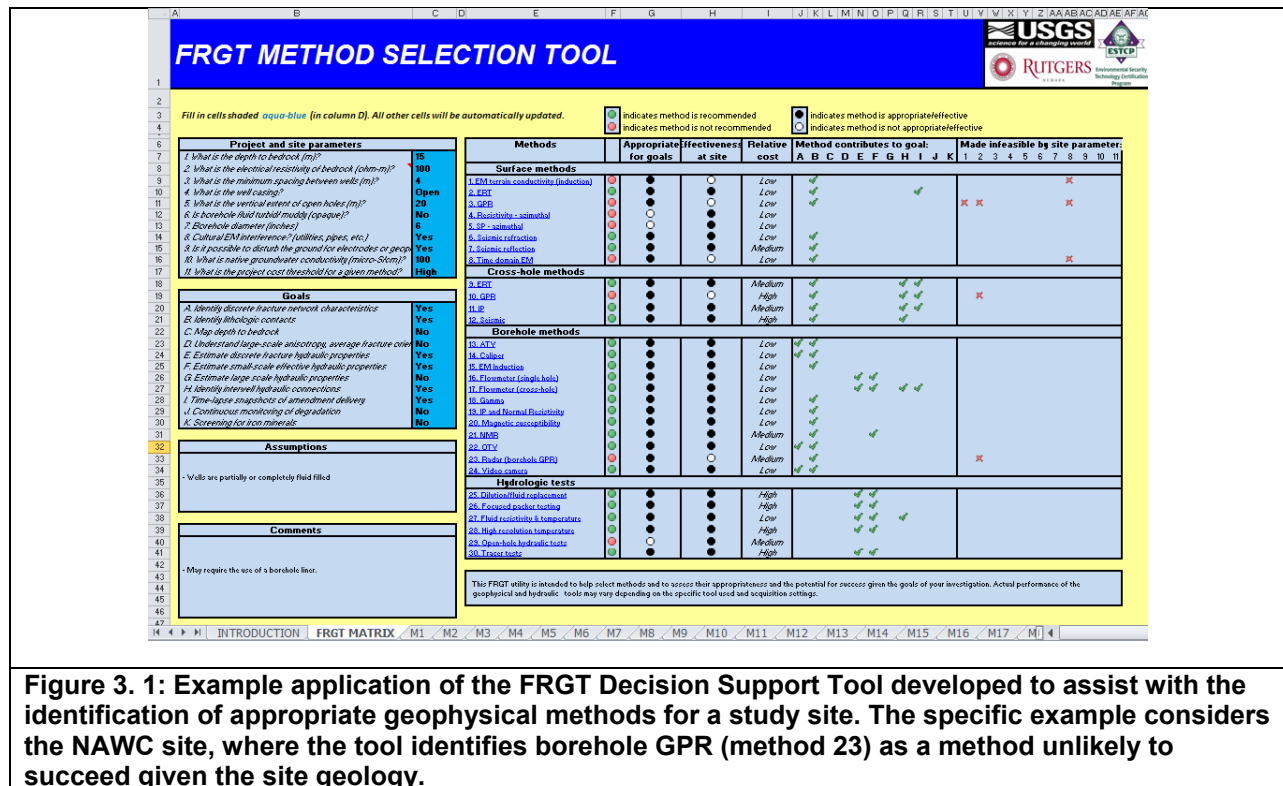
Figure 3. 1: Example application of the FRGT Decision Support Tool developed to assist with the identification of appropriate geophysical methods for a study site. The specific example considers the NAWC site, where the tool identifies borehole GPR (method 23) as a method unlikely to succeed given the site geology.

4.0 SITE DESCRIPTION

The primary study site for this demonstration was the former Naval Air Warfare Center (NAWC), located in West Trenton, NJ (USA), which was used as a facility to test jet engines from 1955-1998. This site is representative of hundreds of contaminated sites in the eastern United States and thus the lessons learned here are potentially applicable to other fractured sedimentary sites. The fractured bedrock aquifer at the site was extensively contaminated with the chlorinated solvent trichloroethylene (TCE) during operations and presently fractures and the rock matrix are contaminated with TCE and its biotic degradation products cis-dichloroethylene (cDCE) and vinyl chloride (VC).

4.1   SITE LOCATION

NAWC is located at the corner of Jack Stephen Way and Parkway Avenue in West Trenton, NJ (Figure 4.1). The location of demonstration boreholes 83-89BR (described later) was in between a driveway for an abandoned industrial building which formerly housed jet engines for flight testing, and a dirt roadway. The topography is flat with low lying vegetation consisting mostly of long grasses. The site is easily accessible with a regular vehicle via Parkway Avenue.
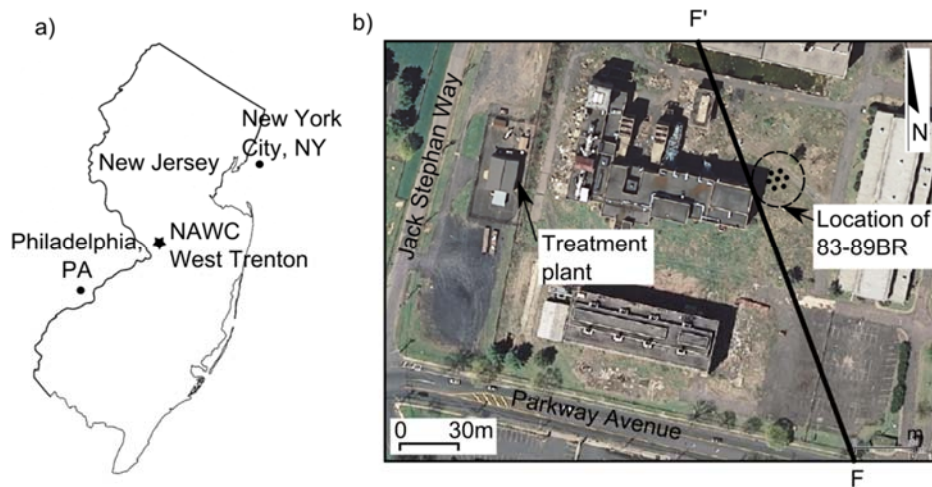
Figure 4.1: Location map for the Naval Air Warfare Center (NAWC) in West Trenton, NJ (from Robinson et al, 2015, *in review*)

4.2   SITE GEOLOGY/HYDROGEOLOGY

The site consists of fractured sedimentary rocks of the Newark Basin. Competent rocks are primarily mudstones and sandstones of the Lockatong and Stockton Formations. Fill, weathered silt, and silty-clay saprolite are underlain by moderately-dipping alternating massive and laminated mudstone units which contain highly fractured black carbon-rich units (Figure 4.2) (Lacombe & Burton, 2010; Tiedeman et al., 2010). This study focused on the unweathered mudstone units where dominant flow pathways identified from hydraulic testing (Section 5.2.4)

are through (1) a series of cross-cutting faults and (2) discrete fracture zones associated with the carbon rich intervals (Lacombe & Burton, 2010; Ellefsen et al., 2012).
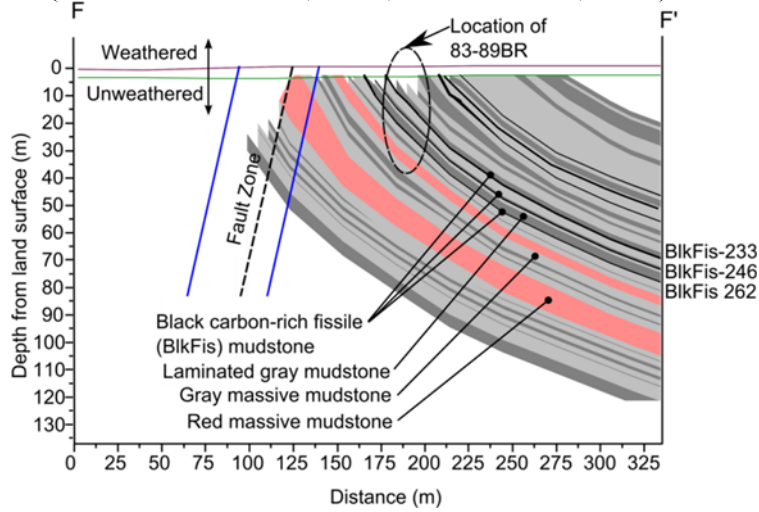
Figure 4.2: Section F-F (see Figure 4.1) showing geologic cross section in the vicinity of 83-89BR boreholes (from Robinson et al, 2015, *in review*).

4.3   CONTAMINANT DISTRIBUTION

Peak chlorinated volatile organic compound (CVOC) concentrations (in µg/L) for wells in the vicinity of 83-89BR on the NAWC site are shown in Figure 4.3. These concentrations were computed as the molar sum of peak concentrations of 'original TCE' consisting of TCE, cDCE and VC. The data for this figure was collected from 1990-2014. Figure 4.3 shows the spatial extent of the contamination as well as the irregularity of concentrations of the plume, hence highlighting the complex fracture networks in fractured rock.
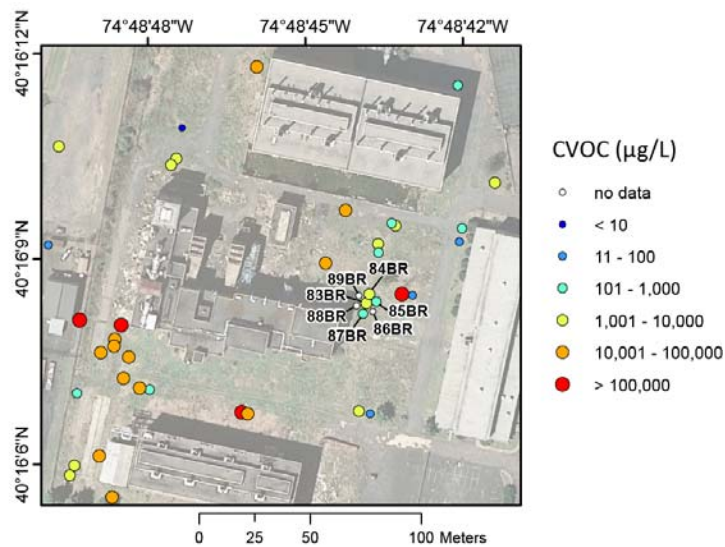
Figure 4.3: Peak molar concentrations of original TCE at wells in the vicinity of 83-89BR for samples collected between 1990-2014 (revised from Goode, et al., 2014).

5.0   TEST DESIGN

5.1   CONCEPTUAL EXPERIMENTAL DESIGN

This demonstration was based on a study of an approximately 1400m^3 volume of fractured rock defined by seven boreholes that were drilled at the NAWC site. The targeted rock volume was selected to intercept multiple permeable bedding plane features known to be contaminated with TCE (Figure 5.1). The operational phases of the demonstration including drilling/coring, borehole geophysical logging, cross-borehole geophysical imaging of rock structure, preliminary tracer tests, followed by cross-borehole time-lapse monitoring of a sequence of tracer tests that ended with a monitored amendment injection. The core and geophysical logging data were acquired to provide hard data to evaluate the performance of the cross-borehole geophysical imaging and monitoring effort that formed the backbone of this demonstration. The core and logging data were also used as constraints in the demonstration of an informed inversion framework required to improve the performance of the cross-borehole geophysical technologies in imaging a fractured rock system. The preliminary tracer test was performed to determine key parameters needed to constrain the design and implementation of the geophysical monitoring tracer tests.

This conceptual design provided the opportunity to demonstrate the full potential of the FRGT when the infrastructure was designed with the geophysical data acquisition in mind (geophysical technologies are often employed as an afterthought and thereby restricted to infrastructure available for other purposes). The arrangement and spacing between the wells was selected based on: (1) consideration of likely tracer/amendment transport rates based on previous hydrogeological research at the site; (2) synthetic studies considering the desired resolution of the cross-hole imaging technologies relative to the targeted fracture zones and expected geophysical contrasts associated with tracer and amendment injections. The experiment design included the construction of first-of-a-kind borehole infrastructure for conducting continuous geophysical monitoring into fractured rock during the injection of tracers into hydraulically isolated intervals of the rock mass. A limited in scope laboratory experiment was performed to identify the most geophysically favorable amendment from candidates known to stimulate TCE biodegradation from prior research. Specific details of each element of the test design are provided in the following subsections.
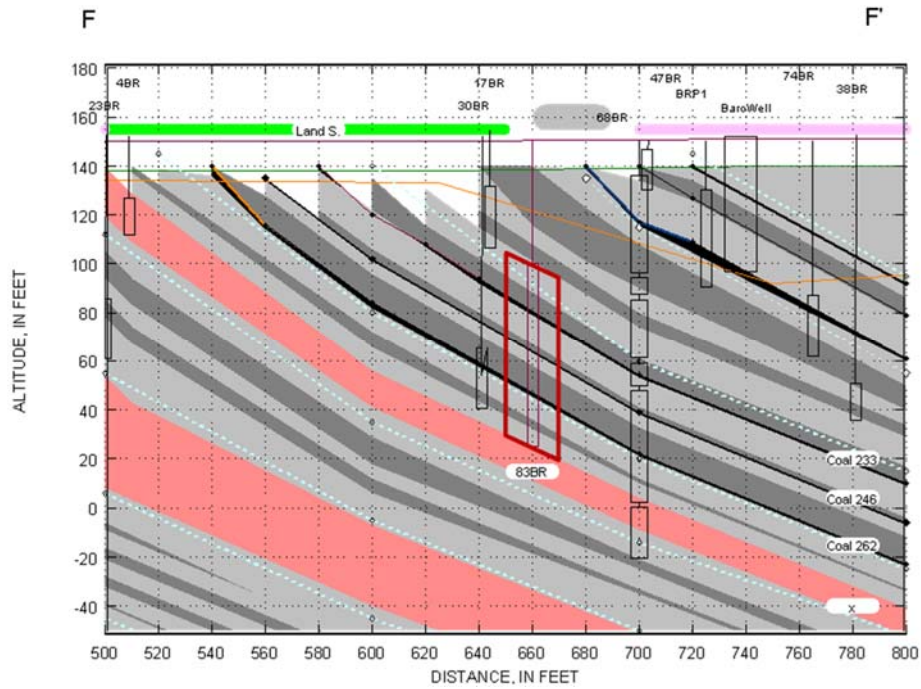
Figure 5.1.1: Cross section F-F' showing the selected region bounded by the array of boreholes selected for this demonstration. The region targets three fractured zone intervals and focuses on a heavily contaminated unweathered zone.

30

5.2 BASELINE CHARACTERIZATION

5.2.1   Drilling, Coring and Well Installation

Seven boreholes, designated sequentially 83BR through 89BR, were drilled along strike in a wagon wheel pattern (Figures 5.2.1.1 and 5.2.1.2). Distances between boreholes were designed such that the information content of ERT imaging during tracer/amendment injections could appropriately capture injection evolution beyond the borehole. At these inter-borehole distances, standard hydraulic testing methods such as borehole water sampling, borehole geophysical logging and/or hydraulic testing can provide valuable supporting information.
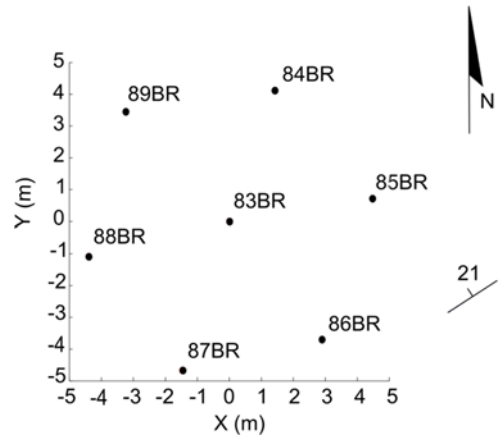
Figure 5.2.1.1: As-built borehole schematic
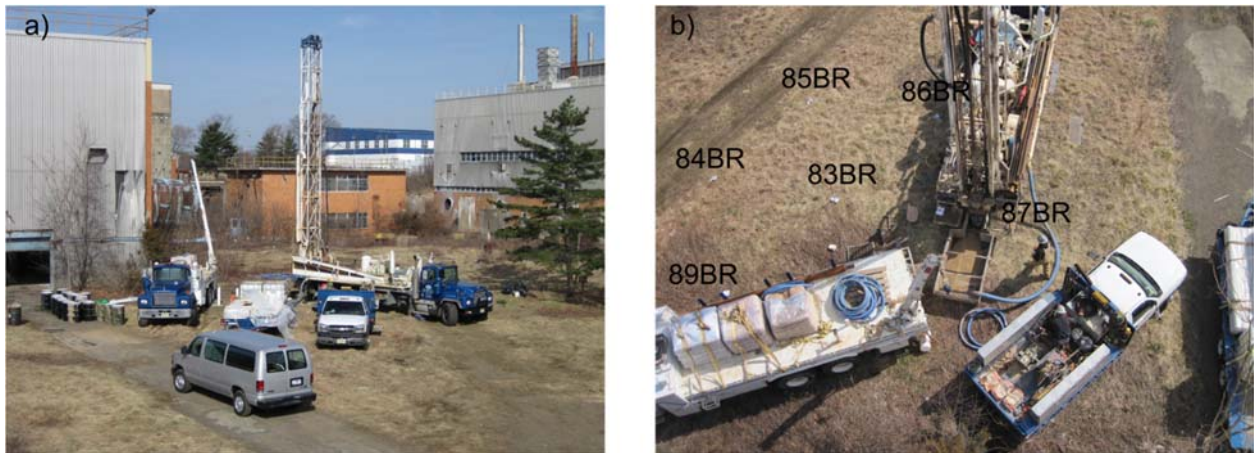
Figure 5.2.1.2: a) Drill rig and site view b) Aerial photo showing drilling locations

The features of interest (i.e. the fracture zones) are within the unweathered geological units (Figure 4.2) such that intact rock samples were not required from the weathered zone. A 10-inch (25 cm) borehole was drilled within the top weathered units. This was lined with a 6-inch (15 cm) PVC casing sealed into place with bentonite. A surface steel casing was then grouted into place (Figure 5.2.1.3).   Drilling depths of 10-inch (25 cm) diameter well sections ranged from 12.50 – 15.85 m below land surface (LS).

Below the weathered rock, a 3.8-inch (10 cm) core bit was used. Cores were catalogued (Figure 5.2.1.4) and chiseled samples were selected for further VOC analysis (primarily from fracture zones but also non-fracture zones) by the USGS Toxic Substances Hydrology research team (Figure 5.2.1.5). Rock core samples were collected and preserved in the field using a modification of the techniques developed by Hewitt (1998) and Sterling and others (2005). After bringing the core barrel to the surface, samples were selected near suspected permeable features

31

and from unfractured strata between permeable features. Typically 5-10 samples were collected from each 5-ft (1.5 m) core section (Figure 5.2.1.5). Samples already having small fragment sizes were placed directly into a preweighed 125-mL septum-capped VOC jar containing 50 mL of methanol and then placed in cold storage for CVOC extraction. Intact rock samples were broken off using a hammer and chisel and pulverized into small fragment sizes using a stainless steel 12,000 psi rock crushing device (Figure 5.2.1.6a). The crushed rock samples were similarly placed into the pre-weighed 125-mL septum-capped VOC jars with 50 mL of methanol and again placed in cold storage for extraction (Figure 5.2.1.6b). This method is considered a total extraction of all CVOCs diffused in or sorbed onto the rock, that is, a 'bulk' sample. CVOCs dissolved in interstitial fluids, or DNAPL present in rock pores would also be extracted to the methanol (Goode et al., 2014).
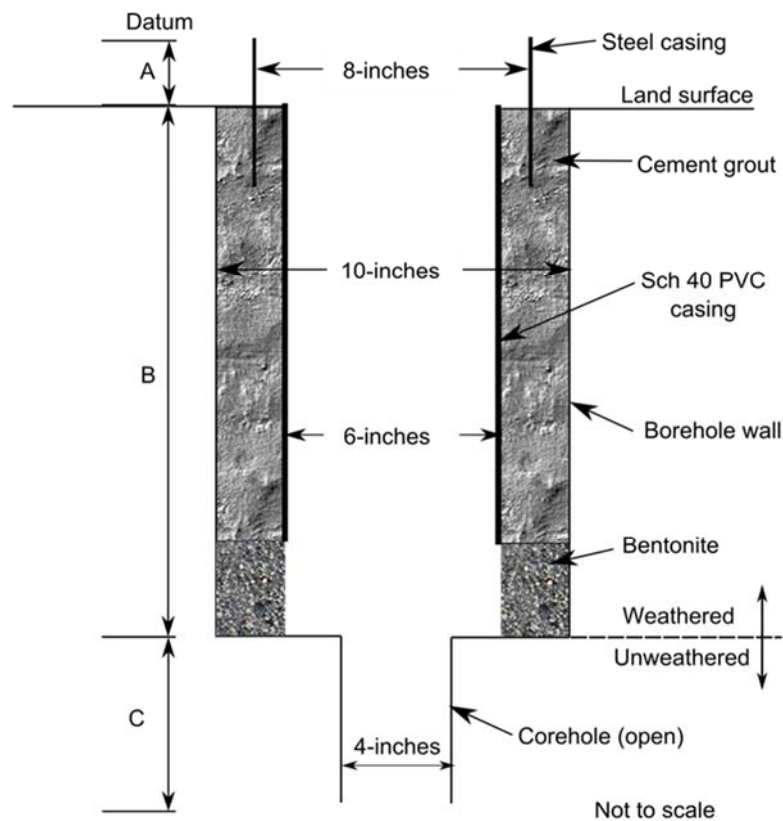
Designation	Description	83BR	84BR	85BR	86BR	87BR	88BR	89BR
A	Landsurface, LS	0.90	0.90	0.90	0.87	0.84	0.80	0.88
B	Bottom of 10 in borehole below LS	14.94	15.85	14.94	12.50	12.50	14.02	15.85
C	Length of open 4 in interval	17.02	19.25	17.17	20.77	20.71	22.45	20.31
	Length of core*	21.34	21.95	21.34	22.25	22.25	21.95	21.95

* Partial collapse of the 4 in interval resulted in the length of the core being larger than the length of the open 4-in interval

Figure 5.2.1.3: Borehole section view for 83-89BR wells.

Figure 5.2.1. 4: Core cataloging

Figure 5.2.1. 5: Core samples extracted during drilling.

Coring depths were such that three known highly fractured carbon units were penetrated, being designated BlkFis 233, BlkFis 246 and BlkFis 262 (Figure 4.2.2).   Uncased 3.8-inch (10 cm) intervals ranged from 17-22.5 m in length. Depth to bottom of borehole below land surface ranged from 32-36.5 m. This demonstration ultimately focused on tracer and amendment injection monitoring into a series of cross cutting faults which were found to be highly transmissive in the cross borehole hydraulic testing (Figure 5.2.4.3).

Figure 5.2.1. 6: a) Crushing of selected core samples and b) preservation of crushed samples in methanol for VOC analysis.

5.2.2 Coring Analysis

Based on the core cataloguing conducted by Pierre Lacombe, USGS, Table 5.2.2.1 reflects borehole intersection depths and thicknesses for cross cutting fault features, fractures and the three coal units, Blk-Fis233, Blk-Fis246 and Blk-Fis262.   The gap between the base of casing and the open borehole section is also shown.

Table 5.2.2.1: Borehole intersection depths from land surface (all units in meters)

Borehole		Base of casing opening (refer to Section 5.2.1. Figure 3)	Cross cutting fault features		Fracture	Fracture	Blk-Fis233	Blk-Fis246	Blk-Fis262
83BR	depth to top	14.63	19.35				25.45	27.89	30.63
	depth to bottom	15.85	20.57				25.76	28.04	30.94
	thickness	1.22	1.22				0.30	0.15	0.30
84BR	depth to top	15.10	20.28		17.82		25.92	28.36	31.41
	depth to bottom	15.86	20.74		17.91		26.23	28.51	31.56
	thickness	0.76	0.46		0.09		0.30	0.15	0.15
85BR	depth to top	14.34	20.28		18.30		24.24	26.68	29.73
	depth to bottom	14.79	20.74		18.76		24.55	26.83	30.03
	thickness	0.46	0.46		0.46		0.30	0.15	0.30
86BR	depth to top	11.63	17.11	20.62			22.45	24.89	
	depth to bottom	12.24	17.88	20.92			22.75	25.04	
	thickness	0.61	0.76	0.30			0.30	0.15	
87BR	depth to top	11.66	17.29	18.82		26.13	22.48	24.91	27.96
	depth to bottom	11.96	17.75	19.28		26.19	22.78	25.07	28.27
	thickness	0.30	0.46	0.46		0.06	0.30	0.15	0.30
88BR	depth to top	13.22	18.71	14.99		20.47	24.50	26.78	29.83
	depth to bottom	14.13	19.32	15.11		20.60	24.80	26.94	30.29
	thickness	0.91	0.61	0.12		0.12	0.30	0.15	0.46
89BR	depth to top	15.28	20.76		17.81	26.55	25.94	28.38	31.43
	depth to bottom	15.73	21.22		17.87	26.62	26.25	28.54	31.74
	thickness	0.46	0.46		0.06	0.06	0.30	0.15	0.30

The intersection depths from this coring analysis were used to validate the ERT characterization results (Section 5.5.2).

5.2.3 Geophysical Logging

Borehole geophysical logging constituted the major source of *a priori* information to be used in boreholes 83BR-89BR to constrain electrical resistivity imaging. Standard logs (as described in Johnson et al., 2009) (Figure 5.2.3.1) and specialized logs collected within each borehole are shown in Table 5.2.3.1.

Figure 5.2.3.1: a) Caliper borehole tool b) Borehole geophysical data collection. All logs calibrated according to ASTM standards and USGS protocols.

Table 5.2.3. 1: Borehole logging methods used in 83BR-89BR

METHODS	83BR	84BR	85BR	86BR	87BR	88BR	89BR
Gamma	X	X	X	X	X	X	X
Caliper	X	X	X	X	X	X	X
Electromagnetic Induction (EMI)	X	X	X	X	X	X	X
Normal resistivity Spontaneous potential (SP) Single point resistance (SPR)	X	X	X	X	X	X	X
Induced polarization (IP)	X	X	X	X	X	-	X
Fluid temperature and conductivity	*	*	*	*	*	X	*
Heat-pulse flowmeter (FM)	*	*	*	*	*	-	*
Cross-hole FM	X	X	X	X	X	-	X
Optical televiewer (OTV)	X	X	X	X	X	X	X
Acoustical televiewer (ATV)	X	X	X	X	X	X	X
Deviation	X	X	X	X	X	X	X
Neutron	X	X	X	X	X	X	X
Nuclear magnetic resonance (NMR)	X		X		X	-	
Radar (reflection and level)				X	X		

X indicates completed; * indicates ambient and post-stress conditions, - not collected due to borehole liner installation

Borehole logs (ATV, OTV, caliper) were used to identify fracture intersection depths (Table 5.2.3.2) and Gamma/Normal logs were used to correlate lithologic units within each borehole to aid in the identification of transmissive fracture zones. Borehole deviation logs were used to position each borehole in the ERT modeling, an important consideration to reduce borehole modeling artifacts (Oldenborger et al., 2005; Wilkinson et al., 2008).

Table 5.2.3.2: Fracture zone intersection depths identified from Caliper, ATV, OTV borehole logs

Borehole identifier	Fracture zone depth*, top (m)	Fracture zone aperture (m)
83BR	19.36	1.21
	25.45	0.31
	27.89	0.15
84BR	21.18	0.46
	18.72	0.09
	26.82	0.31
	29.26	0.15
85BR	21.18	0.46
	19.20	0.46
	25.14	1.31
	28.04	0.15
86BR	17.98	0.77
	21.79	0.31
	23.32	0.30
	25.76	0.15
87BR	18.13	0.46
	19.66	0.46
	26.97	0.06
	23.32	0.30
	25.75	0.16
	28.80	0.31
88BR	19.51	0.61
	15.79	0.12
	21.27	0.13
	25.30	0.30
	27.58	0.16
	30.63	0.46
89BR	21.64	0.46
	18.69	0.06
	27.43	0.07
	29.87	0.15
	26.82	0.31

* Datum=land surface (LS)

Ambient and stressed conditions were tested using single-hole and cross-hole heat pulse flowmeter tests. Single-hole heat-pulse flowmeter (HPFM) testing can identify directional flow under ambient and stressed conditions within a particular borehole. At this site water was injected at the top of the well, and downflow was measured to identify out-flow zones. Minor ambient flow was recorded in boreholes 83BR, 86BR, 87BR. Under an injection rate of 0.050 L/sec (0.8 gpm), boreholes 83BR, 84BR, 85BR, 86BR, 87BR and 89BR (injection rate=0.025 L/sec) showed responses in fractures near the base of casing (BOC). Ambiguity existed in when interpreting HPFM results near the BOC: without vertical isolation it could not be determined whether the response was from the annular space above the BOC or fractures just below this depth.

Cross-hole tests measure the response of nearby boreholes under stressed conditions when an injection occurs (Figure 5.3.2.2). Interconnections between boreholes could be identified; however information on individual transmissive fracture zones was limited due to the fact that there was no vertical isolation within each borehole column.

Figure 5.2.3.2: Cross-hole flowmeter logging whereby a single borehole is stressed with an injection while monitoring the down-hole response of three nearby boreholes with flowmeters. A metal casing extends above the ground surface at each borehole. This top of casing (TOC) was used as the datum for all geophysical logs.

All geophysical logs use the TOC as the datum. Geophysical logs for 83BR are shown (Figure 5.2.3.3) with an interpretative statement. Geophysical logs for 84-89BR are shown in the Appendix along with individual borehole deviations plots (which were critical to incorporate in the ERT modeling).

37

Nuclear magnetic resonance (NMR) logs were collected in a subset of the boreholes. NMR measurements were made with single-frequency measurements in the open section of the boreholes (figure 4). In the NMR measurement, the total water content is directly proportional to the strength of the magnetic field, and the timing of the NMR decay is related to the pore-size distribution. Early-time decays are indicative of small pore sizes where water is bound, and long decay times are indicative of larger pores where water is mobile. At each 0.5-m interval measurement location 50 measurements were taken and stacked, and the results were analyzed to determine the total water content and the mobile and immobile fraction. The results indicate the NMR water content values ranged from 0.01 to 0.49 and were generally under 0.10 for each 0.5-m interval. NMR estimates of total porosity of ~3% were confirmed by laboratory estimates at a depth of 17m measuring 4.1%. The proportions of water content are shown in Figure 5.2.3.4 along with the distributions of the transverse decay (T2 decay) and pore-sizes. Variations in water content appear to coincide with the presence and absence of fractures in the image logs. The estimates of hydraulic conductivity were determined using empirical equations with default values from the literature, and are considered to be relative estimates of hydraulic conductivity.]

GPR reflection data were collected in 86BR and 87BR in single-hole mode (Figure 5.2.3.5) and in cross-hole mode (Figure 5.2.3.6) between these boreholes. The radar data were highly attenuated by the conductive rock units, and there was little depth of penetration into the formation. Hole-to-hole measurements were conducted in zero-offset , level-run profiling mode. In the level run measurements the signal traveled from one hole to the other, but had poor signal strength. The high attenuation of the signal at the NAWC site made directional radar impractical.
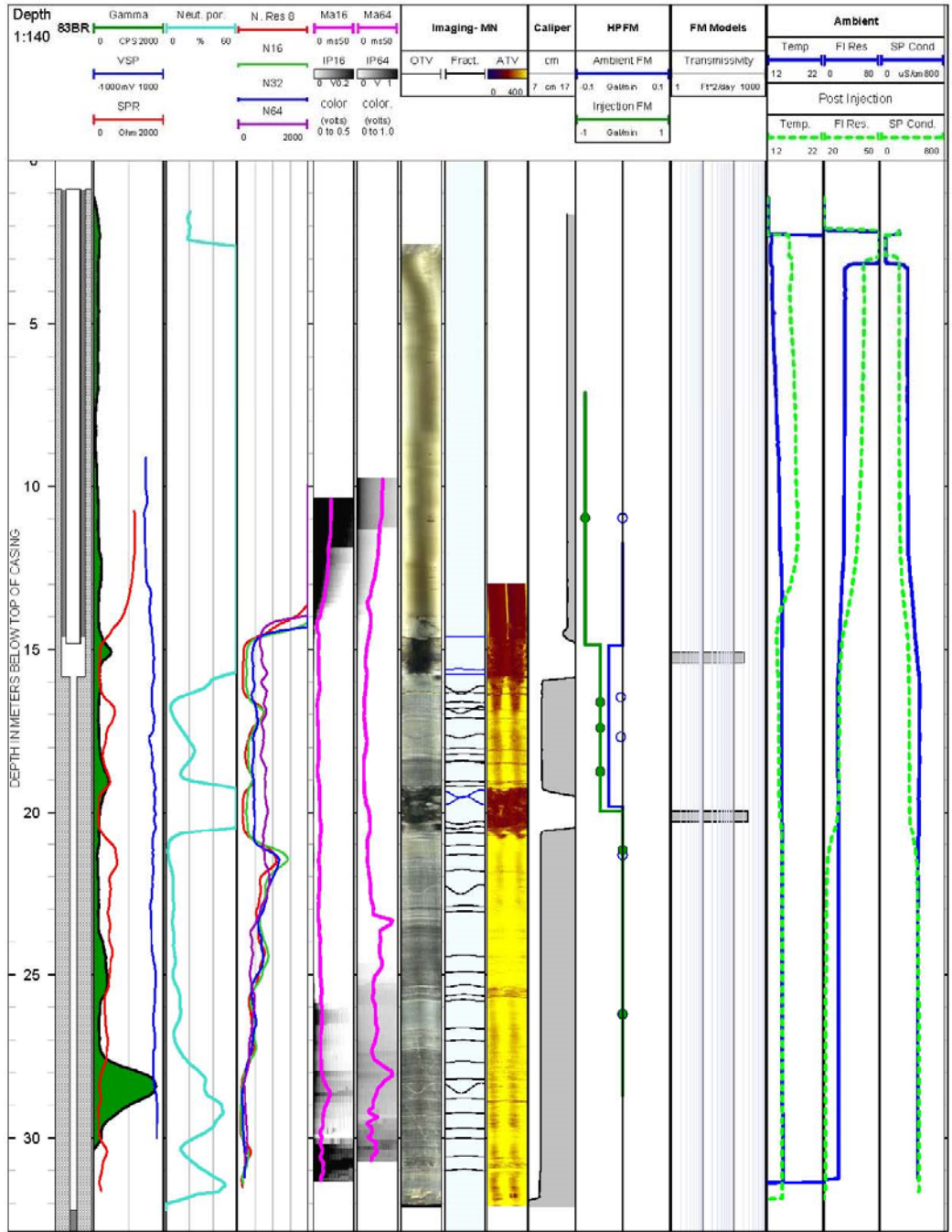
Figure 5.2.3.3: 83BR interpretive notes: The most transmissive and vertically extensive fracture zone is apparent at ~20 m depth below TOC. This zone is evident in caliper, ATV, OTV, neutron porosity, and HPFM logs. A fine grain unit is suggested in the gamma log at ~28 m depth. The other prominent feature in the ATV, OTV and caliper logs is at a depth near the BOC. The HPFM and fluid electrical conductivity and temperature logs indicate it is also hydraulically active under ambient and stressed conditions.
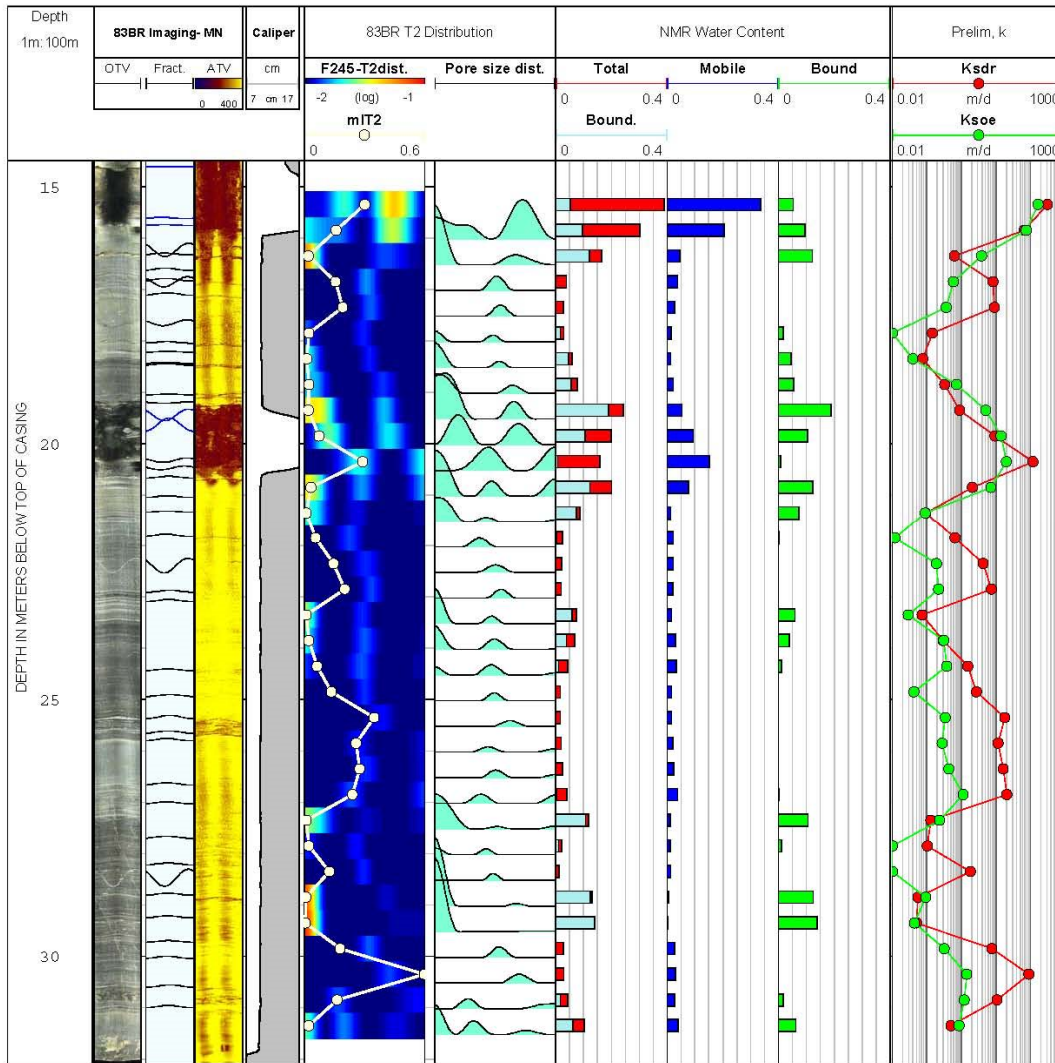
Figure 5.2.3 4: 83BR Nuclear magnetic resonance (NMR)logs showing transverse decay, mean log transverse decay (MLT2), pore-size distribution, water content: total, mobile, bound (immobile), and preliminary estimates of hydraulic conductivity using Schlumberger Doll Research (SDR) and sum of echoes (SOE) equations. NMR logs compare well with fracture locations in the OTV, ATV and caliper logs.
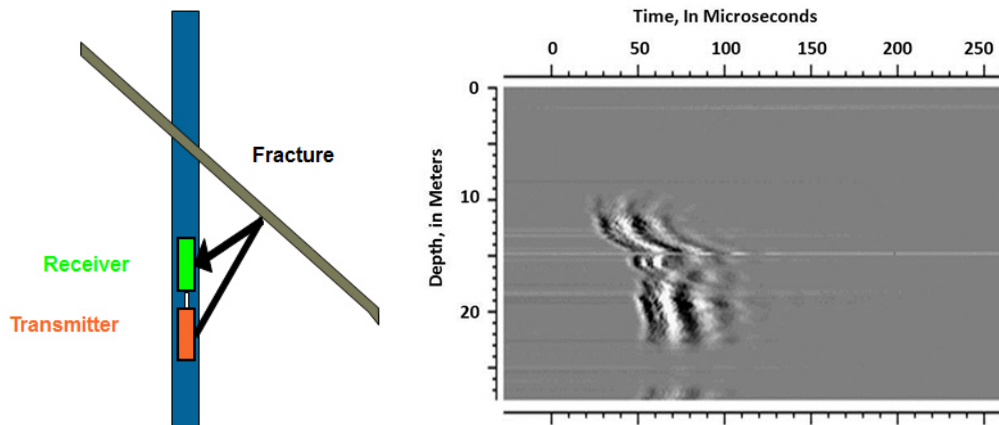
Figure 5.2.3. 5: 87BR schematic of single-hole radar and reflection tomogram showing high attenuation in the open hole below 11 m, shallow depth of penetration, and a large gap in data at 23-27m below top of casing.
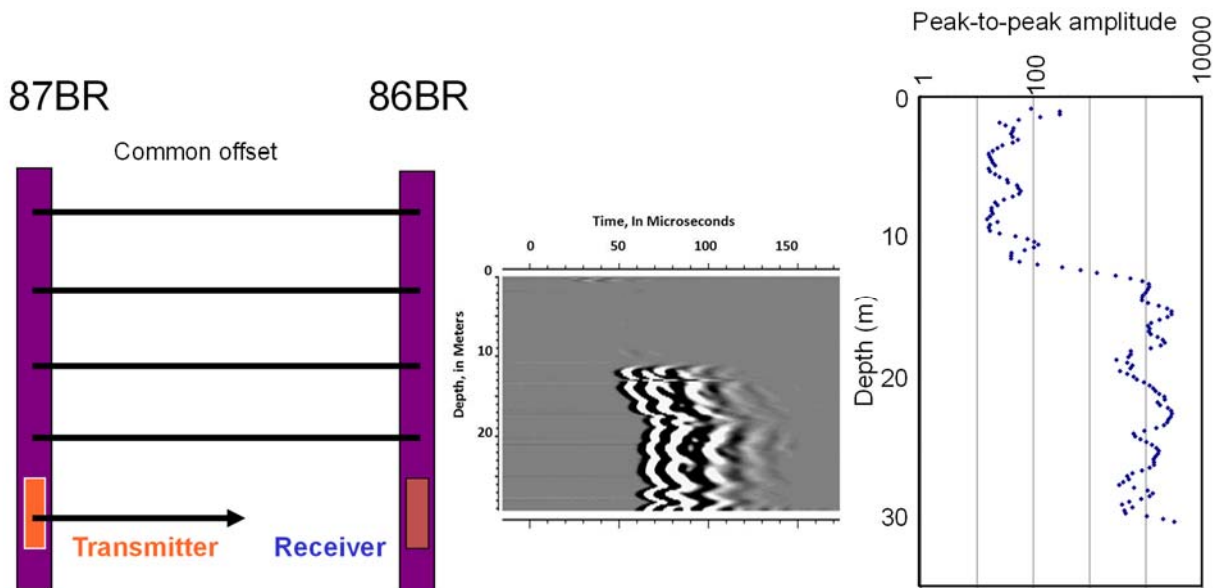
Figure 5.2.3.6: Schematic representation of cross borehole common offset GPR and example results

5.2.4   Hydraulic testing

Cross-borehole aquifer tests were conducted in the boreholes 83BR-89BR to infer locations and extents of permeable fractures (Figure 5.2.4.1). These tests were led by Claire Tiedeman of the USGS (Menlo Park, CA). Discrete intervals, determined from the geophysical logs (Section 5.2.3), were bounded by custom-designed packers within each borehole to isolate fracture zones. The same custom-designed low-pressure packers were also used in the electrode arrays described later. One-hour cross-hole tests were sequentially conducted over 13 intervals. Each test involved pumping from one interval and monitoring drawdown in 19 other intervals. Figure 5.2.4.2 is an example of the data obtained for three intervals in 86BR and 87BR whilst pumping a test interval in 85BR. Large drawdown (e.g. intervals 86b 86c, and 87b) indicates strong connectivity with the test interval in 85BR, whereas muted drawdown (e.g. for intervals 86a and 87c) indicate poor connectivity with the test interval.

Figure 5.2.4. 1: a) Field setup for crosshole aquifer test on wells 83BR-89BR. Blue tank is nitrogen gas used to inflate the packers. b) Typical well setup where the three PVC pipes inside the wellhead give access for pumping and monitoring different isolated intervals.
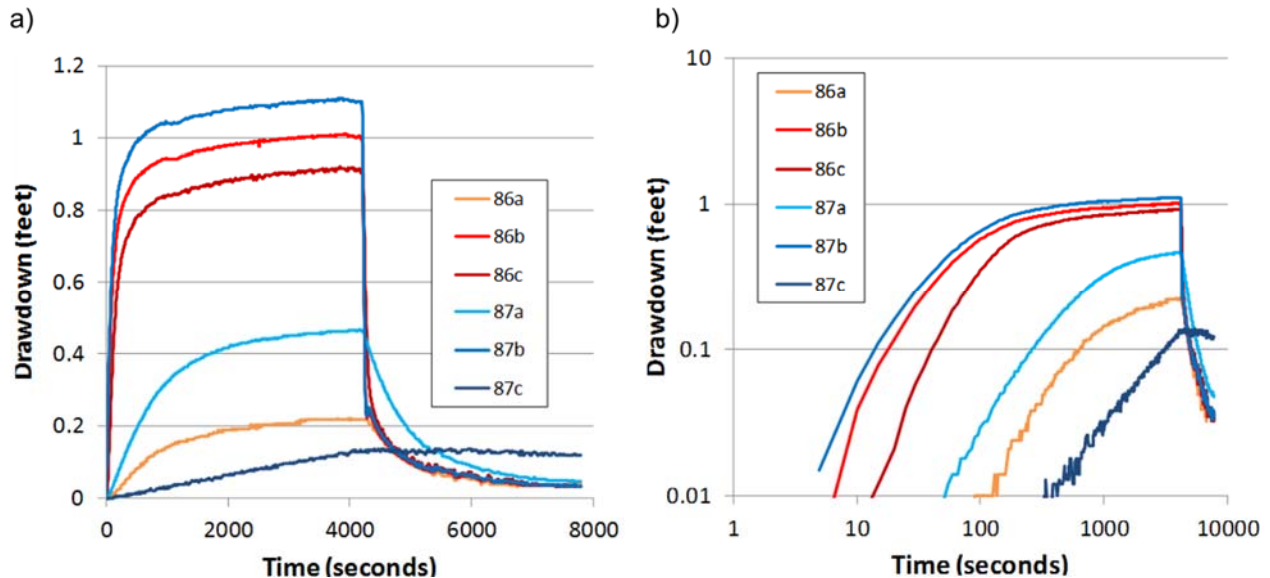
Figure 5.2.4. 2: Drawdown in all intervals of 86BR and 87BR during aquifer test in an interval of 85BR plotted on a) linear scale and b) logarithmic scale (data courtesy of Claire Tiedeman, USGS, Menlo Park, CA).

Figures 5.2.4.3 shows the hydraulic connections qualitatively inferred from the drawdown data. Packer zones with similar colors represent hydraulically connected zones, while the line type qualitatively denotes the level of connectivity inferred from the degree of drawdown observed in response to pumping. Packer zones between 83BR, 85BR and 87BR (solid blue circles) exhibited strong connectivity and were selected as the focus of the tracer studies making up the core of the demonstration described later.
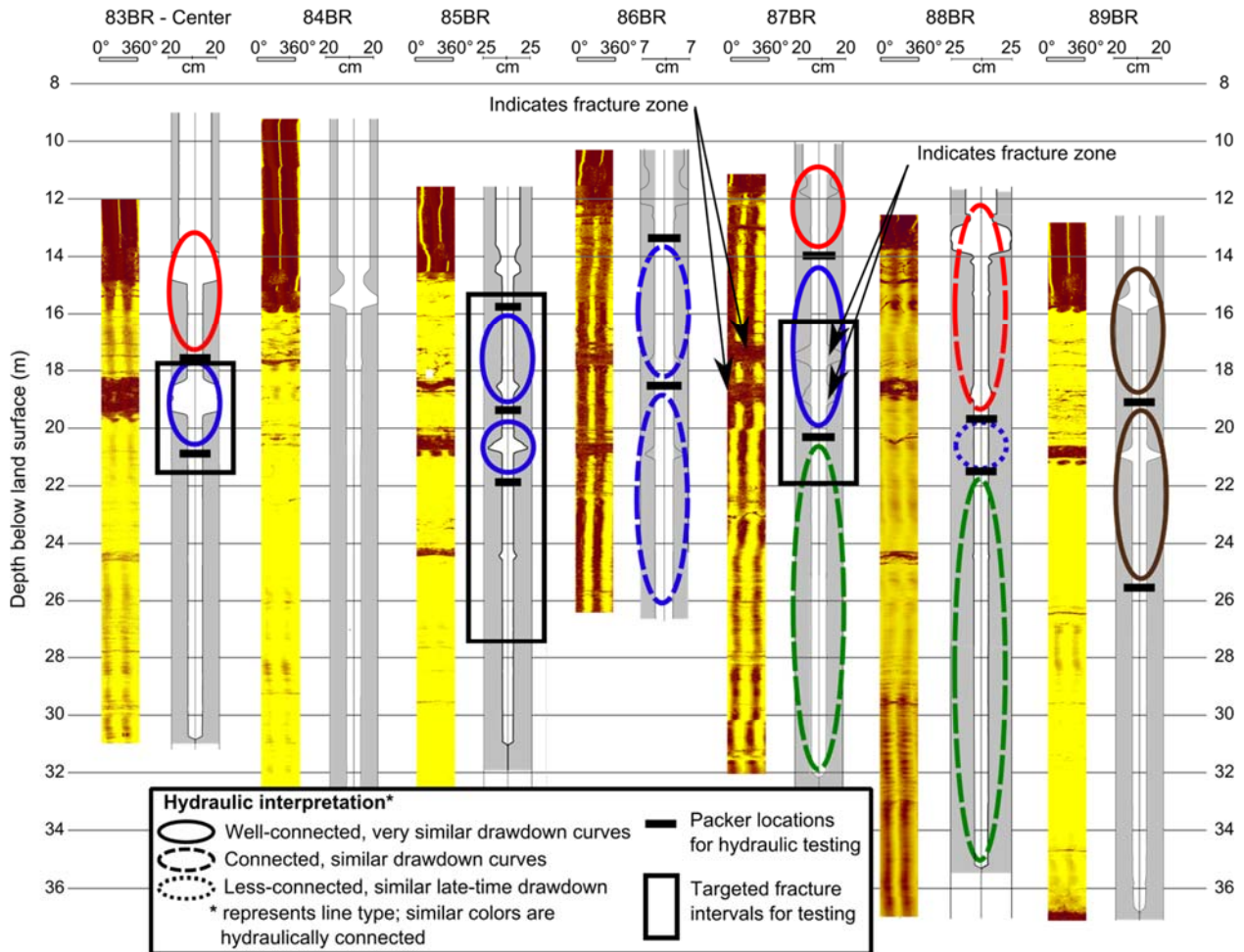
Figure 5.2.4.3: Hydraulic interpretation from drawdown data alongside caliper and ATV borehole logs. Similar colored ovals represent hydraulically connected packer-isolated borehole intervals. Packer placement for hydraulic testing is shown. There were no packers in 84BR, where negligible open-hole drawdown was detected during all aquifer tests. Interpretation generated by Claire Tiedeman (USGS, Menlo Park, CA).

5.2.5 Deuterium Tracer Experiment Conducted in ERT Boreholes to Design Injection and Monitoring of Biostimulation Amendments

In order to put constraints on the injection volume of biostimulation amendments in boreholes 83BR – 89BR and prepare for the ERT monitoring demonstration, a tracer experiment was conducted in these boreholes on March 20, 2013. This experiment used the electrode arrays (Section 5.4.1) that are outfitted with tubing, allowing hydraulic access to a target interval in each borehole, referred to as the "Water Sampling Zone" (WSZ).

The tracer experiment was setup by first pumping water from the WSZ in borehole 83BR (Figure 5.2.5.1). The pumped water was used to prepare a tracer solution by mixing 2000 grams of 99.8% pure deuterium oxide with approximately 200 L of the groundwater. The tracer solution was stored at land surface in a bladder tank to prevent equilibration with the atmosphere.

Figure 5.2.5. 1: Bladder tank used to store the deuterium tracer solution.

The tracer experiment was then conducted by continuously injecting the tracer solution from the bladder tank at land surface into the WSZ in 83BR at a rate of approximately 1 liter per minute (L/min). During the injection of the tracer solution, water samples were collected from the WSZs in boreholes 84BR – 89BR every 15 minutes to monitor for the arrival of deuterium in the groundwater at these monitoring locations. The water samples in 84BR – 89BR were collected by continuously pumping water from the WSZ in each borehole using a peristaltic pump connected to tubing extending from land surface to the WSZ in each borehole. Pumping from the WSZ in 84BR – 89BR was conducted at a rate of approximately 0.1 L/min in each borehole. The tracer solution was injected into 83BR and water samples in 84BR – 89BR were collected over a 10 hour period. Water samples were analyzed for the concentration of deuterium at the USGS Stable Isotope Laboratory in Reston, VA.

The breakthrough curves for deuterium in the adjacent wells are shown in Figure 5.2.5.2. The results of this experiment showed a clear response to the deuterium injection in boreholes 85BR and 87BR. In contrast, the deuterium concentration in 84BR, 86BR, 88BR, and 89BR fluctuated around the ambient deuterium concentration in the groundwater. The breakthrough of deuterium in 85BR occurred approximately 2 hours after the start of the injection in 83BR. The breakthrough of deuterium in 87BR occurred approximately 3 hours after the injection in 83BR.
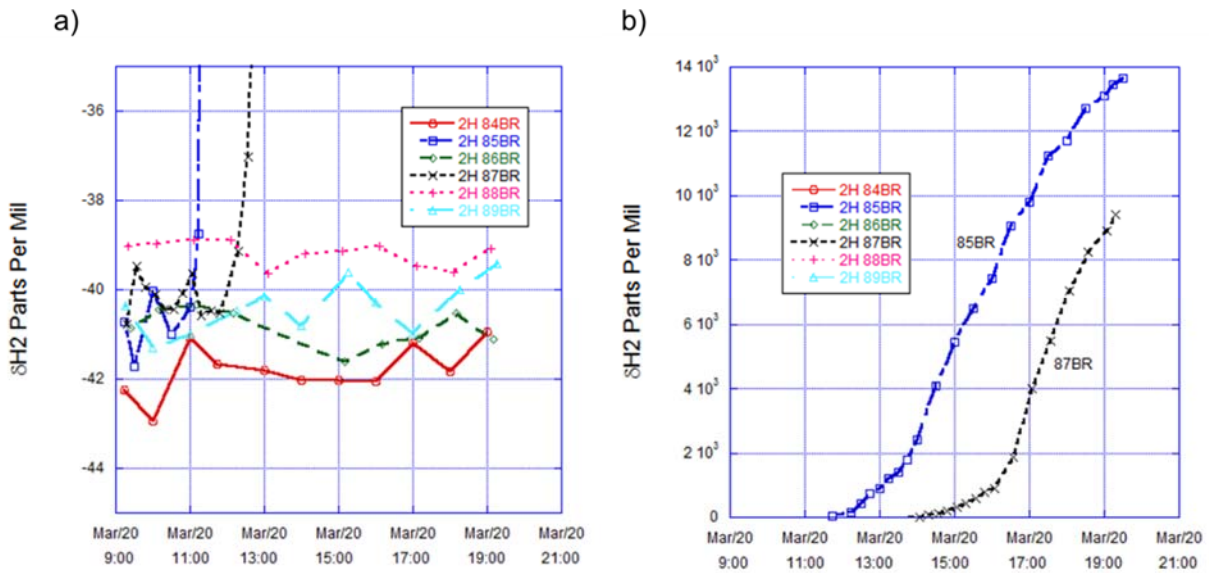
Figure 5.2.5. 2: Breakthrough curves for a) wells surrounding 83BR and b) 85BR and 87BR scaled curves.

These results for the breakthrough curves in boreholes 84BR – 89BR are qualitatively consistent (in terms of time of first breakthrough) with the magnitude of the hydraulic responses observed in crosshole hydraulic tests conducted in 2012 (Section 5.2.4).

There are several complicating issues in the interpretation of the results from the deuterium tracer test. These include:

- Due to problem with the packer assemblies during the experiment, the injection of the tracer solution in 83BR and the pumping of water samples from 84BR – 89BR were conducted in open boreholes. Consequently, the density of the tracer solution may have impacted tracer migration pathways and travel times between the injection borehole and the monitoring boreholes. In addition, the open boreholes may have acted as high permeability pathways vertically connecting the subhorizontal bedding plane parting features in the rock, which may also affect the migration pathways and travel times between the injection and monitoring boreholes.
- The time-varying deuterium concentration monitored in boreholes 84BR – 89BR represents a volumetrically mixed sample. The volume of water in the monitoring borehole acted as a filter on the concentration that was measured in water samples taken at land surface. In addition, volume of water in the tubing and the pumping rate to evacuate the water in the tubing acted as an additional filter on the temporal response of the breakthrough curves.

The effect of the tracer density and the open borehole flow paths on the breakthrough curves cannot be easily evaluated. Similarly, the effect of mixing within the fluid volume in the monitoring boreholes cannot be evaluated because the mixing volume in the monitoring borehole cannot be explicitly identified.

45

However, the test yielded critical information to constrain expected travel times between the wells in the target fracture zone of interest for the ERT demonstration. Taking into account the volume of fluid in the sample tubing with a flowrate of 0.1 L/min, the travel time from the injection well (83BR) to 85BR was approximately 1 hour, and the travel time from the injection well (83BR) to 87BR was approximately 2 hours. Arrival of the tracer solution at 85BR occurred after approximately 60 L of the tracer solution was injected, and the arrival of the tracer solution at 87BR occurred after approximately 120 L of the tracer solution was injected. These volumes and travel times were used to design ERT tracer and amendment injections for the primary demonstration. Critically, this deuterium test provided valuable information used to constrain the configuration of ERT measurements for each snapshot in time of tracer/amendment migration.

5.3 LABORATORY STUDY RESULTS

5.3.1 Amendment Selection Process

The major component of this demonstration project ultimately focused on 3D time-lapse ERT imaging of flow and transport processes of an amendment injection. Several organic substrates capable of anaerobic dechlorination were selected as candidates namely: EOS® acidic pH, EOS® neutral pH and molasses. These substrates are commonly used for enhanced bioremediation and are readily available. For time-lapse ERT imaging, it is important that there is a sufficient measurable conductivity contrast between the native groundwater fluid and the fluid spiked with the amendment injection. Thus, a laboratory study was conducted to determine 1) the conductivity contrast of the amendment with native groundwater as a function of increasing concentrations of a substrate, and 2) calibration curves to potentially convert ERT estimates of electrical conductivity to concentration of substrate (ultimately not done as too uncertain).

Native groundwater was extracted from 83BR (0.491 mS/cm) to which the mass of the substrate was incrementally added. Molasses had the highest conductivity of the three substrates with a maximum conductivity equal to 18.25 mS/cm, which equates to a conductivity contrast of approximately 37 with the native groundwater (Figure 5.3.1).
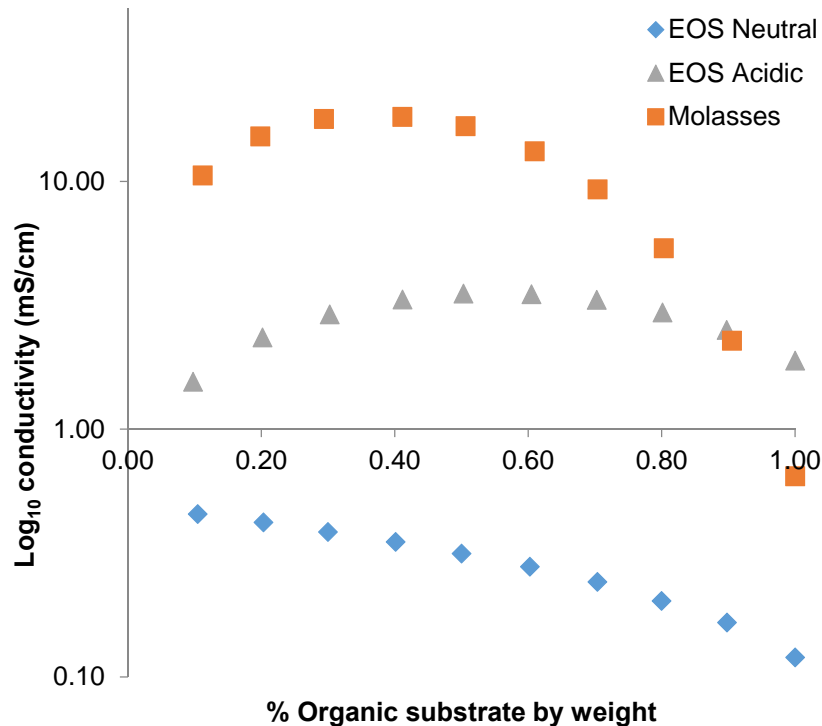
Figure 5.3.1: Amendment calibration curves for EOS Neutral, EOS acidic and molasses

Since sodium bromide (NaBr) was readily available, and was used as the conductive solute in the tracer studies. For the amendment injection, NaBr was used to increase the conductivity contrast of the solution. A laboratory study was conducted on two native groundwater samples to better understand how the interaction between molasses and sodium bromide would affect the conductivity. First, molasses was added to the two native water samples (11.08 g and 11.27 g, respectively) until the maximum conductivity from Figure 5.3.1 was reached.

Conductivities were recorded as 17.86 and 17.9 mS/cm, respectively for each sample. Next, sodium bromide was added incrementally to each water sample; the experiment was ended when the conductivity of the samples reached 62.07 and 61.6 mS/cm, being above typical sea water values (Figure 5.3.2). The sample results agreed well with each other and from this data injected volumes of molasses and sodium bromide could be extrapolated.
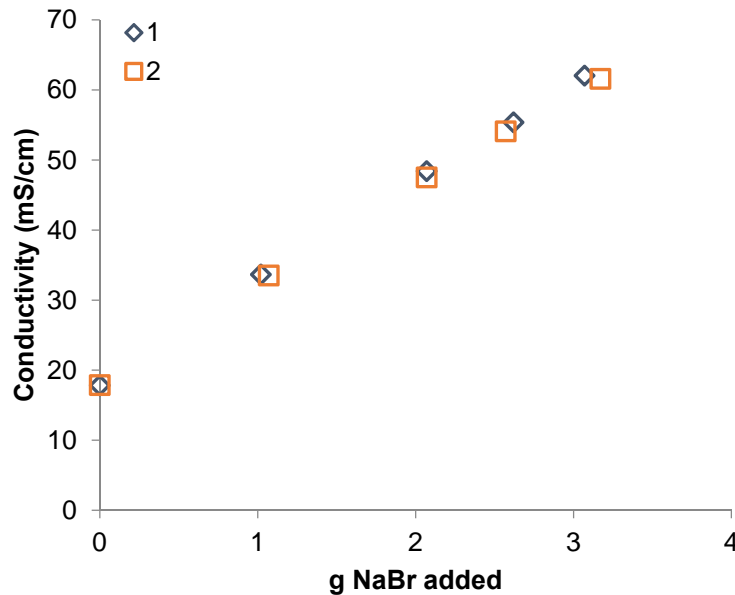
Figure 5.3 2: Graphs for two samples containing molasses with NaBr incrementally added. The two samples show good repeatability.

5.4 DESIGN AND LAYOUT OF TECHNOLOGY COMPONENTS

5.4.1 ERT Background

a) Basic principles of electrical resistivity tomography (ERT)

Electrical resistance (R) is defined as the opposition of material to the flow of an electric current and is specific to a measurement configuration. Measurements of R are calculated from potential measurements ΔV of a known current injection I (i.e. $R = \Delta V / I$) into the subsurface. The general approach involves injecting a current between two electrodes followed by measuring the transfer resistance between two other electrodes. Current injection electrodes in four-point measurements are commonly referred to with the acronyms A and B; potential electrodes in four-point measurements are commonly referred to as M and N (Figure 5.4.1).
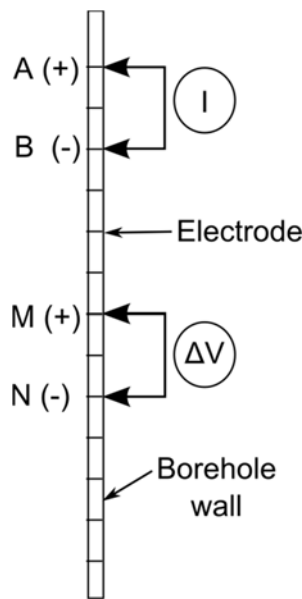
Figure 5.4.1: Schematic of four electrode measurement where current electrodes are designated as A and B and potential electrodes are designated as M and N.

Electrical resistivity (ρ) is an intrinsic physical property of the subsurface and is a measure of a material's ability to conduct an electric current. The potential **V** at any point for current strength I injected at a source **r** for a given resistivity (ρ) is described by the Poisson equation:

$$\nabla \cdot \left(\frac{1}{\rho} \nabla \mathbf{V} \right) = -I \delta(\mathbf{r}) \quad (1)$$

where δ signifies the Dirac delta function. Equation 1 is subject to either Neumann (i.e. no current flow) or mixed-type source-dependent boundary conditions.

For a single current electrode in a homogeneous half-space, Equation 1 simplifies to:

$$V(r) = \frac{\rho I}{2 \pi r}, \quad (2)$$

which defines the potential V as a function of a radial distance r from the current electrode. The potential difference between electrodes M and N where current injection is at A is then given by,

$$V_M = \frac{\rho I}{2\pi}\left(\frac{1}{AM} - \frac{1}{AN}\right), \quad (3)$$

where AM and AN are the distances between current electrode A and potential electrode M (+) and N (-) respectively. For a four electrode measurement, using superposition the total potential difference (V_{MN}) at MN equates to,

$$V_{MN} = \frac{\rho I}{2\pi}\left[\left(\frac{1}{AM} - \frac{1}{BM}\right) - \left(\frac{1}{AN} - \frac{1}{BN}\right)\right], \quad (4)$$

which rearranges to,

$$\rho = 2\pi \frac{V_{MN}}{I} k \quad (5)$$

$$k = \left(\frac{1}{AM} - \frac{1}{BM}\right) - \left(\frac{1}{AN} - \frac{1}{BN}\right) \quad (6)$$

For a heterogeneous earth, the electrical resistivity calculated in Equation 5 is defined as the apparent resistivity, ρ_{app}, since this assumes a homogenous earth. When considering electrodes below the surface (i.e. in a borehole), a factor of 4π is used instead of 2π in Equations 2 through 5 to account for a surface boundary (at z=0). To account for this surface boundary, it is common to use the method of images, and define image lengths A_i and B_i for current electrodes. In Equation 6, k is modified as,

$$k = \left(\frac{1}{A_iM} + \frac{1}{AM}\right) - \left(\frac{1}{B_iM} + \frac{1}{BM}\right) - \left(\frac{1}{A_iN} + \frac{1}{AN}\right) + \left(\frac{1}{B_iN} + \frac{1}{BN}\right). \quad (7)$$

In a DC (direct current) resistivity survey, the configuration of the electrodes can be optimized to minimize the data acquisition time while maximizing the measurement resolution. For n electrodes, a total of $n(n-1)(n-2)(n-3)/8$ four-point electrode configurations exist. Collection of this comprehensive measurement sequence is impractical especially when attempting to capture time-lapse processes. An optimized measurement sequence will depend on site requirements (e.g. measurement errors and resistivity structure) and specific project demands (e.g. resolution and data acquisition speed). Commonly used four-electrode configurations are nested arrays such as Wenner and Schlumberger or dipole-dipole schemes; the advantages and disadvantages of these configurations in resolving horizontal and vertical subsurface features are well documented (for example, Binley & Kemna, 2005). Recognizing a need for optimized measurement sequences, a number of researchers (Blome et al., 2011; Loke et al., 2010; Stummer et al., 2004; Wilkinson et al., 2012; Wilkinson et al., 2006) have explored incrementally adding measurements to an initial dataset that will improve the resolution of the true (in many cases, assumed) model.

Electrical resistivity or its inverse electrical conductivity is sensitive to subsurface variations in moisture content, temperature, lithology, porosity, groundwater composition and clay content (Binley & Kemna, 2005). In this demonstration, the investigated fractured rock environments are below the water table and at depths unaffected by diurnal temperature

fluctuations. In this setting, lithological porosity changes due to the presence of fractures and groundwater composition are expected to dominate the electrical measurement response assuming low surface conduction.

b) Finite element mesh (FEM) generation

Electrical resistance measurements are commonly modeled through finite element methods, necessitating the generation of a finite element mesh (FEM). In 2D, rectangular or triangular shaped elements are common in ERT modeling; in 3D, cuboids, triangular prisms or tetrahedrons are common. This research used tetrahedral mesh elements to allow for flexibility in terms of mesh refinement around small scale features (i.e. fractures, boreholes and electrodes) and incorporation of topography (Rücker et al., 2006) (Figure 5.4.2). Several robust mesh generators are available; TetGen was used since it is integrated with the ERT modeling software, E4D, (discussed below) which was used in this study.
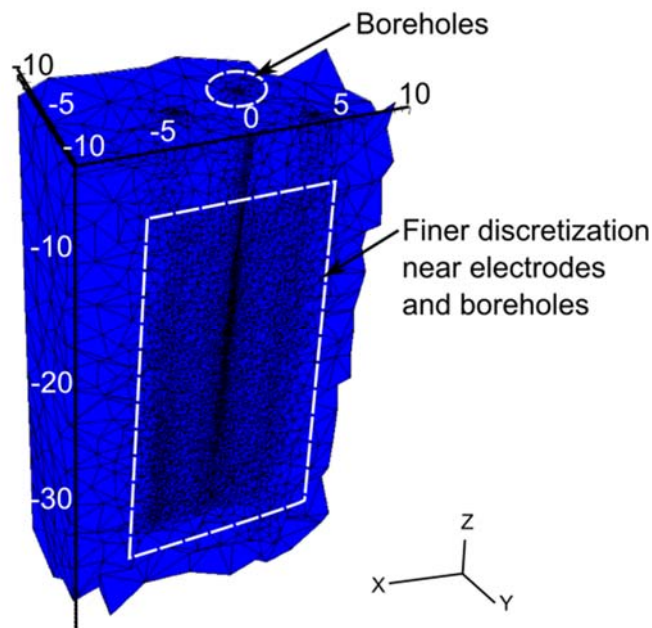
Figure 5.4.2: Example 3D tetrahedral mesh showing finer discretization near boreholes and electrode locations

c) Electrical resistivity tomography modeling

The modeling of ERT measurements was achieved using a modified version of the open source parallel code, E4D (https://e4d.pnnl.gov/) described in Johnson et al., (2010). E4D is a 3D deterministic modeling and inversion code for ERT data (Figure 5.4.3). The code is specifically designed to work on parallel, high-performance computing systems. Parallelized code allows for computational efficiency such that larger inverse problems with millions of parameters, which are used to define small scale features such as boreholes, can be solved.

51

Forward modeling:

Inverse modeling:

Load run/model information
Master broadcast to slaves

Master node broadcasts data
to slaves for inverse
computations

S_1 Compute poles

S_2 Compute poles

... S_n Compute poles

No

S_1 Inverse eqns

S_2 Inverse eqns

... S_n Inverse eqns

Output results

Yes

Is data fit OK?
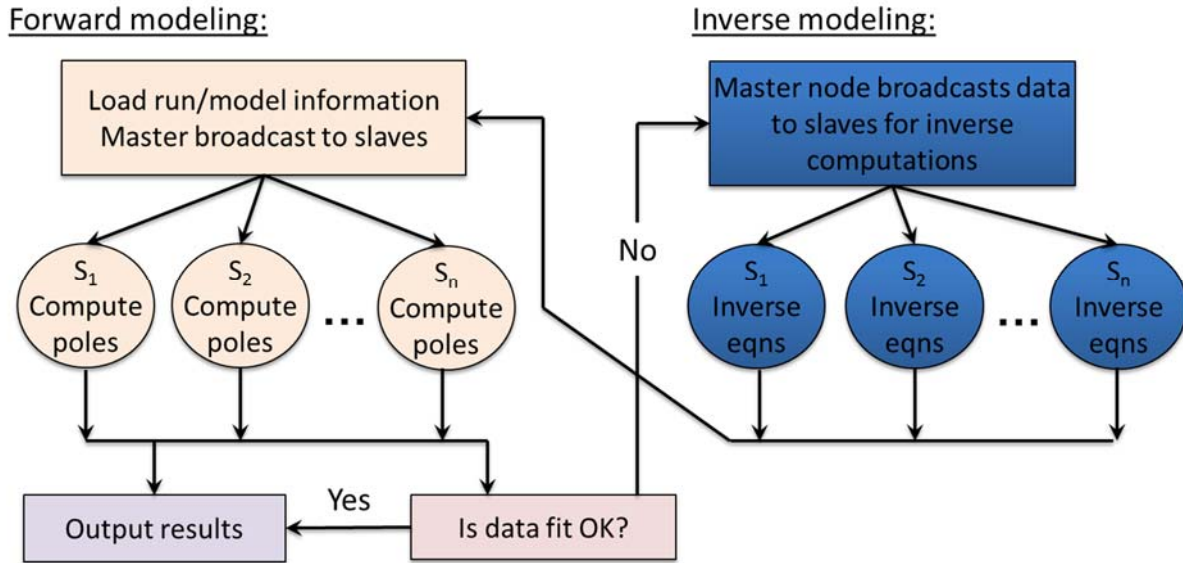
Figure 5.4.3: ERT modeling code schematic adapted from Johnson et al. (2010).

d) Forward Modeling

Forward modeling of an ERT conductivity structure yields a potential at each mesh node in the FEM. To speed computational efficiency parallel modeling of pole solutions can be done (Figure 5.4.3) from which dipole-dipole measurement solutions can be derived. The delta function (which goes to infinity) is used to describe the introduction of current at a point (Equation 1). This can introduce a numerical error near the current source due to inaccurate representation in discrete space of a discontinuous (i.e. the delta) function. Numerical errors are also higher near electrode locations due to high potential gradients. Singularity removal can be used to reduce these numerical modeling errors. In this technique, the potential is split into singular and non-singular components. With the analytical solution for the singular component known, the forward finite element problem reduces to finding the non-singular potential (Lowry et al., 1989; Rücker et al., 2006). Once the non-singular potential is solved, the singular component can be added to obtain the total potential (Blome et al., 2009). Numerical modeling errors associated with large potential gradients can be reduced by using finer elements surrounding electrode locations.

e) Inverse Modeling

Inversion of ERT data is inherently underdetermined (i.e. non-unique), such that the inverse problem is typically formulated as a regularized optimization problem where model constraints are imposed to limit the number of possible solutions. The objective function shown below seeks to optimize the tradeoff between the data misfit and model constraints (Binley & Kemna, 2005; Sasaki, 1994),

$$\Psi(\mathbf{m}) = \Psi_d(\mathbf{m}) + \alpha\Psi_m, \quad (8)$$

where,

52

$$\Psi_d(\mathbf{m}) = \left\| \mathbf{W_d}(\mathbf{d} - f(\mathbf{m})) \right\|, \quad (9)$$

$$\Psi_m(\mathbf{m}) = \left\| \mathbf{W_m}(\mathbf{m} - \mathbf{m_0}) \right\|. \quad (10)$$

In equations 9 and 10, $\|\ \ \|$ signifies the norm of order 2 although other norm measures can be implemented (Farquharson, 2008). The variable Ψ_d is a measure of the difference, between the measured ($\mathbf{d}$) and calculated data ($f(\mathbf{m})$) from the estimated log conductivity distribution ($\mathbf{m}$); Ψ_m is a measure of the complexity in $\mathbf{m}$ or a measure of the difference between $\mathbf{m}$ and some preferred reference model $\mathbf{m_0}$. With an appropriately constructed model weighting matrix ($\mathbf{W_m}$), the reference model $\mathbf{m_0}$ may be non-existent (e.g. ($\mathbf{0}$)), may be a homogeneous medium, or it may contain expected conductivity values used to implement known conductivity constraints. The parameter α optimizes the trade-off between model misfit and data misfit. $\mathbf{W_d}$ is a diagonal data-weighting matrix, where each data weight is equal to the reciprocal of the individual standard deviations defined by a data error model discussed below. The model-weighting matrix ($\mathbf{W_m}$) contains the model constraints and is also known as the regularization matrix. Minimization of Equations 9 and 10 assuming data errors are normally distributed leads to a linear system of equations (Binley & Kemna, 2005; Backus & Gilbert, 1968; Farquharson, 2008):

$$(\mathbf{J_k^T W_d^T W_d J_k} + \propto \mathbf{W_m^T R_m W_m}) \Delta \mathbf{m_k} = \mathbf{J_k^T W_d^T W_d}[\mathbf{d} - f(\mathbf{m_k})] - \propto \mathbf{W_m^T R_m W_m}(\mathbf{m_k} - \mathbf{m_0}). \quad (11)$$

$\mathbf{R_m}$ always depends on the value of $\mathbf{m}$, requiring an iterative solution (iteratively reweighted least squares or IRLS).

At each iteration k the model update vector $\Delta \mathbf{m_k}$ can be solved e.g. by a conjugate gradient least squares algorithm (Johnson et al., 2010; Zhang, 1995). After the first iteration, the reference model, $\mathbf{m_0}$, is assigned the value from model iteration, $\mathbf{m_{k-1}}$, or an already-specified expected conductivity value. $\mathbf{J_k}$ is the Jacobian matrix at iteration k, where each member $J_{ij} = \partial f_i(\mathbf{m_k})/\partial m_j$ for model $\mathbf{m_k}$. The normalized χ^2 misfit error is used as the convergence criteria which is given by

$$\chi^2 = \frac{1}{n-1} \sum_{i=1}^{n} \frac{(d_{obs,i} - f_i(\mathbf{m}))^2}{SD_i^2}, \quad (12)$$

where n is the number of observations and SD_i is the standard deviation for measurement i. When measurement errors are correctly quantified, independent and normally distributed, the data are appropriately fit when $\chi^2 = 1$, which is the typical value used for the convergence criteria.

Time-lapse ERT datasets can be collected to monitor or delineate conductivity changes due to hydrological processes such as the introduction of a contaminant/tracer, salt-water intrusion, and/or porosity changes. In E4D, model parameters can be regularized to background conductivities or to a previous time-step inverse solution. The minimization of the objective function remains the same as in Equation 11 with the normalized χ^2 misfit error (defined in Equation 12) used as convergence criteria.

Assessment of measurement errors for $\mathbf{W_d}$ is critical for ensuring high quality ERT images. Underestimation of measurement errors can result in overly rough 'noisy' images and

overestimation can result in overly smooth images (LaBrecque et al., 1996). Data measurement errors are often assessed with reciprocal measurements (Slater et al., 2000). These measurements are collected by interchanging the current injection electrodes (A and B) with the potential electrodes (M and N). In theory, the resistances should be equal. Measurements with a high reciprocal error can be filtered from the dataset and a functional relationship between measured resistances and data error can be developed and applied to all measurements (Koestel et al., 2008; Slater et al., 2000). In some cases, good data quality results in low reciprocal errors such that forward numerical modeling errors can dominate overall errors.

5.4.2 Advances in ERT modeling

Sharp electrical conductivity contrasts at discrete fractures and boreholes require care in ERT inversion. Because many solutions will fit the data equally well, the most popular methodology for ERT imaging is usually   to resolve the least amount of structure in a geologically meaningful model (DeGroot-Hedlin & Constable, 1990), commonly referred to as smoothness constrained inversion. This approach is unlikely to produce the most meaningful geologic model for fractured rock given the introduction of a highly conductive borehole which can introduce borehole artifacts (Doetsch et al., 2010). Electrode misplacement in boreholes can result in inversion artifacts (Wilkinson et al., 2008) which can potentially be limited by incorporating borehole deviations within the discretization of the model space.

Typically in a smoothness constrained inversion, a similarity constraint equation is included between adjacent elements in the formulation of the regularization matrix $\mathbf{W_m}$ (Figure 5.4.4). This is shown between elements 1 and 2; and relative weighting between elements can be adjusted as shown between elements 1 and 7 (Figure 5.4.4). Where available field information is known, additional regularization (i.e. model) constraints can be added to limit the number of non-unique solutions resulting in a more realistic inverse model. Smoothness constraints between different regions in the discretization can be relaxed or 'disconnected' (Figure 5.4.4) by removing a constraint equation between elements in the formulation of $\mathbf{W_m}$. For example, in Figure 5.4.4, a constraint equation is omitted between elements 2 and 3. Such a regularization disconnect (RD) enables the inversion to place a sharp conductivity contrast across a boundary, if supported by the data, without penalty.   If a conductivity is known within particular elements in the model space (e.g. from a borehole conductivity probe), the conductivity within these elements can be constrained to this value, and relative weighting can also be adjusted, as shown in the last three constraint equations (Figure 5.4.4).
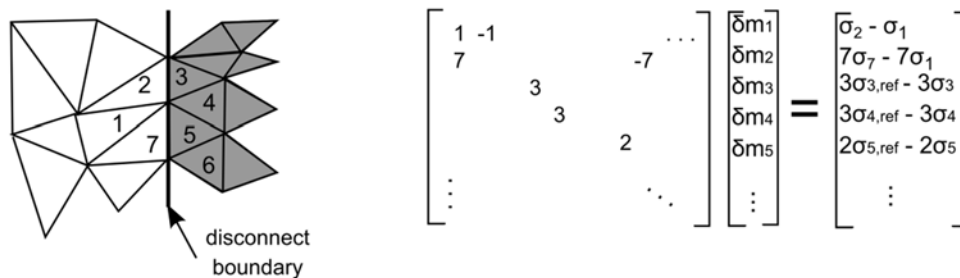
Figure 5.4.4: Regularization matrix formulation for finite element mesh (FEM) elements

E4D (https://e4d.pnnl.gov/) described in Johnson et al., (2010) is a 3D deterministic modeling and inversion code for ERT data. Enhanced capabilities in E4D and licensing for external users were developed under this demonstration project. The code is specifically designed to work on parallel, high-performance comput   ing systems. Parallelized code allows for computational efficiency such that larger inverse problems with millions of parameters, which are used to define small scale features such as boreholes, can be solved. The code allows for additional model constraints to be applied based on field data available. Originally described as compactness constraints (Farquharson, 2008; Last & Kubik, 1983), E4D designates functional forms as *reweighting functions*. Reweighting functions are evaluated for a defined *structural metric code*, which defines a relationship between a target element in the FEM and an adjacent element or a reference value. This representation of model constraints allows for ultimate flexibility when inputting available field data and parameters. Model constraints allow a user to add reliable information to the inverse problem, of which the solution is non-unique. This limits the possible number of solutions; however any model constraint must be supported by the data. An inversion model will only *converge* if the desired data misfit criteria are met. For complete information a user manual for E4D (partly developed under this project) is available for download at https://e4d.pnnl.gov/ (T. Johnson, 2014).

In this project, the inverted cumulative distribution function (CDF), which is one of the four reweighting functions, was used to favor a blocky structure in the fractured mudstone rock to simulate the presence of fracture zones (Figure 5.4.5a). Borehole conductivity logs were used to define lower and upper bound conductivity limits within the boreholes (Figure 5.4.5b and 5.4.5c). Within time-lapse inversions where a conductive tracer was added (Sections 5.5 and 5.6) constraints were added to encourage a more conductive host rock than background inversions.

Smoothness constraints were relaxed at borehole boundaries and borehole deviation logs (Section 5.2.3) were incorporated to define these boundaries. This allowed electrodes to be more accurately positioned in the model space while limiting borehole artifacts. A comprehensive assessment of these ERT code advancements can be found in Section 6.0.
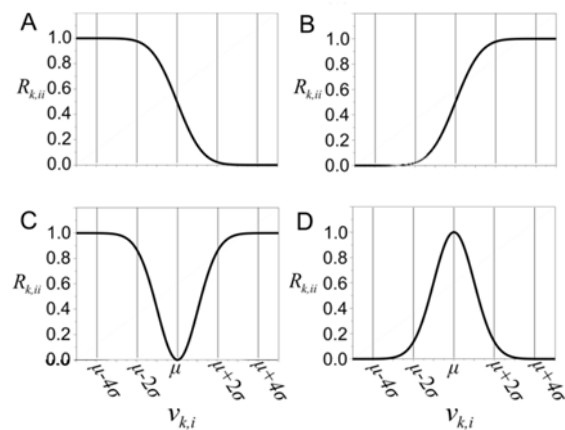
Figure 5.4.5: Reweighting functions in E4D (https://e4d.pnnl.gov/) A) The weighting of $v_{k,i}$ begins to minimize if the value of $v_{k,i}$ drops below $\mu+2\sigma$, reaching the full weight if $v_{k,i}$ drops below $\mu-2\sigma$. B) The weighting of $v_{k,i}$ begins to minimize if the value of $v_{k,i}$ rises above $\mu-2\sigma$, reaching the full

weight if $v_{k,i}$ rises above $\mu+2\sigma$. C) The weighting of $v_{k,i}$ begins to minimize if the value of $v_{k,i}$ deviates from μ, reaching the full weight if $v_{k,i}$ deviates from μ more than (approximately) 2σ. D) The weighting of $v_{k,i}$ begins to minimize as the value of $v_{k,i}$ approaches μ, reaching the full weight when $v_{k,i}$ is equal to μ. Different values of $v_{k,l}$ are referred to as a structural metric codes.

5.4.3 ERT Arrays: Design, Construction, Installation

A critical element of this demonstration involved the design, development and construction of a first of its kind integrated packer/electrode water sampling assembly for ERT monitoring of tracer/amendment injections during tracer injection into an isolated interval of a borehole associated with fracture zones. Seven such arrays were custom-built for this project and allowed simultaneous (1) isolation of borehole intervals, (2) tracer injection into specific intervals, (3) fluid sampling at isolated test intervals via a sampling port, and (4) ERT data acquisition using a string of electrodes. Geophysical logs (Section 5.2.3) and hydraulic tests (Section 5.2.4) were extensively reviewed to determine appropriate isolation intervals for individual arrays (Figure 5.4.6). Caliper, ATV, OTV logs indicated locations of intersecting fracture zone depths within each borehole; in conjunction with single and cross borehole double-packer hydraulic tests, intervals of high transmissivity were inferred and considered in the design of these arrays.

The placement of packers was chosen such that fracture intervals were isolated from one another and discrete fracture zones could be targeted for tracer injections (Figure 5.4.7).   The particular intervals that were the focus of the tracer studies and amendment injection coincided with highly transmissive fracture zones (Figure 5.4.7). Water sampling and injection depths were within the borehole vertical sections that contained this highly transmissive fracture zone. Aside from hydraulically isolating intervals during tracer tests, packers can also limit the electrical current flow along the borehole via the conductive fluid, which can limit current penetration into the formation and hence limit ERT resolution. We desired this added benefit of using packers while conducting ERT imaging and also quantitatively evaluated this assumption as proposed in several studies (Binley & Kemna, 2005; Coscia et al., 2011; Doetsch et al., 2010; Sugimoto, 1999).
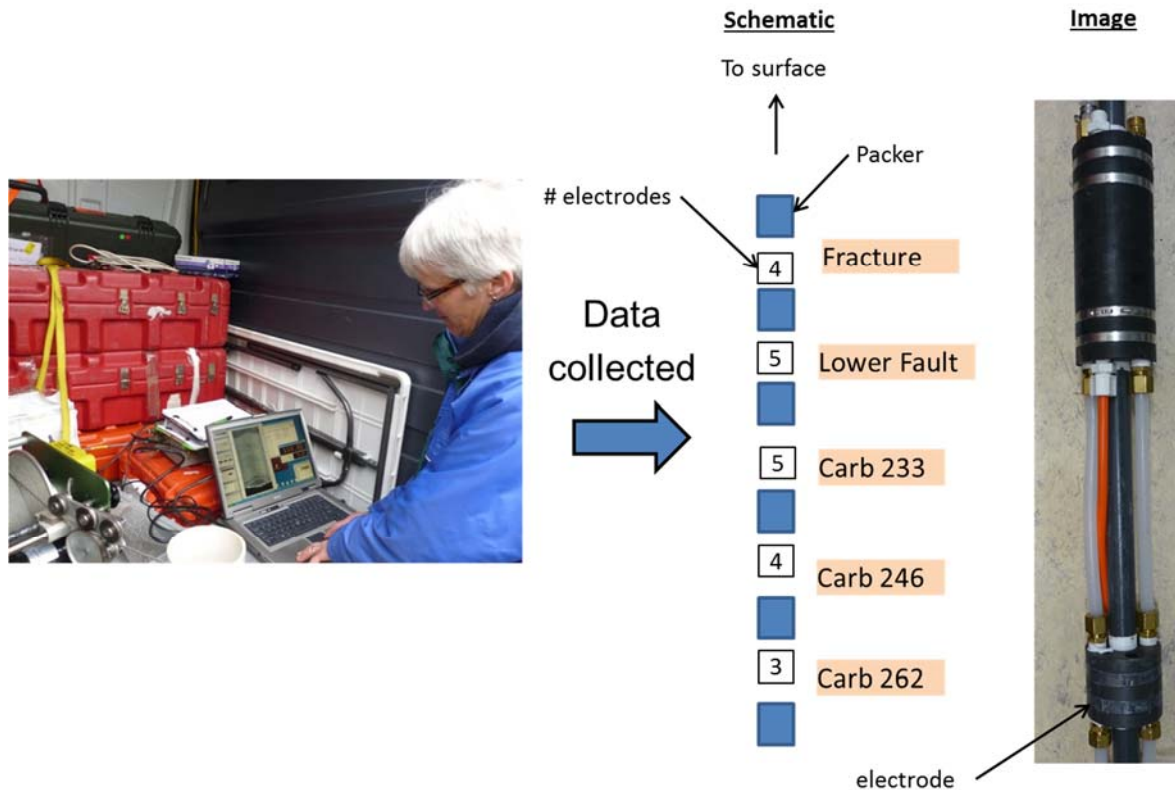
Figure 5.4.6: Schematic showing how borehole geophysical data was used in the decision making process of laying out the electrode arrays.

A total of 143 electrodes were used across the seven boreholes, each being constructed from two, 1" lead strips (Figure 5.4.8). Both electrodes and packers were threaded onto a ¾" schedule 80 PVC pipe (Figure 5.4.9b). A cross section of the electrodes and packers is shown in Figure 5.4.9c, which contained one ¼" ID (inner diameter) opening and three ½" ID openings. These four openings allowed for three air supply lines and a water sample line. A motorcycle tire inner tube was used as the inflatable material on each of the packers. Four (4) low profile clamps were used to secure the inflatable material to the packer block. The low profile clamps minimized any movement during installation which would compromise the air-tight seal on the packers. The low pressure packers were tested to maintain 15 psi of pressure above hydrostatic. During hydraulic testing (Section 5.2.4) vertical isolation was achieved if the packers were inflated 10 psi above hydrostatic pressures. So as not to overinflate upper packers relative to lower packers (i.e. due to the increasing hydrostatic pressure with depth) different airlines were used for top, middle and bottom packers. Using different airlines also provided flexibility to target multiple fractures (where desired) within a middle or bottom vertical section. Electrodes were spaced 0.8 m apart, representing a compromise between available open-hole lengths at NAWC and desired ERT image resolution. A total of 40 packers were used in the seven electrode arrays (Figure 5.4.7a). Arrays were constructed in sections in the Near Surface Geophysics laboratory at Rutgers University Newark (Figure 5.4.8a).
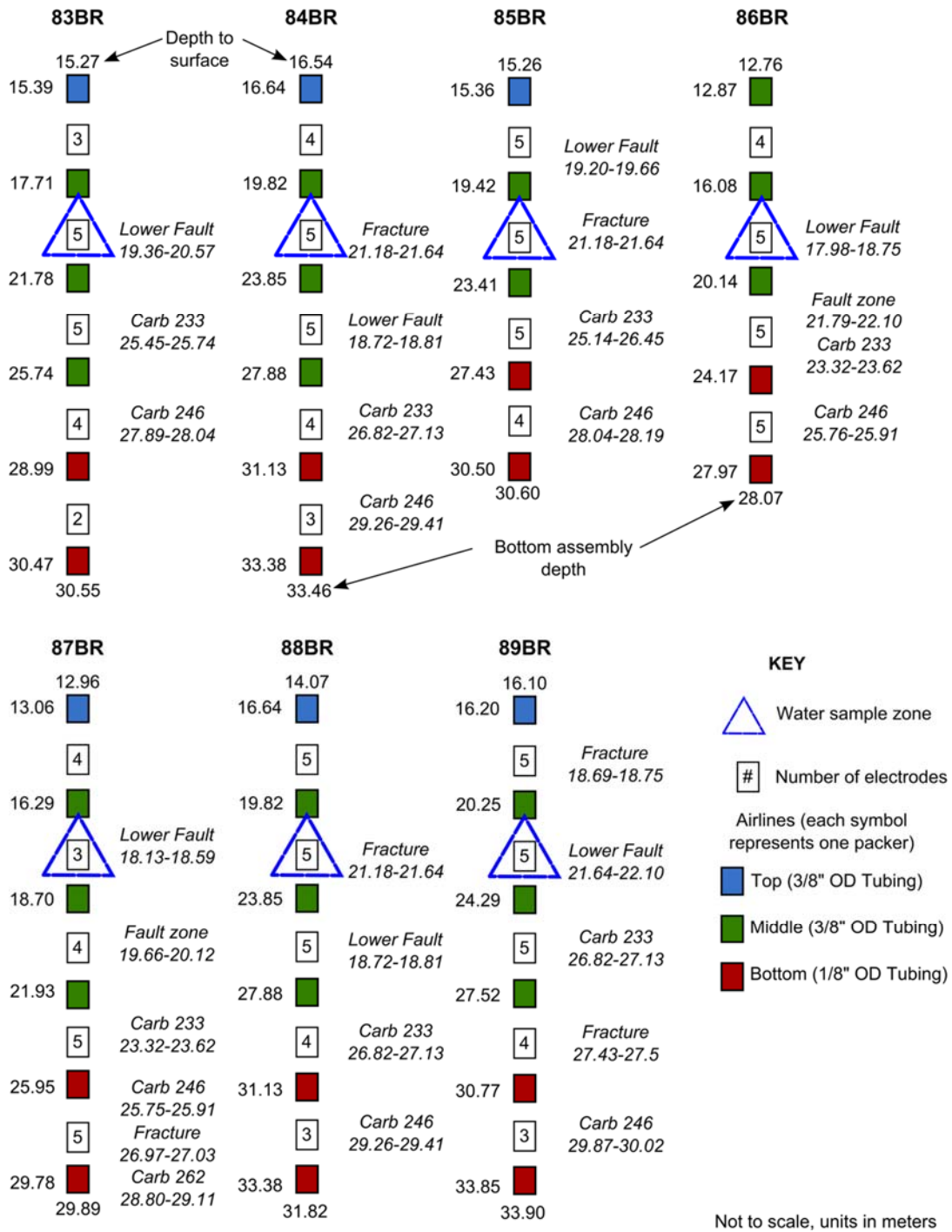
Figure 5.4.7: Electrode array design schematic alongside fracture zone interpretations from borehole geophysical logs and coring

58
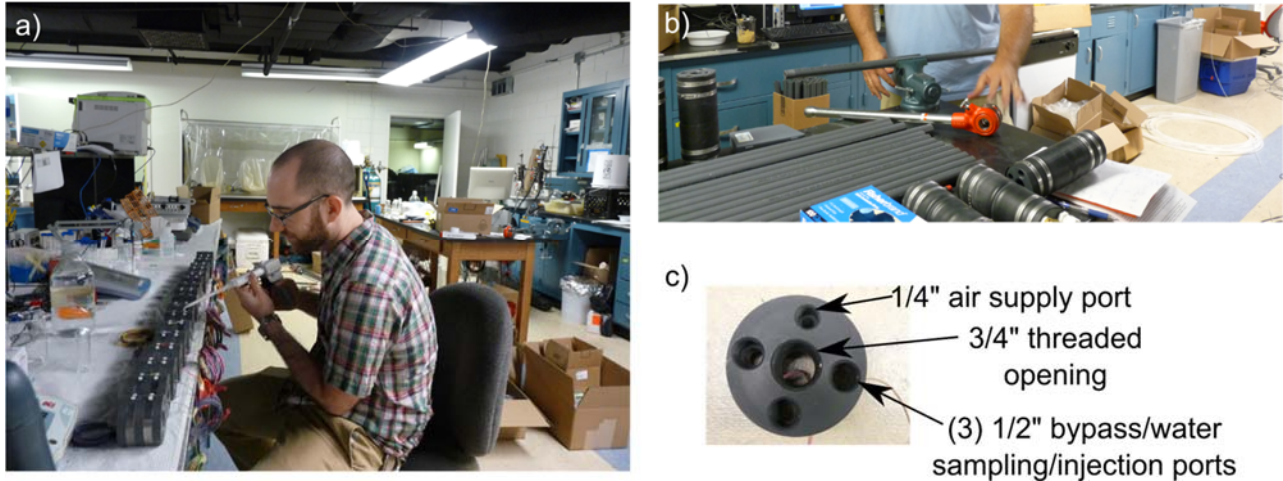
Figure 5.4.8: a) Electrode construction b) Preparation of threaded PVC piping c) Cross section of electrode/packers.
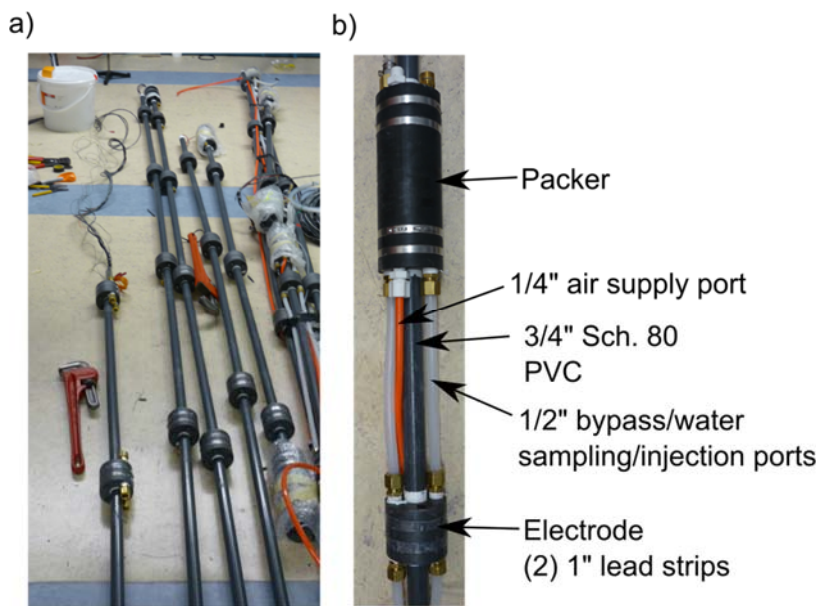
Figure 5.4.9: a) Electrode array section built in the Rutgers laboratory b) Detailed view of packer and electrodes in arrays.

Electrode arrays were transported to the NAWC demonstration site in 3-4.5 m (10-15 ft) sections and were assembled on-site followed by ground level testing of the packer system and contact resistance checks of electrodes (Figure 5.4.10a). Lengths of arrays ranged from approximately 29-34 m (95-113 ft) (Table 5.4.1). A 4 to 5 person crew was needed for array installation in order to prevent dragging the packers or adding strain to any connections, (Figure 5.4.10b and c).

Table 5.4.1: Electrode array details (per borehole)

Borehole Label	No. Electrodes	No. Packers	Length of ERT imaging (ft)
83BR	19	6	50.13
84BR	21	6	55.51
85BR	19	5	50.32
86BR	19	5	50.52
87BR	21	6	55.54
88BR	22	6	58.23
89BR	22	6	58.56

Figure 5.4.10: a) Assembly and ground testing of electrode array at NAWC b) Installation of electrode array into borehole c) Five person crew installation of electrode array.

Air regulators were attached to top, middle and bottom packer airlines at the surface to assure that pressure at the lowest packer in the set was 10 psi above hydrostatic pressure (Figure 5.4.11). To maintain these pressures over the long periods required for this study, all airlines were hooked up to nitrogen tanks. For the seven arrays, three nitrogen tanks were used, hooked up to either two or three boreholes airlines.
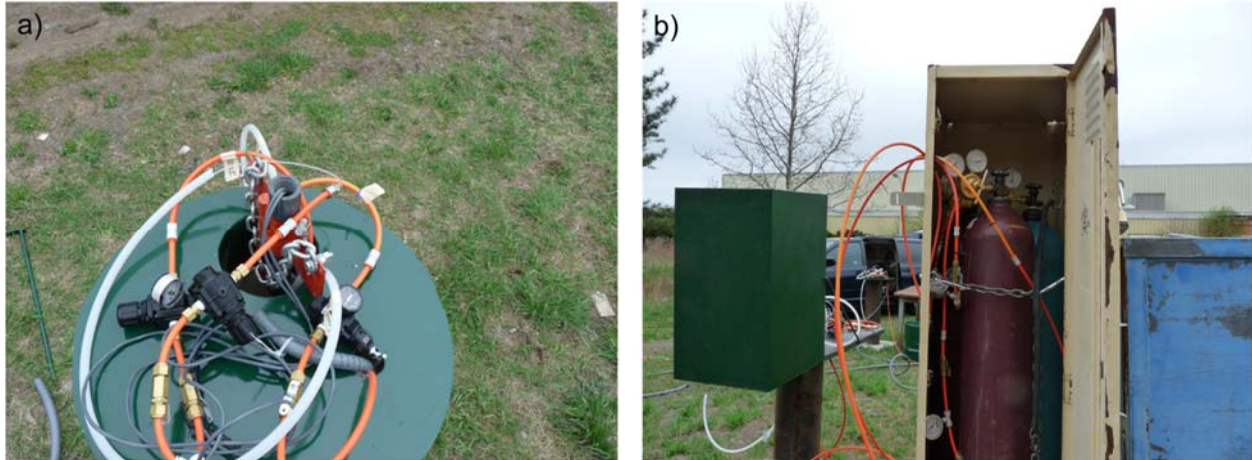
Figure 5.4.11: a) Air regulators for top, middle and bottom packer air lines b) Centrally located locker containing three nitrogen tanks supplying air lines in the seven boreholes.

5.5 FIELD TESTING

5.5.1 Preliminary ERT Considerations

a) Initial borehole testing

Initial testing of the ERT arrays was performed to ensure the quality of the raw ERT data collected at the site. These tests validated that there were no cross connections between electrodes and electrode connection mappings were accurate. Within each borehole, dipole-dipole measurements were conducted whereby a current was injected in the top electrodes within the array and potentials were observed along the borehole (Figure 5.5.1.1a). This was then reversed by injecting current at the bottom two electrodes and recording potential at dipole pairs working upwards away from the bottom. As expected, decreasing potentials were observed as the distance from the current injection pair increased. In cross borehole pair testing, a current was injected into parallel electrodes in adjacent boreholes while potentials were measured from parallel electrodes in adjacent boreholes (Figure 5.5.1.1b); as the distance increased from the current injection, the measured potentials again decreased. Measurement polarities were also consistent with all electrode configurations tested. These tests provided confidence in the assumption that there were no short circuits between electrodes due to flaws in the array construction and/or installation.

Figure 5.5.1.1: ERT measurement testing configurations a) within each borehole b) cross borehole

The resistivity instrument used in this study, an IRIS Syscal Pro 10 channel receiver, provides a high speed data acquisition mode ideal for capturing time-lapse ERT measurements during tracer and amendment injections to monitor flow and transport processes. The high speed data acquisition mode does not stack measurements and the current injection interval is automatically set to a minimum, thus there may be a compromise to data quality. In order to test the data quality for the high speed acquisition mode, we acquired the same survey (1,135 measurements) under the same conditions in standard versus high speed modes. Normal and reciprocal measurements (i.e. whereby current and injection electrodes are interchanged) were collected. The principle of reciprocity states that these two measurements should be identical and that the difference between them provides an excellent measure of data

quality. Data quality for the high speed mode was also assessed by comparing differences between resistance magnitudes acquired in the high speed mode versus measurements made with the standard acquisition mode. Figure 5.5.1.2 is a histogram comparing the percent differences between ERT datasets acquired in standard and high speed mode. The maximum and minimum x-axis values have been scaled to show ±50% differences to emphasize in this distribution that the majority of measurements (99%) have less than 10% variation. The 19 measurements that are not included in this histogram represent 1.7% of the total measurements.
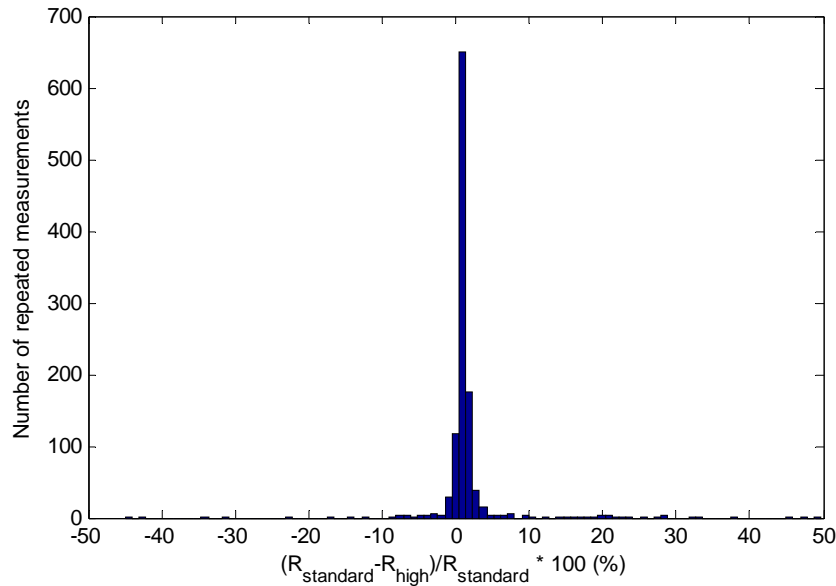
Figure 5.5.1.2: A comparison of the same ERT survey acquired in standard versus high speed mode.

A histogram of reciprocal errors acquired in standard and high speed mode is shown in Figure 5.5.1.3. All reciprocal errors greater or less than 10% have been removed to better show the distribution of reciprocal errors within the ±10% range. Based on this distribution, the data acquired in high speed mode actually slightly outperforms the standard mode data quality. Thus, based on Figures 2 and 3, we deemed the high speed data acquisition mode sufficient for this ERT time-lapse monitoring.
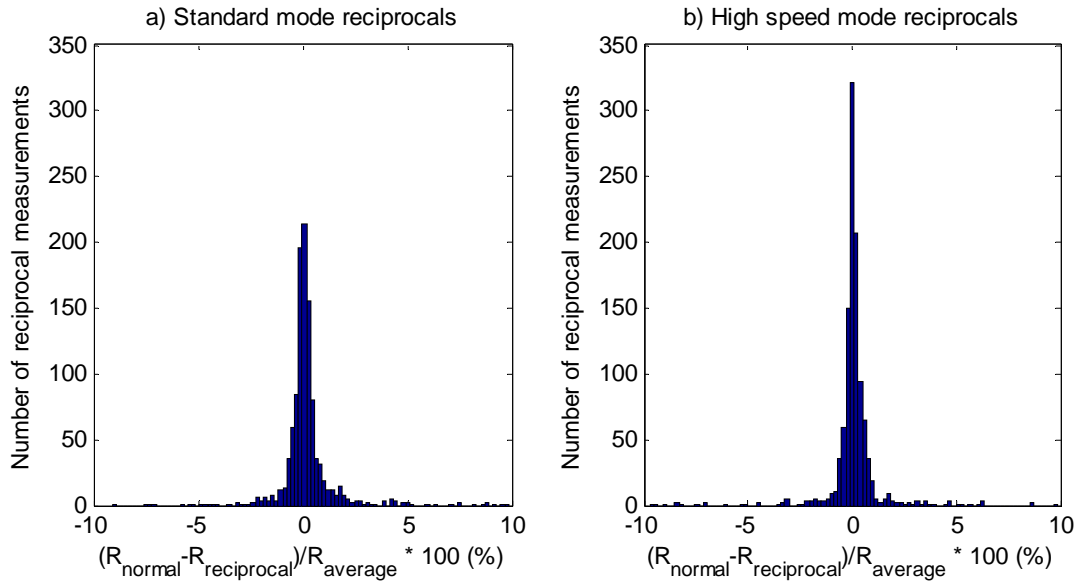
Figure 5.5.1.3: Histogram of reciprocal error for data acquired in a) standard mode and b) high speed mode. The total number of reciprocals is 1,136.

b) Effect of packers on ERT measurements

The need for packers to hydraulically isolate intervals of a borehole for hydraulic testing and to remove the effect of flow and storage in the borehole is well recognized in hydrogeological studies (Becker & Shapiro, 2000; Berkowitz, 2002; Brown & Slater, 1999; Tiedeman et al., 2010). In ERT, a fluid-filled borehole similarly introduces a highly electrically conductive pathway (assuming the rock is relatively resistive) for current to channel between two injection electrodes (Binley & Kemna, 2005; Coscia et al., 2011; Doetsch et al., 2010; Sugimoto, 1999), thereby reducing current penetration into the surrounding rock (Robinson et al., 2013). A few ERT studies have explored the use of packers (Labrecque & Yang, 2001) or rubber disks (Coscia et al., 2011) in down-hole arrays in an attempt to isolate electrodes and thereby limit the borehole current-channeling effect. However, these studies did not evaluate the effectiveness and/or merit of such packers in the imaging.

To better understand if the influence of the packers on resistance magnitudes, ERT measurements were first collected with packers inflated and then deflated (encouraging current channeling) within individual boreholes. A dipole-dipole type measurement sequence, where the spacing between the current (i.e. transmitting) electrodes is equal to the spacing between the potential (i.e. receiving) electrodes, was used for this test as placing both current electrodes in the same borehole enhances current channeling along the borehole (i.e. as opposed to cross borehole measurements). Boreholes 83BR, 84BR and 89BR each contained more packers than any of the other seven boreholes, so these were chosen to illustrate the differences in resistances between measurements when the packers were inflated versus those when packers were deflated.

Assessment of raw ERT measurements suggests that the packers significantly limit current flow along the boreholes (Figure 5.5.1.4). The data collected within 88BR (no packers used) are highly repeatable (Figure 5.5.1.4b), with no repeated measurement having a difference greater than 0.1 Ω. The average percent change for all measurements in this test is 0.3 percent. In contrast, the data differences in 83BR, 84BR and 89BR when packers are inflated relative to uninflated show much larger changes for numerous measurements (Figure 5.5.1.4a). The

64

average percent changes across all measurements in these boreholes due to inflation of the packers are 3.3, 7.7 and 5.6 percent, respectively.
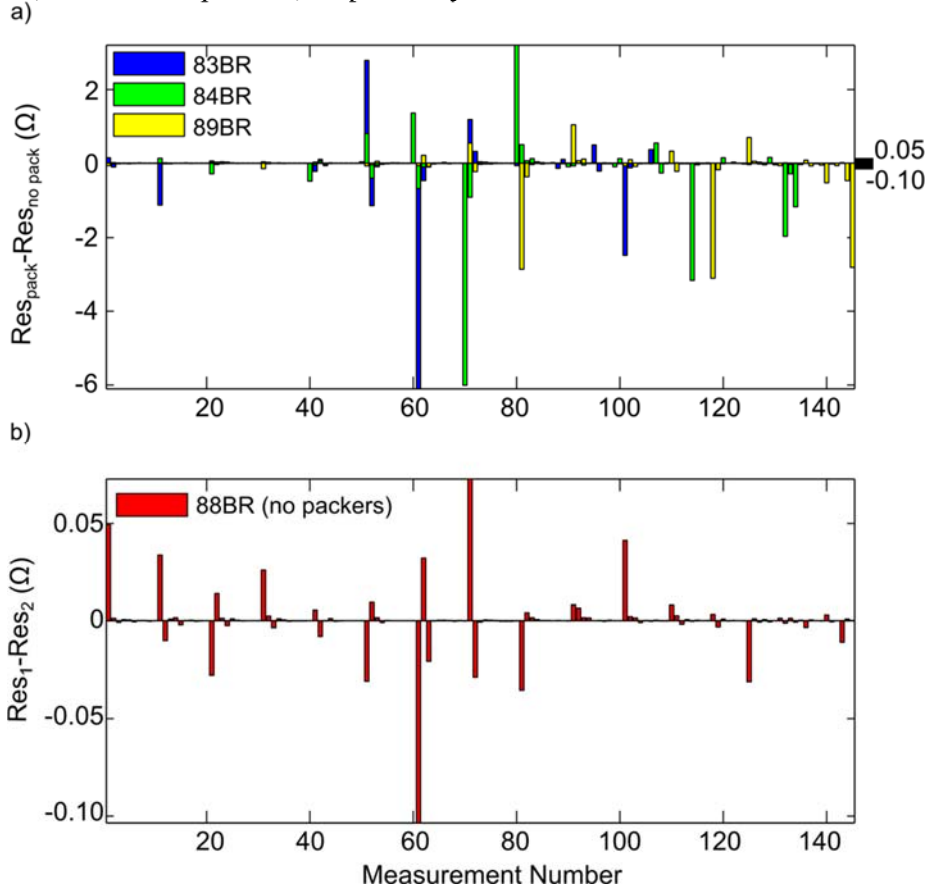
Figure 5.5.1.4: a) Measurements collected with packers inflated (Res_pack) and deflated (Res_no pack) within single boreholes (83BR, 84BR and 89BR) demonstrate the effect of packers on limiting current flow along the borehole. b) For comparative purposes, the difference between two consecutive datasets (Res_1 and Res_2) where packers were deflated in both cases is shown for 88BR. Note the difference in y-axis scales where the scale of b) is denoted on the right side y-axis a).

To reveal the effect of data differences on the inverted models, a difference inversion was performed for 83BR, whereby data obtained with packers deflated were used to invert a background model. Relative changes from this background model were then determined using 83BR data when packers were inflated. Figure 5.5.1.5a represents the conductivity structure for 83BR data with packers deflated. The inverted conductivity structure for 83BR data with packers inflated looks almost identical, and is thus not shown for brevity. The difference inversion image (Figure 5.5.1.5b) shows maximum conductivity changes of only 1% between packer locations in the vicinity of fracture zones (i.e. there are no changes below 28 m).
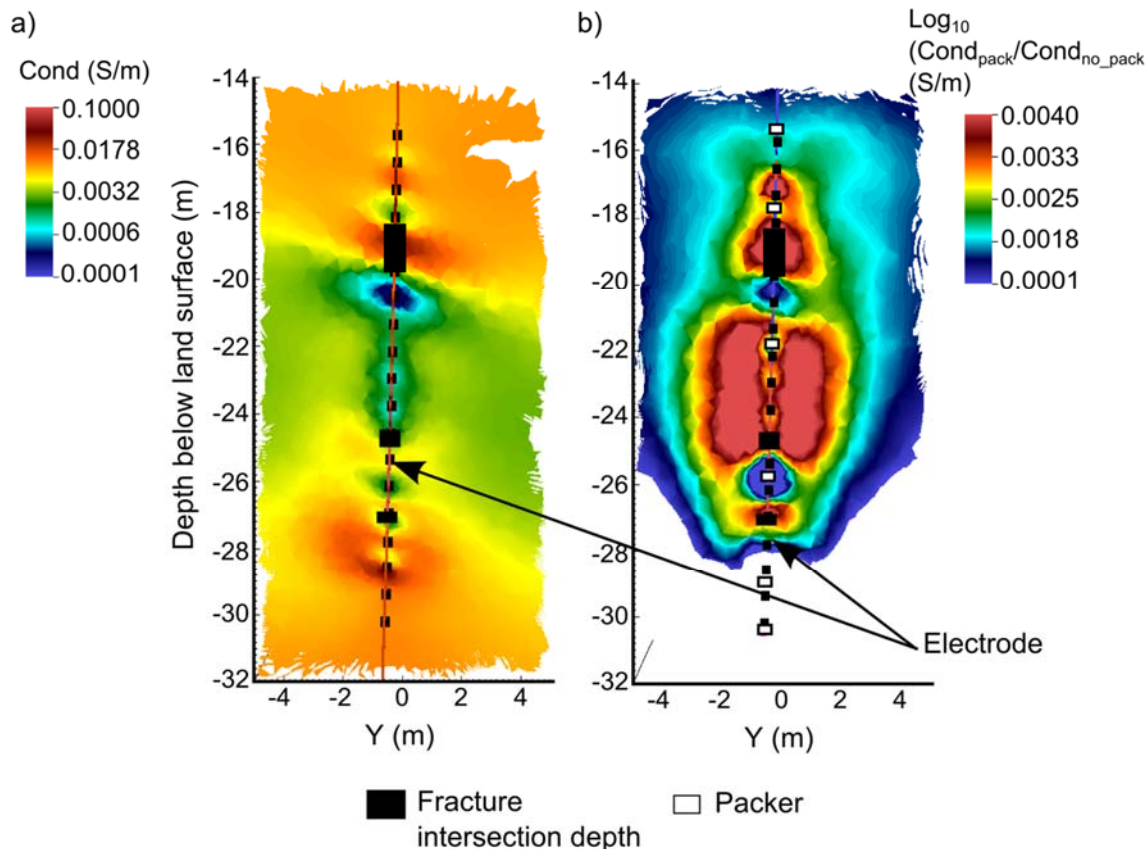
Figure 5.5.1. 4: a) Inverted ERT image for 83BR single borehole data collected with packers deflated, and b) difference inversion showing relative changes in conductivity from packer data using a) as a background model.

Inflated packers were shown to help reduce current flow along the boreholes where both current injection electrodes are within the same borehole. Measureable differences in the data well above the differences observed in 88BR with no packers led to higher conductivities within the formation near fracture zones (Figure 5.5.1.5b). However, the effects of employing the packers at this site on the inverted images were small with less than a 1% change in inverted conductivity. Synthetic tests are consistent with this finding (Robinson et al., 2013). At NAWC, the contrast between the host rock and borehole fluid varied by only a factor of 10. The use of packers to limit current flow in more resistive environments (i.e. granitic rock) will likely result in more pronounced effects on the measurements. Additionally, the effectiveness of packers was limited by the fact that it was impractical to have more than 6 packers per borehole; additional packers would presumably result in greater reductions in current flow along the borehole. Finally, the measurements used here to test the influence of packers explored where current channeling would be more prevalent due to both current electrodes being in the same borehole. During the tracer test (described later) all current injections were between electrodes straddling the boreholes, so the influence of packers would conceivably be even less pronounced than observed in these tests.

66

5.5.2 Static ERT Characterization

a) ERT measurement sequence

For n electrodes, a total of $n(n-1)(n-2)(n-3)/8$ four-point electrode configurations exist. Collection of this comprehensive measurement sequence is time prohibitive and impractical for dynamic systems where temporal changes occur in time frames less than the time required for data collection. An optimum measurement sequence will depend on site requirements (e.g. measurement errors and resistivity structure) and specific project demands (e.g. resolution and data acquisition speed). Commonly used four-electrode configurations are nested arrays such as Wenner and Schlumberger or dipole-dipole schemes; the advantages and disadvantages of these configurations are well documented (for example, Binley & Kemna, 2005). Recognizing a need for optimized measurement sequences, a number of researchers (Blome et al., 2011; Loke et al., 2010; Stummer et al., 2004; Wilkinson et al., 2012; Wilkinson et al., 2006) have explored incrementally adding measurements to an initial dataset that will improve the resolution of the true (in many cases, assumed) model.

For this project a modified Compare-R method (Wilkinson et al., 2006) was used to construct a cross borehole (i.e. current electrode pairs straddled between boreholes and potential electrode pairs straddled between boreholes) measurement sequence. Such sequences are expected to help to minimize current channeling along the boreholes. Nearest neighbor type configurations were then appended to this sequence similar to the survey used in Robinson, et al., (2013). Vertical Wenner (n=1) borehole profile configurations were also appended to the dataset and collected throughout the ERT tracer tests to capture vertical variations in conductivity along each borehole profile over a shorter time frame than required for the 3D survey. The entire dataset contained 5,487 measurements (i.e. for a total of 10,974 normal and reciprocal).

The normal and reciprocal data acquisition sequences were optimized according to instrument specifications for a 10-channel instrument. The normal measurement sequence contained 6,312 measurements and was acquired in approximately 20 minutes. The reciprocal measurement sequence contained 7,468 measurements and was acquired in approximately 25 minutes.

b) ERT static inversion images

Characterization ERT images are shown as cross section slices along borehole boundaries: 87-83-85BR (Figure 5.5.2.1), 88-83-84BR (Figure 5.5.2.2), and 89-83-86BR (Figure 5.5.2.3). Electrically conductive zones are shown in red (i.e. higher conductivity) and more resistive zones are shown in blue. The images highlight a structure of alternating conductive and resistive layers oriented similar to alternating massive and laminated beds shown in Figure 4.2. The results of the coring analysis (Section 5.2.2) are shown within each borehole where fracture intersection depths and apertures are marked as black rectangles. Generally, these fracture intersection depths align well with electrically conductive units and lithological boundaries. An electrically conductive pathway is shown between borehole pairs 87BR and 83BR and borehole pairs 83BR and 85BR. This region was chosen as the focus of the tracer and amendment injection studies of the demonstration. In the time-lapse analysis of the ERT data, the characterization dataset shown here was used as the background model.
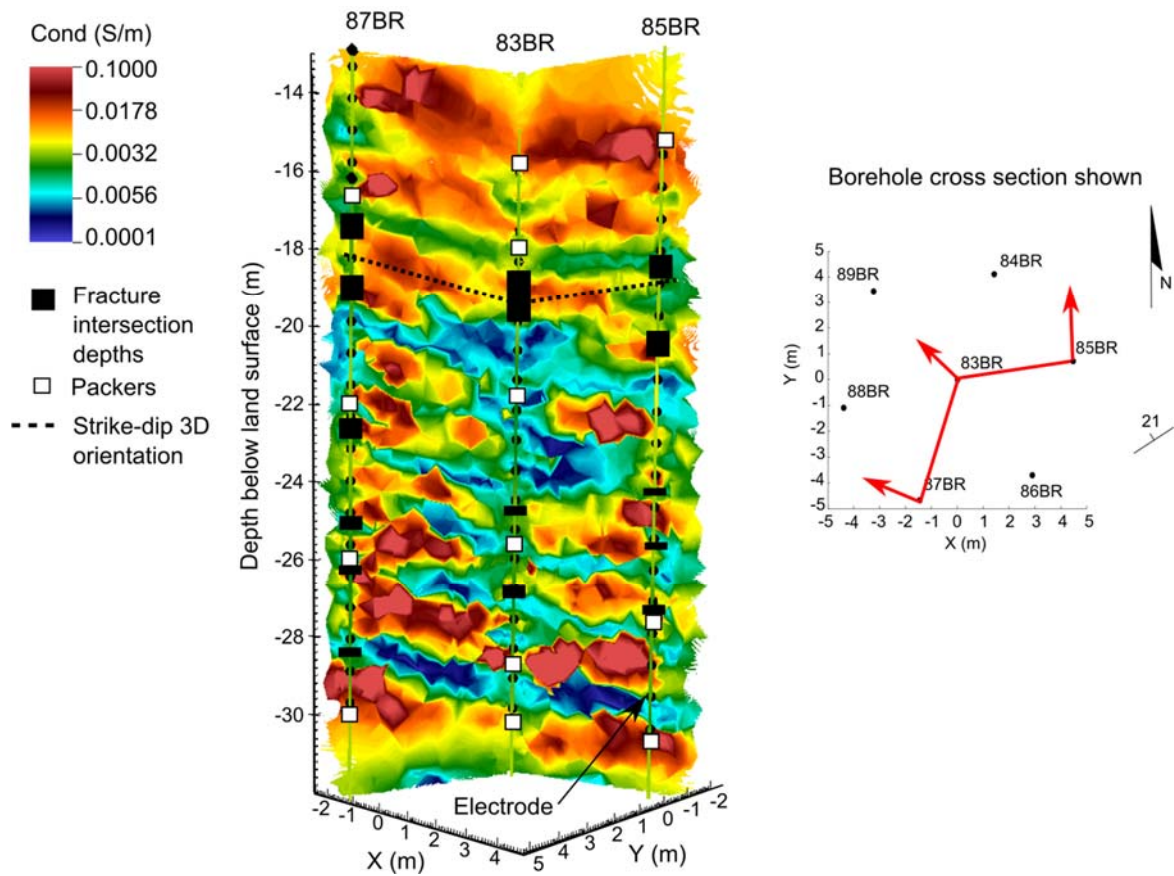
Figure 5.5.2. 1: Electrical resistivity image for slice 85-83-87 with fracture intersection depths and packers, and strike-dip 3D orientation. In order to present an unobstructed view of 83BR, 85BR and 87BR, 86BR is not shown.
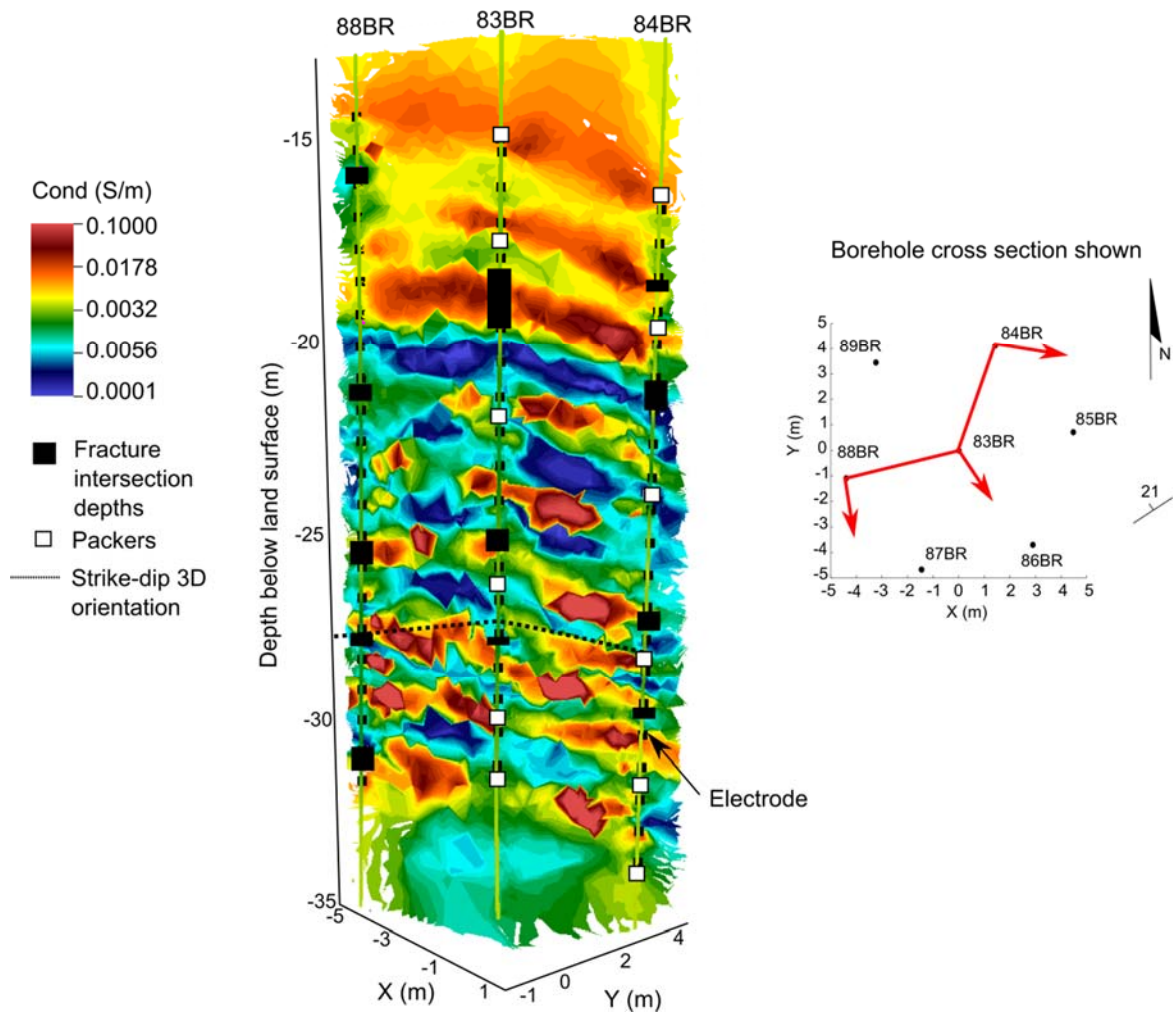
Figure 5.5.2. 2: Electrical resistivity image for slice 88-83-84 with fracture intersection depths and packers, and strike-dip 3D orientation. In order to present an unobstructed view of 88BR, 83BR and 84BR, 89BR is not shown.
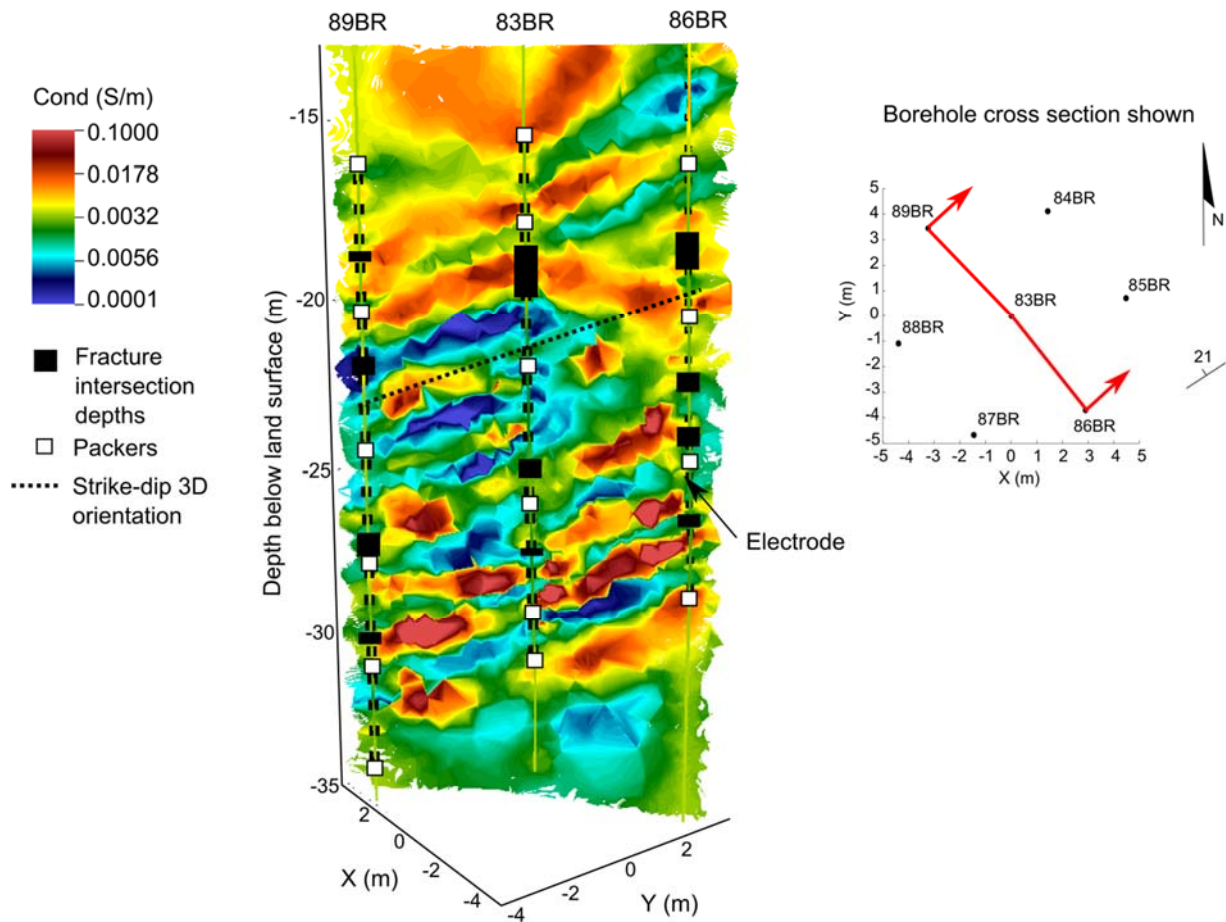
Figure 5.5.2. 3: Electrical resistivity image for slice 89-83-86 with fracture intersection depths and packers, and strike-dip 3D orientation. In order to present an unobstructed view of 89BR, 83BR and 86BR, boreholes 88BR and 87BR are not shown.

The optimized sequence constructed for the ERT tracer tests was compared with two other field measurement sequences through a visual comparison of inversion images. Figure 5.5.2.4 shows inverted images from 1) a quasi-3D sequence containing 7,045 complete measurements comprised of 2D panels only, and 2) a rotating dipole sequence containing 13,351 complete measurements of a fully 3D cross panel sequence. The images have similar overall structure while more contrasts in between borehole locations are emphasized in the optimized survey.
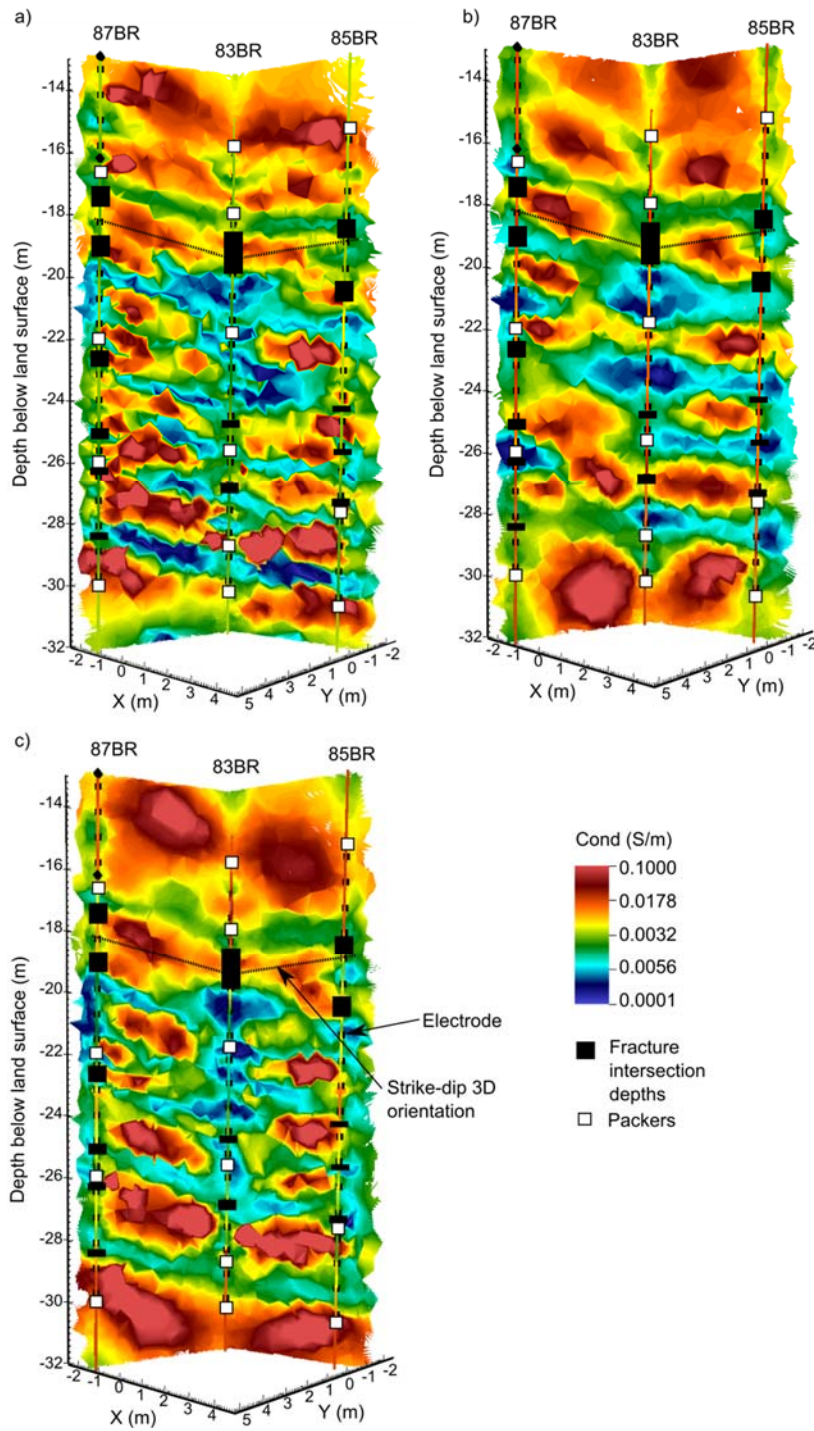
Figure 5.5.2. 4: Inverted characterization images where measurement sequences are a) 3D optimized cross borehole survey combined with dipole-dipole sequence (5,263 measurements) b) 3D rotating dipole sequence (13,351 measurements) an d c) quasi-3D sequence of 2D panels (7,045 measurements).

5.5.3 ERT Tracer tests and Amendment Injections

a) Overview

A major part of this demonstration focused on showcasing the ability of ERT to capture the progress of amendment injections into fractured rock. The motivation was that ERT has the potential to provide high resolution information on the fate of amendment injections and to provide information on system state changes at relevant scales that integrate the physical property variations controlling flow and transport. A technical challenge was to design an appropriate tracer/amendment strategy that would fully demonstrate the rich information content available from time-lapse ERT. Previous amendment injections at the NAWC site conducted under other SERDP funding had highlighted the major uncertainty associated with the delivery of amendments into contaminated fracture zones and the fate of the amendments beyond the boreholes. The following sections describing the evolution of tracer test designs that were performed at the NAWC site under this project, and ultimately resulted in a showcase demonstration of the ability of ERT to resolve amendment delivery at an unprecedented spatiotemporal scale.

b) 83BR-85BR Blank

A tracer test whereby native groundwater only was injected into the formation, here referred to as a blank tracer test, was conducted between well pairs 83BR and 85BR on November 13, 2013 (Figure 5.5.3.1). The purpose of this test was twofold: 1) to serve as a trial run to understand the logistics involved in performing an ERT tracer test, and 2) to determine ERT noise levels in the data that might result from the operation of the injection pump and the resulting movement of fluid in the formation. The water sampling zone tubing included on the arrays was used for all injections and extractions in 83BR and 85BR.

Figure 5.5.3 1: Extraction of native groundwater from 83BR into a 200-gallon bladder on the surface. The center well with the extraction tubing and peristaltic pump is 83BR.

First, 43.2 L (11.4 gallons) of native groundwater was pumped from 83BR into a 200 gallon bladder. The aquifer was allowed to equilibrate after this extraction pumping. This was followed by injection of native groundwater down hole into 83BR for 1 hour and 41 minutes. After terminating the fluid injection into 83BR, the peristaltic pump and tubing was reconfigured to pump from the water sampling zone in 85BR. One of the packers in 85BR was deflated to increase the length of the water sampling zone in accordance with results of hydraulic testing.

In the ERT monitoring of the electrically conductive tracer tests (described later), limiting temporal smearing during ERT data acquisition was an important consideration for capturing meaningful time-lapse changes. This prevented the acquisition of normal and reciprocal measurements for every timeframe of the tracer injection, a complete normal + reciprocal dataset therefore only being acquired prior to and at the end of the each tracer test. The same was therefore done for this blank tracer test for consistency. As this tracer study was performed before ERT measurement optimization was complete, a reduced in size ERT sequence containing 2,998 cross borehole types of measurement was chosen for this test. In addition to a complete background dataset, normal (i.e. no reciprocals) ERT measurements were collected throughout the testing: 10 datasets during the extraction of native groundwater from 83BR; 10 datasets while the formation was equilibrating; 8 datasets during injection at 83BR; and 8 datasets during extraction from 85BR. In total, 38 ERT datasets were acquired, including the background (pre) and post datasets.

c) 83BR-85BR

The first ERT conductive tracer test was performed between 83BR and 85BR on December 19-20, 2013 (Figure 5.5.3.2). The test was designed in three stages: 1) inject a small volume of conductive tracer (9.5 L) into 83BR; 2) inject a larger volume of native groundwater into 83BR to encourage the conductive tracer into the fracture zone towards 85BR (18.9 L) while eliminating any residual tracer in 83BR; 3) extract fluid from 85BR following the injections to further promote the movement of the conductive 'slug' towards this borehole for ERT imaging.

Figure 5.5.3 2: a) Extraction pumping from 85BR after injection of a conductive fluid and native groundwater in 83BR b) ERT data collection

Native groundwater was first extracted from 83BR to which sodium bromide (considered a good conservative tracer at the site) was added. Native groundwater and conductive tracer fluid specific conductances were 0.43 mS/cm and 12.16 mS/cm, respectively, which equates to a

conductivity contrast of 28. The tracer fluid injection took 15 minutes and the native groundwater injection took 31 minutes. There was a 6-minute delay between the end of the native groundwater injection at 83BR and the groundwater extraction at 85BR.

Water samples were collected during the extraction pumping at 85BR, beginning 20 minutes after the extraction pump was turned on, then approximately every 20 minutes for 4 hours. The water sampling interval was then increased to every 2-3 hours. Extraction pumping from 85BR was continued overnight in an attempt to remove any residual tracer from the subsurface.

Normal and reciprocal measurements were collected before any disturbance to the system. One dataset was collected during the conductive injection; two datasets were collected during the native groundwater injection. During the extraction pumping from 85BR, datasets were acquired approximately every 1/2 hour (i.e. almost continuously) for 3 hours, then every hour for another 11 hours.

d) 83BR-87BR

The second ERT tracer test was conducted between 83BR and 87BR on January 16-17, 2014 (Figure 5.5.3.3). Based on experience learned from the first ERT tracer test between 83BR-85BR, this test was designed to: 1) slow down injection fluid travel times and the injection time frame; 2) illuminate a preferential flow path promoting tracer fluid arrival at an expected borehole; and 3) inject a tracer fluid with a higher conductivity contrast between the ambient fluid with the knowledge that conductive tracer fluid from the previous 83BR-85BR tracer study resided within the system. Based on hydraulic testing results (Section 5.2.4), the travel time between 83BR and 87BR was approximately 1 hour longer (at an extraction rate of 0.1 L/min), thus this borehole pair was chosen for this next trial.

The tracer injection was prepared from native groundwater pumped from 83BR (approximately 30 L). The ambient fluid specific conductance was 0.52 mS/cm. Approximately 1,000 g of NaBr was added to the pumped native groundwater, resulting in a fluid specific conductance of 38.49 mS/cm (i.e. a conductivity contrast of 74); based on the laboratory analysis, tthis equated to a concentration of the fluid of 28.3 g/L.   Native groundwater was extracted from 83BR (approximately 60 L) to be injected immediately following the conductive fluid. A

Figure 5.5.3 3: : Field configuration for 83BR-87BR tracer test

hydraulic gradient was established at 87BR and pumping began at this borehole 30 minutes prior to the injection at 83BR. The conductive tracer fluid was continuously injected over 51 minutes and the following native groundwater was subsequently injected over 114 minutes.

74

Water samples were collected within the water sampling zone in 87BR every hour and a conductivity monitoring probe was placed within the outflow tubing. Background ERT datasets were collected and monitoring began 5 minutes after extraction pumping began at 87BR. A total of 22 ERT datasets were acquired over this tracer test.

e) 87BR-85BR

An ERT tracer test was conducted between 87BR and 85BR on April 16-18, 2014 and involved two separate fluid injections, whereby a conductive tracer injection was subsequently followed by a resistive tracer injection. Based on the results of previous tracer tests described above, the tracers were injected in successive pulses using a peristaltic pump, where a pumped injection at 87BR occurred for five minutes and then the pump was shut off to collect an ERT dataset. ERT imaging occurred only when the injection pump was off in order to limit temporal smearing over the 20 minute acquisition time. After the entire tracer volume was injected into 87BR, withdrawal from the extraction borehole, 85BR, occurred in the same fashion i.e., in five minute pulses, with the pump again turned off between each pulse (Figure 5.5.3.4). Water samples were collected during the pulsed extraction from 85BR. ERT imaging again only occurred when the extraction pump was off. To subsequently remove tracer mass from the system, the extraction borehole (85BR) was pumped for a minimum of 16 hours. During this period, water samples were collected every 10 minutes for one hour, then hourly afterwards. Figure 5.5.3.5 presents a flowchart of the 87BR-85BR tracer experiment steps with step numbers denoted in square brackets [ ]. Table 5.5.3.1 contains the specific details of the ERT tracer test for each part of this experiment.
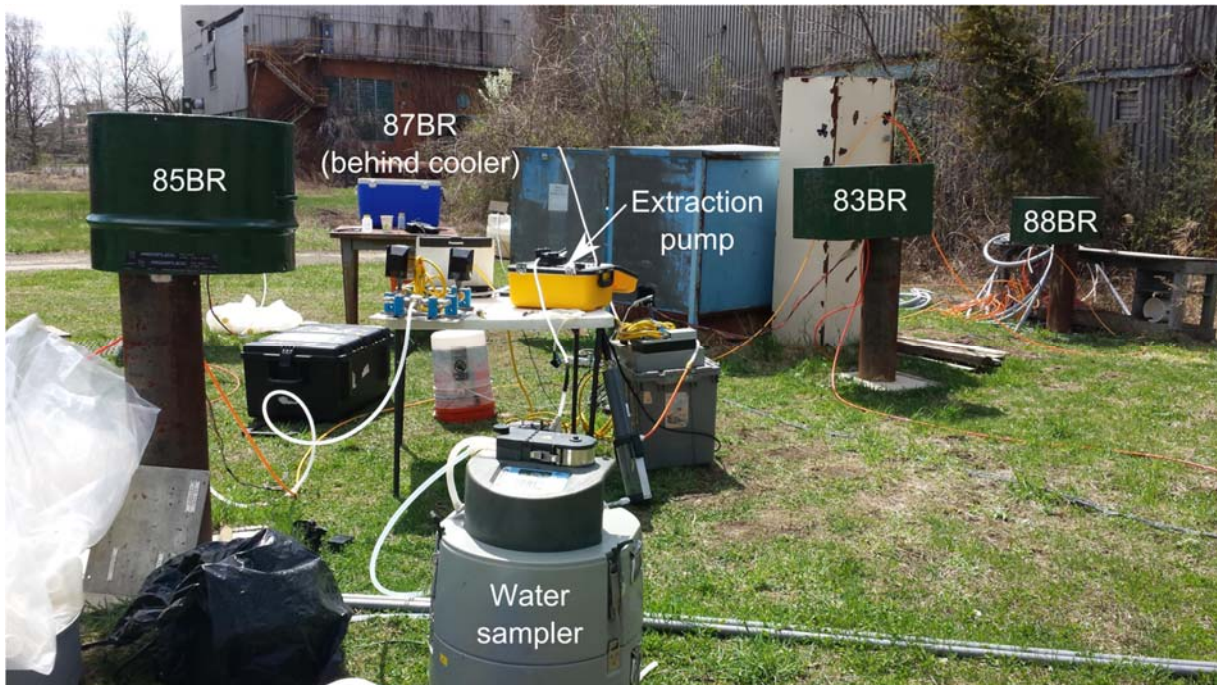
Figure 5.5.3 4: Field set-up for 87BR-85BR tracer test during extraction from 85BR.

Native groundwater (22 L) was pumped from 87BR and used as the background medium for the conductive tracer injection (step [1] in Figure 5.5.3.5). Based on the high dilution effect observed during the earlier tracer tests, a conductivity contrast of 89 was used between the native groundwater (0.60 mS/cm) and tracer solution (53.47 mS/cm). Samples of the injected tracer solution analyzed with ion chromatography (IC) had an average bromide concentration of 40.6 g/L. In addition to ERT datasets collected during the nine pulsed conductive injections in (step [1] in Figure 5.5.3.5), another ERT dataset was collected under static conditions shortly after the entire conductive volume was injected. This was followed by pulsed extraction with acquisition of five ERT data sets (step [2] in Figure 5.5.3.5). Finally, extended extraction (step [2a] in Figure 5.5.3.5) occurred for 16.5 hours.

Figure 5.5.3 5: Flow chart of tracer test where numbers of ERT data acquisitions and water samples (WS) are indicated in parentheses ( ).

Deionized water (DI) was subsequently used as a resistive tracer and pulse-injected into 87BR for twelve intervals (step [3] in Figure 5.5.3.5). The fluid specific conductance for the DI water injected was 1.8×10^{-3} mS/cm, being 333 times more resistive than background concentrations (the true contrast may have been higher due to the presence of residual tracer from the conductive injection). Five pulsed extractions occurred at 85BR after the resistive

injection (step [4] in Figure 5). This was followed by 19.17 hours of extraction (step [4a] in Figure 5.5.3.5).

Table 5.5.3. 1: ERT Tracer test details

Description	# pulsed injections	Approximate injection volume (L)	# water samples*	Approximate extraction volume (L)
[1] Conductive Injection	9	22	-	-
[2] Conductive Extraction	-	-	6	14
[2a] Extended Extraction	-	-	22	473
[3] Resistive Injection	12	34	-	-
[4] Resistive Extraction	-	-	5	8
[4a] Extended Extraction	-	-	25	674

* For [2] and [4], the # water samples = # pulsed extractions

Further ERT measurements (step [5] in Figure 5.5.3.5) were collected one and three weeks after tracer injection. One week after the tracer test, water was extracted from 85BR for four hours to facilitate further removal of tracer mass and to monitor bromide concentrations. Water samples were collected every five minutes for the first half hour, then hourly. ERT measurements were collected before and after the extraction. At three weeks post-tracer test, only ERT measurements were collected under no pumping conditions.

f) ERT Monitoring of Amendment Injection into 87BR

After successful 3D ERT imaging of tracer migration in the 87BR-85BR tracer test, a similar design was utilized to inject an amendment in 87BR on July 29, 2014. This test differed from previous tracer tests in that there was no planned extraction of fluid from any of the surrounding boreholes; the intention was to leave the injected amendment in-place in order to monitor for electrical changes associated with the possible biodegradation of trichloroethylene (TCE), cis-dichloroethylene (cDCE) and vinyl chloride (VC). Molasses was selected as the amendment agent and sodium bromide was added to the molasses solution to increase the conductivity contrast between the formation and the fluid.

Sixty (60) L of native groundwater (0.533 mS/cm) was extracted from 87BR to which sodium bromide (6,134 g) and molasses (21,876 g) were added (Figure 5.5.3.6a) to give a fluid specific conductance of 50.2 mS/cm. Seventeen injections were pulsed into 87BR (flowrate=1.2 L/min) initially at 3 minutes intervals with increased injection times corresponding to decreasing heads within the amendment reservoir. The amendment was mixed before each injection in case settling occurred in the amendment reservoir (Figure 5.5.3.6b). ERT measurements were collected after each pulsed injection. Table 5.5.3.2 lists the ERT surveys collected after the last pulsed conductive injection.
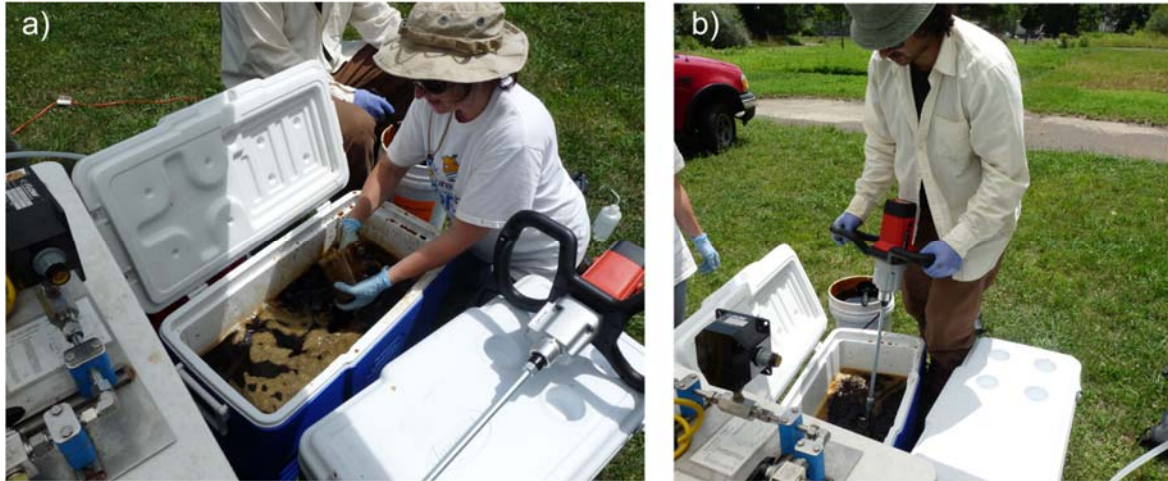
Figure 5.5.3 6: a) Adding molasses to native groundwater from 87BR b) mixing amendment solution before injection into 87BR

Table 5.5.3.2: ERT datasets collected since last pulsed injection on 7/29/2014 2:14:00 PM

Sample Date/Time	Days elapsed	hh:mm
7/29/14 15:25	0	01:11
7/29/14 17:00	0	02:46
7/29/14 20:10	0	05:56
7/29/14 23:15	0	09:01
7/30/14 5:15	0	15:01
7/30/14 8:05	0	17:51
7/30/14 11:35	0	21:21
7/30/14 14:35	1	00:21
8/5/14 8:40	7	18:26
8/8/14 8:55	10	18:41
8/12/14 8:35	14	18:21
8/29/14 9:10	31	18:56
9/12/14 9:35	45	19:21
9/19/14 9:42	52	19:28
10/1/14 9:18	64	19:04

Water samples from within the water sample zones of individual arrays were collected prior to and after the amendment injection in an effort to find evidence for biodegradation surrounding particular boreholes after the injection. Based on the hydraulic testing and flowmeter logging, we expected a response within 87BR, the injection borehole, and hydraulically connected boreholes 83BR and 85BR. Borehole 84BR was also sampled as a control, as we did not expect to see the same trends in key compounds here due to the isolation of this borehole from 83BR, 85BR and 87BR. Prior water samples were collected on 7/9/2014, or 20 days before the injection; afterwards, samples were collected on 8/25, or 27 days after the injection. Concentrations of key compounds were determined by laboratory analysis including trichloroethylene, cis-1,2-dichloroethene, trans-1,2-Dichloroethene, 1,1-dichloroethene and vinyl chloride.

5.6 ERT TRACER AND AMENDMENT INJECTION RESULTS

a) Overview

In all the ERT tracer test results shown, evidence of the tracer in the ERT data is delayed due to the travel time of the tracer fluid in the 1/2" tubing from the surface to the injection depth which is 18.5 m in 83BR and 17.5 m in 87BR. Thus, it was typical for ERT detection to occur after the first or second injection and not immediately after the injection began.

b) 83BR-85BR Blank

A representative dataset was chosen to compare raw data changes from the background dataset throughout the stages of the blank tracer test (Figure 5.6.1). Figure 5.6.1 has been scaled to show ±100% changes from the background dataset to highlight that the noise distribution for the 2,998 measurements is centered just below 0%. Data collected during the movement of native groundwater (i.e. pumping stages) is shown to have a similar noise distribution as when fluid is not moving (i.e. equilibration and after the completion of the test). For all 37 datasets collected throughout and following the blank tracer test, only 4,403 out of 110,926 (i.e. 4%) have a percent difference greater than 2%.
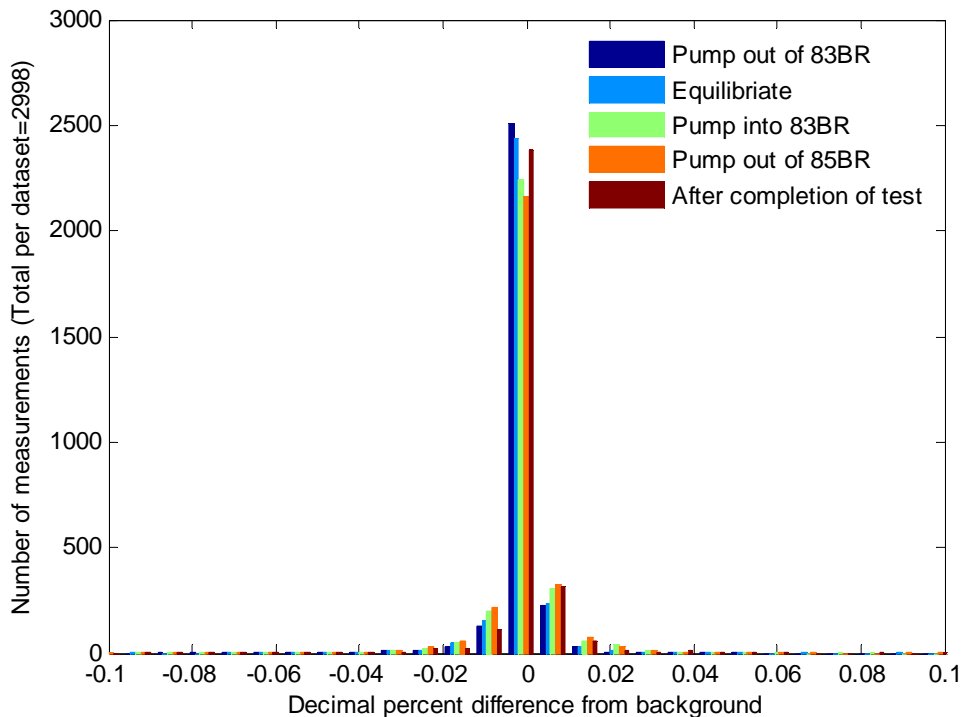
Figure 5.6.1: Differences from the background dataset for representative datasets collected during different stages of the blank tracer test. This figure has been scaled to show ±100% changes from the background dataset.

These tests quantified the represent noise levels in the ERT data during a pumped tracer test and demonstrated that the pumping and fluid circulation induced in the fractures had an insignificant effect on the ERT data.

c) 83BR-85BR

Raw ERT data provide a first pass overview of changes in electrical resistivity occurring within the 83BR-89BR well field as a result of tracer injections. Figure 5.6.2 is a comparison of the averaged apparent resistivity from a background dataset relative to datasets collected since the start of the tracer injection. Positive values on the y-axis indicate that the apparent resistivity at a particular time is smaller (i.e. a lower apparent conductivity) than the background dataset. A steady decrease in apparent resistivity with time is evident until approximately 90 minutes after the start of the tracer injection, which can be attributed to the conductive tracer injection. After this, changes remain level except for an abrupt change between 200 and 300 minutes. There was no modification to the system between these datasets which were collected within a half hour of one another; however, the ERT data acquisition was switched to remotely acquire data from this time onward. Given the stable values throughout the remote data collection, we attributed this change to this switch although a review of our procedure did not reveal any obvious reason for these differences. While all values on the y-axis are positive, the magnitudes of the percentage changes plotted are quite small.
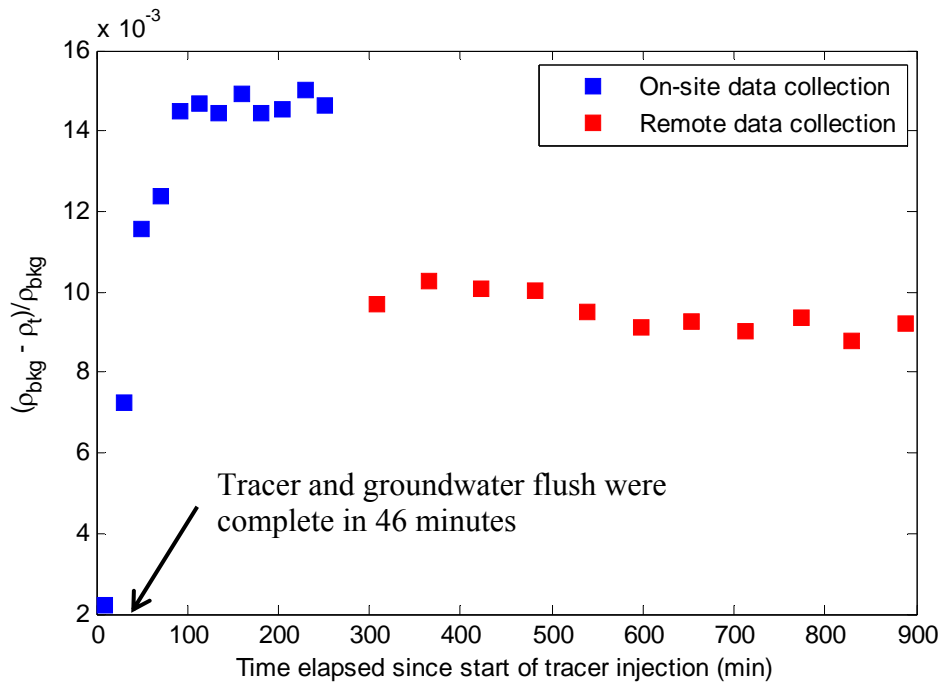
Figure 5.6.2: Percent difference in averaged apparent resistivities between the background dataset and subsequent datasets for the 83-85BR tracer study. The tracer was injected over 15 minutes and the native groundwater flush was complete 31 minutes after the start of the tracer injection.

ERT vertical apparent conductivity profiles collected within each borehole revealed no significant conductivity changes relative to background values in any borehole except in the injection borehole, 83BR (Figure 5.6.3). The initial change in conductivity in 83BR during the

conductive injection was maintained throughout the extraction at 85BR. There were no notable conductivity changes in boreholes 84BR, 88BR and 89BR.   Boreholes 87BR, 85BR and 86BR are shown in Figure 5.6.3 for comparison and chosen due to expected hydraulic connections inferred from cross borehole hydraulic testing.
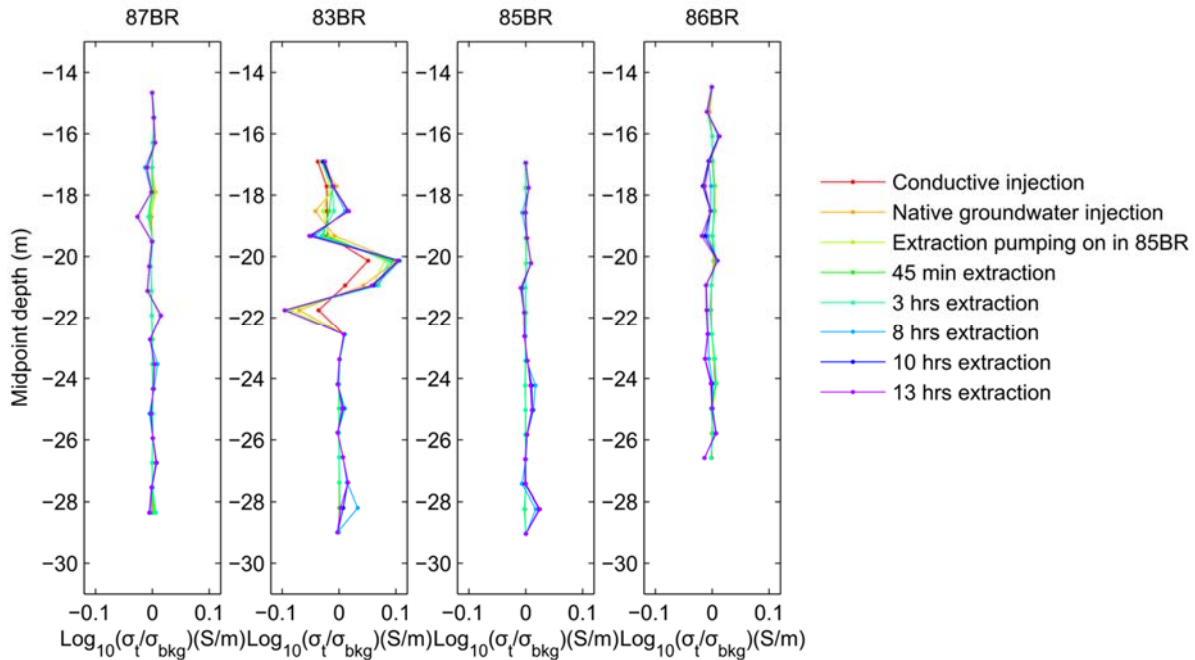
Figure 5.6.3: Relative changes from background conductivities in vertical borehole ERT profiles.

The ERT in-borehole vertical profile measurements did not capture any evidence of tracer breakthrough at the non-injection wells. When attempting to inverse model the time-lapse datasets relative to the background dataset, there was not enough change in the data to reveal any significant change in the conductivity structure. This is reasonable given the small changes in apparent resistivities shown in Figure 5.6.2.   The vertical ERT profile in 83BR suggests that the native groundwater injection following the conductive injection had little effect on residual tracer remaining in this borehole. This first conductive injection was therefore considered unsuccessful.

d) 83BR-87BR

ERT data were acquired before and during the conductive and native groundwater injections. However, datasets beyond the injection time frame had many measurements with potential readings close to zero while current injections were within a reasonable range; these datasets needed to be discarded due to the large number of non-plausible potential measurements. A review of the instrumentation revealed an electrode extension unit had low battery power. Nine acceptable datasets were collected after the extraction pump was turned on in 87BR, which corresponds to the time frame during the conductive injection until 20 minutes before the end of the native groundwater injection.

Similar to Figure 5.6.2, Figure 5.6.4 is a comparison of the averaged background apparent resistivity to average apparent resistivities from time-lapse datasets. The injection from the surface was completed after 65 minutes and decreases in average apparent resistivity are

evident with time. Changes from the background dataset remain level after approximately 100 minutes.
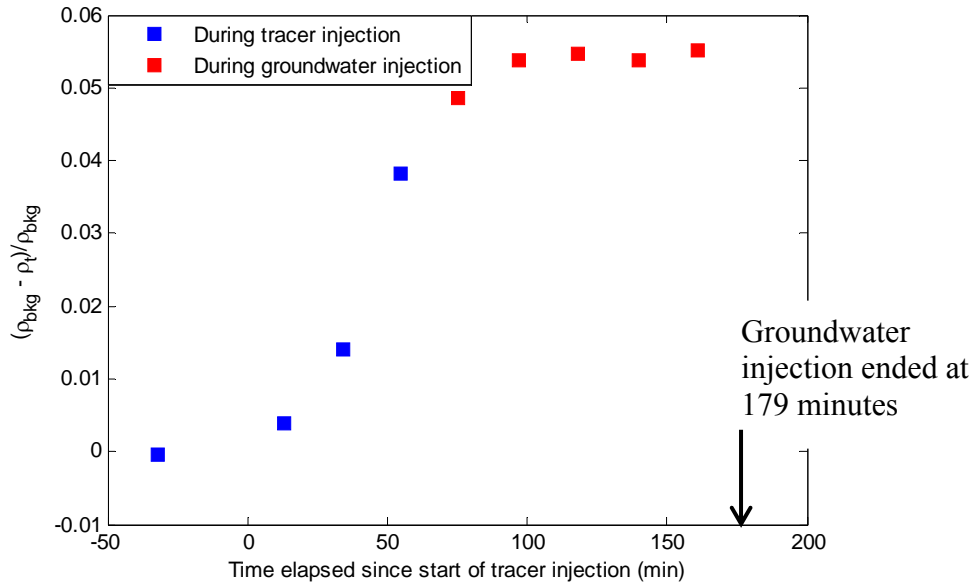
Figure 5.6.4: Percent difference in averaged apparent resistivities for time-lapse datasets from a background dataset for 83-87BR tracer study due to the conductive injection at 83BR.   The injection was complete after 65 minutes and the groundwater flush was complete after 179 minutes.

Vertical apparent conductivity profiles collected during the injections demonstrate significant localized changes within 83BR, with no changes detected within 87BR, the extraction borehole. A slight decrease in conductivity was captured in 85BR, which may demonstrate the displacement of conductive residual from the previous conductive tracer test between well pairs 83BR and 85BR as a result of the pumping.

Inverted time-lapse resistivity changes showed no evidence of the tracer until after the completion of the conductive injection (Figure 5.6.6a). An increase in conductivity associated with the evolution of a conductive plume is observed (Figure 5.6.6b-c) leveling off (Figures 5.6.6d-e), and consistent with the single borehole results shown in Figure 5.6.5. The isocontour plotted in Figure 5.6.6 is $\log10(Cond_t/Cond_0) = 0.04$, representing a 9.6% change in conductivity. Meaningful interpretation of time-lapse ERT imaging requires identification of conductivity changes in the images that can reliably be assigned to variations in subsurface conductivity structure (i.e. due to tracer injection in this case). Random conductivity changes appear at depth in the images when the isocontour is set less than 0.04. Images where the isocontour was set less than 0.04 did not change the interpretation near the injected fracture zone and only artifacts at depth were removed from the images shown in Figure 5.6.6. Thus, we considered $\log10(Cond_t/Cond_0) = 0.04$ to represent an appropriate threshold value. In this specific tracer injection experiment the ERT imaging demonstrated that the tracer largely stayed close to the injection well for the duration of the measurements.
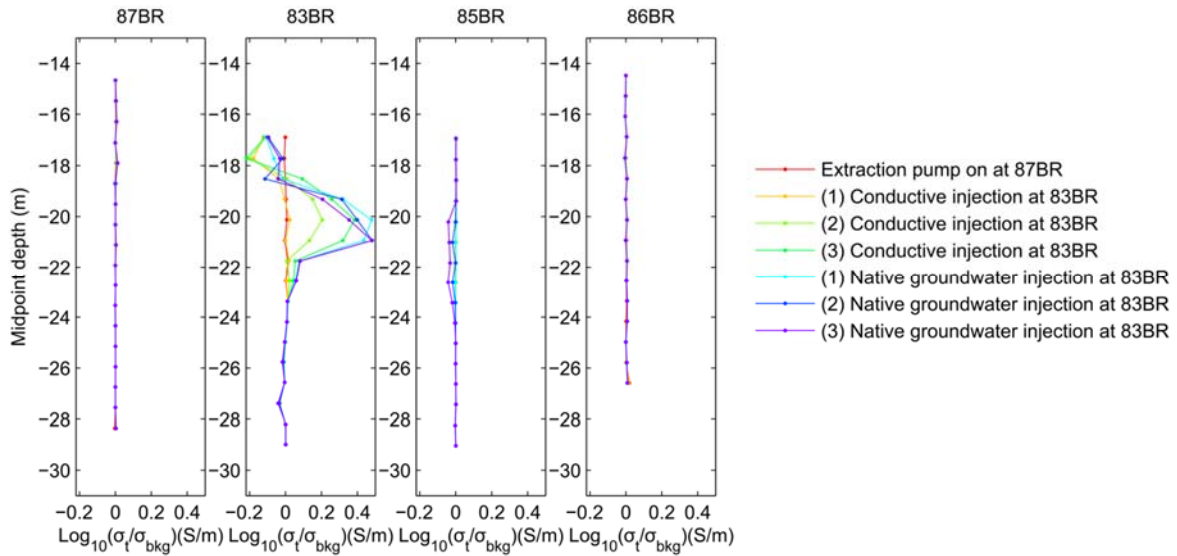
Figure 5.6.5: Vertical apparent conductivity profiles representing relative changes from background values for boreholes 87BR, 83BR, 85BR and 86BR.
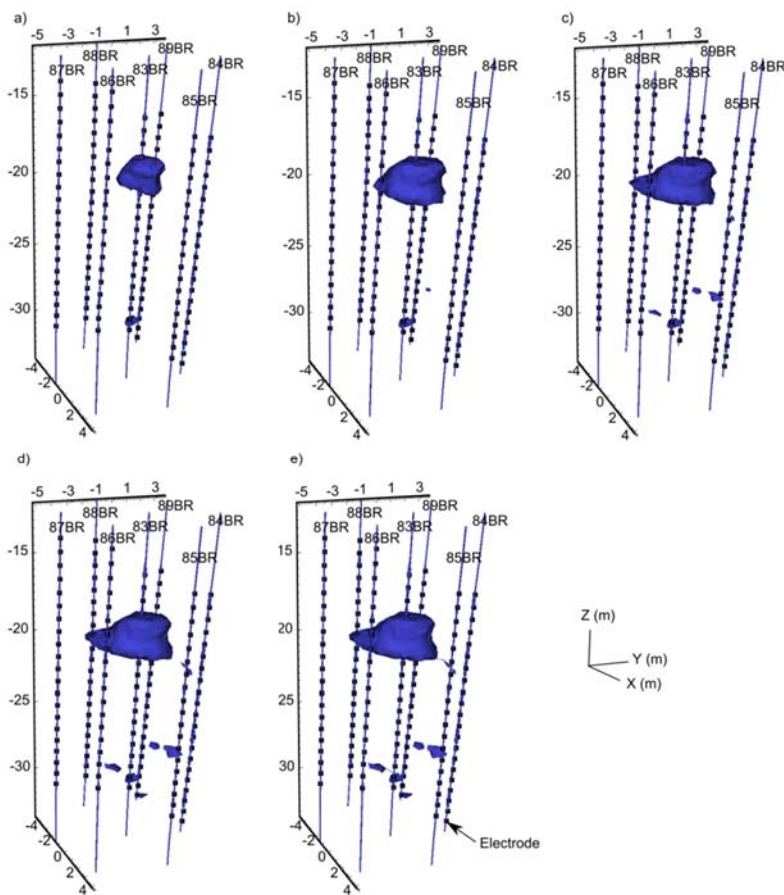
Figure 5.6.6: 3D time-lapse ERT inversion images for a) near the end of the conductive injection b) c) d) and e) during the native groundwater injection. Injections were continuous over time. The isocontour log10(Cond$_t$/Cond$_0$) = 0.040 is shown.

e) 87BR-85BR

Percentage differences between the averaged apparent resistivity from a background dataset and averaged apparent resistivities from time-lapse datasets throughout the tracer study are shown in Figure 5.6.7. A sharp decrease in resistivity (i.e. an increase in conductivity) from the background dataset is evident during the conductive injection (blue squares). Extraction from 85BR following the conductive injection shows a negative trend indicative of removal of the conductive tracer mass from the system (red squares). Changes during the resistive injection (green squares) remain steady from the background value. Following the resistive injection (black squares) a decreasing trend is evident from the background apparent resistivity with some rebound during the last collected dataset.
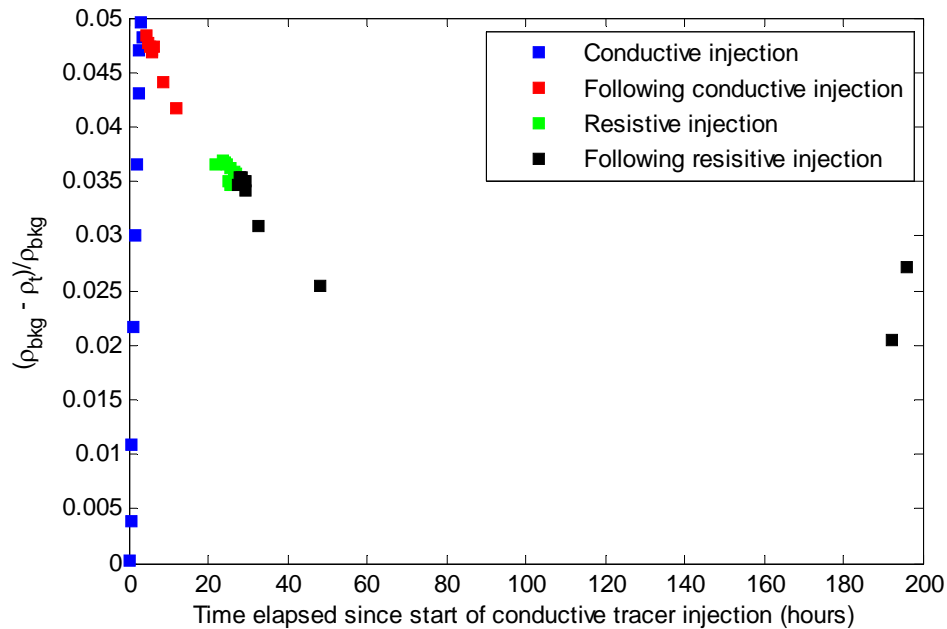
Figure 5.6.7: Percent difference in averaged apparent resistivities for time-lapse datasets from a background dataset for 87-85BR tracer study.

Relative changes in borehole apparent conductivities profiles for 83BR, 85BR and 87BR (the only boreholes showing significant changes) before and during the four stages of the tracer test are shown in Figure 5.6.8, with 86BR shown for comparison. Figure 5.6.8 only shows a subset of the datasets collected at the end of step [1] through step [4a] within the ERT tracer test. The largest conductivity changes occur within 87BR and 83BR during the conductive injection. The effect of the resistive injection is seen in 87BR, with small to insignificant changes occurring in 83BR and 85BR. Extractions from 85BR appear to decrease conductivities in all boreholes (except 86BR).
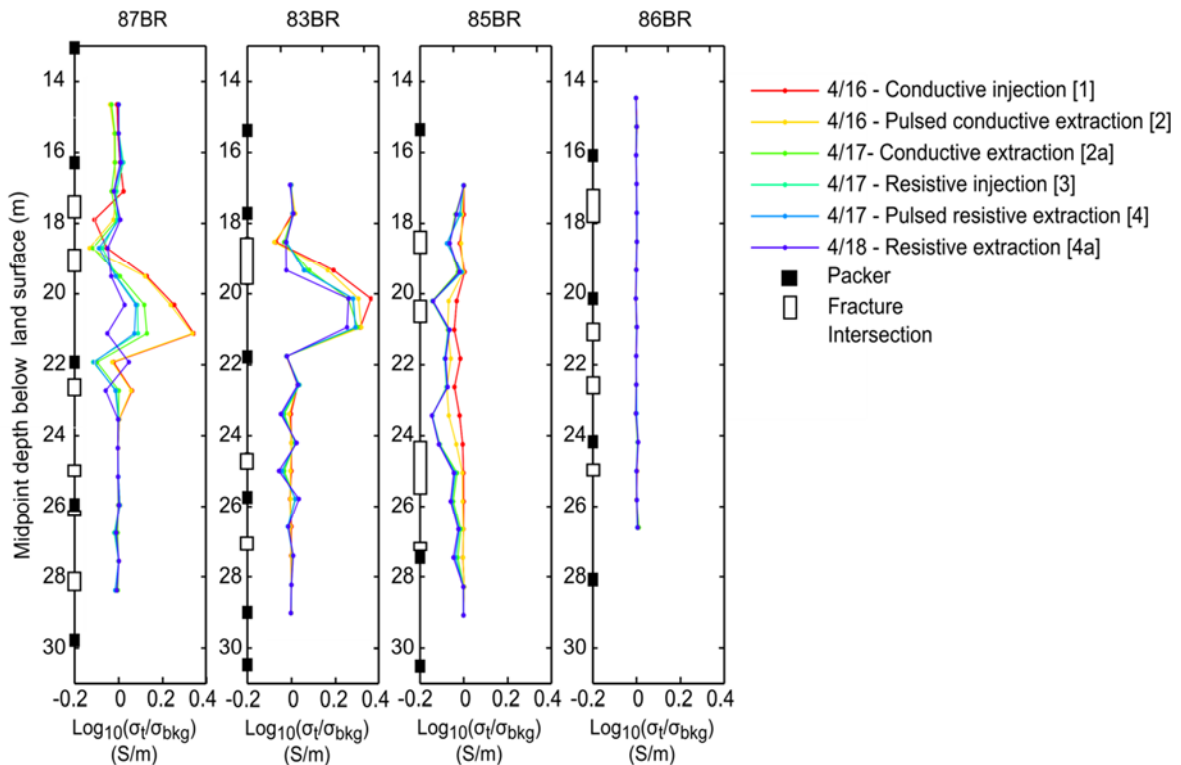
Figure 5.6.8: A subset of vertical apparent conductivity depth profiles for wells showing the largest conductivity changes: 87BR, 83BR, 85BR before and during the four-part tracer test. The response for 86BR (assumed to be unconnected) is shown for comparison.

To determine the minimum isocontour plotted in the time-lapse ERT images in this tracer test, a rigorous approach was taken whereby a synthetic study was performed and forward models were generated from the baseline and final conductive injection inversions. Noise was added to these datasets based on the error model used for the field datasets (described above) and a time-lapse inversion was performed. It was found that random inversion artifacts inconsistent with the migration of the tracer began to appear in the images when the minimum isocontour (of log10 conductivity relative to the background conductivity) was less than 0.035 S m^{-1}/S m^{-1}. Therefore, we assumed the ERT inversion detection capability to be equal to 0.035 S m^{-1}/S m^{-1}, representing a change in conductivity equal to 8.4%. All plots therefore show a minimum isocontour equal to this value.

A plan view of the migration of the conductive injection (step [1]) determined from the 3D ERT tracer study is shown in Figure 5.6.9A as relative changes from the background conductivity. The largest changes in spatial extent appear after the 3rd injection (Figure 5.6.9A-a) and persist until after the final (9th) injection (Figure 5.6.9A-h) and illuminate the migration of a conductive plume from 87BR to 83BR and in the direction of 88BR. Migration of the tracer to 85BR is not implied in these images. The evolution of the vertical extent of the conductive injection is shown in Figure 5.6.9B for the same time steps as in Figure 5.6.9A. The changes in conductivity are confined to the targeted fracture zone interval. The conductive plume appears just below the 2nd fracture zone in 87BR (at about 19 m below land surface (b.l.s.) and appears to enter 83BR at the bottom of the top fracture zone (at about 19.5 m b.l.s.).

86
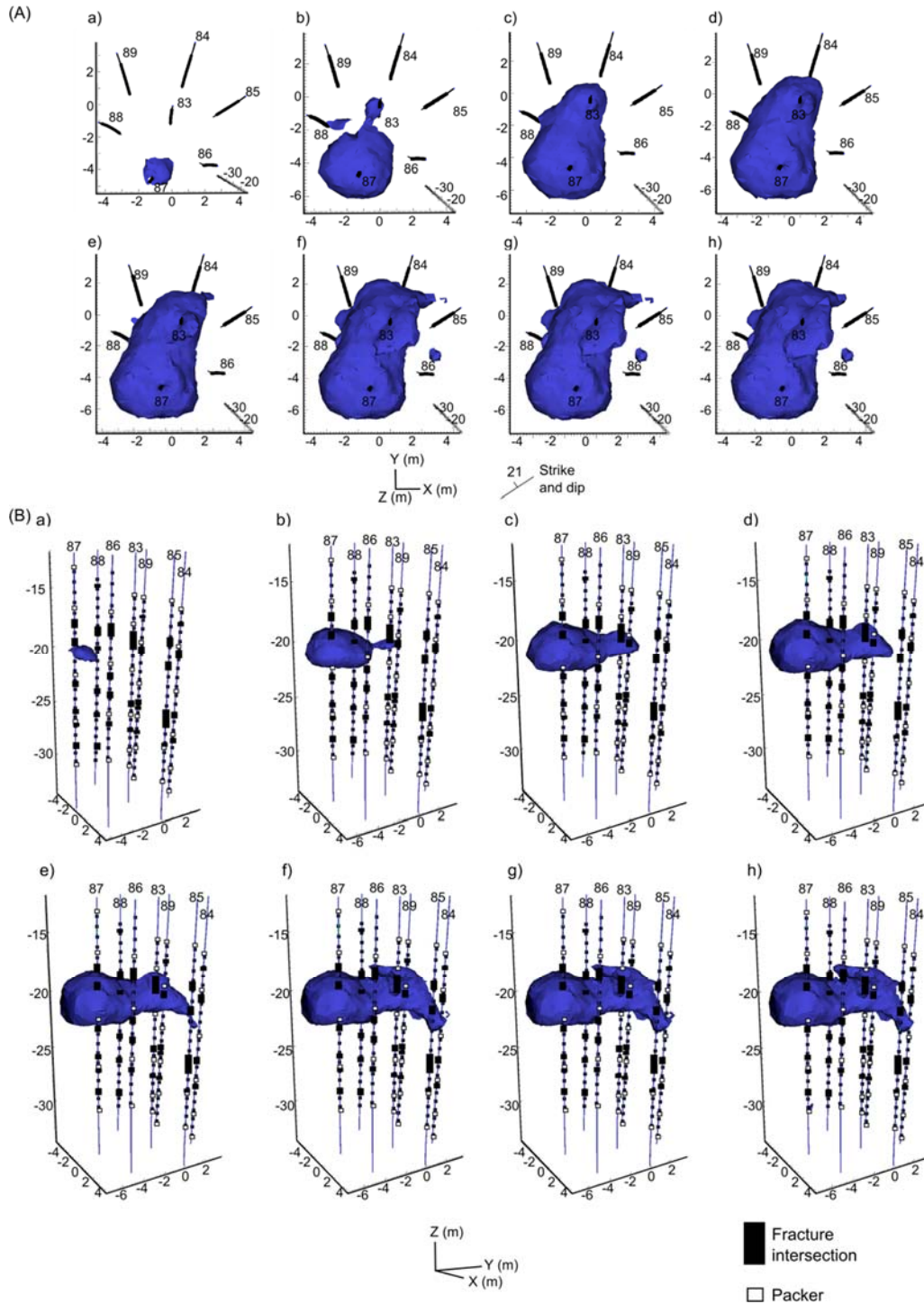
Figure 5.6.9: Time-lapse ERT image of relative change in electrical conductivity ($cond_t$ = conductivity at time slice 't', $cond_0$ = conductivity of background) during tracer injection showing (A) Plan view (B) elevation view. Images a-g represent the 2nd to 10th (last) injections. The 7th injection has been omitted due to minor conductivity changes from the previous injection. The isocontour shown is $log10(Cond_t/Cond_0) = 0.035$.

Figures 5.6.10a through 5.6.10d show time-lapse images from datasets collected on the same day as the tracer injection tests beginning with the last conductive injection (Figure 5.6.10a is the same as part h of Figure 5.6.9B). Figures 5.6.10b-c show conductivity changes after the first and last deionized water injections, respectively. Figure 5.6.10d is for data acquired after 4 hours of extraction pumping from 85BR following the deionized water injection. Note that the resistive injection has little effect on the images shown in Figures 5.6.10b-d.

Following the completion of the tracer test, extraction from 85BR for 20 hours has a dramatic effect on the relative change in conductivity with changes focused around 83BR. (Figure 5.6.10e) There is a decrease in the conductive plume surrounding 83BR one week following the tracer test (Figure 5.6.10f); after four hours of extraction from 85BR (Figure 5.6.10g), the plume is no longer visible. However, note that a decreased conductivity contrast between the tracer and the native groundwater due to fluid movement will limit ERT detection. Three weeks after the tracer injections, a conductive plume persists around 83BR in the ERT image (Figure 5.6.10h), possibly suggesting back-diffusion of conductive tracer (i.e. from this tracer injection or previous injections) from the matrix into the mobile domain.
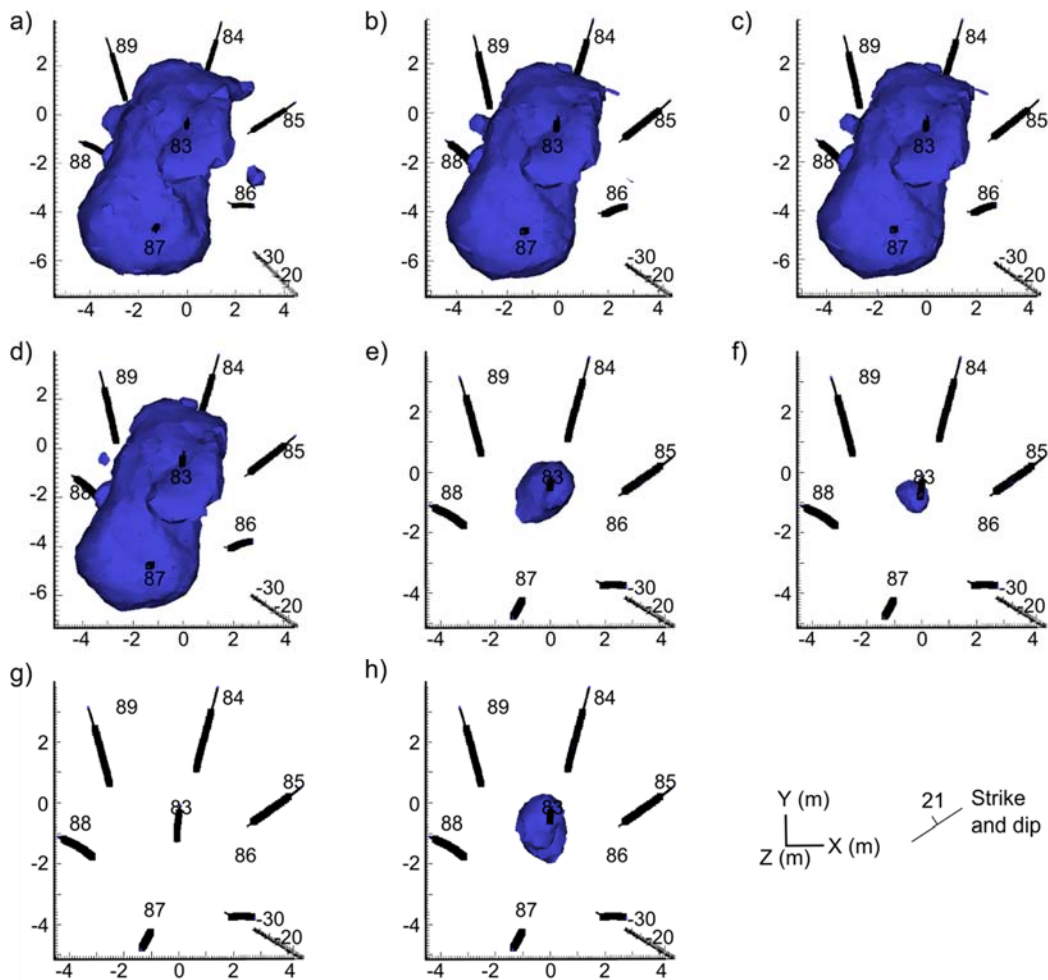
Figure 5.6.10: Time-lapse ERT images of relative change in electrical conductivity (Cond$_t$ = conductivity at time slice 't', Cond$_0$ = conductivity of background) following the conductive tracer injection: a) 30 minutes after the final conductive injection before extraction at 85BR (also shown

in Figure 11h); b) 1st deionized water injection; c) last deionized water injection; d) 4 hours after 85BR extraction following deionized water injection; e) 20 hours after 85BR extraction following deionized water injection; e) One week following completion of tracer test f) One week following completion of tracer test after 4 hours of extraction from 85BR; f) Three weeks following the tracer test. The isocontour shown is log10(Cond$_t$/Cond$_0$) = 0.035.

This tracer injection experiment provided valuable information at a plot scale appropriate for capturing migration pathways under a pulsed-tracer injection test. The 3D spatial extent of the tracer migration highlights flow and transport within a heterogeneous fractured rock system. The major flow pathways observed, particularly for the conductive injection, are likely in part due to the higher-density of the bromide tracer causing down-dip migration. Available geologic data and the hydraulic connections inferred from the drawdown data are consistent with the migration pathways imaged in Figures 5.6.9 and 5.6.10. The 3D extent of the tracer could not have been resolved using standard borehole geophysical methods or hydraulic testing alone. For example, while the ERT images generally show tracer migration pathways that are down-dip in the direction of strike, more complexity is revealed, particularly surrounding 88BR. The images indicate that a convoluted tracer transport pathway extending close to 88BR exists between 83BR and 87BR. This is consistent with results of the preliminary deuterium oxide tracer study (Section 5.2.5) whereby longer travel times were found between borehole pairs 83-87BR compared to borehole pairs 83-85BR. The results indicate that characterizing fractured rock with ERT clearly enhances understanding of tracer transport pathways relative to point measurements from boreholes alone.

f) Amendment Injection

The seventeen ERT datasets collected during the amendment injection show a consistent increase in average apparent conductivity relative to the background (Figure 5.6.11). Following completion of the amendment injection, ERT datasets continued to exhibit an increase in apparent conductivity until approximately 30 hours after the amendment injection. A comparison of Figures 5.6.7 and 5.6.11 shows that the amendment injection datasets exhibit larger changes in apparent conductivity (for the same pulsed injection design) even though the fluid specific conductance of the tracer and amendment fluids was about equal: 53.47 mS/cm versus 50.2 mS/cm, respectively.
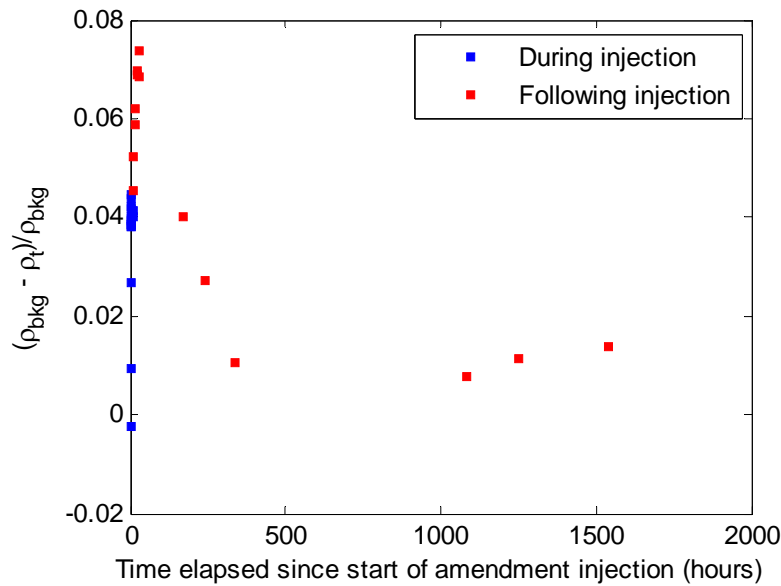
Figure 5.6.11: Percent difference in averaged apparent resistivities for time-lapse datasets from a background dataset for the amendment injection at 87BR.

Following the amendment injection, the vertical ERT profiles exhibit a clear decrease in apparent conductivity (Figure 5.6.12). In 87BR, 83BR and 85BR vertical downward migration of the residual amendment appears likely as evidenced by apparent conductivity increasing at depths below the injection interval over time. Interestingly, 86BR exhibits changes in apparent conductivity below 22 m depth post-injection, although these changes are small compared to the other surrounding boreholes.
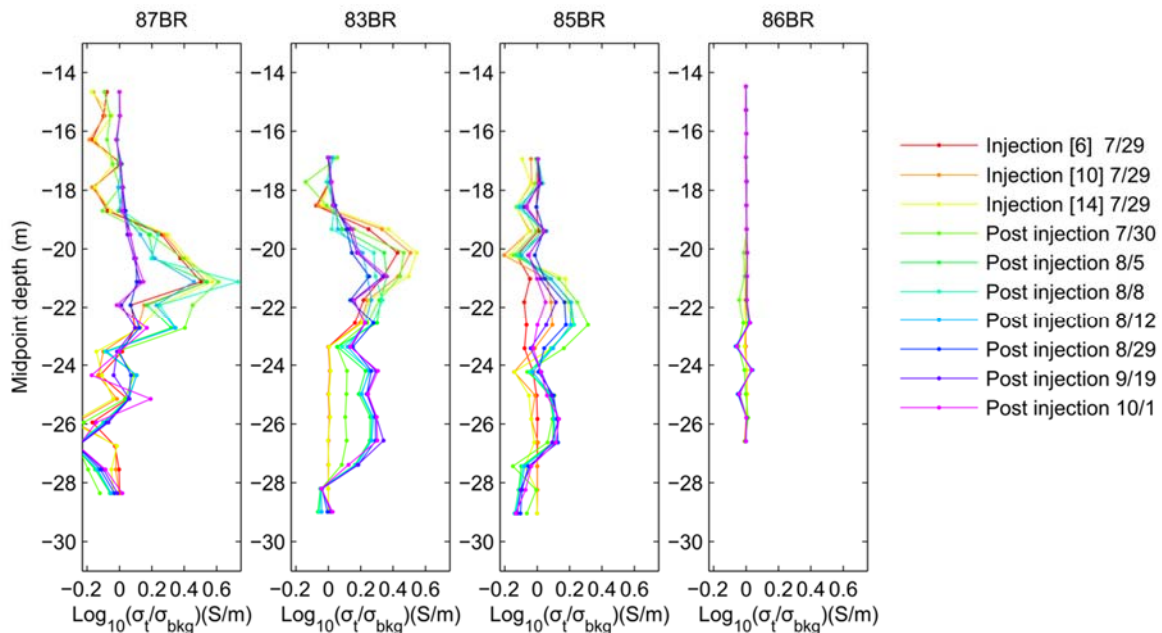
Figure 5.6.12: Vertical ERT profiles within injection borehole 87BR and boreholes with the largest conductivity changes, 83BR and 85BR. Borehole 86BR is shown for comparison. Amendment

injection numbers in square brackets [ ] represent the sequential injection number (out of 17 total injections).

As in the 87BR-85BR tracer study, a synthetic study was performed to determine the minimum isocontour for 3D ERT images. We anticipated that the minimum isocontour might be higher than that for the previous 87-85BR tracer study given the expected larger changes due to the addition of the amendment. Synthetic datasets were generated from inverted models of the background and last injection; data noise representative of the field datasets was added to these synthetic datasets. A time-lapse inversion of these synthetic datasets showed conductivity artifacts when the minimum isocontour was less than 0.07 S m^{-1}/S m^{-1}. In the actual images, spatially broad changes in conductivity began to appear when the minimum isocontour was less than 0.08 S m^{-1}/S m^{-1}. Most researchers acknowledge that characterizing ERT data noise remains challenging, particularly with instrumentation providing ever superior data quality such that errors in the modeling and inversion mechanics become more significant. We presume that the difference between the minimum isocontours defined for the 87BR-85BR tracer test versus the amendment injection (0.08 versus 0.07 S m^{-1}/S m^{-1}) stems from unidentified systematic and numerical errors.

Inverted 3D ERT images during-and-post amendment injection (Figures 5.6.13 and 5.6.14) show the evolution of a conductive plume beginning at the injection borehole (87BR), followed by migration to 83BR and then to 85BR (Figure 5.6.13a-d). The most extensive conductivity changes are shown post injection (Figures 5.6.13e-f) whilst localized conductivity changes are noteable at depth around boreholes 87BR, 83BR and 85BR.   A plan view of the conductivity changes (Figure 5.6.14) better shows that these changes are primarily localized around these boreholes and do not extend into the formation. Fourteen days following the amendment injection (Figures 5.6.13g and 5.6.14g), the highest conductivity changes are at about 29 m depth in 87BR and between boreholes 83BR and 85BR. These changes are less spatially extensive 64 days following the amendment injection.

The time-lapse ERT measurements provide valuable information at a plot scale appropriate for capturing migration pathways under a pulsed-amendment injection test. The 3D spatial extent of the tracer migration highlights flow and transport within this heterogeneous fractured rock system. Available geologic data and the hydraulic connections inferred from the drawdown data (Figure 3) are consistent with the migration pathways imaged in Figures 5.6.13 and 5.6.14. The 3D extent of the amendment could not have been resolved using standard borehole geophysical methods or hydraulic testing alone. For example, while the ERT images generally show tracer migration pathways that are down-dip in the direction of strike (Figures 9 and 10), a complex, channelized flow is revealed, particularly in the transport of the amendment around 86BR. <u>The images of the amendment injection show strong evidence for channelized flow within the bedding plane fracture zone and provide unique temporal information on the evolution of the amendment into this zone.</u>
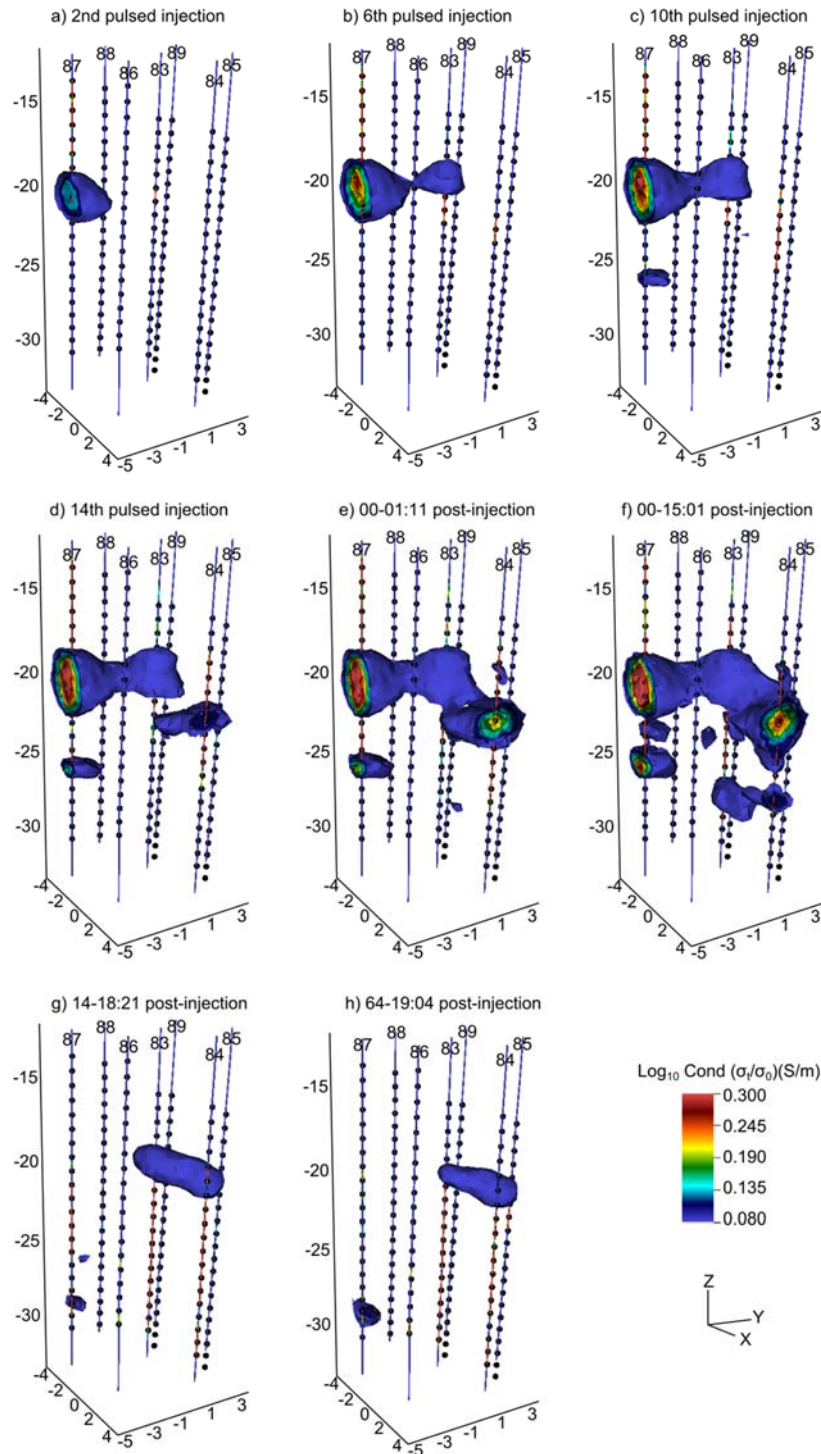
Figure 5.6.13: Elevation view of time-lapse 3D ERT conductivity changes during and post amendment injection.   The time formats of the post injection images e) f) g) and h) are dd (days)-hh:mm. One contour equal to 0.08 S/m is used as an image threshold.
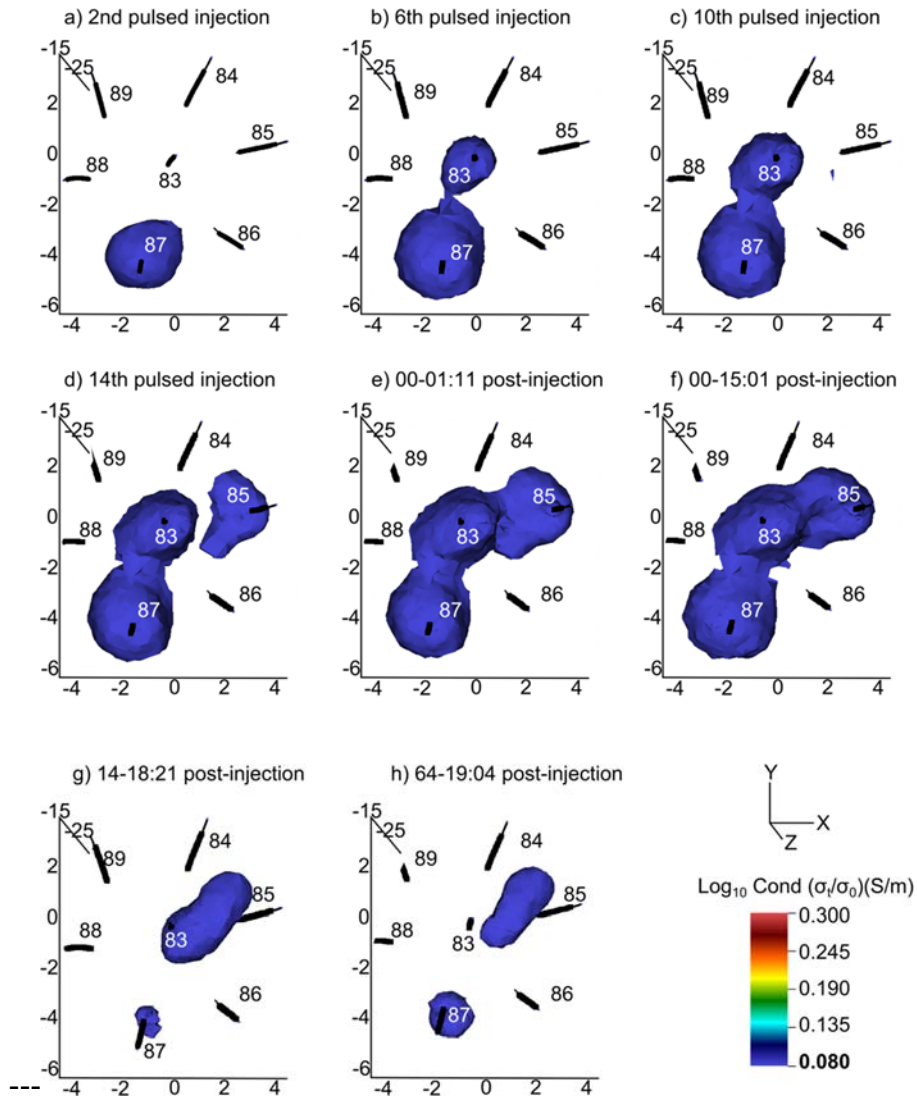
Figure 5.6.14: Plan view of time-lapse 3D ERT conductivity changes during and post amendment injection. Individual figures a-h correspond to elevation views in Figure 5.6.13. One contour equal to 0.08 S/m is used as an image threshold.

93

6.0   PERFORMANCE ASSESSMENT

The performance assessment deals with: [1] assessment of ERT imaging of fractures associated with inverse modeling and code improvements implemented during this study using selected synthetic and field examples; [2] assessment of characterization imaging at NAWC and the former Eastland Woolen Mill (Corinna, ME) based on comparison against supporting borehole logging and hydraulic data; [3] assessment of tracer/amendment imaging from direct measurements of fluid specific conductance at boreholes and analysis of groundwater chemistry. Each of these issues is considered below.

6.1 ASSESSMENT OF ERT CODE IMPROVEMENT

Section 5.4.2 highlights ERT coding advancements developed for this project in E4D (https://e4d.pnnl.gov/). A critical contribution of this code was the ability to incorporate field data in the form of model constraints and apply these model constraints to small scale features such as boreholes. Such work was needed to advance ERT in fractured rock settings by dealing with the problems that arise with the conductive boreholes. An evaluation of applying these constraints was undertaken using datasets from a former quarry and fractured rock field site, Middlebarrow Quarry (UK). The study region named the strike panel consisted of 10 boreholes along the strike of a bedding plane feature dipping at 12º toward the east (Figure 6.1). Datasets collected in the 1990s consisted of time-lapse ERT 2D panel data, fracture intersection depths within each borehole and borehole fluid specific conductances. Borehole deviations were not available. The original analysis of the data was limited to 2D due to lack of available ERT codes and computing resources. Using E4D to analyze these ERT datasets represented an important advancement over previous analysis methods by allowing for 3D discretization of boreholes and incorporation of available information to constrain the inversion result.
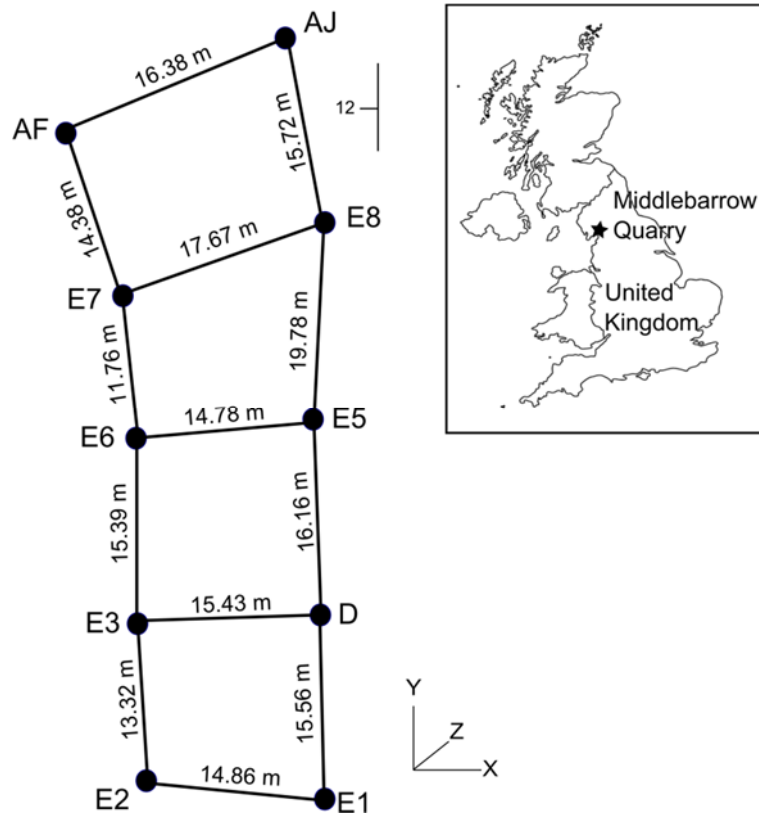
Figure 6.1: Strike panel with inset of study area (modified from Slater et al., (1997).

Model constraints were incrementally added to evaluate the effect on the characterization inversion model. These characterization models were then used to evaluate time-lapse datasets.

In Figure 6.2a, a regularized smoothness inversion was performed, which is the standard inversion technique available in off-the-shelf inversion modeling software. High conductivity halos along the borehole boundaries are evident in this image which is unrealistic given a known sharp conductivity contrast between the boreholes and the host rock. In Figure 6.2b, the implementation of model constraints allowed for a sharp contrast at the borehole boundaries and the host rock and incorporated borehole fluid specific conductance values within the boreholes. This resulted in high conductivity halos being replaced by low conductivity halos at borehole boundaries. Time-lapse results using a regularized smoothness inversion (Figure 6.2a) as a background model are shown in Figure 6.2c. Similarly, the time-lapse results using field-based model constraints from Figure 6.2b are shown in Figure 6.2d. The spatial extents of the time-lapse changes are more localized when the field-based model constraints are implemented (Figure 6.2d) which is more consistent with a fractured rock environment.
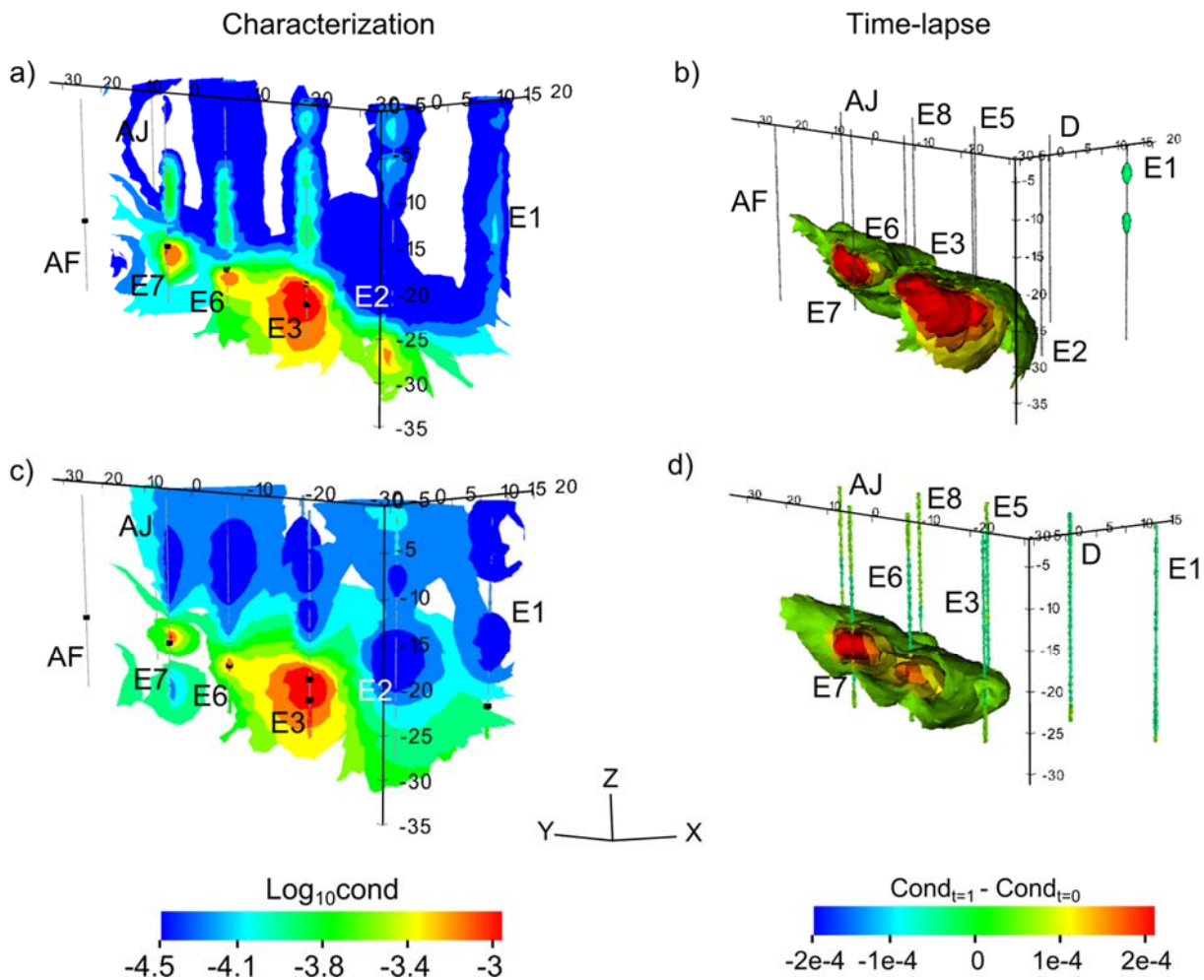
Figure 6.2: Field datasets showing benefits of using borehole regularization disconnects and borehole conductivity constraints in characterization (a and c) and time-lapse (b and d) images b.

To further understand the manifestation of the low conductivity halos (Figure 6.2b) with the model constraint implemented, a synthetic study was performed whereby boreholes were offset 1 m from their actual location. Figure 6.3b demonstrates how halos surrounding boreholes result from a regularized smoothness inversion. Promoting sharp resistivity contrasts at borehole boundaries and constraining the electrical conductivity of the borehole fluids (simulating fluid specific conductance data) removes these halos (Figure 6.3c) and results in an inversion more representative of the true model (Figure 6.3a). While applying the same model constraints as in Figure 6.3c, offsetting boreholes results in a re-introduction of these artifacts when borehole locations are not accurately modeled in fractured rock ERT data (Figure 6.3d). This highlights the importance of accurate borehole and electrode placement; using these constraints can limit unwanted artifacts in the host rock (Figure 6.3c).
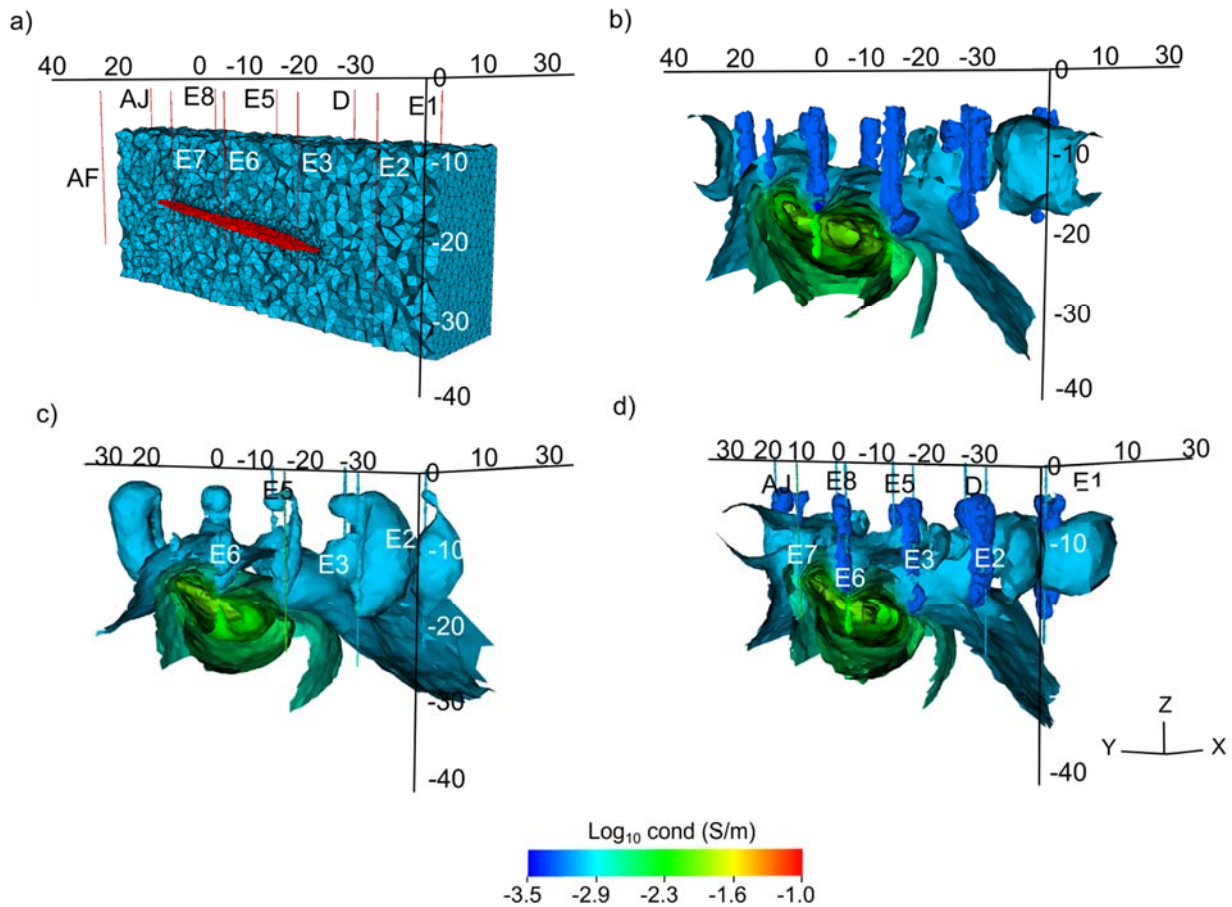
Figure 6.3: Synthetic simulations that show borehole artifacts can be greatly reduced with correct modeling of borehole locations and using borehole conductivity data as a constraint in the inversion. (a) The conductivity model is shown sliced at x=5 m with mesh discretization and fracture location. (b) Smoothness inversion without consideration of the boreholes shows the borehole artifacts that result. (c) Constraining the electrical conductivity of the borehole fluids and removing smoothness constraints along borehole boundaries significantly reduces borehole artifacts. (d) Offsetting the boreholes by 1 m reintroduces the borehole artifacts. For better viewing, light shadowing of isocontours is displayed.

We further highlight the importance of discretizing boreholes with a characterization ERT image obtained at NAWC. In Figure 6.4a, boreholes are included in the discretization and smoothness constraints are removed from these boundaries, while in Figure 6.4b boreholes are not included in the discretization and a standard regularized smoothness inversion (as could be done with a commercially available software package) is performed. The benefits are clear in this image comparison: discretizing the boreholes change the interpretation in between the boreholes and removes the conductive halos along the boreholes that contaminate the entire image. The parallel computing capability of E4D (which allows for many elements to be discretized at borehole locations) combined with borehole constraints allow additional information surrounding and in between boreholes to be extracted from the ERT datasets.
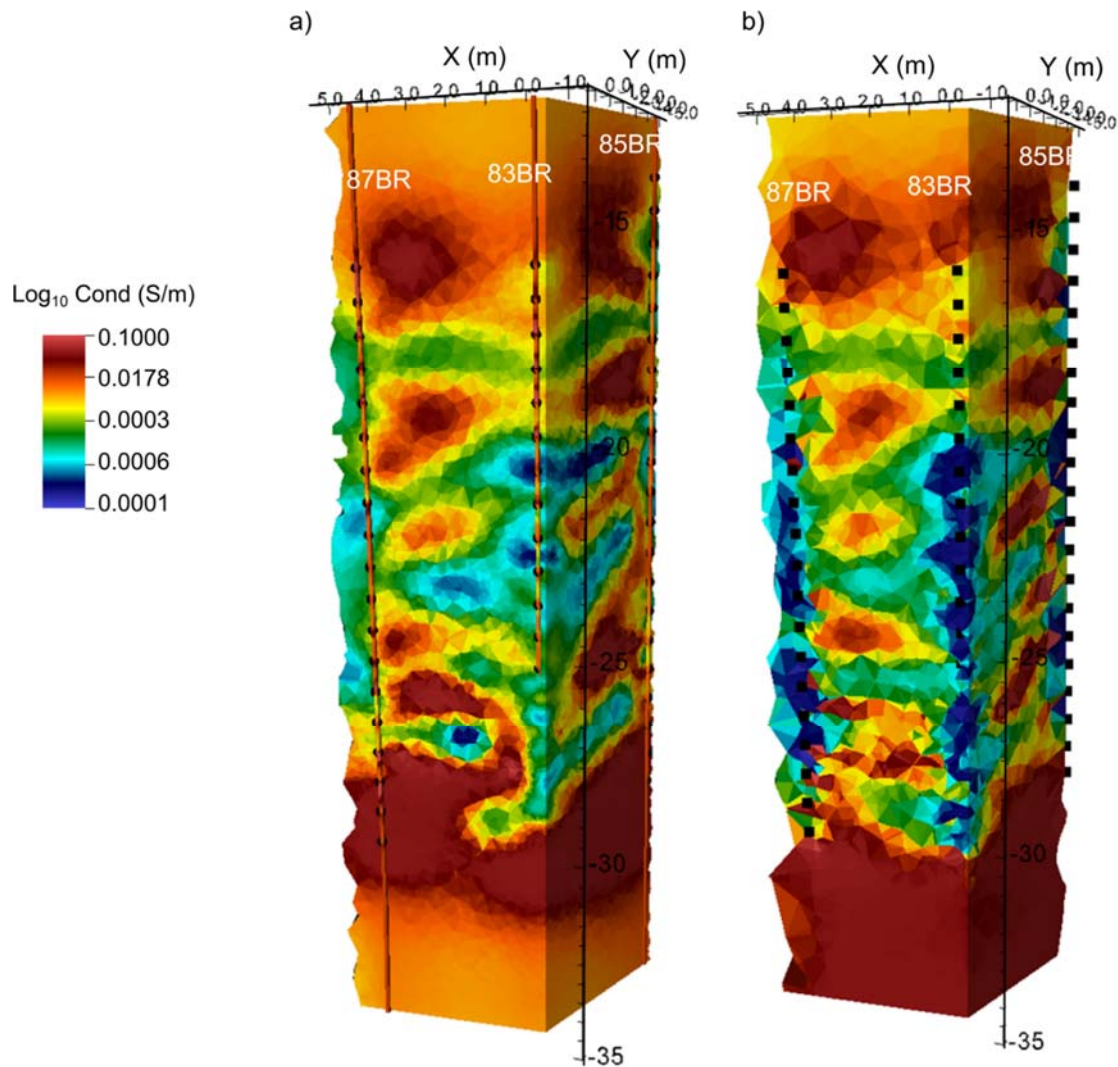
Figure 6.4: Inversion modeling for static ERT datasets at NAWC where boreholes are discretized (a) and not explicitly discretized (b). Note how vertical anomalies along the boreholes dominate the image in (b) and are clearly removed by the improvements shown in (a)

The ERT code advances in E4D allowed model constraints to be implemented which resulted in a more realistic interpretation in a fractured rock environment.   The parallel computing capability of E4D allowed for enough parameters in the modeling such that all boreholes could be discretized, an important consideration shown to effect the interpretation of ERT datasets surrounding and in between boreholes in fractured rock.

6.2 ASSESSMENT OF CHARACTERIZATION IMAGING AT NAWC

Borehole geophysical logs represent the gold standard when ground-truthing ERT models with regard to localized information within boreholes. The ERT inversion results from a cross-section slice along 87-83-85BR (same as Figure 5.5.2.1) are shown alongside OTV logs for 85BR and 87BR. This section highlights structure along the planes of primary interest with regard to the tracer tests.   Massive (M) and laminated (L) units have been annotated. Generally, lighter units correlate with less conductive massive units while darker units correlate with more conductive laminated units. Fracture intersection depths identified in the OTV logs mostly occur at the interface between a massive unit and laminated unit (e.g. M* in Figure 6.5). Most fracture zones are too small to be directly resolved in the ERT characterization imaging.

However, ERT imaging reveals an extensive electrically conductive zone between borehole pairs 87BR and 83BR and borehole pairs 83BR and 85BR (solid blue circles in Figure 5.2.4.3). This zone falls within the interval defined the targeted fractured interval boundary (Figure 6.5) for the tracer injections based on the highly connected (blue) zone determined from the drawdown data acquired in the cross hole hydraulic testing (Figure 6).

In summary, alternating high and low resistivity layering observed in the ERT images agree well with alternating units observed in OTV logs. The largest high conductivity feature identified in the ERT imaging coincides with the most hydraulically connected unit from hydraulic testing.
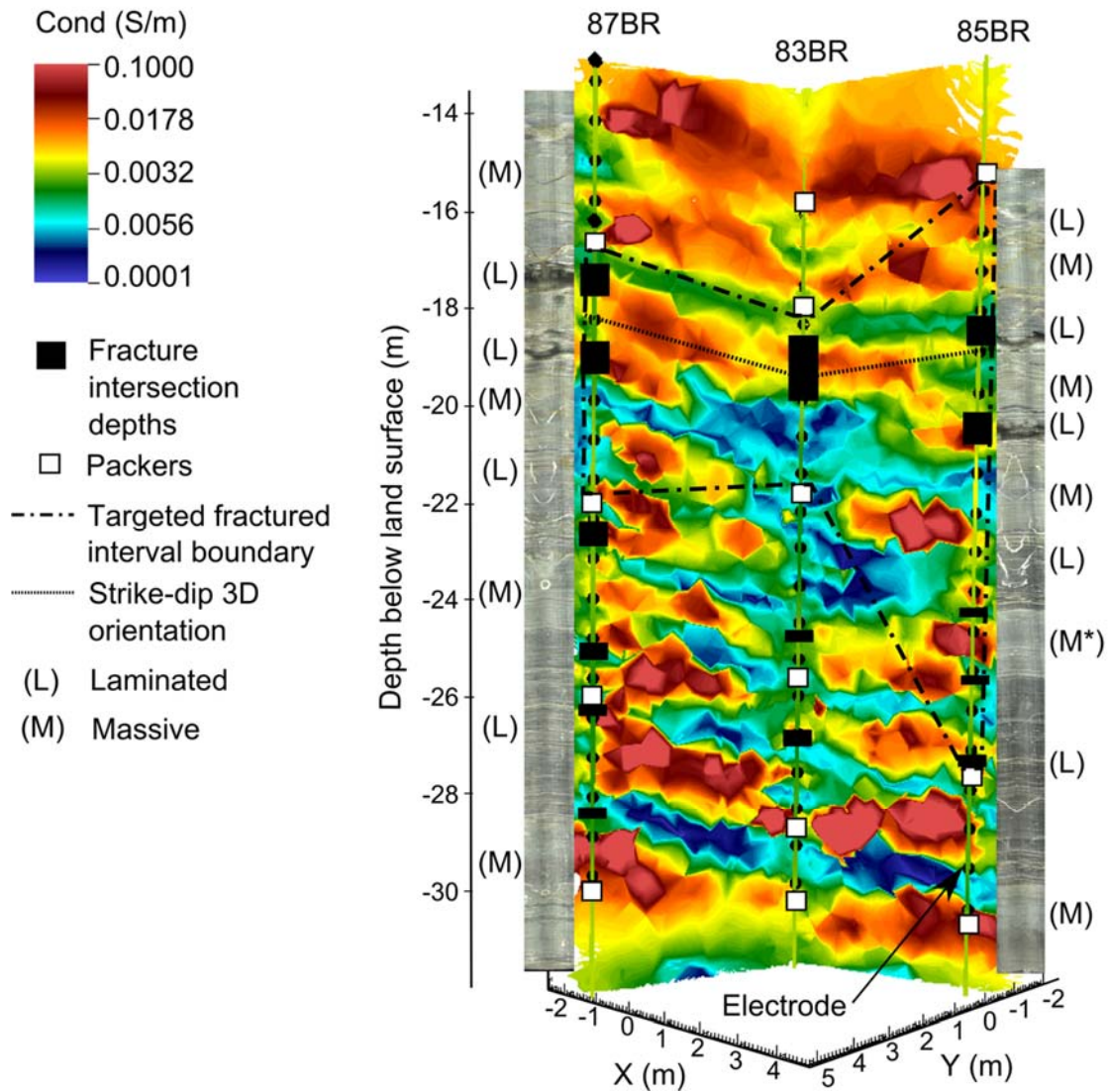
Figure 6.5: Electrical resistivity image for slice 85-83-87 with fracture intersection depths, packers and strike/dip of formation noted, showing alternating conductive and resistive layering partly resulting from the alternating laminated and massive mudstones at the site. The optical televiewer (OTV) log for 85BR and 87BR is shown for comparison. In order to present an unobstructed view of 83BR, 85BR (tracer extraction well) and 87BR (tracer injection well), 86BR is not shown.
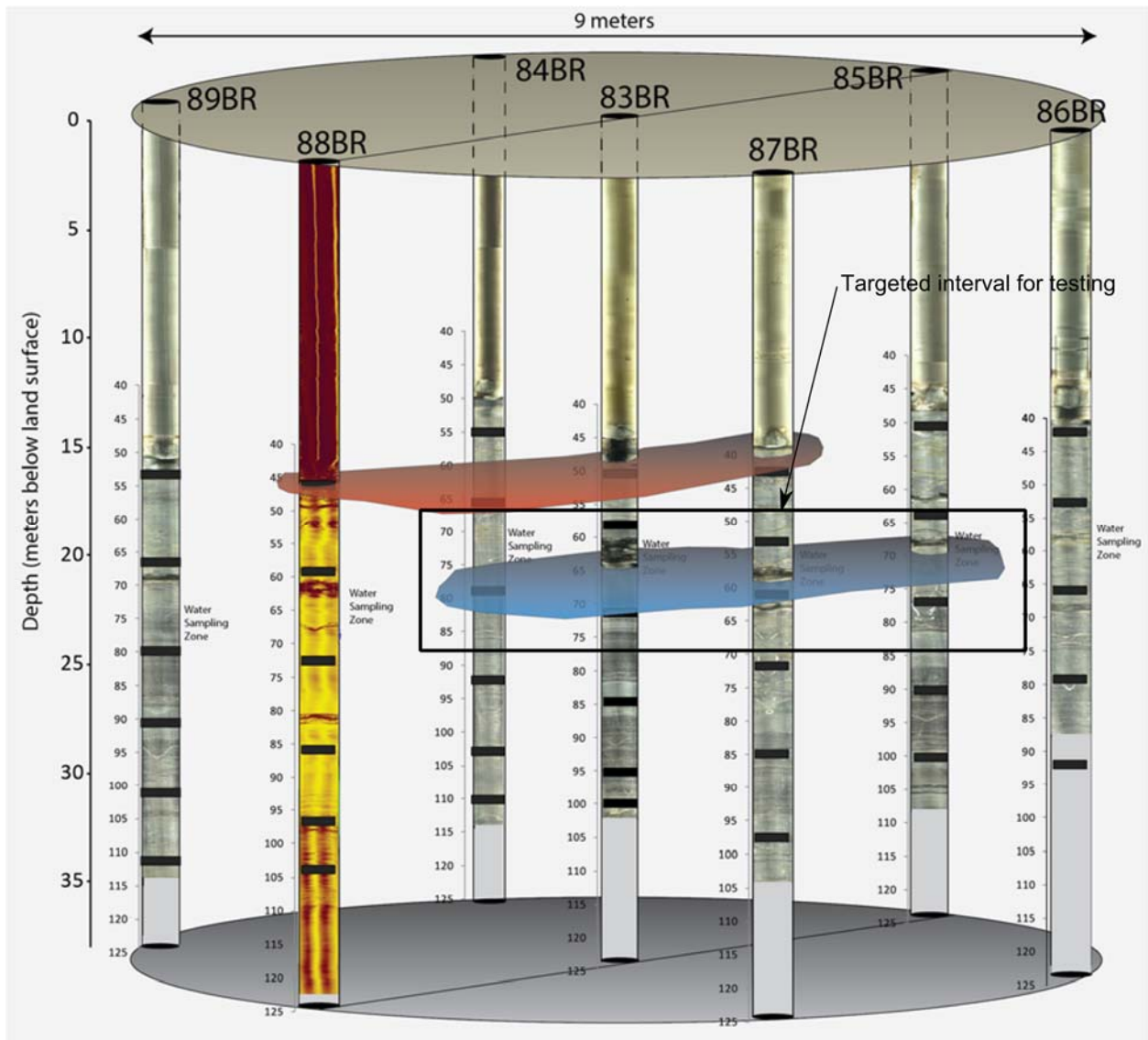
Figure 6.6: Interpretation of hydraulically connected pathways from cross-borehole drawdown data. The blue zone shown between 87-83-85BR agrees well with connected units in the ERT inversion characterization model and was the targeted interval.

6.3 ASSESSMENT OF TRACER TESTS

We use the water chemistry from samples taken during each tracer and amendment test to validate overall results from ERT datasets and modeling. Note the representative element volumes (REV) of the water samples are quite different and vary by over an order of magnitude. Water samples are indicative of processes occurring at individual boreholes within the sampling zone only, whereas ERT data can yield a comprehensive overview of changes occurring within the 83BR-89BR well field. However, ERT is only sensitive to bulk changes in conductivity, not bromide concentrations used in the tracer studies or molasses concentrations used in the amendment injections. We used fluid specific conductivities from localized water samples as an indicator of bulk conductivity changes likely to be detectable from ERT. Given the differences

100

in scale and the fact that ERT data only see bulk changes in specific conductance, we look to ground-truth our ERT findings with common trends in the datasets rather than absolute values.

a) 83BR-85BR

The results of laboratory analysis of water samples from 85BR (extraction well) during the 85BR-83BR ERT tracer test are shown in Figures 6.7 and 6.8. There was no water sampling during the 46 minute conductive injection and native groundwater flush in 83BR. After this, water samples were collected from the extraction borehole, 85BR, every 20 minutes for approximately 4 hours and then every 90 minutes for approximately 11.5 hours (Figure 6.7). There is evidence of early tracer breakthrough in the bromide concentrations, however these do not correlate well with the fluid specific conductances (Figure 6.7). Bromide concentrations in 85BR have an initial spike followed by a steep decline in the first 20 minutes with minor variations thereafter (Figure 6.7). The fluid specific conductance data show only minor changes ($< 3.5\%$ from background) and do not indicate significant changes associated with the tracer arrival at 85BR.
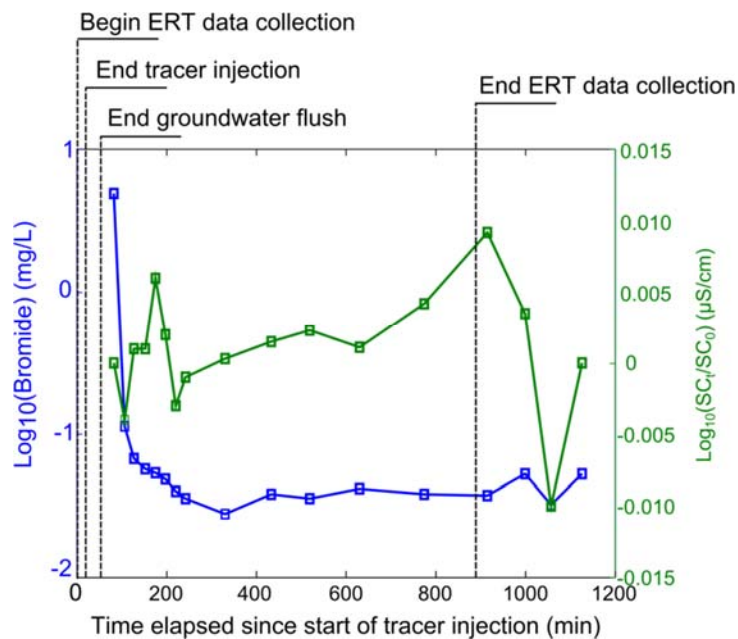
Figure 6.7: Bromide and fluid specific conductance (SC) data recorded at 85BR during the 83-85BR tracer study. The tracer and groundwater flush was complete after 46 minutes after which the extraction pump was turn on at 85BR and water samples were collected.

Comparing bromide concentrations to fluid specific conductances from water samples shows no significant correlation ($R^2<0.01$) (Figure 6.8). Correlation coefficients between fluid specific conductances and chloride and sulfate concentration were also low ($R^2<0.01$). Given this, we deem it is unlikely that the early time increase in bromide concentration represents the tracer migration. After 200 minutes there is no evidence of the tracer within 85BR which is entirely consistent with data from the vertical ERT profiles (Figure 5.6.3).
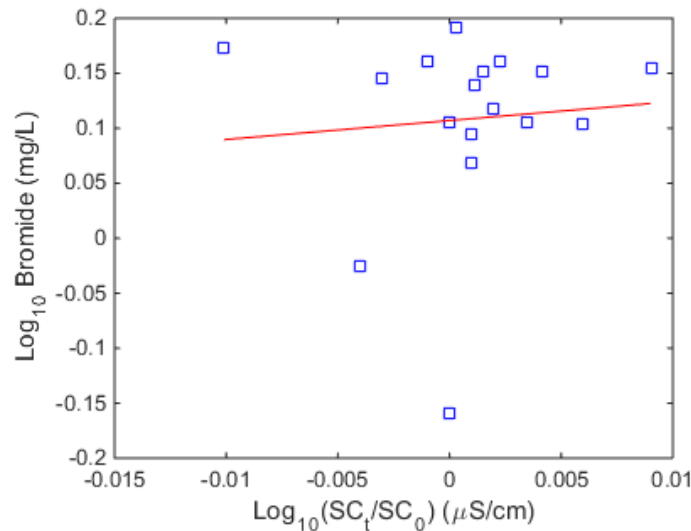
Figure 6.8: Water sampling data shows no significant correlation between bromide concentrations and relative fluid specific conductance (SC).

There is consistency between the changes in the ERT data and the water chemistry results for this tracer test. As there is no correlation between bromide concentrations and fluid specific conductance values, there is no evidence that increases in bromide concentration are due to the presence of the tracer at 85BR, the extraction well. ERT predictions that tracer did not migrate to 85BR are consistent with what would be interpreted from direct measurements of specific conductance e.g. from an array of specific conductance probes. Arrival of the bromide tracer is not detectable in specific conductance (and hence ERT) data.

b) 83BR-87BR

The results of laboratory analysis of water samples from 87BR (extraction well) during the 83BR-87BR ERT tracer test are shown in Figures 6.9 and 6.10. Bromide concentrations peaked about one hour after the conductive injection was finished at 83BR and then rapidly decreased. There is evidence of a less pronounced second breakthrough at 87BR peaking around 1000 minutes after the tracer was injected (Figure 6.9).   Counter-intuitive to expected fluid specific conductance changes, values decreased in the first 200 minutes after the tracer was injected. We presume fluid uptake from the radial influence of the extraction pump could have had an effect here. An increase in fluid specific conductance was observed at approximately 200 minutes after the tracer was injected. As minimal changes in fluid specific conductance were observed in the isolated interval during this tracer test (apart from the changes at 200 minutes), it was hypothesized some of the tracer was in a lower fracture zone. After deflating packers in 87BR (middle zone only) we observed an increase of approximately 90 mS/cm in fluid specific conductance values at 1000 minutes (Figure 6.9), possibly indicating some connectivity between 83BR and lower sections of 87BR.
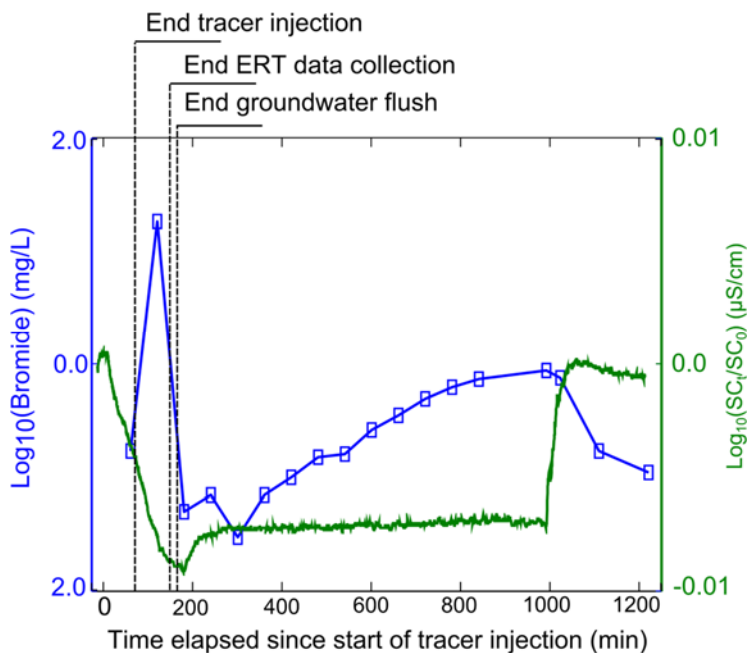
Figure 6. 9: Water sampling data from 87BR for the 83-87BR tracer study. ERT data were collected for the first 161 minutes of the tracer test. The tracer injection was complete after 65 minutes and the groundwater flush was complete after 179 minutes.
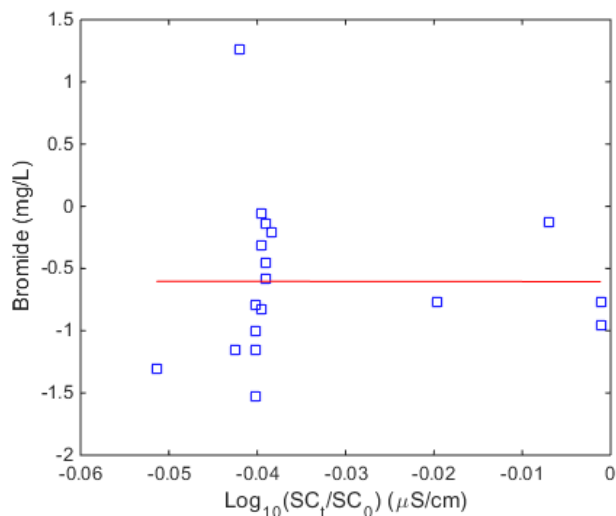
Figure 6.10: No statistical correlation is observed ($R^2 < 0.01$) between bromide concentrations and changes in fluid specific conductance values from water samples extracted from 87BR.

As per the 83BR-85BR study, bromide concentrations and changes in fluid specific conductance are poorly correlated ($R^2 < 0.01$). Fluid specific conductance values are also not significantly correlated with chloride concentrations ($R^2 < 0.01$) and weakly correlated with sulfate concentrations ($R^2 = 0.39$) (data not shown for brevity).

Due to previously noted ERT instrumentation issues (Section 5.6), ERT datasets were only acquired during the first 161 minutes after the tracer injection began in 83BR. This time frame coincides with only the first two water samples collected in this test (Figure 6.9). Whilst bromide concentrations show a rapid increase, possibly corresponding to the tracer arrival, fluid specific conductance values actually decrease between these times. The lack of any significant response in the vertical ERT profiles and the cross-borehole images away from 83BR is consistent with these direct observations. The imaged conductivity changes surrounding the injection borehole from ERT (Figure 6.11) are impossible to verify without borehole samples. However, we find consistency between conductivity changes within vertical ERT profiles and ERT inversion results (Figures 5.6.5 and 5.6.6).

In comparing early time datasets (<= 161 minutes), we find consistency between changes in fluid specific conductances at 87BR from water sampling and results from ERT datasets. While bromide concentrations indicated a rapid tracer breakthrough in 87BR followed by a less concentrated secondary breakthrough, ERT is sensitive to bulk changes in conductivity and the fluid specific conductance data does not support that a significant change occurred at the extraction borehole, 87BR.
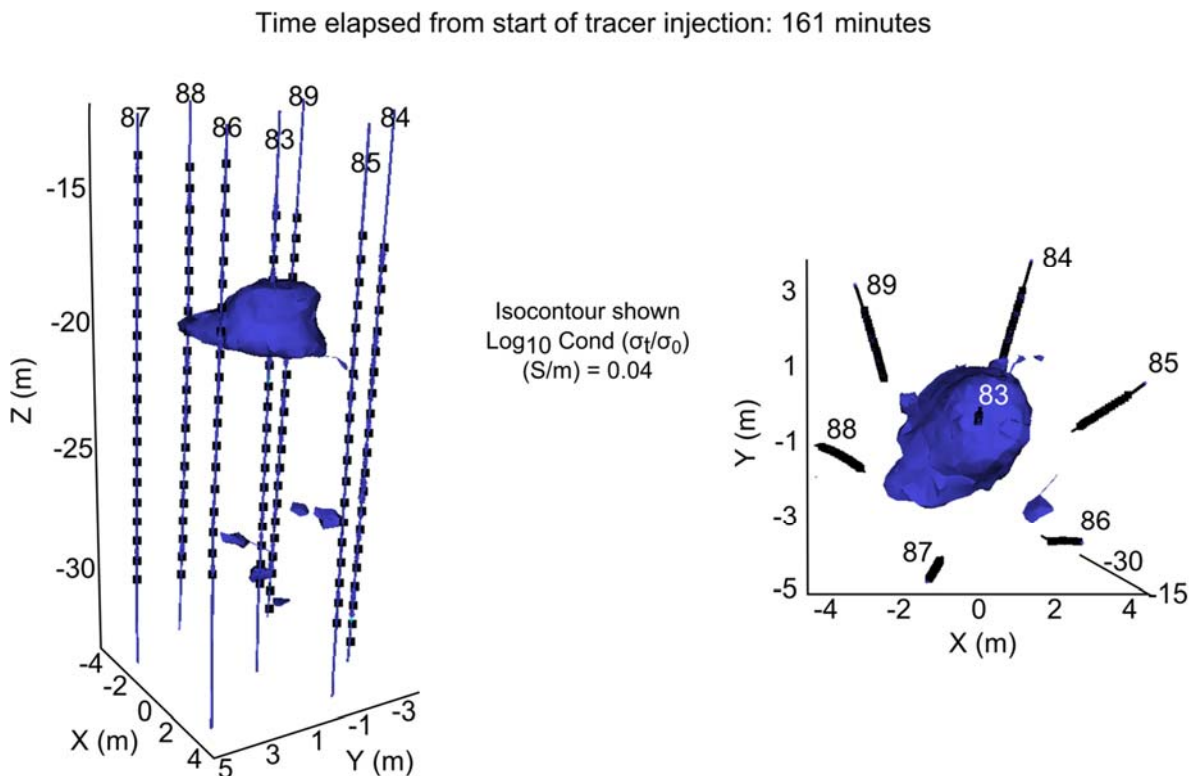
Figure 6.11: ERT spatial delineation of the injected tracer at 83BR in the 83-87BR tracer study. Conductivity changes from background appear localized to 83BR in the first 161 minutes after the tracer injection consistent with no evidence for increases in specific conductance at 87BR from direct measurements.

104

c) 87BR-85BR

Bromide and fluid specific conductance data from 85BR (only acquired during the extraction phases of the tracer test) are shown in Figure 6.12. After the conductive injection, there is a sharp decrease in bromide concentration and fluid specific conductance during the pulsed extraction from 85BR. This unexpected initial influx of resistive fluid into 85BR may be from radial pumping outside the circumference of the 83-89BR well field. Bromide concentrations and fluid specific conductance values subsequently increase during the continuous extraction phase after the conductive injection, indicating delayed tracer arrival. Water samples showed decreased fluid specific conductance and bromide values during the resistive injection; this was followed by increasing values (Figure 6.12). Between 50 and 200 hours, bromide and fluid specific conductances within 85BR decreased slightly. Extraction pumping occurred at 85BR at 200 hours, whereby a marked decrease in fluid specific conductances and bromide concentrations are shown (Figure 6.12).

Unlike in previous tests, fluid specific conductance values are well-correlated with bromide concentrations ($R^2=0.67$) (Figure 6.13a) and sulfate concentrations ($R^2=0.72$) (Figure 6.14b) but not with chloride concentrations ($R^2<0.01$) (data not shown for brevity).
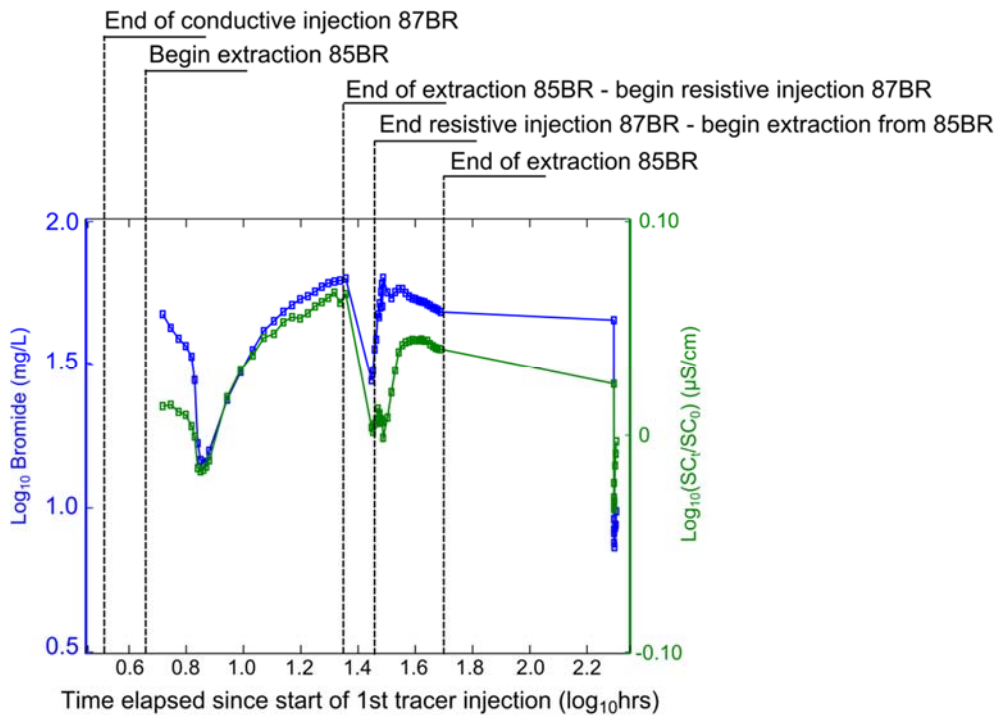
Figure 6.12: Fluid specific conductance and bromide concentrations for samples from 85BR during the 87BR-85BR ERT tracer injection test. At 200 hours, 4 hours of extraction pumping at 85BR occurred.

105
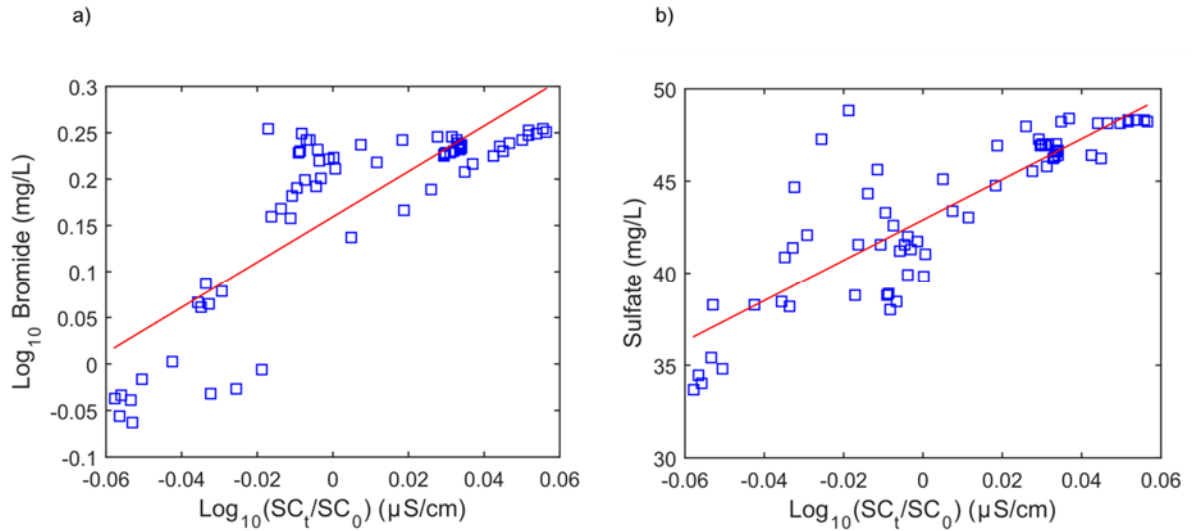
Figure 6.13: a) Bromide and changes in fluid specific conductance (SC) show similar trends in the 87-85BR tracer test (R^2=0.67) and b) Sulfate concentrations and changes in fluid specific conductance (SC) show a significant correlation in the 87-85BR tracer test (R^2=0.72).

In this case, there is compelling evidence in the water sampling data that the tracers reached 85BR within the water sampling zone. However, analysis of ERT images alone might suggest that the tracer did not extend to this borehole. In this case, the sampling and analysis of water samples highlights the inherent limitations of ERT associated with image resolution even at the relatively high borehole density used in this study. Fluid specific conductance and bromide analysis of water samples from 85BR during the conductive and resistive extraction phases reveal that conductive tracer did reach 85BR (Figure 6.12) during the continuous extraction from this borehole although this could not be resolved in the ERT images (Figure 5.6.9), which only reliably show changes greater than a threshold value of 8.4%. Fluid specific conductance readings during and following the resistive injection possibly reveal the presence of the resistive tracer at 85BR, although this again was not resolvable in the ERT images. Given the results of the hydraulic tests, tracer migration to the extraction borehole was anticipated and expected, consistent with the specific conductance and bromide analyses. ERT resolution is limited by multiple factors, including (1) the conductivity contrast between the tracer fluid and the pore fluid in the immobile and mobile domains, (2) the possibility of narrow fracture zones important for tracer transport that are smaller than the ERT image resolution and (3) the numerical errors in the ERT modeling which exceed the actual data errors indicated by reciprocal measurements in this case. While large conductivity contrasts between the native groundwater and the tracer fluids were used in this test (factors of 89 and ~333), dilution of the tracer caused by the subsequent extraction, combined with the relatively low conductivity contrast between the host rock and the fracture zones probably limited the magnitude of the conductivity contrast to be less than the minimum required for ERT detection with the survey design used here. Furthermore, the ERT data may be relatively insensitive to conductivity changes within a thin fracture zone extending towards 85BR, thereby rendering the inversion unable to resolve tracer migration within the fracture.

Despite these limitations, the time-lapse ERT measurements provide valuable information at a plot scale appropriate for capturing migration pathways under a pulsed-tracer

106

injection test. The 3D spatial extent of the tracer migration highlights flow and transport within a heterogeneous fractured rock system. The major flow pathways observed, particularly for the conductive injection, are likely in part due to the higher-density of the bromide tracer causing down-dip migration.   Available geologic data and the hydraulic connections inferred from the drawdown data are consistent with the migration pathways imaged in Section 5.6 Figures 5.6.9 and 5.6.10. The 3D extent of the tracer could not have been resolved using standard borehole geophysical methods or hydraulic testing alone. For example, while the ERT images generally show tracer migration pathways that are down-dip in the direction of strike, more complexity is revealed, particularly surrounding 88BR. The images provide evidence of a convoluted tracer transport pathway extending close to 88BR and between 83BR and 87BR. This is consistent with results of the preliminary deuterium oxide tracer study (Section 5.2.5) whereby longer travel times were found between borehole pairs 83-87BR compared to borehole pairs 83-85BR.

Characterizing fractured rock with ERT enhances understanding of tracer transport pathways relative to point measurements from 85BR alone. ERT imaging revealed pronounced conductivity changes occurring within 83BR, but not the extraction borehole 85BR where water samples were collected. Overall changes in ERT datasets (Section 5.6, Figure 7) and localized apparent conductivities within 85BR (Section 5.6, Figure 5.6.8) for ERT datasets agree well with water sampling trends.

d) Amendment injection

There was limited water sampling during the amendment injection as the idea was to inject the amendment (i.e. a food supply) in pulses with no extraction well, promoting the opportunity to capture electrical signatures associated with biodegradation processes.   We relied on the previous tracer testing between 87BR and 85BR to confirm sufficient conductivity contrast in conjunction with the pulsed injection design for the amendment injection to be imaged with ERT.

Water samples were collected prior to 7/9/2014 and 27 days after 8/25/2014 the amendment. The VOC analysis results are shown in Table 1 and Figure 6.11. We expected to see evidence of biodegradation in boreholes 83BR, 85BR and 87BR since the ERT images (Section 5.6 Figures 5.6.13 and 5.6.14) predict migration of the amendment near these boreholes. We expected to see no evidence of biodegradation in 84BR which was predicted from hydraulic testing (Section 5.2.4), borehole geophysical data (Section 5.2.3) and ERT imaging (Section 5.6 Figures 5.6.13 and 5.6.14).

Table 6.1: Water sample analysis of key compounds in boreholes 83BR, 84BR, 85BR and 87BR prior to and after amendment injection in 87BR

Borehole	Sample date	Trichloroethylene (ug/L)	cis-1,2-Dichloroethene (ug/L)	Vinyl Chloride (ug/L)
83BR	7/9/2014	216.46	625.68	9.30
84BR	7/9/2014	928.11	1864.86	524.92
85BR	7/9/2014	158.50	416.46	20.74
87BR	7/9/2014	129.36	353.09	9.16
83BR	8/25/2014	56.09	596.89	13.29
84BR	8/25/2014	207.36	4096.52	504.45
85BR	8/25/2014	98.45	383.30	14.81
87BR	8/25/2014	59.44	325.26	7.32

Bacteria degrade TCE preferentially by reductive dehalogenation to cis-DCE. The cis-DCE then degrades to VC but usually at a slower pace than the TCE to cis-DCE degradation. There is evidence of TCE decreases in all wells (83BR, 84BR, 85BR and 87BR) (Figure 5a). The only well sampled that shows a significant increase in cis-DCE is 84BR (Figure 5b). In all other wells, cis-DCE decreases or remains about the same. The causes for this may be: (a) the short time frame with respect to degradation processes (1 month), (b) the low concentration of molasses reaching the contaminated water in the fractures, or (c) the dilution of the water in the fractures with the injection water. There is little change in the concentrations of VC (Figure 5c), although percent changes appear high due to the low magnitudes of these concentrations (Figure 5d).

Initial water sampling provided no conclusive evidence of biodegradation induced by the amendment injection. We would need longer term monitoring (beyond the duration of this demonstration project) to evaluate the effects of the amendment injection. The initial data suggests biodegradation in all the sampled boreholes, including 84BR. Any biodegradation at 84BR via input at 87BR is not supported by the borehole or ERT datasets. However, further water sampling over longer time scales than this project duration would need to be conducted to support this initial water sampling data.

The amendment injection is consistent with the movement of tracer during the 87-85BR tracer injection and indicates a channelized flow path in this bedding plane between boreholes 87-83-85BR. Such information could be used to estimate bedding plane fracture surface area affected by amendment injections.
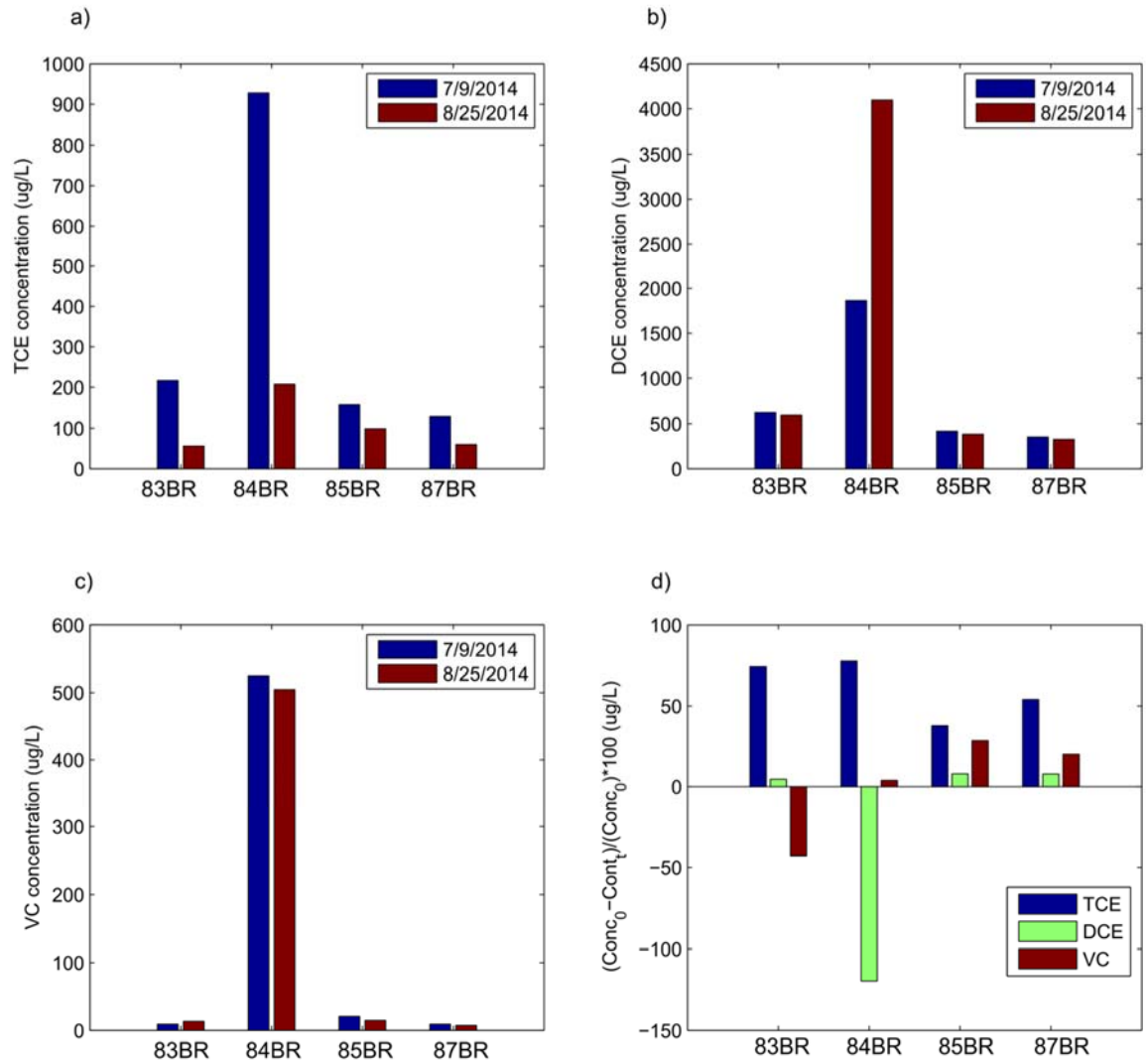
Figure 6.14: A visual comparison of absolute changes in a) TCE b) DCE c) VC concentrations prior to and after the amendment injection within sampled boreholes 83BR, 84BR, 85BR and 87BR. d) Percent changes in concentrations from initial values (7/9/2014) of TCE, DCE and VC within 83BR, 84BR, 85BR and 87BR.

7.0   COST ASSESSMENT

The costs associated with implementation of geophysical technology include both capital and operational costs. In this section, we focus on the specific technology developed and showcased in our work, i.e., the packer/electrode arrays for use in fractured-rock settings. Costs associated with geophysical logging can be readily obtained from commercial contractors.

These packer/electrode arrays were designed by our team and fabricated at Rutgers University during the course of our work. Capital costs associated with materials and fabrication were recorded, as detailed below. We base the following cost model and calculations on costs associated with deployment at the NAWC site. We assume boreholes with similar construction and depth, and we base drilling costs on those seen at the NAWC site. We note that drilling costs can vary substantially with geographic area, rock type, and depth.

We present cost analyses for operational implementation of our technology under two scenarios: (1) monitoring a single amendment injection, with one ERT 'snapshot', and (2) monitoring a series of amendment injections at one location, with multiple ERT 'snapshots' collected on different occasions, and (3) monitoring a single amendment injection at multiple locations across a site. We also assess the worth of our technology relative to conventional sampling. Assigning value/cost to geophysical information is challenging, as the information content of geophysical results includes both qualitative and quantitative aspects. <u>Furthermore, geophysical information is never a direct substitute for conventional methods, but a complement.</u> We adopt a modeling framework to quantify the number of conventional wells required to provide the same spatial information as provided by a specified number of packer/electrode arrays, based on our findings at the NAWC site.

7.1   COST MODEL

Table 7.1 presents the cost elements based on implementation of time-lapse 3D electrical tomography at the NAWC site, focusing on use of the packer/electrode technology developed in our work. Under our project, 7 wells were drilled to 130' depth and instrumented with packer/electrode arrays, giving a unit well cost of ~$12K. Cost reports include an array unit cost of $4.3K, including materials and labor for fabrication; hence the incremental cost of instrumenting a borehole is on the order of 36%. Cost savings are possible with (1) volume pricing for large numbers (25+) of arrays, or (2) mass production of packer/electrode arrays.

Costs are also reported for fieldwork and data analysis associated with baseline characterization and subsequent site visits for additional time-lapse snapshots. Note that costs are not included for transportation or mobilization. Although transportation costs were minor for our project, as the site is close to both Rutgers and the USGS NJ office, these costs are highly site- and project-dependent and must be considered for future implementations.

Table 7. 1: Cost Model for Implementation of Time-Lapse 3D Electrical Tomography at the NAWC site

Cost Element	Data Tracked During the Demonstration	Costs	
Packer/electrode arrays with 25 electrodes and 8 packers (unit cost)	• Materials, fabrication costs, and deployment	Fabrication, labor 16 hrs	$800
		Materials[1]	$3,700
Drilling	• Drilling contract for 7 boreholes, 130' deep	$82,000 (total cost)	
Installation of arrays	• Time in the field	Field technicians, 40 person-hrs	$2000
Servicing/repairing arrays	• Time in the field	Field technicians, 40 person-hrs	$2000
Waste disposal and abandonments of wells	Standard disposal and abandonment, no cost tracking	NA	
ERT characterization or monitoring "snapshot"	• Field technician on site • Data analysis, assuming software access	Scientist, 16 hrs Field technician, 8 hrs	$1200 $400
Electrical power	• No unique requirements recorded	NA	
Borehole geophysics	Standard pricing, no cost tracking	NA	
Transportation/mobilization	Standard pricing, no cost tracking	NA	
Software for ERT data analysis	• Public-domain codes used in this work, otherwise standard pricing	NA	
Long-term monitoring	• Cost per 'snapshot' • Additional site visits and data analysis, with cost savings based on previous work setting up data analysis	Scientist, 4 hrs Field technician, 8 hrs	$300 $400

[1] Materials include packer core ($840), electrodes ($1,125), bladder tubing ($150), wire ($250), PVC pipe ($413), connectors ($500), and sampling tubing ($161), assuming 25 electrodes, 8 packer cores, and wells ~130 ft deep.

7.2   COST DRIVERS

The major cost driver responsible for variation in costs between different deployments centers on drilling costs. Use of the packer/electrode arrays requires boreholes, the cost of which is a function of rock type, local economics, distance between the site and drilling contractors (i.e., mobilization costs), local or state regulations for well abandonment procedures, etc. Drilling costs, however, also drive costs for conventional sampling and testing and thus are not prohibitive for geophysical work.

A minor cost driver for use of our packer/electrode arrays are the cost of materials, which fluctuate with the price of copper, aluminum, and lead used in the fabrication of wire and electrode materials. In our cost model above, variations on the order of 20% in material costs would translate into array price variations on the order of $700, or ~15% of array cost. As noted above, the incremental cost of instrumenting a borehole at NAWC with a packer/electrode array is approximately 36% of the cost of the borehole. With a 20% increase in the price of metals, we might anticipate the incremental cost of instrumentation to rise to 40% the cost of drilling. Costs of the packer/electrode arrays in a field-deployment could potentially be reduced by moving a small number of packer/electrode arrays between wells to build up the required data. However, this would still require packer assemblies in other wells to maintain isolation of fracture zones, and would incur additional personnel costs for fieldwork. We therefore restrict our assessment to the case of a packer/electrode array for every well drilled as done at NAWC.

7.3   COST ANALYSIS

In this section, we present the costs associated with implementation of our technology operationally and then present a comparison of our technology and conventional sampling to quantify the economic value of geophysical information. Cost analysis is based on a fractured-rock site, with characteristics similar to the NAWC site: shallow water table, depth to bedrock on the order of 50 feet, total depth of boreholes on the order of 100 feet. Drilling costs are assumed separate from the geophysical effort; thus, the geophysical effort is leveraging existing infrastructure. We assume access to electrical power on site and infrastructure for housing of instrumentation. We also assume a secure site, such that geophysical infrastructure is protected from vandalism and (or) theft. The goals of geophysical imaging are assumed to focus on monitoring the injection of amendments to identify the region affected by amendment. We consider three possible application scenarios with varying goals, complexity, and cost: (1) monitoring a single amendment injection at one location, with one post-injection ERT 'snapshot' (Table 7.2); (2) longterm monitoring at a single amendment injection location, with multiple ERT 'snapshots' collected on different occasions (Table 7.3); and (3) monitoring a single amendment injection at multiple locations across a site, in one post-injection field campaign (Table 7.4).

In Scenario 1, we envision a small-scale, short-term field effort to understand the distribution of amendment following injection at single location, similar to our experiment at NAWC. Packer/electrode arrays are installed in seven boreholes surrounding a central injection borehole. Deployment and instrument setup is performed by a 2-person team over 2.5 days and baseline ERT data collected. In a second 1-day trip, a single field technician collects data for a snapshot showing amendment distribution. Data analysis is performed by a scientist in 2 days for the

112

baseline data, and 1 day for the subsequent snapshot. The total cost associated with Scenario 1 is $36,200.

In Scenario 2, we envision a longer-term effort to track the amendment over time as it migrates from one injection location. Assuming the same installation as in Scenario 1, we now assume data collection on a quarterly basis for two years following amendment injection, producing a total of 6 post-injection shapshots. The total cost for Scenario 2 is $43,100.

In Scenario 3, we envision a large scale, short-term effort to develop a snapshot of amendment distribution across a site following a series of injections at 5 different locations. The seven packer/electrode arrays are moved between the different locations during both the initial setup and monitoring trips, now each 2 weeks of work. Note that, depending on site layout, some arrays might not require all reinstallations, if ERT wells are shared by multiple injection wells. Analysis time scales with the volume of data, and thus increases by a factor of 5 compared to Scenario 1. We also assume a $5K contingency for possible repair costs and labor arising from removal and reinstallation of arrays, on the order of $5K. The total cost for Scenario 2 is $59,000.

Table 7. 2: Cost Model for Implementation of Time-Lapse 3D Electrical Resistivity Tomography (ERT) under Scenario 1

Cost Element	Description	Costs	
7 Packer/electrode arrays (total cost)	• Materials, fabrication costs, and deployment	Fabrication, labor 16 hrs	$5,600
		Materials	$25,900
Installation of arrays	• Time in the field	Field technicians, 80 person-hrs	$2,000
Waste disposal and abandonments of wells	Standard disposal and abandonment, no cost tracking	NA	
ERT characterization "snapshot"	• Field technician on site • Data analysis, assuming software access	Scientist, 16 hrs Field technician, 8 hrs	$1,200 $400
Subsequent ERT "snapshot"	• Field technician on site • Data analysis, assuming software access	Scientist, 8 hrs Field technician, 8 hrs	$600 $400
Transportation/mobilization	• Travel and shipping (local assumed)		$500
			$36,200

Table 7. 3: Cost Model for Implementation of Time-Lapse 3D Electrical Tomography under Scenario 2

Cost Element	Description	Costs	
7 Packer/electrode arrays (total cost)	• Materials, fabrication costs, and deployment	Fabrication, labor 16 hrs	$5,600
		Materials	$25,900
Installation of arrays	• Time in the field	Field technicians, 80 person-hrs	$2,000
Waste disposal and abandonments of wells	Standard disposal and abandonment, no cost tracking	NA	
ERT characterization "snapshot"	• Field technician on site • Data analysis, assuming software access	Scientist, 16 hrs Field technician, 8 hrs	$1,200 $400
6 subsequent ERT "snapshot"	• Field technician on site • Data analysis, assuming software access	Scientist, 48 hrs Field technician, 48 hrs	$3,600 $2,400
Transportation/mobilization	• Travel and shipping (local assumed)		$2,000
			$43,100

Table 7.4: Cost Model for Implementation of Time-Lapse 3D Electrical Resistivity Tomography under Scenario 3

Cost Element	Description	Costs	
7 Packer/electrode arrays (total cost)	• Materials, fabrication costs, and deployment	Fabrication, labor 16 hrs	$5,600
		Materials	$25,900
Installation of arrays	• Time in the field	Field technicians, 160 person-hrs	$8,000
Waste disposal and abandonments of wells	Standard disposal and abandonment, no cost tracking	NA	
ERT characterization or monitoring "snapshot"	• Field technician on site • Data analysis, assuming software access	Scientist, 80 hrs Field technicians, 160 hrs	$6,000 $8,000
Subsequent ERT "snapshot"	• Field technician on site • Data analysis, assuming software access	Scientist, 8 hrs Field technician, 8 hrs	$600 $400
Transportation/mobilization	• Travel an d shipping (local assumed)		$500
Repair costs	• Associated with removal/reinstallation of arrays		$5000
			$59,000

Cost-benefit analysis for geophysical surveys is challenging, because (1) the information content of geophysical results includes both qualitative and quantitative aspects, and (2) geophysical information is never a direct substitute for conventional methods, but a complement. We contend that the appropriate use of geophysical imaging is to fill gaps in space and (or) time between conventional samples. Based on this idea, we seek to quantify the economic value of geophysical results by estimating the number of conventional wells required to give the same information as a set number of geophysical wells. We perform this analysis using a hypothetical model closely based on experimental results from NAWC, collected in this project.

Using our ERT results from the amendment injection at NAWC, we developed a realistic but hypothetical 3D electrical conductivity model for amendment distribution at the site (Figure 7.1a). The surface area of the amendment-affected fracture zone is 40.6 m^2. In a 'synthetic modeling experiment,' we compute hypothetical ERT data for this model, corrupt the data with random 5% Gaussian noise, and analyze the data using the same approach as applied to real field data from NAWC, obtaining the result in Figure 7.1b.The ERT result does not provide perfect resolution of the amendment plume, but rather provides a smooth image of reality, as is expected from geophysical imaging. Based on the ERT results, one would infer the amendment-treated area has a surface area of 28.9 m^2.

In the absence of geophysical imaging capabilities, one might interpolate a plume boundary based on data collected on a regular grid of wells in the same area, obtaining the result shown in Figure 7.1c. The conventional results for 9 or 16 wells on a regular grid provide surface-area estimates of 19.7 and 27.2, respectively. We consider grid spacings with 9-225 boreholes and estimate surface area for each spacing (Figure 7.2). This analysis shows that conventional sampling on a regular grid requires on the order of 70 wells to reliably obtain surface-area estimates equal to or superior to those obtained from 3D ERT using 7 wells. Although specific to the NAWC-site problem characteristics and fracture-zone geometry considered here, the ERT-instrumented wells could be considered to provide 10X the information content of conventional sampling on a regular grid. These results serve to underscore the value of electrode-instrumented relative to conventional wells. Assuming an incremental cost of ~36%, instrumenting wells with electrodes is highly cost effective.
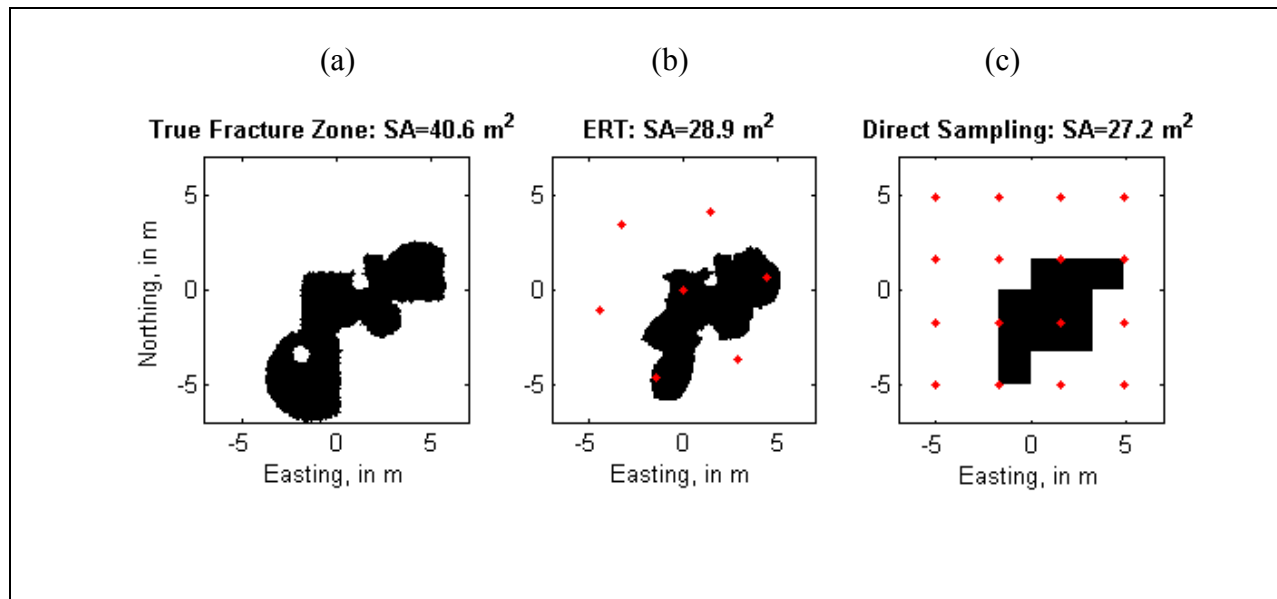
Figure 7. 1: (a) Hypothetical amendment-treated fracture zone including surface area calculation, (b) estimated amendment-treated fracture zone based on ERT between 7 boreholes, and (c) estimated amendment-treated fracture zone inferred from direct sampling at 16 wells on a regular grid.
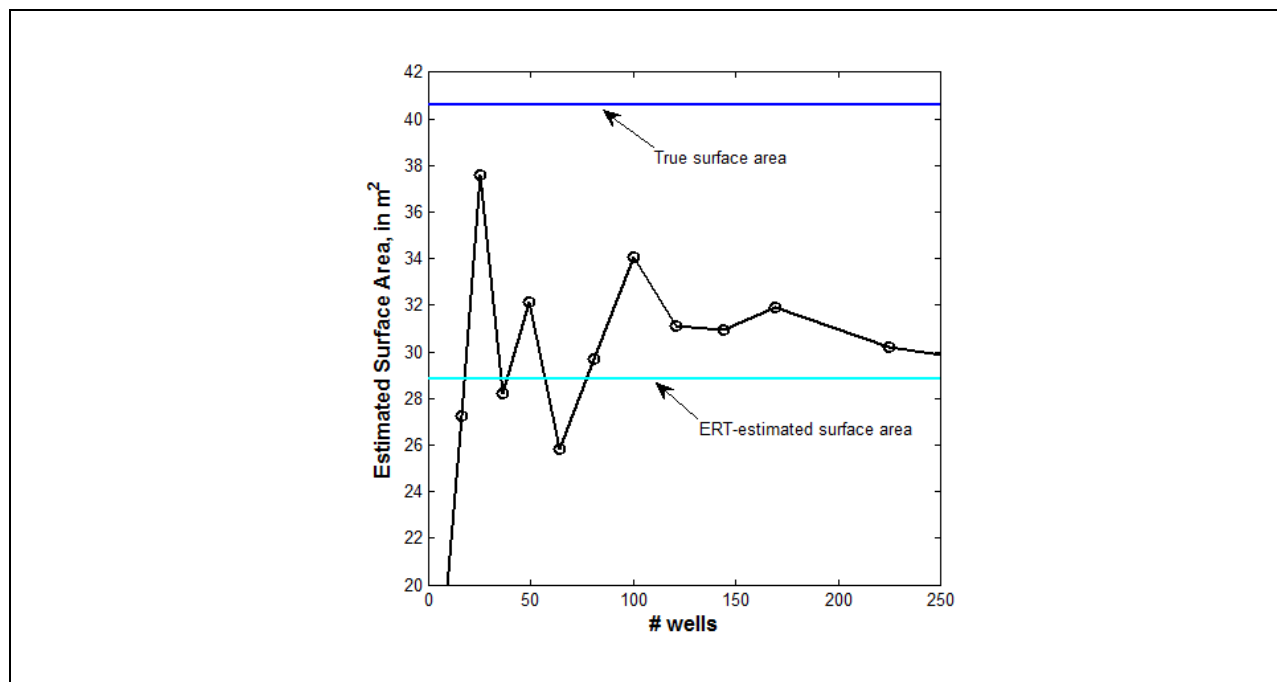
Figure 7. 2: Estimated surface area for direct sampling on a regular grid, compared to ERT-estimated surface area for 7 wells, and true surface area. Conventional sampling on a regular grid requires 70+ wells to reliably perform better than ERT with 70 wells.

8.0   IMPLEMENTATION ISSUES

REGULATORY ISSUES

Most of the technologies explored in the FRGT are not subject to any specific regulations beyond what is typical for working in boreholes at contaminated sites and acquiring samples (i.e. 40 hour HAZWOPER training). Unlike older neutron probes for porosity measurements, the nuclear magnetic resonance borehole tool does not involve an active neutron source, and no specific regulations apply to this tool.

Some states regulate the length of open holes to prevent cross contamination between multiple fractures or aquifers connected to the borehole. This demonstration required open hole intervals in excess of 55 ft. State of New Jersey permitting restricts open hole intervals to 25 ft. We requested a deviation from the state Department of Environmental Protection, and the deviation was readily obtained for this project given the nature of the site and the research program. However, such deviations may prove problematic at some sites. Regulations on open holes vary from state to state.

Metal borehole casings would prevent the effective use of most geophysical techniques included in the FRGT, although some of the tools in the FRGT can operate effectively though PVC casing. For example, borehole GPR data can be effectively acquired in PVC cased holes, and some geophysical logging tools based on the principles of EM induction can be used to obtain borehole resistivity profiles in PVC-cased holes. However, ERT and IP methods used extensively in this demonstration cannot be run in PVC cased holes. The exception is when the PVC casing is slotted screen (as used in groundwater supply wells or piezometers), as the slots permit electrical contact with the formation.

We note that technology developed in the course of this research—electrode/sampling/packer arrays—help to address the open-hole regulatory implementation issue, as we can hydraulically isolate fractures while enabling tracer experiments and electrical monitoring.

END-USER CONCERNS

From our tech transfer efforts the primary concerns expressed by remediation professionals have largely focused on the complexity of the technology and the limited exposure of the professional community to the concepts of geophysical imaging. Decision making factors regarding whether to utilize the technology mainly evolved around cost and associated benefit with respect to achieving monitoring and remediation targets.

The project involved a substantial technology transfer effort where end-user reservations were specifically addressed through lectures, field demonstrations and hands-on Q&A sessions with individuals. In total, our tech-transfer courses directly engaged 230 remediation professionals and regulators. Feedback on the courses has been overwhelmingly positive. Evaluations obtained

from the short courses were generally very good to excellent (see Appendix * for a list of summary evaluations) and the field demonstrations were very popular. Numerous potential end users commented that the field demonstrations were critical to helping them understand the concepts behind the FRGT techniques and the relevance of the approach to their own field sites. The three short courses offered on this project are summarized below:

A Short Course in Contaminated Fractured Rock Hydrogeology and Geophysics, 04/30/2013: this course was offered for 8 hours of continuing education credits to licensed remediation professionals in NJ and PA. The course was hosted by American Institute of Professional Geologists (AIGPG) – Northeastern Section (licensing organization). The course was run at College of New Jersey (Trenton) with field demonstrations at the Naval Air Warfare Center (NAWC) project site. This short course was attended by 80 remediation professionals who spent an afternoon learning about the challenges of contaminated fractured-rock characterization at the NAWC site. The course covered challenges in the characterization/monitoring of fractured rock aquifers, borehole geophysical logging methods, focused packer testing, cross-borehole geophysical methods and flow meter surveys. It also included a detailed site tour given by project senior personnel Pierre Lacombe (USGS, NJ).

A Short Course in Contaminated Fractured Rock Hydrogeology and Geophysics 11/19/2013-11/20/2013: This course was held at U. Connecticut and utilized demonstration wells available at the USGS office in Storrs, CT for the field demonstrations. Co-PI Day-Lewis led this effort that was offered to environmental professionals through the Environmental Professionals Organization of Connecticut (EPOC) for eight Continuing Education Course (CEC) technical credits. Due to the significant field component, this one day course was taught two days in a row, November 19-20, with approximately 50 environmental professionals attending this course each day. Feedback on the course was overwhelmingly positive, with numerous attendees praising the field demonstrations and the hands-on element of the short course.

Contaminated Fractured Rock Hydrogeology and Geophysics, 03/21/14: Offered through the Licensed Site Professionals Association (LSPA) of Massachusetts for continuing education credit, the course was the third conducted under the auspices of the ESTCP grant. Instructors included organizers co-PI Day-Lewis and PI Slater, and instructors from USGS, Rutgers, and Tufts University, where the course was run. The course involved lectures and demonstrations of geophysical and hydrologic field techniques. Students included 50 licensed professionals from the northeastern US.

The team has also strived to take advantage of tech transfer activities via social media as promoted by ESTCP officials. For example, the team compiled a webpage announcement on the successful demonstration of ERT for monitoring an amendment treatment into a contaminated fracture zone at the NAWC site. This announcement is available at http://www.ncas.rutgers.edu/geophysical-tomography-visualizes-amendment-delivery-and-transport-fractured-rock. With the assistance of Marvin Unger and Carmen Lebron, this link was posted to numerous social media sites relevant to remediation professionals and regulators. This includes the following LinkedIn groups: Bioremediation; Contaminant Transport in Fractured Bedrock; Environmental Assessment Association; Environmental In Situ Remediation Specialists; Groundwater Remediation Search/Destroy Methodologies; In Situ GW Remediation Technologies; Fractured Bedrock; The DNAPL Forum. It was also posted to the Environmental

Restoration Program, SERDP & ESTCP pages on Facebook page; Google+ and Twitter (again with the help of Marvin Unger).

The team found that dedicated tech transfer efforts will be critical to overcoming the resistance of the end user community to adopting the FRGT approach at contaminated sites. Most remediation professionals come from an environmental engineering or chemistry background, and thus have limited exposure to geophysics concepts, which are heavily used in exploration (petroleum and mining). Although social media and webinars can play an important role, experience gained under this project suggests that field demonstrations are important to allow the end user to recognize how these techniques work and over what scales they can be used for site characterization and monitoring. End users will need to be educated on key elements required to conduct meaningful ERT imaging in fractured rock, including; [1] acquiring accurate borehole deviation logs and including them in the modeling; [2] fully 3D data acquisition and inversion; [3] using borehole specific conductance data to constrain the borehole modeling.

PROCUREMENT ISSUES

Data acquisition systems used in this project are standard commercial off-the-shelf [COTS] purchases. For example, all the ERT datasets were acquired with an Iris Sycal Pro receiver that was purchased in 2003. This instrument is still sold with only minor modifications over the last ten years.

Procurements issues rendered some proposed components of the FRGT impractical. Most significantly, the SP monitoring and inversion was abandoned due to two factors:

[1] SP electrodes: Accurate SP measurements require the construction or purchase of high quality non-polarizing electrodes. Such electrodes are relatively straightforward to purchase or construct for surface applications. However, waterproof non polarizing electrodes designed to work at the hydrostatic pressures associated with the investigation depths at NAWC (and other demonstration sites considered) are not readily available and challenging to construct. We located one vendor (Geonesis, France) but the waterproof electrodes were approximately $200 each and not guaranteed to work at the +50 ft of hydrostatic pressure at NAWC. Furthermore, the ERT deployment involved 144 electrodes and a similar array configuration for the SP monitoring was planned; the procurement cost of $29k on electrodes alone was not in the budget for the project and was not considered worth the investment given the uncertainty regarding whether the electrodes would perform at the planned depths. We experimented with constructing our own waterproof SP electrodes in the laboratory but with limited success. A second issue was how to incorporate the SP electrodes on the integrated packer-electrode-water sampling arrays constructed for the ERT monitoring. It was not clear how this could be done without sacrificing the effectiveness of the ERT data acquired during the project. When coupled to the uncertain value of the SP component of the FRGT (being one of the least developed methods), abandoning the SP measurements was considered the most appropriate course of action so that we could focus our efforts on the other components of the FRGT that are closer to implementation by end users.

ERT data analysis codes are increasingly available through appropriate licensing agreements [commercial versus academic]. This demonstration supported the development and licensing of the ERT code that was used for all the image analysis. With partial support provided from this project, co-PI Tim Johnson developed his ERT code E4D (https://e4d.pnnl.gov/Pages/Home.aspx) for public use with no licensing restriction. Commercial codes also now exist, for example ERT Lab produced by MPT Technologies (http://www.mpt3d.com/software.html). However, commercial codes may be limited in terms of the complexity of the problem (number of electrodes, number of data) they can handle. One consideration for large imaging problems as demonstrated in this project is available computing power. The large finite element models used to predict theoretical measurements based on assumed resistivity structures require large amounts of memory and processing power. For example, each 3D image of the resistivity structure at NAWC took 55 minutes to create using 144 processors on the PNNL high performance computing cluster available to this demonstration project.

In-borehole instrumentation was based on a custom-built prototype developed specifically for this demonstration. It included a novel first-of-a-kind integration of electrodes, packers for isolating sections of boreholes and water sampling ports for assessment. No COTS equivalent for this assembly currently exists. However, it is possible to purchase COTS electrode arrays for down-borehole applications (e.g. MPT Technologies offers such arrays) but these will not include any infrastructure for isolating sections of a borehole or for groundwater sampling. This currently represents the largest procurement issue preventing end users from adapting the ERT component of the FRGT that was the focus of this specific demonstration.

9.0 REFERENCES

Labrecque, D., & Yang, X. (2001). Difference Inversion of ERT Data : a Fast Inversion Method for 3-D In Situ Monitoring. Journal of Environmental and Engineering Geophysics, 6(2), 83–89

Aal, G. Z. A., Slater, L. D., & Atekwana, E. A. (2006). Induced-polarization measurements on unconsolidated sediments from a site of active hydrocarbon biodegradation. Geophysics, 71(2), H13-H24.

Arns, C., 2004, A comparison of pore size distributions derived by NMR and X-ray-CT techniques, Physica A, 339(1-2), 159-165.

Backus, G., & Gilbert, F. (1968). The Resolving Power of Gross Earth Data. Geophysical Journal International, 16(2), 169–205. doi:10.1111/j.1365-246X.1968.tb00216.x

Berner, R. A. (1963). Electrode studies of hydrogen sulfide in marine sediments. Geochimica et Cosmochimica Acta, 27(6), 563-575.

Binley, A., & Kemna, A. (2005). DC resistivity and induced polarization methods. In Hydrogeophysics (pp. 129-156). Springer Netherlands.

Blome, M., Maurer, H. R., & Schmidt, K. (2009). Advances in three-dimensional geoelectric forward solver techniques. Geophysical Journal International, 176(3), 740–752. doi:10.1111/j.1365-246X.2008.04006.x

Blome, M., Maurer, H., & Greenhalgh, S. (2011). Geoelectric experimental design — Efficient acquisition and exploitation of complete pole-bipole data sets. Geophysics, 76(1), F15–F26. doi:10.1190/1.3511350

Coates, G. R., D. Marschall, D. Mardon, and J. Galford, 1997, A New Characterization of Bulk-Volume Irreducible Using Magnetic Resonance, SPWLA 38th Annual Logging Symposium, 2-14

Coscia, I., Greenhalgh, S. A., Linde, N., Doetsch, J., Marescot, L., Gu, T., … Green, A. G. (2011). 3D crosshole ERT for aquifer characterization and monitoring of infiltrating river water. Geophysics, 76(2), G49–G59

Day-Lewis, F. D., Lane, J. W., Harris, J. M., & Gorelick, S. M. (2003). Time-lapse imaging of saline-tracer transport in fractured rock using difference-attenuation radar tomography. Water Resources Research, 39(10).

deGroot-Hedlin, C., & Constable, S. (1990). Occam's inversion to generate smooth, two-dimensional models from magnetotelluric data. Geophysics, 55(12), 1613–1624. doi:10.1190/1.1442813

Doetsch, J. a., Coscia, I., Greenhalgh, S., Linde, N., Green, A., & Günther, T. (2010). The borehole-fluid effect in electrical resistivity imaging. Geophysics, 75(4), F107–F114. doi:10.1190/1.3467824

Ellefsen, K. J., Burton, W. C., & Lacombe, P. J. (2012). Integrated characterization of the geologic framework of a contaminated site in West Trenton, New Jersey. Journal of Applied Geophysics, 79, 71-81.

Farquharson, C. G. (2008a). Constructing piecewise-constant models in multidimensional minimum-structure inversions. Geophysics, 73(1), K1–K9

Goode, D. J., Imbrigiotta, T. E., & Lacombe, P. J. (2014). High-resolution delineation of chlorinated volatile organic compounds in a dipping, fractured mudstone: Depth- and strata-dependent spatial variability from rock-core sampling. Journal of Contaminant Hydrology. doi:10.1016/j.jconhyd.2014.10.005

Gregoire, C.; Joesten, P. K.; Lane, J. W., Use of borehole radar reflection logging to monitor steam-enhanced remediation in fractured limestone - results of numerical modelling and a field experiment. Journal of Applied Geophysics 2006, 60, (1), 41-54.

Johnson, T. C., Versteeg, R. J., Day-Lewis, F. D., Major, W. and Lane, J. W., 2014, Time-Lapse Electrical Geophysical Monitoring of Amendment-Based Biostimulation. Groundwater. doi: 10.1111/gwat.12291.

Johnson, T. C., Versteeg, R. J., Ward, A., Day-Lewis, F. D., & Revil, A. (2010). Improved hydrogeophysical characterization and monitoring through parallel modeling and inversion of time-domain resistivity andinduced-polarization data. Geophysics, 75(4), WA27-WA41.

Kleinberg, R. L., Sezinger, A, Griffin, D.D. and M. Fukuhara, 1992, Novel NMR apparatus for investigating an external sample, Journal of Magnetic Resonance, 97, 466–485

Koestel, J., Kemna, A., Javaux, M., Binley, A., & Vereecken, H. (2008). Quantitative imaging of solute transport in an unsaturated and undisturbed soil monolith with 3-D ERT and TDR. Water Resources Research, 44(12), n/a–n/a. doi:10.1029/2007WR006755

LaBrecque, D. J., Miletto, M., Daily, W., Ramirez, A., & Owen, E. (1996). The effects of noise on Occam's inversion of resistivity tomography data. Geophysics, 61(2), 538–548. doi:10.1190/1.1443980

Lacombe, P. J., & Burton, W. C. (2010). Hydrogeologic Framework of Fractured Sedimentary Rock , Newark Basin , New Jersey, (2), 35–45. doi:10.1111/j1745

Lane, J. W. J.; Joesten, P. K.; Haeni, F. P.; Vendl, M.; Yeskis, D. In *Use of borehole-radar methods to monitor the movement of a saline tracer in carbonate rock at Belvidere, Illinois*, Symposium on the Application of Geophysics to Engineering and Environmental Problems, Chicago, IL, 1998; Environmental and Engineering Geophysical Society: Chicago, IL, 1998; pp 323-332.

Lane, J. W., Jr.; Haeni, F. P.; Versteeg, R. In *Use of multi-offset borehole-radar reflection method in fractured crystalline bedrock at Mirror Lake, Grafton County, New Hampshire*, Symposium on the Application of Geophysics to Engineering and Environmental Problems, Chicago, IL, 1998; Chicago, IL, 1998; pp 359-368.

Last, B. J., & Kubik, K. (1983). Compact gravity inversion. Geophysics, 48(6), 713–721. doi:10.1190/1.1441501

Loke, M. H., Wilkinson, P. B., & Chambers, J. E. (2010). Fast computation of optimized electrode arrays for 2D resistivity surveys. Computers & Geosciences, 36(11), 1414–1426. doi:10.1016/j.cageo.2010.03.016

Lowry, T., Allen, M. B., & Shive, P. N. (1989). Singularity removal: A refinement of resistivity modeling techniques. Geophysics, 54(6), 766–774. doi:10.1190/1.1442704

Minsley, B. J.; Sogade, J.; Morgan, F. D., Three-dimensional source inversion of self-potential data. Journal of Geophysical Research-Solid Earth 2007, 112, (B2).

Naudet, V.; Revil, A.; Rizzo, E.; Bottero, J. Y.; Begassat, P., Groundwater redox conditions and conductivity in a contaminant plume from geoelectrical investigations. Hydrology and Earth System Sciences 2004, 8, (1), 8-22.

Niva, B.; Olsson, O.; Blumlung, P. Grimsel test site: Radar crosshole tomography with application to migration of saline tracer through frature zones; Swedish Geological Co.: Uppsala, Sweden, 1988.

Olsson, O.; Falk, L.; Forslund, O.; Lundmark, L.; Sandberg, E., Borehole Radar applied to the Characterization of Hydraulically Conductive Fracture-Zones in Crystalline Rock. *Geophysical Prospecting* **1992,** *40*, (2), 109-142.

Paillet, F. L., Flow modeling and permeability estimation using borehole flow logs in heterogeneous fractured formations. Water Resour. Res. 1998, 34, (5), 997-1010.

Robinson, J., Johnson, T., & Slater, L. (2013). Evaluation of known-boundary and resistivity constraints for improving cross-borehole DC electrical resistivity imaging of discrete fractures. Geophysics, 78(3), D115–D127.

Robinson, J., Johnson, T., & Slater, L. (2015). Challenges and opportunities for fractured rock imaging using 3D cross-borehole electrical resistivity. Geophysics, 80(2), E49-E61.

Roubinet, D., Irving, J., and Day-Lewis, F.D., 2015, Development of a new semi-analytical model for cross-borehole flow experiments in fractured rock, Adv. In Water Resources, doi:10.1016/j.advwatres.2014.12.002.

Rücker, C., Günther, T., & Spitzer, K. (2006). Three-dimensional modelling and inversion of dc resistivity data incorporating topography - I. Modelling. Geophysical Journal International, 166(2), 495–505. doi:10.1111/j.1365-246X.2006.03010.x

Sasaki, Y. (1994). 3-D resistivity inversion using the finite-element method. Geophysics, 59(11), 1839–1848

Slater, L. D.; Binley, A.; Brown, D., Electrical imaging of fractures using ground-water salinity change. *Ground Water* **1997,** *35*, (3), 436-442.

Slater, L., Binley, a. ., Daily, W., & Johnson, R. (2000). Cross-hole electrical imaging of a controlled saline tracer injection. Journal of Applied Geophysics, 44(2-3), 85–102. doi:10.1016/S0926-9851(00)00002-1

Slater, L., Near Surface Electrical Characterization of Hydraulic Conductivity: From Petrophysical Properties to Aquifer Geometries—A Review. Surveys in Geophysics 2007, 28, (2), 169-197

Slater, L.; Ntarlagiannis, D.; Yee, N.; O'Brien, M.; Zhang, C.; Williams, K. H., Electrodic Voltages In The Presence Of Sulfide: Implications For (1) Monitoring Natural Microbial Activity, And (2) Sp Electrode Performance. Geophysics 2008, 73, (2), F65-F70.

Stumm, F.; Chu, A.; Lange, A. D.; Paillet, F. L.; Williams, J. H.; Lane, J. W., Jr. Use of advanced borehole geophysical techniques to delineate fractured-rock ground-water flow and fractures along water-tunnel facilities in Northern Queens County, New York; 00-4276; USGS: 2001; p 12.

Stummer, P., Maurer, H., & Green, A. G. (2004). Experimental design: Electrical resistivity data sets that provide optimum subsurface information. Geophysics, 69(1), 120–139. doi:10.1190/1.1649381

Sugimoto, Y. (1999) Electrical crosshole imaging. The Leading Edge, (December), 1425–1428

Tiedeman, C. R., Lacombe, P. J., & Goode, D. J. (2010). Multiple well-shutdown tests and site-scale flow simulation in fractured rocks. Ground Water, 48(3), 401–15. doi:10.1111/j.1745-6584.2009.00651.x

Walsh, D., E. Grunewald, P. Turner, and I. Frid, 2010, Javelin: A Slimhole and Microhole NMR Logging Tool, Fast times, 15(3), 67-72.

Weller, A., Slater, L., Nordsiek, S., & Ntarlagiannis, D. (2010). On the estimation of specific surface per unit pore volume from induced polarization: A robust empirical relation fits multiple data sets. Geophysics, 75(4), WA105-WA112.

Wilkinson, P. B., Chambers, J. E., Lelliott, M., Wealthall, G. P., & Ogilvy, R. D. (2008). Extreme sensitivity of crosshole electrical resistivity tomography measurements to geometric errors. Geophysical Journal International, 173(1), 49–62. doi:10.1111/j.1365-246X.2008.03725.x

Wilkinson, P. B., Loke, M. H., Meldrum, P. I., Chambers, J. E., Kuras, O., Gunn, D. a., & Ogilvy, R. D. (2012). Practical aspects of applied optimized survey design for electrical resistivity tomography. Geophysical Journal International, 189(1), 428–440. doi:10.1111/j.1365-246X.2012.05372.x

Wilkinson, P. B., Meldrum, P. I., Chambers, J. E., Kuras, O., & Ogilvy, R. D. (2006a). Improved strategies for the automatic selection of optimized sets of electrical resistivity tomography measurement configurations. Geophysical Journal International, 167(3), 1119–1126. doi:10.1111/j.1365-246X.2006.03196.x

Wright, D. L.; Jr., L. J. W. In *Mapping hydraulically permeable fractures using directional borehole radar and hole-to-hole tomography with a saline tracer*, Symposium on the

Application of Geophysics to Engineering and Environmental Problems, Chicago, IL, 1998; Environmental and Engineering Geophysical Society: Chicago, IL, 1998; pp 379-388.

Zhang, J. (1995). 3-D resistivity forward modeling and inversion using conjugate gradients. Geophysics, 60(5), 1313. doi:10.1190/1.1443868

APPENDICES

APPENDIX A: POINTS OF CONTACT

POINT OF CONTACT Name	ORGANIZATION Name Address	Phone Fax E-mail	Role in Project
Lee D. Slater	Department of Earth & Environmental Sciences Rutgers-Newark 101 Warren St, Smith 136 Newark, NJ 07102	Tel: 973-353-5109 Fax: 973-353-1965 lslater@rutgers.edu	Principal Investigator
Fred Day-Lewis	U.S. Geological Survey, Office of Groundwater, Branch of Geophysics 11 Sherman Place, Unit 5015 Storrs CT 06269	Tel: 860-487-7402 x21 Fax: 860.487.8802 daylewis@usgs.gov	Co-Principal Investigator
Timothy Johnson	Energy and Environment Directorate Pacific Northwest National Laboratory 902 Battelle Boulevard P.O. Box 999, MSIN K9-33 Richland, WA 99352	Tel: 509-372-4715 Fax: 509-372-6089 tj@pnl.gov	Co-Principal Investigator
Allen Shapiro	U.S. Geological Survey National Research Program 12201 Sunrise Valley Drive Mail Stop 431 Reston, VA 20192 USA	Tel: 703-648-5884 Fax: 703-648-5274 ashapiro@usgs.gov	Co-Principal Investigator
John W. Lane	U.S. Geological Survey, Office of Groundwater, Branch of Geophysics 11 Sherman Place, Unit 5015 Storrs CT 06269	Tel: 860-487-7402 x13 Fax: 860.487.8802 jwlane@usgs.gov	Co-Principal Investigator

APPENDIX B: NAWC BOREHOLE GEOPHYSICAL LOGS

83BR: Borehole deviation
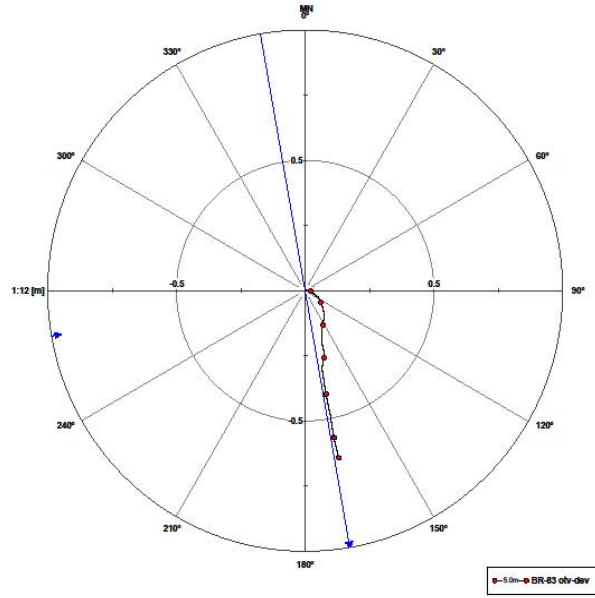
84BR
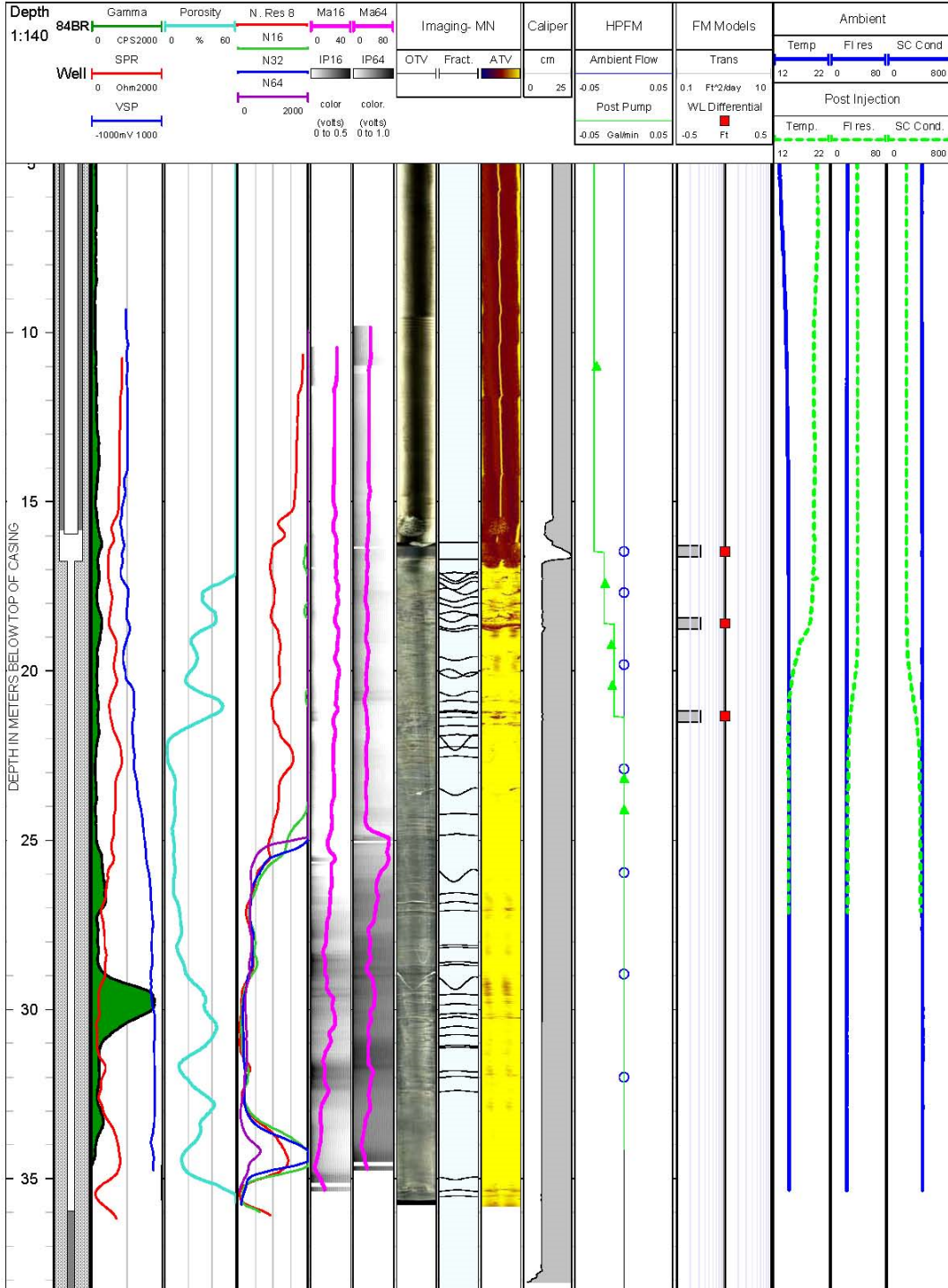
**84 interpretive notes: There are several small diameter fractures at depths less than 23 m which have flow gradients only under stressed conditions. A unit at 30 m depth contains finer grains according to the gamma log. The most prominent feature in the ATV, OTV and caliper logs is below the BOC and appear to be measuring amplitudes in the annular space.**
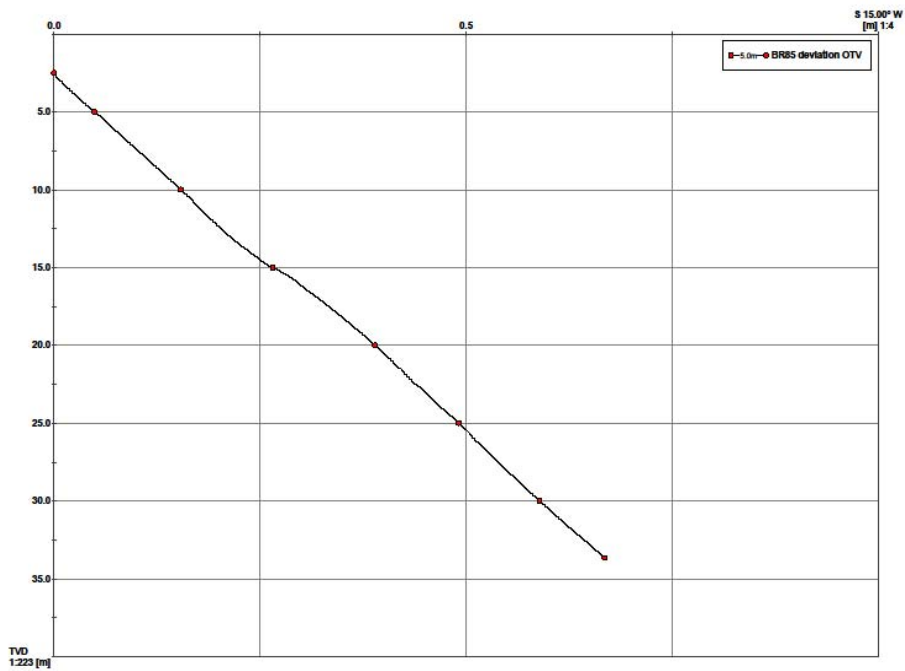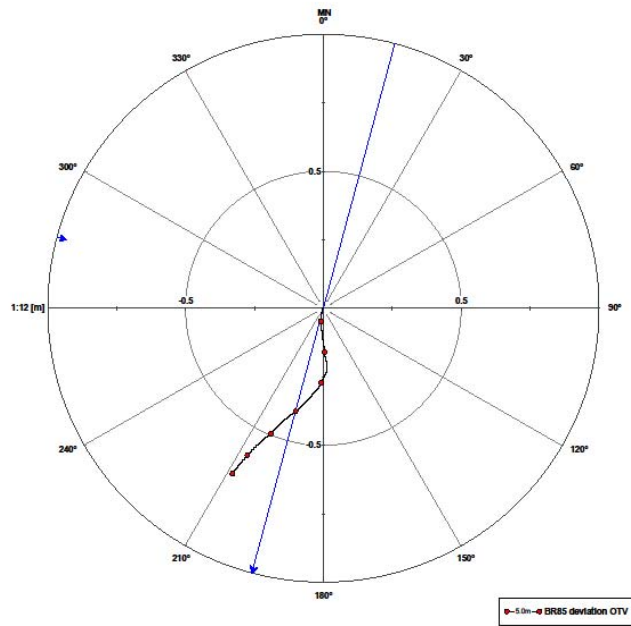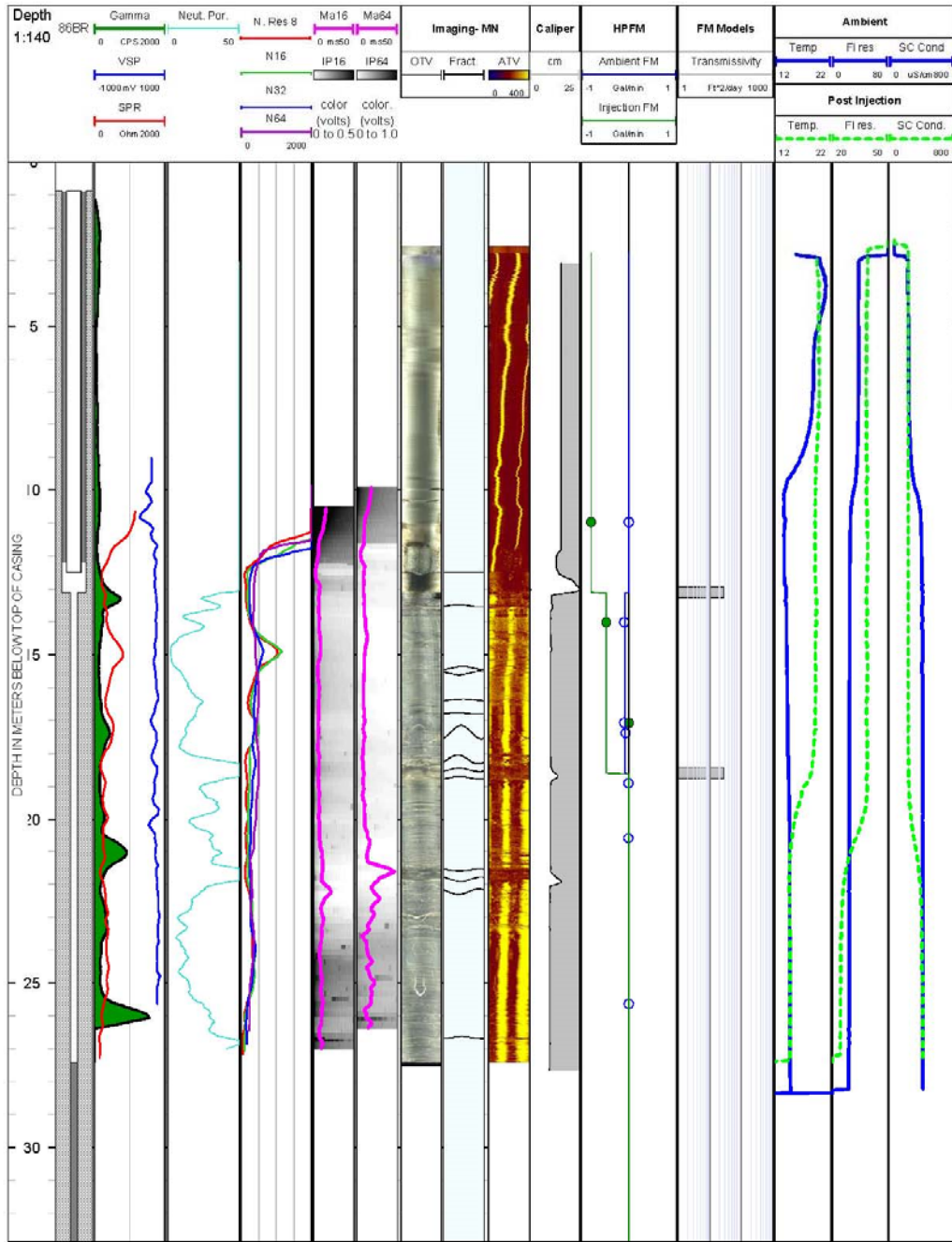
84BR: Borehole deviation
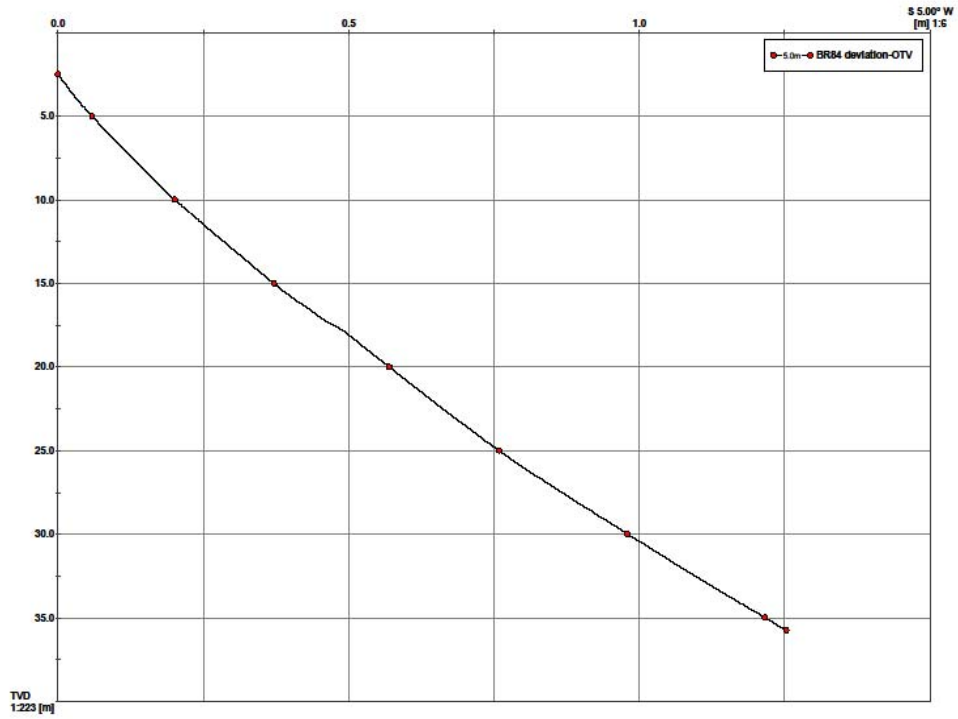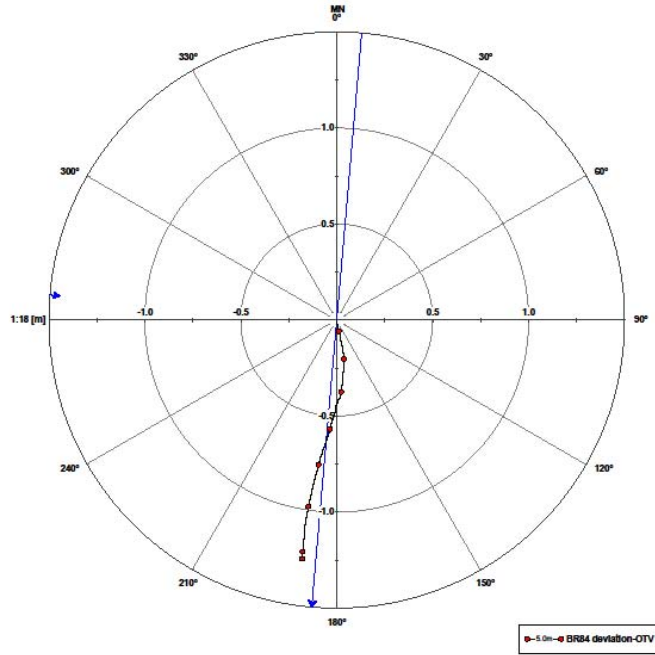
85BR
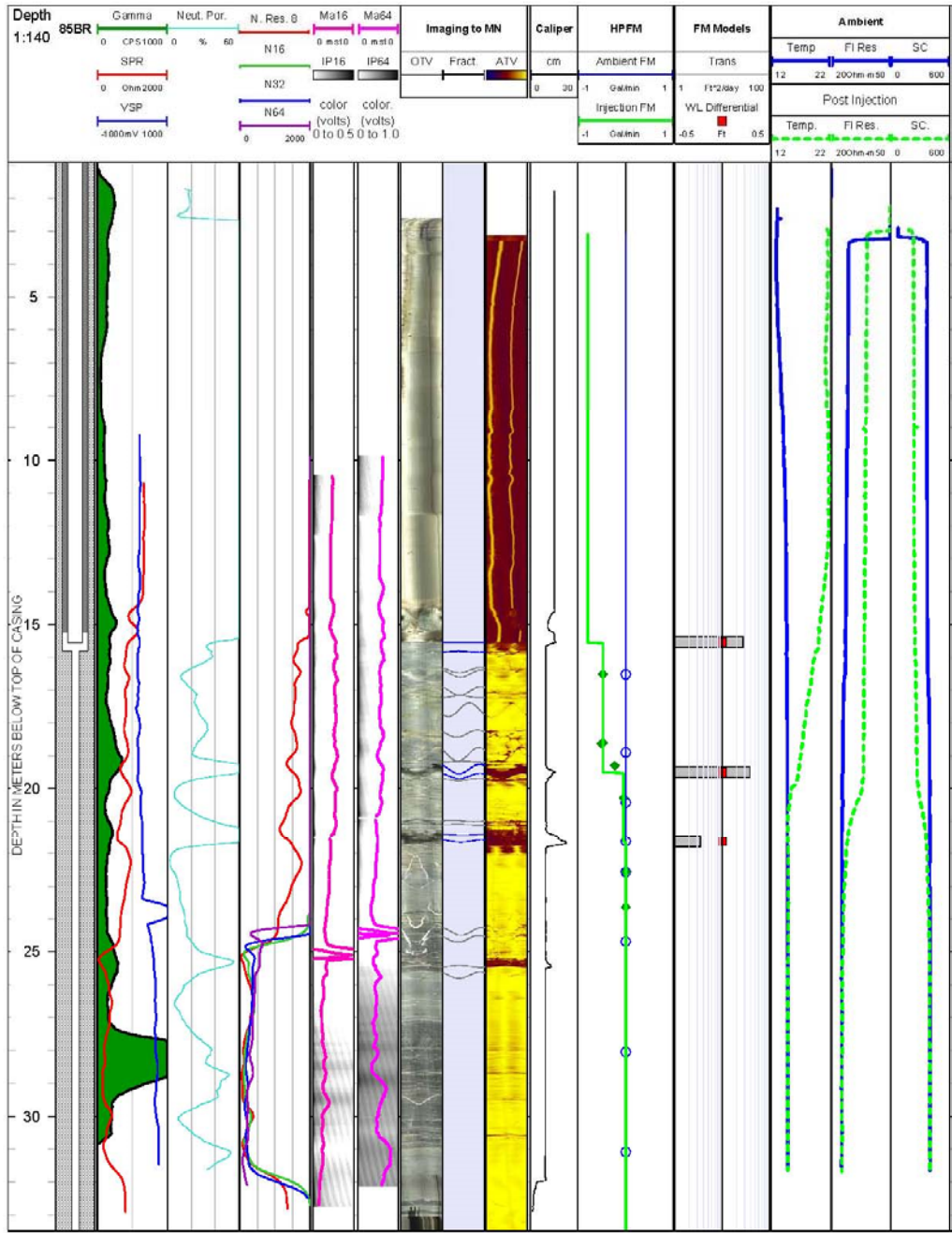
85 interpretive notes: There are fractures at depths of 19, 21 and 25 m. There is no flow under ambient conditions but under stressed conditions, the fracture at 21 m depth has the largest flowrate. A unit at 28 m depth contains finer grains according to the gamma log. There is a feature in the ATV, OTV and caliper logs BOC. IP logs appear to be capturing a polarizing effect at 25 m depth.
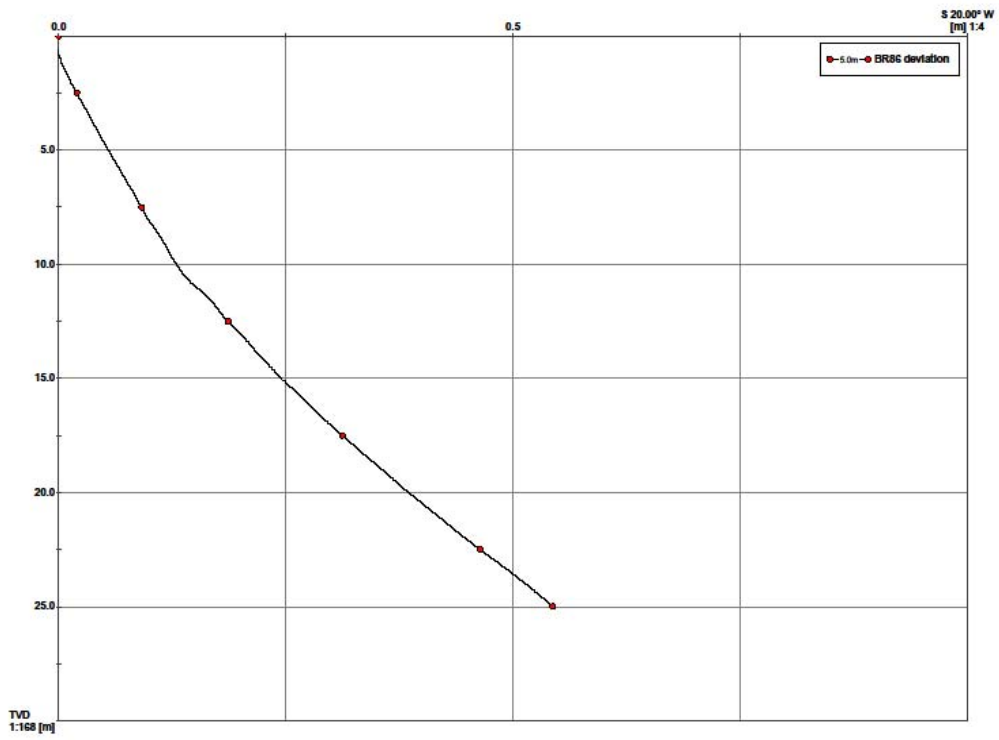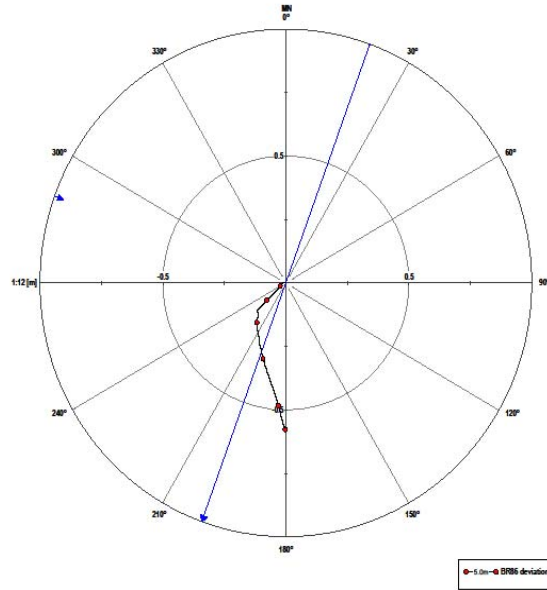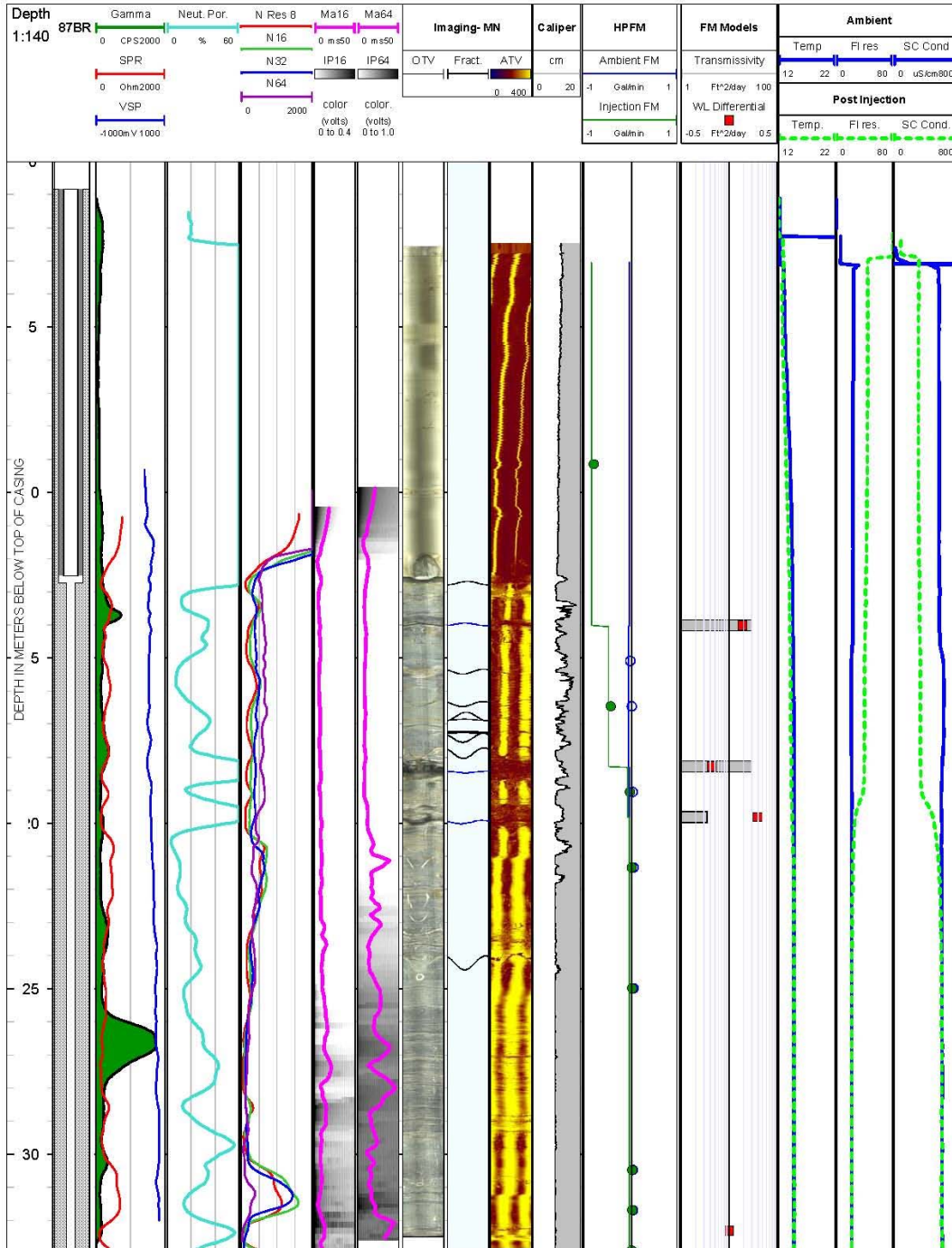
85BR: Borehole deviation

86BR

86 interpretive notes: There are fractures at depths of 18 and 22 m. There is flow under stressed conditions in the fracture at 18 m depth . A breakout feature is shown at the BOC. A unit at 26 m depth contains finer grains according to the gamma log. IP logs appear to be capturing a polarizing effect below 32 m depth.

86BR: Borehole deviation

133

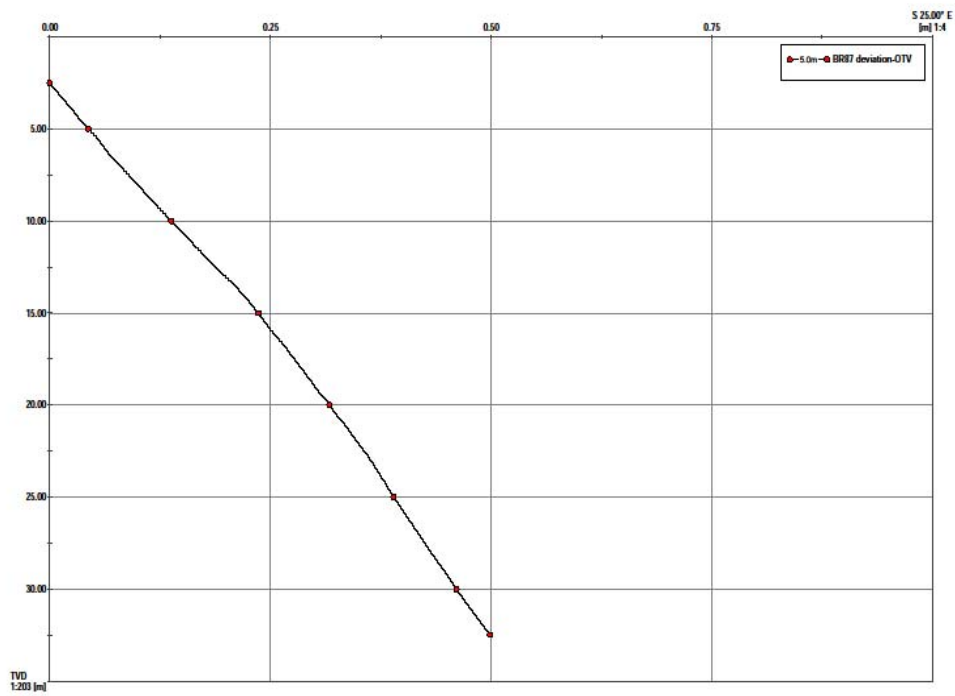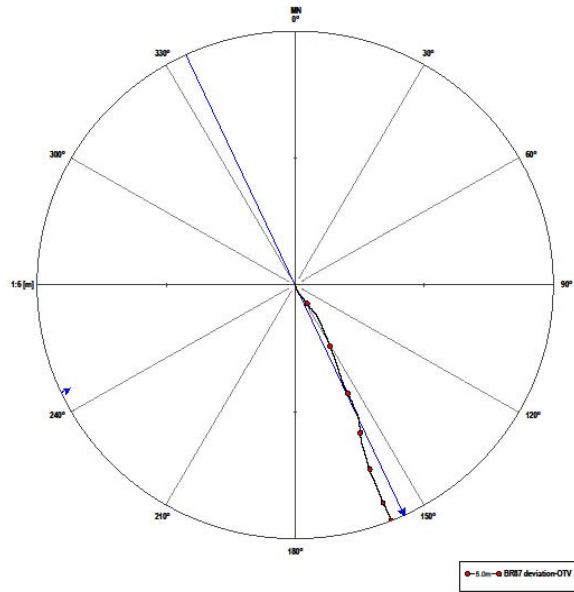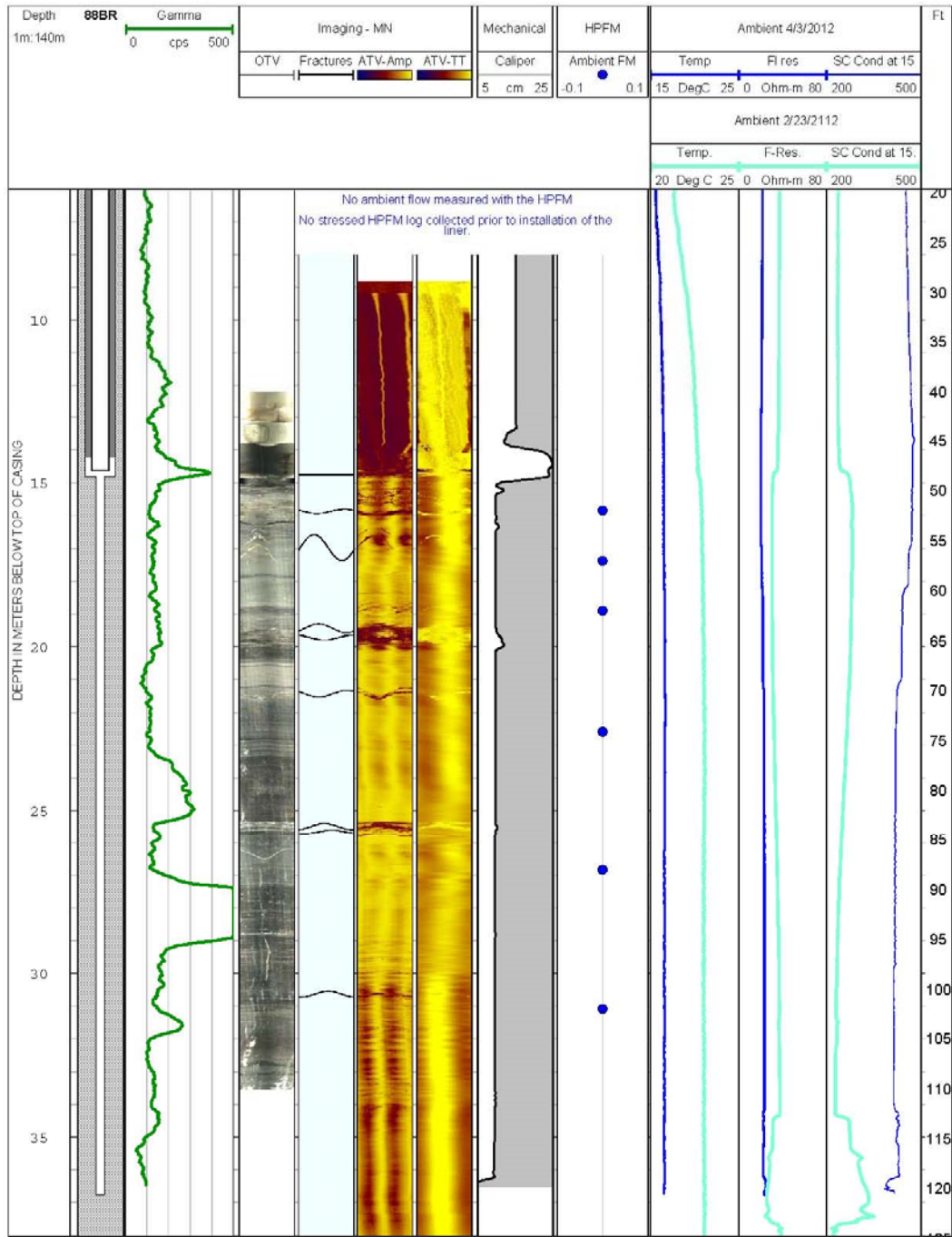## 87BR

87 interpretive notes: Caliper logs are unclear but fractures are evident at 18 and 20 m in ATV and OTV logs. There is flow under stressed conditions in the fracture at 18 m depth. A unit at 27 m depth contains finer grains according to the gamma log. IP logs appear to be capturing a polarizing effect below 21 m depth.
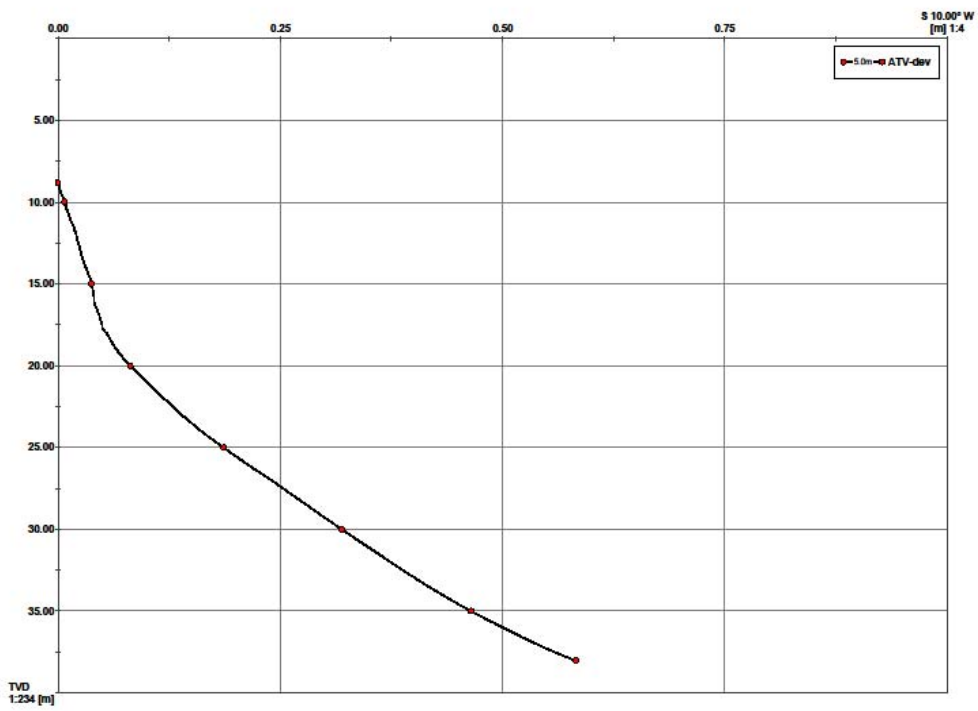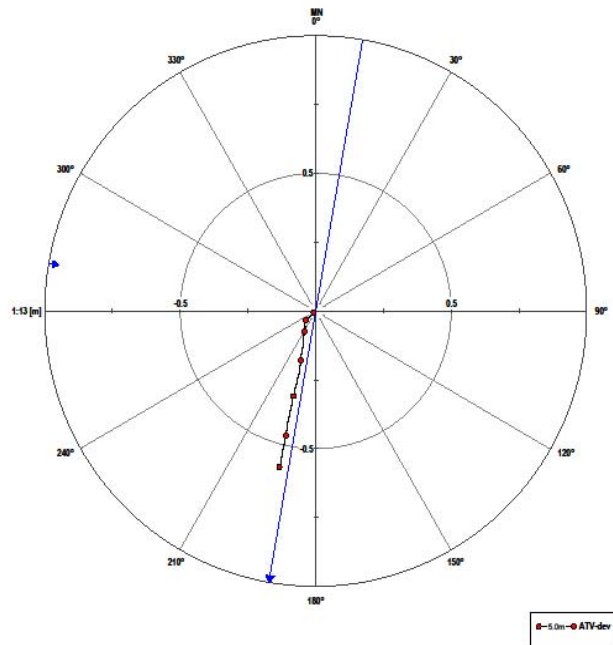
87BR: Borehole deviation

88BR

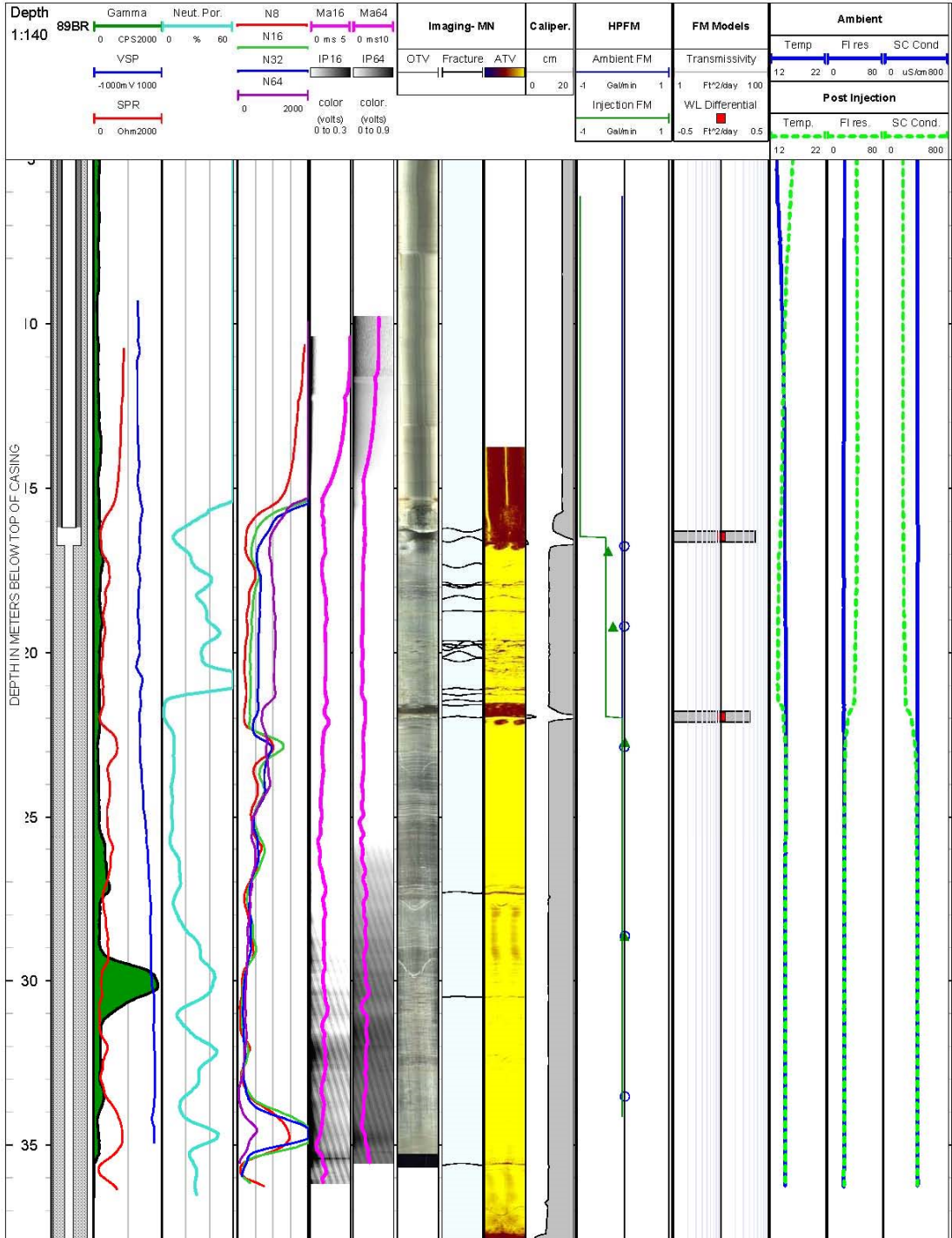**88 interpretive notes: Caliper logs are show a breakout feature at the BOC. Fractures are evident at 20 and 26 m in ATV and OTV logs. There is no flow under ambient conditions. A unit at 28 m depth contains finer grains according to the gamma log. There were a limited number of logs in this borehole due to the installation of a liner.**
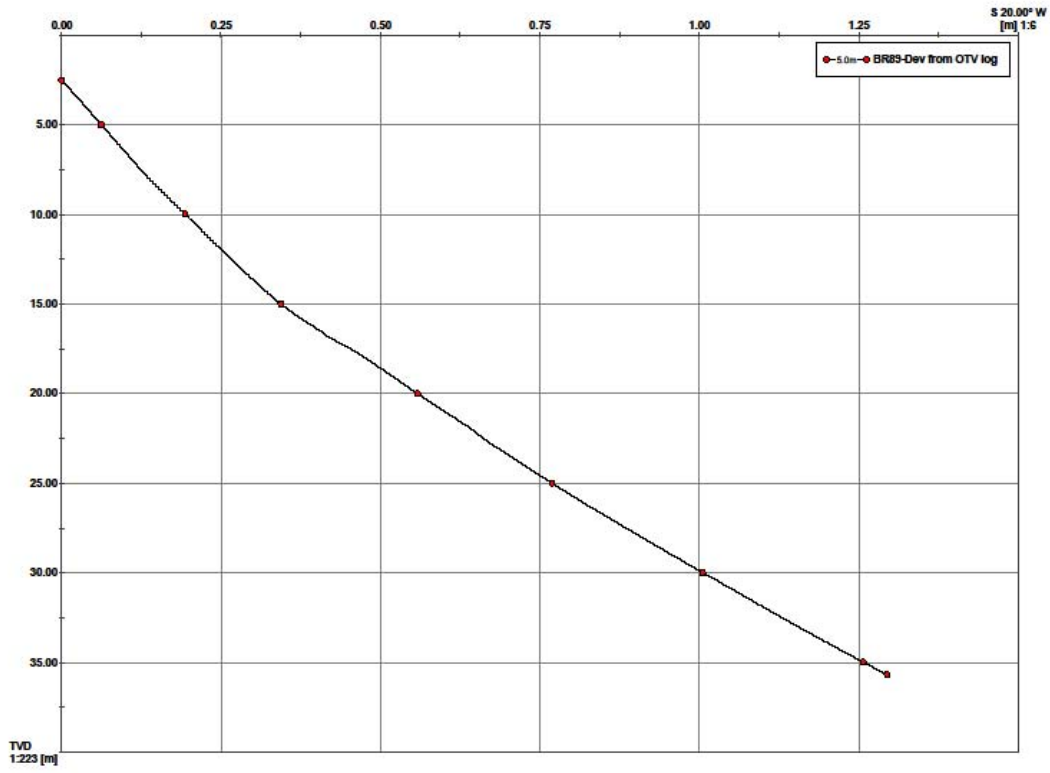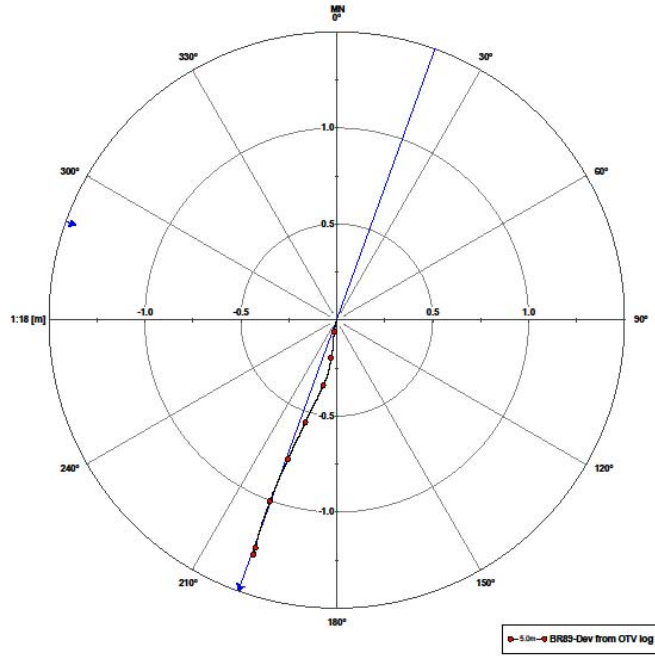
88BR: Borehole deviation

137

89BR

89 interpretive notes: Caliper logs are show a breakout feature at the BOC. Fractures are evident at 22, 27, 30 and 36 m in ATV and OTV logs. There is flow under stressed conditions in the fracture at 22 m depth. A unit at 30 m depth contains finer grains according to the gamma log.

89BR: Borehole deviation

APPENDIX C: DEMONSTRATION AT EASTLAND WOOLEN MILL (EWM) SUPERFUND SITE

C1. Site Description

The Eastland Woolen Mill (EWM) Superfund Site OU-1 is located in Corinna, ME. The site includes the former Eastland Woolen Mill and local areas contaminated by the release of hazardous substances from this textile mill, which began operation in approximately 1909, with activities ceasing in 1996. Chlorobenzenes (mono, di, tri, and tetra) have been detected in the soil, groundwater, surface water, and sediment. Site geology is controlled by the Waterville Formation, a rock unit that underlies a broad swath of central Maine. The Waterville Formation is a dark gray slate or phyllite, alternating with delicate thin layers of light gray siltstone or sandstone, and characterized by water bearing bedding plane fractures.

An array of open boreholes in the source area that were drilled for the 2002-2004 study remains accessible (Figure S-1). Six inch diameter holes were drilled from 85 to 250 feet deep into rock. Available characterization data include [1] rock matrix sampling for contaminant mass, [2] borehole logging and packer testing, and [3] heat pulse flow meter (HPFM) interference testing, [4] electrical resistivity tomography (ERT) and a forced gradient tracer study. Rock mass contamination was primarily determined from methanol extracted rock chip sampling for mono-di and trichlorobenzene (chlorobenzenes). Available borehole logs include [i] standard electric logs, [ii] caliper, [iii] temperature, [iv] acoustic televeviewer, and [v] borehole image processing system. Transmissive fractures zones of interest in this study were primarily identified from HPFM. Figure B1 is a site map showing all boreholes and denotes borehole inter-distances for wells included in this demonstration: BM-32, BM-34, BM-35 and BM-36. Three-dimensional ERT was originally planned to include boreholes BM-34, BM-04 and BM-37. However open intervals were not available for imaging using these boreholes. In addition, drilling logs indicated a depth of approximately 61 m (200 ft) in BM-35, although only approximately 32 m (107 ft) was available below the casing. For this demonstration, DBHGPR was performed in BM-32 and BM-36 and results compared to televiewer data.
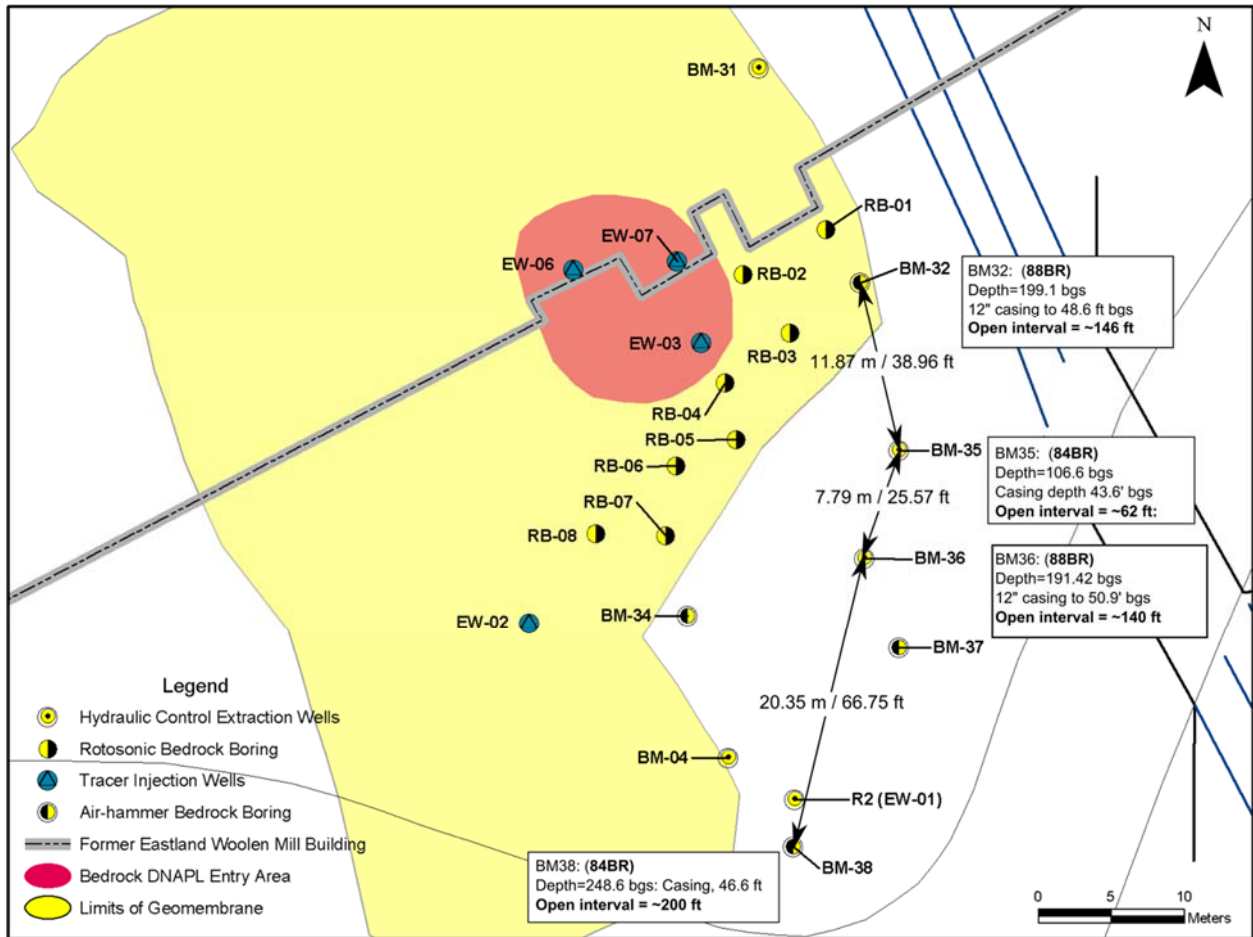
Figure C.1: Site map of the Eastland Woolen Mill Superfund Site. The boreholes available for ERT and GPR imaging were BM-32, BM-35, BM-36 and BM-38 which permitted 2D panel data only to be collected. Existing electrode arrays used at the NAWC site from boreholes 84BR and 88BR were retrofitted for ERT imaging at this field site.

C2. Methods

a) Field

Existing arrays from NAWC were retrofitted for ERT imaging at EWM. Arrays from boreholes 84BR and 89BR (refer to Figure 5.4.7) were chosen as these arrays had the most in-line electrodes (21 and 22 electrodes, respectively) and the absence of isolated intervals (i.e. with the removal of packers in these arrays) would have the least impact. Retrofitting consisted of extending electrode wiring to account for the greater depths at EWM. The inflatable rubber on each packer was also swapped for more puncture resistant bladder tubing.

Each electrode array was approximately 20 m (65 ft) in length such that it was necessary to raise and lower the array in BM32, BM36 and BM38 to collect cross borehole measurements for the entire open depths. The array in borehole BM35 remained at the same depth throughout all surveys due to the limited depth length of open hole. The ERT survey consisted of 4,664 complete (i.e. normal and reciprocal) measurements which included cross borehole and in-hole

141

electrode configurations. Three ERT surveys, corresponding to raising and lowering the array(s), were collected for each borehole pair (Figure C.1) for a total panel data acquisition of 13,992 measurements.

Single and cross-hole GPR methods were used to image the bedrock surrounding the boreholes. GPR data were acquired in 3 modes: single-hole, directional, and level-run profiling (Figure C2 and C3). The pelitic schist at the EWM site is less conductive than the formation at the NAWC site in New Jersey, and radar penetrated the resistive rock surrounding the boreholes. Single-hole 100-MHz data were collected in BM36, BM32, and BM38 to determine the direct arrival time and attenuation from which velocity, dielectric permittivity and apparent attenuation were determined. The velocity was used in the analysis of the directional radar data to determine the distance to reflectors, the radial depth of penetration, and dip of reflectors. DBHGPR data were collected using antennas with center frequency of 60-MHz in BM32 and BM36 and were interpreted for features that surround and intersect the borehole. Hole-to-hole level-run data were collected in two well pairs BM35 to BM36 and BM36 to BM38.
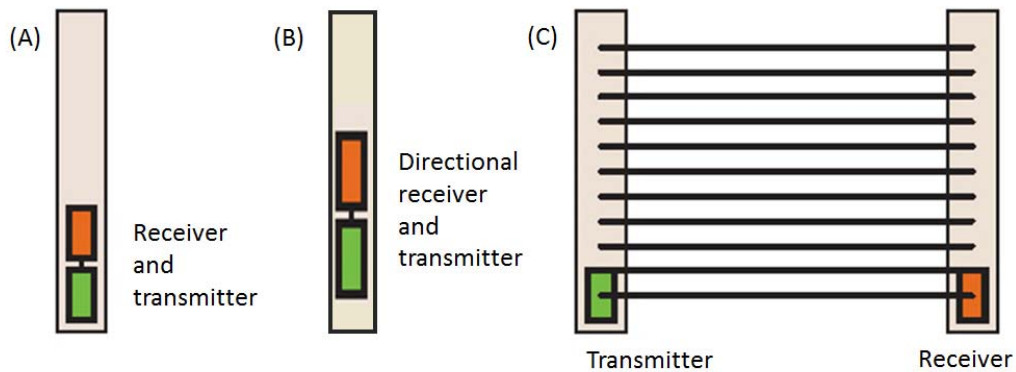

Figure C.2: Borehole GPR collection modes: (A) single-hole, (B) directional reflection, (C) level-run hole-to-hole mode.

Figure C.3: Borehole GPR collection in EWM BM38 single mode (left) and level run between BM32 and BM35 (right)

b) ERT Modeling

All available site data were incorporated into the ERT modeling to be used as constraints in the inversion regularization (refer to Sections 5.4.1 and 5.4.2 for details). Specifically, borehole deviation data were extracted from previously collected borehole logs and explicitly discretized into the FEM to allow for a sharp conductivity contrast at this boundary. ATV and OTV logs were reviewed to determine the strike and dip of the bedding plane within each borehole; this information was used as an anisotropic constraint in the formation.

c) Radar Interpretation

Single-hole vertical profiling data were used to determine the velocity and attenuation of the radar waves in the rock adjacent to the borehole. By profiling along the borehole, a two-dimensional record of EM reflection is created, with depth on the y-axis and two-way radar-wave travel time on the x-axis (Figure C4). For DBHGPR surveys, a series of two-dimensional records are created every 10 degrees from magnetic north (Figure C5). The velocity determined in the single-hole vertical profiling was used to process the directional data. DBHGPR data were processed and interpreted to identify the depth, orientation, and vertical spatial continuity of the reflectors that intersect and surround the boreholes. Circular, planar reflectors are assumed in the analysis. Borehole deviation data from previously collected image logs were used to process the hole-to-hole GPR level-run data.
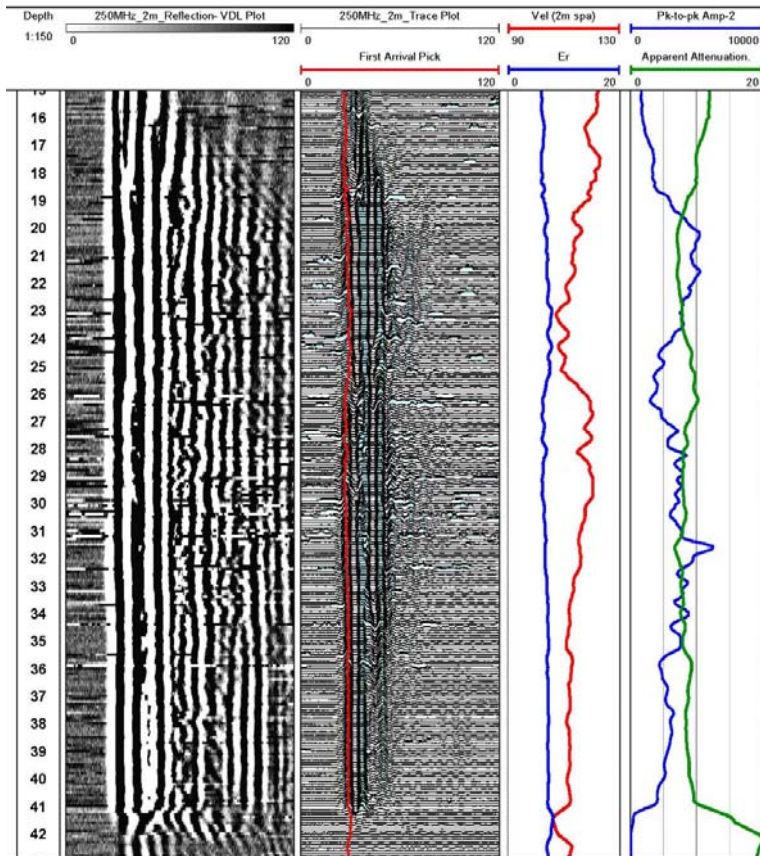

Figure C.4: Single-hole GPR reflection data from BM36 showing the radar data in two left panels and interpretation of first arrival, velocity, dielectric permittivity (Er), amplitude, and apparent attenuation.
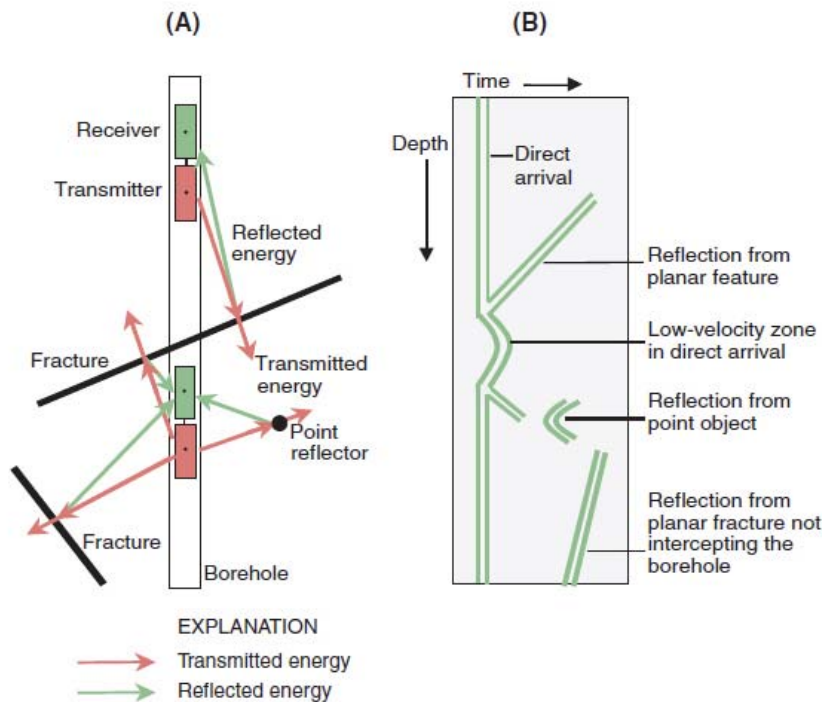
Figure C.5: Borehole GPR (A) schematic showing transmitter and receiver configuration in single-hole reflection and (B) typical reflection patterns for direct arrival, point reflectors, planar reflectors that intersect the borehole, and reflectors whose projections intersect the borehole below the drilled depth or above the land surface.

C3. Results and discussion

The retrofitted bladder tubing used for the packers on the ERT arrays held up well as no tears or abrasions were evident. However, the clamps used for an air-tight seal between the bladder tubing and the packer block failed. While we assume that the packer block assembly did somewhat promote vertical isolation at these intervals, the seal was not air-tight.

Inversion modeling reveals complex features of high and low conductivity bedding planes interconnecting these boreholes (Figure C.6). We presume that fractures are located within or along the boundaries of these contrasts. Limited fracture intersection data were available from the drillers logs and most recorded features were at depths below 50 m. In BM32 a sizeable fracture intersection matches well with a high conductivity contrasting feature at a depth of 20 m.

Static ERT images are shown here to delineate bedding plane features and orientation effectively. However, because ERT is dependent on many field variables (refer to Section 5.4.1) and fracture apertures are quite small, it would be difficult to extrapolate to dominant hydraulic pathways based on this image alone. However, this ERT characterization image could serve as a

144

starting point to map a remedial injection into this formation and be used to choose isolation zones within each borehole.
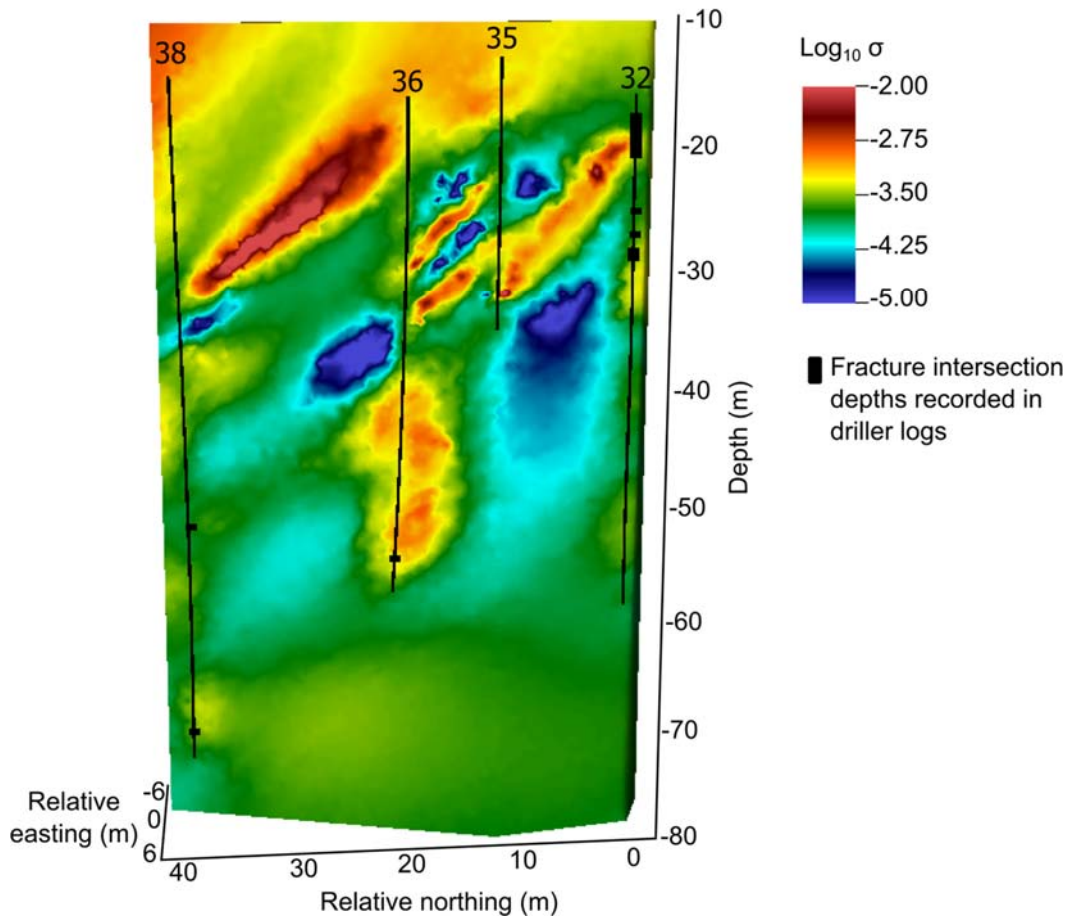

Figure C. 6: Inversion results from ERT data collected between boreholes pairs BM32/BM35, BM35/BM36 and BM36/BM38.

Single-hole GPR logs were collected to assess the travel time of the first arrival and the amplitude of the first arrival, which provided velocity, dielectric permittivity, and relative attenuation of the rock at the borehole wall. An analysis of the direct arrival of the radar waves and attenuation is used to identify low-velocity zones that might be related to fractures or contrasts in rock types (Figure C7 at depths of 24-27 m and 36-41 m, which coincides with felsic zones in the OTV log). Results in BM36 show little change in the velocity of the bedrock between the bottom of casing at 15.5 m and an anomalously high conductivity zone at 41 m to the bottom of the borehole. GPR indicated an average velocity of 107 meters per microsecond (m/us), which was used to determine the distance to reflectors, the radial depth of penetration, and dip of reflectors in the directional GPR.

145
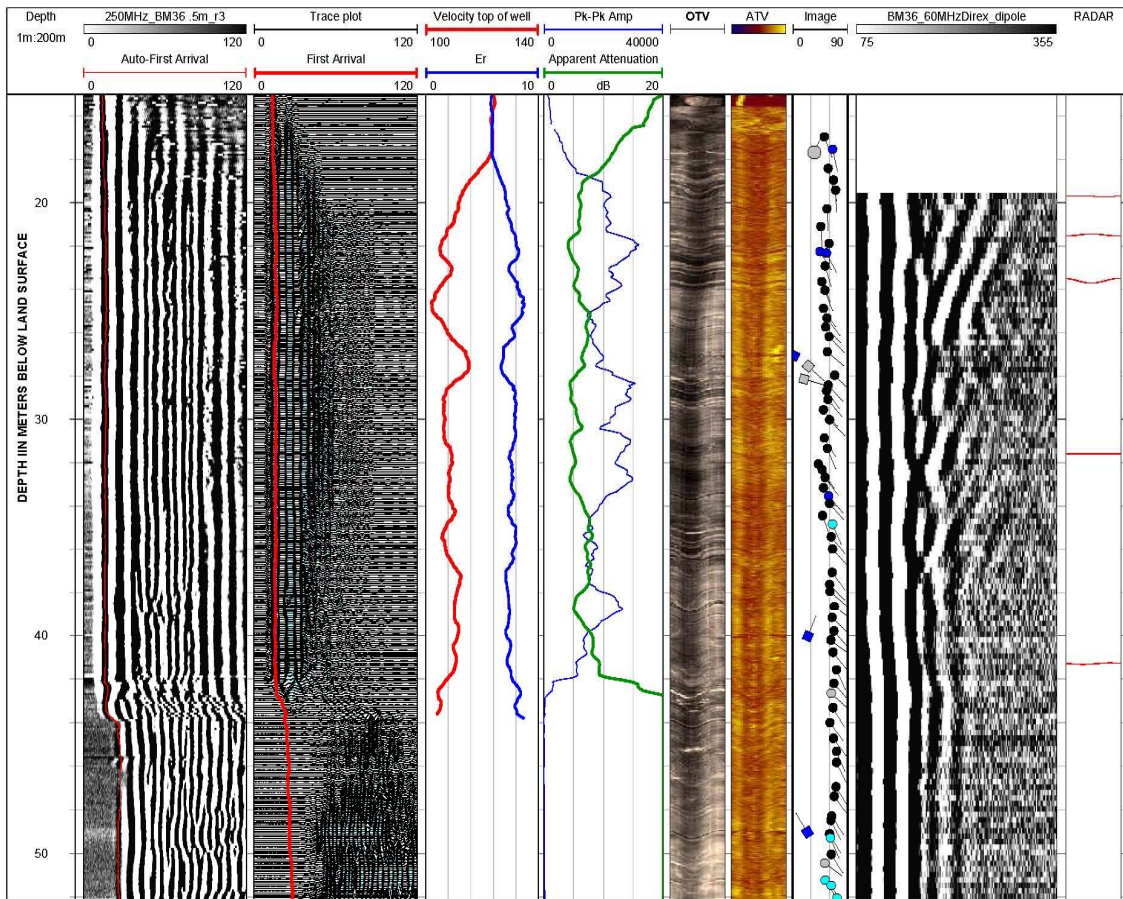
Figure C.7: Single hole GPR data collected in BM36. 250 MHz reflection data, first arrival, velocity, dielectric permittivity (Er), amplitude, and apparent attenuation are shown the four left panels of data. Radar logs can be directly compared to OTV, ATV, and tadpole plots from borehole imaging. The panel on the far right shows the dipole component of the 60-MHz DBHGPR data collected in BM36.

DBHGPR data were inspected for zones that were characterized by a lower velocity and higher attenuation (relative to the surrounding rock), which are consistent with water filled fractures. A few chevron-like reflectors are visible in the dipole component of the 60-MHz directional radar data (right panel in Figure C.7, depths of approximately 28, 36 and 42 meters). The directional radar data were interpreted for depth and orientation of features that intersect the borehole and features whose projections intersect the borehole below the full depth of the well or above open section of the borehole or above the land surface (as indicted by a negative depth). Reflectors identified in the DBHGPR are summarized in Table C1. For radar surveys collected at the site radar reflections were detected up to 15-20 m from the borehole. The features interpreted in the DBHGPR data are shown graphically in the form of projection plots, tadpole plots, and stereoplots to depict the orientation of the features (Figure C.8). In addition, three-dimensional displays of the fracture networks underscore that many of the features identified do not intersect boreholes (Figure C.9), highlighting one of the major strengths of directional borehole radar to see beyond boreholes. The majority of features strike to the northeast and have shallow to

146

moderate dips towards the southeast. A steeply dipping feature was observed in the bedrock surrounding the borehole, and projects to a depth of about 10 m (behind casing).
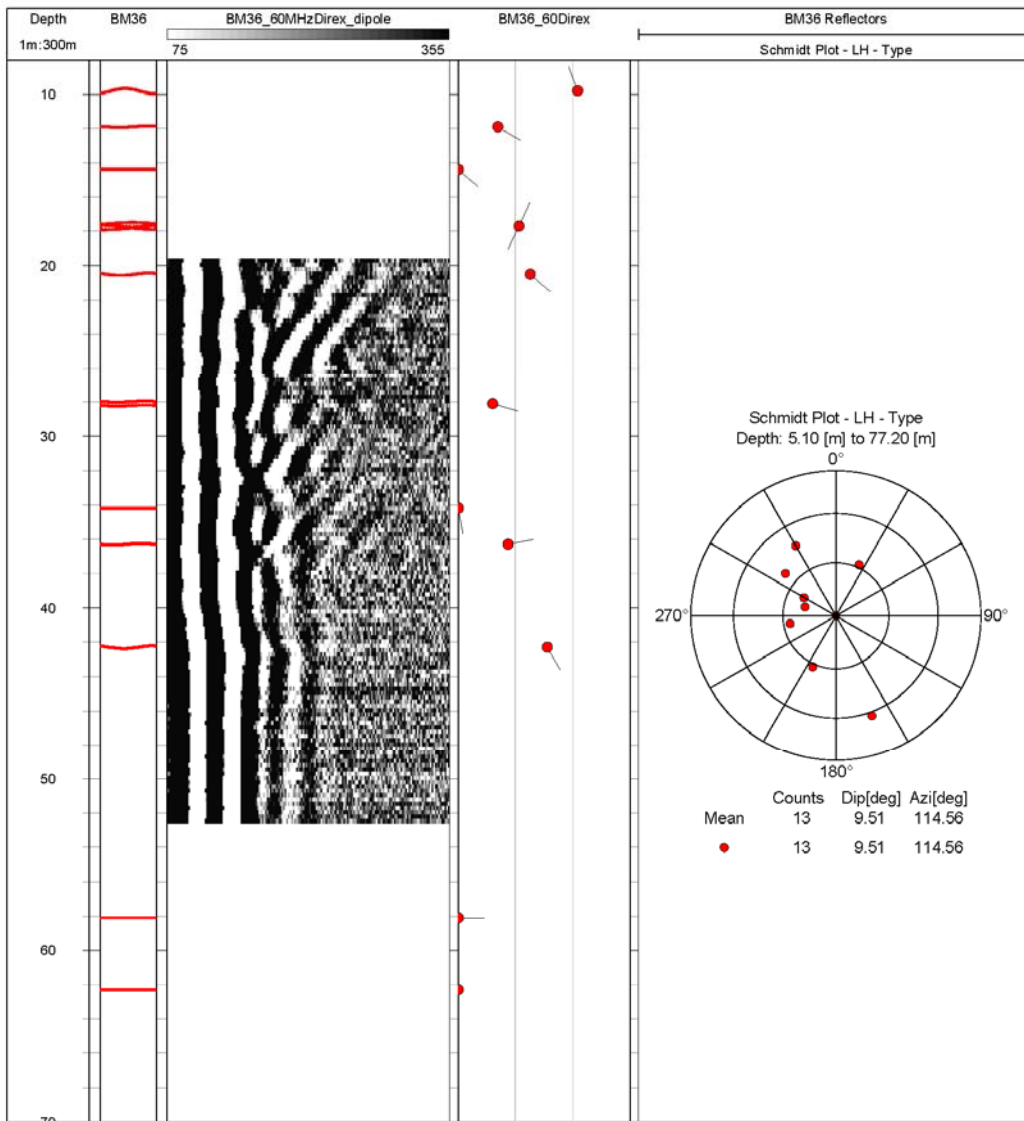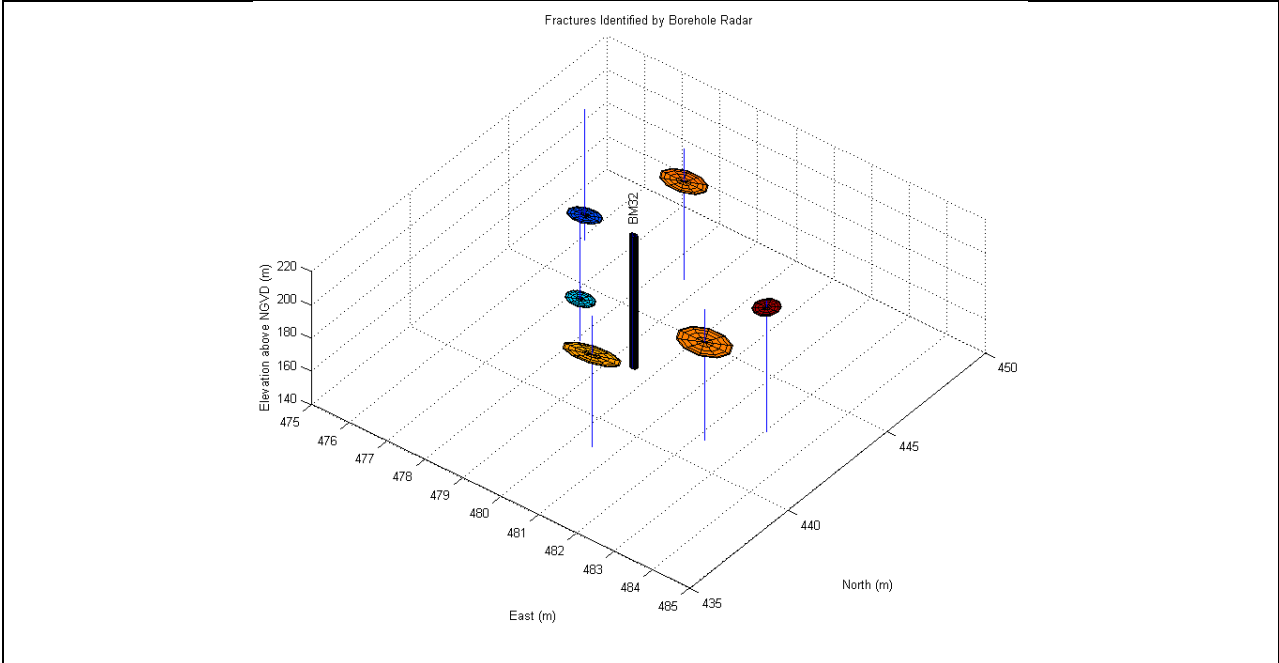

Figure C.8: Interpretation of oriented features identified in directional GPR data. The projected image (far left, are in direct comparison with image data), tadpole, and stereographic projection plots.
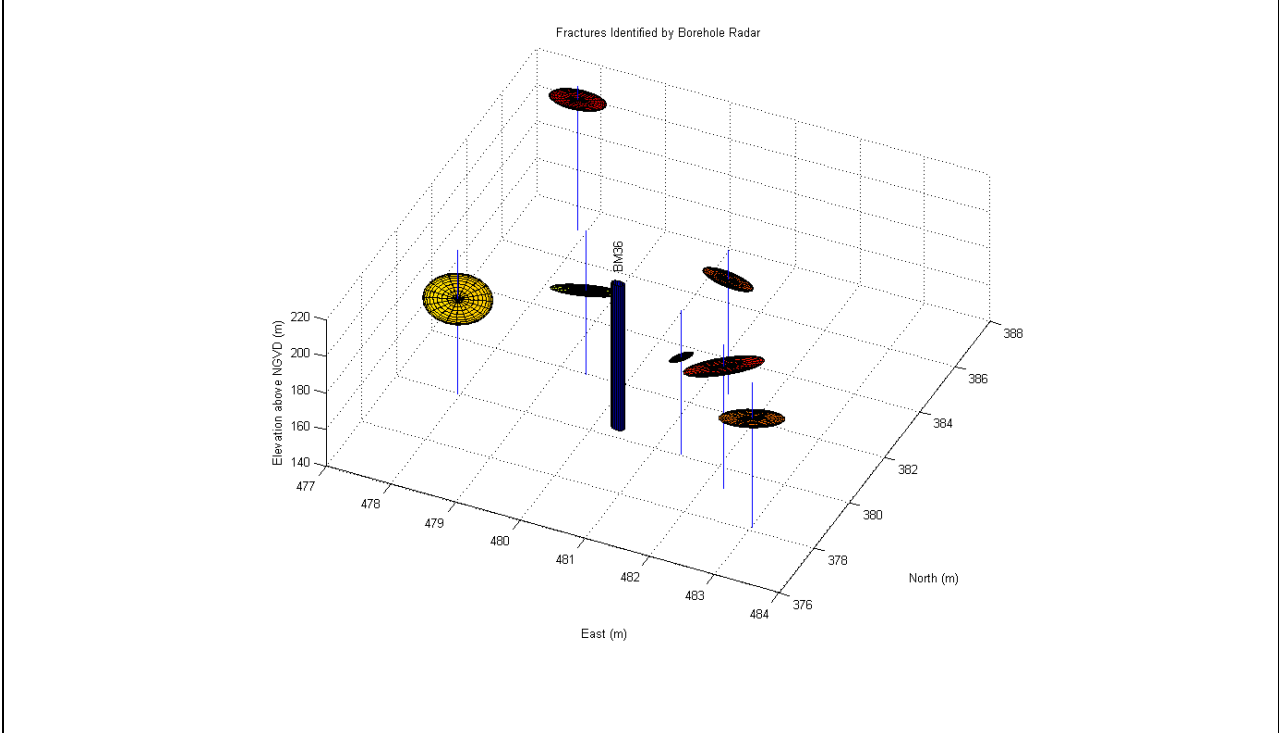
(A)

(B)

Figure C.9: Borehole reflection-mode GPR for (A) BM32 and (B) BM36. Data were processed to identify reflector orientation and extent, and are visualized here as planar disks. Note that not all features intersect the borehole. Fractures are colored according to elevation to facilitate visualization.
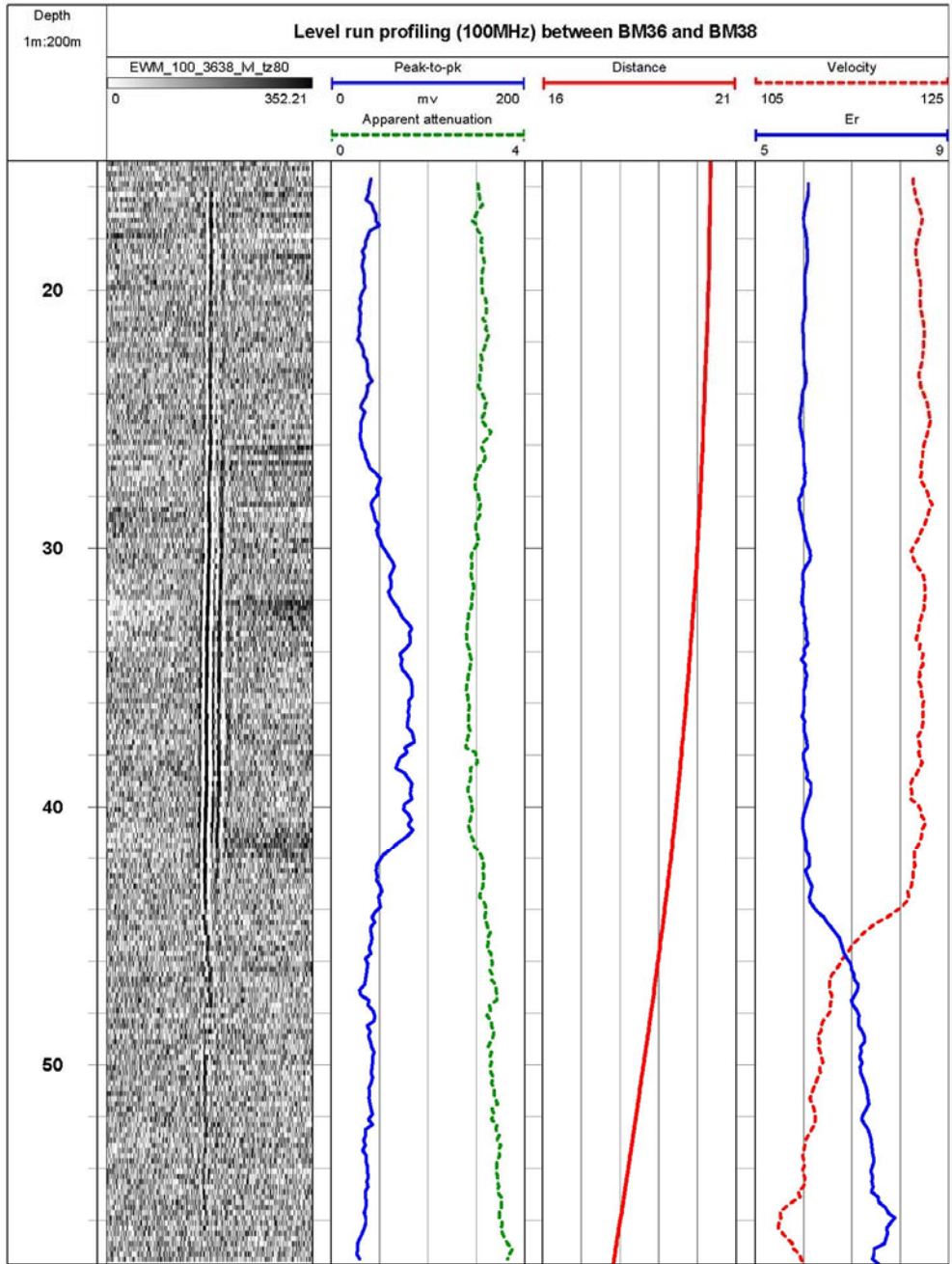
Figure C.10: Level run profiling between BM36 and BM38. Transmission velocity, dielectric permittivity, and apparent attenuation were computed for profile.

Hole–to-hole level run profiling between BM36 and BM38 showed a weak but discernible first-arrival signal across the approximate 20 m spacing. The transmission velocity was computed using the first arrival time and the inter-well spacing corrected for the borehole deviation. Results indicate a decline in the velocity and increase in attenuation in the lower part of the profile, which is consistent with the zone of increased electrical conductivity imaged in the bottom of BM36 (Figure C6). The signal strength in the BM36 to BM38 profile was lower than

149

the signal strength between the shorter-spaced well pair BM35 to BM36 (Figure C.11). No large scale structures are evident in the transmission profiles.
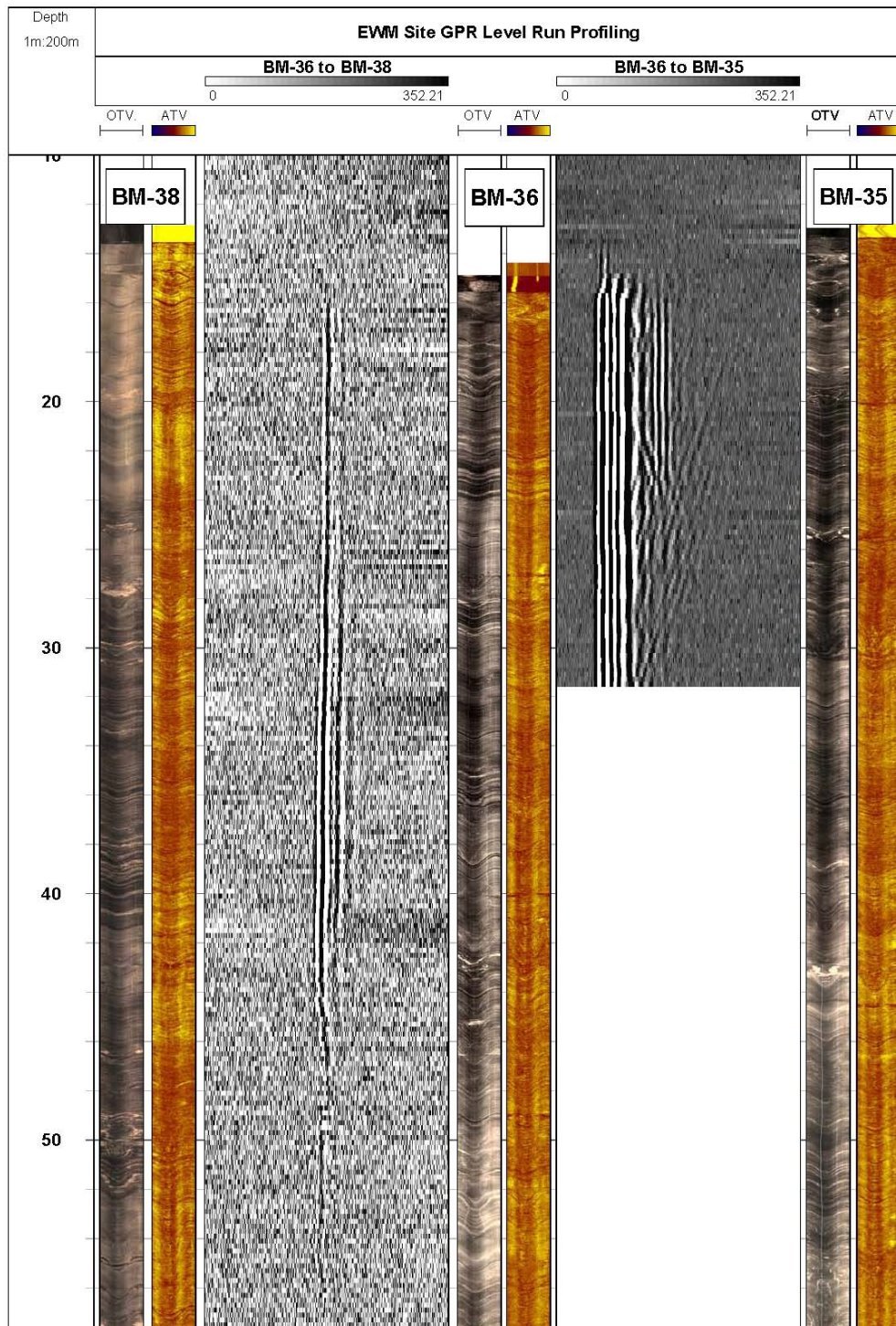

Figure C.11: Comparison of borehole image logs and level-run GPR between BM-38, BM-36, and BM-35.
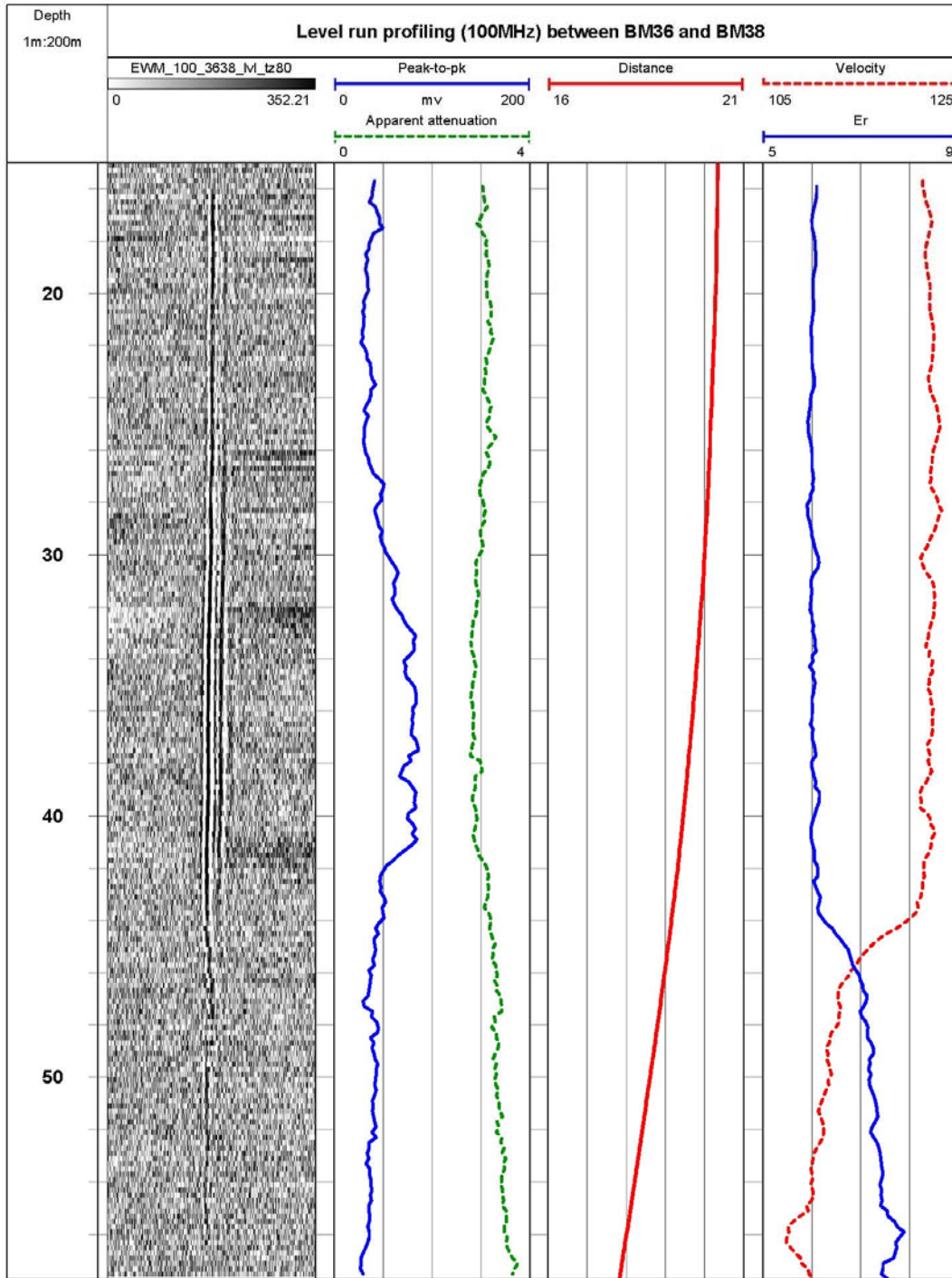
Figure C.12: Results of level-run data profiling between well pairs BM 36 and BM 38 using the 100 MHz antennas.

Table C.1: Summary of the reflectors identified with DBHGPR data

Depth (m)	Depth (ft)	Dip Azimuth (Magnetic North)	Strike (Magnetic North)	Dip	Reflector Identified (U=Upper, L=Lower, C=Crossing (both limbs))	OTV and/or Radar	Reflector Continuity (1= very good, 5=poor)	Directional Confidence (1=very strong, 5=un-certain)	Imaged Reflector Length (m)	Reflector Length from Borehole (m)	Notes
9.8	32.2	340	250	62.6	L	radar only	5	4	0.9	7.68	Reflector was imaged far from the borehole, and was not imaged near the borehole
11.9	39.0	120	30	20.7	L	radar only	4	2	1.62	5.52	
14.4	47.2	130	40	0	L	radar only	5	4	0*	0*	
17.7	58.1	24.5	294.5	31.9	L	OTV	4	5	0.90	4.40	+/- 180 degrees, differs from televiewer interpretation
20.5	67.3	130	40	37.6	L	radar only	4	4	1.11	5.17	
28.1	92.2	106.4	16.4	18.1	L	OTV	5	5	0.62	3.25	
34.2	112.2	170	80	0	L	radar only	5	5			unable to trace distance
36.3	119.1	80	350	26.2	U	radar only	4	4	2.00	5.60	
42.3	138.8	150	60	46.6	U	radar only	4	4	1.11	4.75	
58.1	190.6	90	0	0	U	radar only	5	4	0*	0*	
62.3	204.4	330	240	0	U	radar only	4	5	0*	0*	+/- 180 degrees

ND: Not determined

Strike is in right-hand-rule, where the dip is 90 degrees to the right of strike

Code indicates the color code used in the televiewer interpretation (in WellCAD)

* A horizontal reflector will have a reflector length of zero

APPENDIX D: EXAMPLE COURSE EVALUATIONS FROM TECH TRANSFER EFFORTS

This project involved a substantial technology transfer effort where end-user reservations were specifically addressed through lectures, field demonstrations and hands-on Q&A sessions with individuals. In total, our tech-transfer courses directly engaged 230 remediation professionals and regulators. Feedback on the courses has been overwhelmingly positive. Evaluations obtained from the short courses were generally very good to excellent and the field demonstrations were very popular. Numerous potential end users commented that the field demonstrations were critical to helping them understand the concepts behind the FRGT techniques and the relevance of the approach to their own field sites. Course evaluation materials for two of the short courses are provided in this appendix.

[1] **A Short Course in Contaminated Fractured Rock Hydrogeology and Geophysics, 04/30/2013**: this course was offered for 8 hours of continuing education credits to licensed remediation professionals in NJ and PA. The course was hosted by the American Institute of Professional Geologists (AIGPG) – Northeastern Section (licensing organization). The course was run at College of New Jersey (Trenton) with field demonstrations at the Naval Air Warfare Center (NAWC) project demonstration site.

[2] **A Short Course in Contaminated Fractured Rock Hydrogeology and Geophysics 11/19/2013-11/20/2013**: This course was held at U. Connecticut and utilized demonstration wells available at the USGS office in Storrs, CT for the field demonstrations. Co-PI Day-Lewis led this effort that was offered to environmental professionals through the Environmental Professionals Organization of Connecticut (EPOC) for eight Continuing Education Course (CEC) technical credits. Due to the significant field component, this one-day course was taught two days in a row, November 19-20, with approximately 50 environmental professionals attending this course each day. Feedback on the course was overwhelmingly positive, with numerous attendees praising the field demonstrations and the hands-on element of the short course.